Ultra-coherent nano-mechanical resonators for quantum optomechanics at room temperature

PAR

Amir Hossein GHADIMI

acceptée sur proposition du jury:

Prof. C. Moser, président du jury
Prof. T. Kippenberg, directeur de thèse
Prof. M. Roukes, rapporteur
Prof. Ph. Feng, rapporteur
Prof. G. Villanueva, rapporteur

ÉCOLE POLYTECHNIQUE
FÉDÉRALE DE LAUSANNE

Suisse
2018

To my parents, who were my first science teachers in life,
To their sanctifies and their support in every step of my life.

Acknowledgements

Working in experimental physics, demands a certain degree of vision, precipitant, patience and a great team. I was fortunate to work with and around many people that supported me in different steps of this long path. I want to thank all these individuals who either directly on indirectly had positive impact on my PhD. First and most important, my thesis advisor, *Prof. Tobias Kippenberg*. When I first met Tobias, I was only a young bold bachelor student with no particular experience with mico-fabrication or optical measurements. He decided to give me the opportunity to join his lab, one of the best labs in the world. Working with Tobias is very hard and challenging as he is a very demanding advisor. But if you are a dedicated hardworking student who enjoys science and working long hours in the lab with tons of idea, it is hard to find any advisor better than Tobias. He has the resources and more importantly the vision and the courage to listen to the ideas and support them, no matter how naive and crazy they sounds, . Even if it is against his personal belief. He gave me the complete freedom and support to follow my own ideas during my PhD. This experience although was extremely difficult and challenging, as working alone on high risk projects costs me few extra years in PhD and lots of sleepless nights, it was worth it and extremely fruitful at the end. An example of this, is when I proposed the grand idea of ultra-high C_0 project and the ultra-high Q resonators as its first phase at the beginning of my forth year. By the end of my third year, I have worked on several different projects with few minor results and no paper of my own. In this situation, any other professor wouldn't take my proposal seriously. But Tobias was open minded enough to put his trust on my proposal as a completely new direction in his lab, on a student who should have have been considered a failed PhD student at that time by any measurable metric, and give me the chance and resources to pursue it. Three years later, this project resulted in the most important achievement of my PhD including several major publications such a publication in Science. It is joyful to see that my proposal is now the main research direction of the optomechanics team in our lab and will be followed by next generation of students. There are no proper way for me to truly thanks Tobias. I only hope I have shown and that I deserved his supports by my hardworking and success in future.

I couldn't finish my PhD without the support and guidance of one individual: *Dr. Dalziel Wilson*. Dal has been more than just my postdoc and colleagues. He was my closest fiend in the lab, a great mentor and an older brother. Everything that I know about optics, optomechanics, writing scientific articles and scientific thinking, I learn it from Dal. He is my oldest and longest collaborator and the only team member that I had for many years. Not only he personally trained me in the lab, down to how to align a mirror or pull a tapered fiber or make

Abstract

Mechanical oscillators are among the most important scientific tools in the modern physics. From the pioneering experiments in 18th by founding fathers of modern physics such as Newton, Hooke and Cavendish to the ground braking experiments in the 21th century where the merge of two massive black holes 1.3 billion light-year away detected on earth by a gravitational wave detectors[1], the high Q mechanical oscillators were at the core of many monumental experiments in physics. Their ability to couple to many different physical quantities such as mass [2, 3], charge[4], acceleration[5], electro-magnetic forces[6] and optical fields[7] makes them an ideal candidate for sensing applications. In addition, their intrinsically low dissipation rates (Γ_m) results in reduced coupling to the thermal bath. Since the invention of micro/nano-technology in the second half of the 20th century and ability to control the dimensions at micro and nano-scales, new horizon was opened up for mirco/nano-mechanical oscillators. Miniaturization of the mechanical oscillators made them small and stiff enough to be used in our handheld electronics where dozens of mechanical sensors such as accelerometers and gyroscopes are used in our laptops and smartphones everyday.

Besides these technological advancements, since the beginning of 21th century, a new opportunity for mechanical oscillators emerged: the idea of "putting mechanics into quantum mechanics"[8] and observing the quantum effects of these massive classical oscillators. Aside from the numerous technical challenges for achieving this goal, two fundamental obstacles has to solved: **I)** Even the smallest nano-mechanical oscillators still consist of billions of atoms and molecules and are orders of magnitude more massive that the traditional "quantum objects" such as atoms and molecules. Larger mass results in smaller zero point motion — the length scale where quantum effects are visible — which means in order to "see" these quantum effects, we have to detect smaller displacement than ever before [9]. **II)** The second challenge is the low frequency of the mechanical oscillators which makes their thermal Brownian energy, orders of magnitude larger than the quantum ground state of the oscillator — the energy scale where the quantum effects are visible — as $\bar{n}_{\text{th}} \approx \frac{k_B T}{\hbar \Omega} \gg 1$ even for a $\Omega/2\pi \sim 1$ GHz oscillator at room temperature.

Both of these obstacles, can be seen as the competition between few fundamental rates: thermal decoherence and measurement rate/mechanical frequency. Thermal decoherence is the rate at which the mechanical oscillator exchange phonons — quanta of mechanical energy ($\hbar\Omega$)— with its thermal environment and is given by $\Gamma_{\text{decoherence}} = \bar{n}_{\text{th}}\Gamma_m$. The first obstacle translates to having the measurement rate being faster than the decoherence rate of the mechanical oscillator, $\Gamma_{\text{measurement}} \gg \Gamma_{\text{decoherence}}$ [10]. This means in order to see the

Acknowledgements

quantum coherent motion of the mechanical oscillator, we have to "look" at it before it has time to exchange random thermal energy with its environment. In other words, the life time of the quantum states of macroscopic objects are limited by their thermal decoherence rate and we have to interact with the oscillator in this short lifetime. The second obstacle on the other hand, reduces to having the mechanical frequency larger than its thermal decoherence rate, $\Omega_m \gg \Gamma_{\text{decoherence}}$. Over the past 15 years, the field of cavity opto-mechanics was very successful in improving the measurement schemes and designing new opto-mechanical systems with higher measurement rates. Recently measurement rate higher than decoehrence rate became possible at cryogenic temperatures[11]. The second obstacle on the other hand, is purely a mechanical design and mechanical oscillator has to be designed to be "quantum enabled"[12]. One traditional approach to reduce the thermal decoherence in the field of opto-mechanics was to operate at cryogenic temperatures to reduce $\bar{n}_{\text{th}}$. However, if we want to observe quantum effects of mechanical oscillators are room temperature — a long standing goal in the field cavity opto-mechanics — the only route to achieve this is to isolate mechanical oscillator from its thermal bath, namely reducing it dissipation rate. Therefore pursuing the mechanical oscillator with reduced dissipation, is at the core of the efforts and key to observe quantum effects of mechanical oscillators at room temperature and is the focus of this thesis. In this thesis, we review several strategies to reduce mechanical losses and achieve unprecedented mechanical quality factors. First we observe that the presence of the initial tensile stress in the mechanical oscillator, would lead to enhancement of its intrinsic material losses through a process known as "dissipation dilution"[13]. Then we study the geometrical origin of dissipation dilution through the basic equations of motion and find that "geometrical nonlinearity" is responsible for this enhancement[14]. Next we attempt to analytically calculate the dissipation dilution for the beam and membrane geometries and observe that the curvature near the clamping points (clamping losses) is the major limitation in the performance of the high stress Si_3N_4 micro-mechanical resonators. We present theoretical and experimental result of three strategies to enhance the $Q\times$ frequency product and Q/m as the two main figures of merit associated to the two fundamental challenges of observing quantum effects of micro-mechanical oscillators. In our third and most effective strategy, we demonstrate that the co-localization of flexural motion of the a Si_3N_4 with the region of geometrically enhanced stress would lead a previously unaccessible regime of mechanical quality factors. Using a spatially non-uniform phononic crystal pattern of high aspect ratio beam (thickness of 20 nm and length of 7 mm) we produce picogram-mass flexural modes with room-temperature Q factors as high as 800 million and $Q \times f$ products exceeding 10^{15} Hz — both in fact unprecedented for a mechanical oscillator of any size. At ambient temperature, the devices we study can have force sensitivities of $aN/\sqrt{Hz}$ and at the same time perform hundreds of oscillations within their thermal decoherence time. These results signal a paradigm shift in the control of dissipation in nanomechanical systems, with impact ranging from precision force microscopy to tests of quantum gravity. With these results, the long standing goal of observing the qunautm effect of macroscopic objects at room temperature is within a reach. Combining the reported material independent approach presented in this thesis with crystalline or 2D materials may lead to further improvement, of as yet unknown limitation.

x

Résumé

Les oscillateurs mécaniques font partie des plus importants outils scientifiques de la physique moderne. Depuis les expériences pionnières au 18e siècle par les pères fondateurs de la physique moderne, tels que Newton, Hooke et Cavendish, jusqu'au 21e siècle avec la mesure extraordinaire de la fusion de deux trous noirs massifs distants de 1.3 milliards d'années lumières par un détecteur d'ondes gravitationnelles sur Terre [1], les oscillateurs mécanique de haut facteur qualité (Q) ont été au coeur de bon nombre d'expériences monumentales en physique. Leur capacité à être couplés à de nombreuses différentes quantités physiques telles que la masse [2, 3], la charge [4], l'accélération [5], les forces électro-magnétiques [6] et les champs optiques [7] les rend idéaux comme senseurs. De plus, leur très bas taux de dissipation (Γ_m) les isolent du bain thermique. Depuis l'inventions des technologies à l'échelle micro et nanoscopiques dans la deuxième moitié du 20e siècle, de nouveaux horizons se sont ouvert pour les micro- et nano-oscillateurs mécaniques. Leur miniaturisation les a rendu suffisamment petits et rigides pour être utilisés dans l'électronique portable, et des douzaines d'oscillateurs sont incorporé dans chaque téléphone et ordinateur comme accéléromètres et gyroscopes de nos jours.

D'autre part, une nouvelle opportunité a émergé pour les oscillateurs mécaniques depuis le début du 21e siècle : l'idée de "mettre la mécanique dans la mécanique quantique" [8] et d'observer les effets quantiques de ces oscillateurs massifs classiques. En sus des nombreux défis technologiques pour accomplir ce but, deux obstacles fondamentaux doivent être franchis : **I)** Le plus petit nano-oscillateur est constitué de milliards d'atomes et de molécules et est plus massif que les "objets quantiques" traditionnels tels que les atomes et molécules par des ordres de grandeurs. Une plus grande masse résulte en de plus faibles fluctuations de l'état du vide (zero-point motion), qui donne l'échelle de longueur à laquelle les effets quantiques deviennent visibles. Pour pouvoir "voir" les effets quantiques, il faut détecter des déplacements à une échelle bien plus faible que précédemment [9]. **II)** Le deuxième défi est dû à la fréquence basse des oscillations mécaniques, qui rendent leur énergie thermique brownienne très grande par rapport à l'énergie de l'état fondamental quantique, qui est l'énergie à laquelle les effets quantiques sont visibles, avec $\bar{n}_{\text{th}} \approx \frac{k_B T}{\hbar \Omega} \gg 1$ pour une oscillateur de $\Omega/2\pi \sim 1$ GHz à température ambiante.

Ces deux obstacles peuvent être perçus comme une compétition entre deux taux fondamentaux : le taux de décohérence thermique et le taux de mesure/fréquence mécanique. La décohérence thermique est le taux auquel l'oscillateur mécanique échange des phonons (les quanta d'énergie mécanique ($\hbar\Omega$) avec son environnement thermique, donné par

Acknowledgements

les systèmes que nous étudions peuvent avoir des sensibilité de force d'un aN/$\sqrt{\text{Hz}}$ et en même temps osciller des centaines de fois pendant le temps de décohérence. Ces résultats signalent un changement de paradigme dans le control de la dissipation pour les systèmes nanomécaniques, avec des applications tels que la microscopie de force ou pour tester la gravité quantique. Avec ces résultats, le but de longue date d'observer les effets quantiques d'objets macroscopiques à température ambiante devient atteignable. Combiner l'approche présentée dans cette thèse qui est indépendante du matériau, et des matériaux crystallins ou bidimensionnels pourrait mener à des améliorations supplémentaires, sans qu'une limite soit pour l'instant connue.

Zusammenfassung

Mechanische Oszillatoren gehören zu den wichtigsten wissenschaftlichen Hilfsmitteln in der modernen Physik. Von den Experimenten der Gründern der modernen Physik wie Newton, Hook und Cavendish bis zu bahnbrechenden Experimenten im einundzwanzigsten Jahrhundert, wo die Vereinigung zweier massiver schwarzer Löchern 1.3 Milliarden Lichtjahre entfernt auf der Erde mittels Gravitätswellendetektoren beobachtet wurde [1]. Mechanische Oszillatoren mit hohem Qualitätsfaktor Q waren der Schlüssel zu vielen monumentalen Experimenten in der Physik. Ihre Fähigkeit die verschiedenen physikalischen Grössen wie Masse [2, 3], Ladung [4], Beschleunigung [5], elektromagnetische Felder [6] und optische Felder [7] zu koppeln macht sie zum idealen Kandidaten für Messanwendungen. Zusätzlich führen ihre intrinsisch sehr kleinen Dissipationsraten (Γ_m) zu einer verringerten Kopplung zum thermischen Bad. Die Erfindung der Mikro- und Nanotechnologie in der zweiten Hälfte des zwanzigsten Jahrhunderts und damit der Möglichkeit Dimensionen in der Mikro- und Nanoskala zu manipulieren, öffnete einen neuen Horizont für mikro- und nanomechanische Oszillatoren. Das Miniaturisieren der mechanischen Oszillatoren machte sie klein und steif genug um in unserer Alltagselektronik, wie beispielsweise dutzende mechanische Sensoren wie Akzelerometer und Gyroskope in unseren Laptops und Smartphones, verwendet zu werden.

Neben diesen technologischen Fortschritten seit dem einundzwanzigsten Jahrhundert entwickelte sich eine neue Möglichkeit für mechanische Oszillatoren: die Idee von "Mechanik in der Quantenmechanik" [8] und der Beobachtung von Quanteneffekten von massiven klassischen Oszillatoren. Neben den zahlreichen technischen Herausforderungen um dieses Ziel zu erreichen müssen zwei fundamentale Probleme gelöst werden: **I)** Selbst die kleinsten nanomechanischen Oszillatoren bestehen aus Milliarden von Atomen und Molekülen und sind damit Grössenordungen schwerer als traditionelle "Quantenobjekte" wie einzelne Atome und Moleküle. Grössere Masse führt zu einer kleineren Nullpunkt-Bewegung, jene Längenskala auf der Quanteneffekte sichtbar sind. Das bedeutet, um diese Quanteneffekte zu "sehen", müssen wir kleinere Verschiebungen als je zuvor messen [9]. **II)** Die zweite Herausforderung ist die niedrige Frequenz mechanischer Oszillatoren, welche die thermische Energie Grössenordnungen grösser sein lässt als die Grundzustandsenergie des mechanischen Oszillators – die Energieskala auf der Quanteneffekte sichtbar sind – weil $\bar{n}_{\text{th}} \approx \frac{k_B T}{\hbar \Omega} \gg 1$ selbst für einen $\Omega/2\pi \sim 1$ GHz Oszillator bei Raumtemperatur ist.

Beide diese Hürden können als ein Wettstreit zweier fundamentaler Raten gesehen werden: thermische Dekohärenzrate und Messrate/mechanische Frequenz. Die thermische Dekohärenzrate mit der mechanische Oszillator Phononen – Quanta der mechanischen Energie

Acknowledgements

($\hbar\Omega$) – mit seiner Umgebung austauscht. Diese ist gegeben durch $\Gamma_{\text{decoherence}} = \bar{n}_{\text{th}}\Gamma_m$. Die erste Hürde lässt sich als Messrate schneller als Dekohärenzrate eines mechanischen Oszillators interpretieren, $\Gamma_{\text{measurement}} \gg \Gamma_{\text{decoherence}}$ [10]. Dies bedeutet, dass man um quantenmechanische Effekte zu beobachten, bevor der Oszillator zufällige thermische Energie mit seiner Umgebung ausgetauscht hat, "schauen" muss. In anderen Worten, die Lebenszeit eines Quantenzustands eines makroskopischen Objektes ist durch die thermische Dekohärenzrate limitiert und damit müssen wir mit ihm in dieser kurzen Lebenszeit interagieren. Die zweite Hürde lässt sich darauf herunterbrechen, dass die mechanische Frequenz grösser als die mechanische Dekohärenzrate sein muss, $\Omega_m \gg \Gamma_{\text{decoherence}}$. In der letzten fünfzehn Jahren war das Feld der Kavitätenoptomechanik im Verbessern dieser Messverfahren und der Entwicklung neuer optomechanischer Systeme mit hohen Messraten sehr erfolgreich. Neulich würden Messraten höher als die Dekohärenzrate in kryogenischen Temperaturen erreicht [11]. Die zweite Hürde ist dahingegen rein mechanischer Natur. Es muss ein mechanischer Oszillator entworfen werden, um "quantenfähig"zu sein [12]. Ein traditioneller Ansatz, die thermische Dekohärenzrate im Feld der Quantenoptomechanik zu reduzieren, ist es das Experiment bei kryogenischen Temperaturen zu betreiben, um die mittlere thermische Besetzungszahl $\bar{n}_{\text{th}}$ zu reduzieren. Um jedoch Quanteneffekte eines mechanischen Oszillators bei Raumtemperatur zu beobachten– ein seit Langem bestehendes Ziel der Quantenoptomechanik–, führt kein Weg an der Isolierung des mechanischen Oszillators von seiner thermischen Umgebung, also der Reduzierung der Dissipationsrate, vorbei. Daher ist ein mechanischer Oszillator mit verringerter Dissipation einer der Hauptanstrengungen und der Schlüssel, um Quanteneffekte mechanischer Oszillatoren bei Raumtemperaturen zu messen und der Fokus dieser Arbeit.

In dieser These stellen wir verschiedene Strategien vor, um mechanische Verluste zu verringern und beispiellos hohe Qualitätsfaktoren zu erreichen. Zuerst beobachten wir, dass die Anwesenheit von ursprünglicher Zugspannung im mechanischen Oszillator zu einer Verstärkung der intrinsischen Materialverluste durch einen Prozess namens "Verlustsverdünnung"[13] führt. Später studieren wir die geometrischen Ursprünge von Verlustsverdünnung durch die grundlegenden Bewegungsgleichungen und finden heraus, dass "geometrische Nichtlinearitäten" für diese Verstärkung zuständig sind [14]. Danach versuchen wir analytisch die Verlustsverdünnung von Balken- und Membrangeometrien zu berechnen und beobachten, dass die Krümmung nahe der Klemmpunkte (Klemmverluste) die grösste Limitierung in dem Betriebsverhalten von Hochspannungs-Si_3N_4-Mikroresonatoren darstellt. Wir stellen sowohl theoretische als auch experimentelle Resultate vor, die $Q\times$-Produkt und Q/m, welche die zwei Gütezahlen in Verbindung mit den zwei fundamentalen Herausforderungen Quanteneffekte eines mechanischen Oszillators zu beobachten, sind, verbessern. In unserer dritten und effektivsten Strategie zeigen wir, dass die Delokalisierung von Flexbewegungen in Si_3N_4 mittels geometrisch verstärkter Spannung zu einem zuvor unerreichten Regime von mechanischen Quatiltätsfaktoren führt. Mit räumlich nicht-uniformen phononischen Kristallstrukturen auf Balken mit hohem Aspektverhältnis (Dicke von 20 nm und Länge von 7 mm) produzieren wir Pikogramm schwere Flexmoden mit Raumtemperatur Q-Faktoren von bis zu 800 Millionen und $Q \times f$-Produkten über 10^{15} Hz – beide unübertroffen für mechanische Oszillatoren jeder Grösse. Bei Umgebungstemperatur erreichen die Geräte, die wir studieren,

Kräftesensitivitäten von aN/$\sqrt{\text{Hz}}$ und können zur selben Zeit hunderte von Oszillationen während ihrer thermischen Dekohärenzzeit durchführen. Diese Resultate signalisieren einen Paradigmenwechsel in der Kontrolle von Dissipation in nanomechanischen Systemen mit Einfluss von Präzisionskraftmikroskopie bis zu Quantengravitation. Mit diesen Resultaten scheint das seit Langem bestehende Ziel, Quanteneffekte von makroskopischen Objekten bei Raumtemperatur zu beobachten, in Reichweite. Die Kombination des materialunabhängigen Ansatzes, präsentiert in dieser Arbeit, mit kristallinen oder 2D Materialien kann zu weiteren Verbesserungen mit unbekannten Limitationen führen.

List of Publications

- **A.H. Ghadimi**, S.A. Fedorov, N.J. Engelsen, M.J. Bereyhi, R. Schilling, D.J. Wilson, T.J. Kippenberg. "Elastic strain engineering for ultralow mechanical dissipation", **Science**, eaar6939, 2018

- **A.H. Ghadimi**, D.J. Wilson, T.J. Kippenberg. "Radiation and internal loss engineering of high-stress silicon nitride nanobeams ", **Nano letter**, Vol 17, Issue 6, pp 3501–3505, 2017

- M.J. Bereyhi, A Beccari, S.A. Fedorov, **A.H. Ghadimi**, R. Schilling, D.J. Wilson, N.J. Engelsen, T.J. Kippenberg. "Clamp-tapering increases the quality factor of stressed nanobeams ", **Arxiv**, arXiv:1810.00414, 2018

- S.A. Fedorov, N.J. Engelsen, **A.H. Ghadimi**, M.J. Bereyhi, R. Schilling, D.J. Wilson, T.J. Kippenberg. "Generalized dissipation dilution in strained mechanical resonators", **Arxiv**, arXiv:1807.07086, 2018

- V. Sudhir, D.J. Wilson, R. Schilling, H. Schütz, S.A. Fedorov, **A.H. Ghadimi**, A. Nunnenkamp, T.J. Kippenberg. "Appearance and Disappearance of Quantum Correlations in Measurement-Based Feedback Control of a Mechanical Oscillator", **Physical Review X**, Vol. 7, Issue 1, 2017

- R. Schilling, H. Schütz, **A.H. Ghadimi**, V. Sudhir, D.J. Wilson, T.J. Kippenberg. "Near-Field Integration of a SiN Nanobeam and a SiO 2 Microcavity for Heisenberg-Limited Displacement Sensing", **Physical Review Applied**, Vol. 5, Issue 5, 2016

- D.J. Wilson, V. Sudhir, N. Piro, R. Schilling, **A.H. Ghadimi**, T.J. Kippenberg. "Measurement-based control of a mechanical oscillator at its thermal decoherence rate", **Nature**, Vol. 524, pp. 325-329, 2015

- S. Manzeli, A. Allain, **A.H. Ghadimi**, A. Kis. "Piezoresistivity and strain-induced band gap tuning in atomically thin MoS2", **Nano letter**, Vol. 15, pp. 5330–5335, 2015

In progress:

- **A.H. Ghadimi**, T.J. Kippenberg. "Ultra-high cooprativity near-field optomechanical systems for quantum coherent control at room temperature"

- **A.H. Ghadimi**, M.J. Bereyhi, D.J. Wilson, T.J. Kippenberg. "Fabrication of ultra high aspect ratio Si_3N_4 nano-beam resonators with reduced dissipation "

Contents

Contents

1 Ultra-high-Q mechanical resonators

1.1 History of the pursuit of the high-Q mechanical resonators

From the early days of classical mechanics, in the pioneering experiments by the founding fathers of modern physics such as Newton, Hooke and other leading scientists of 18th and 19th century, mechanical oscillators were the work horse of modern science. In fact, many of these initial experiments were "optomechanical" experiments, a canonical example is the Cavendish's experiment. In a fascinating series of experiments in 1798, Henry Cavendish used "torsion balance" mechanical oscillators in what could be considered as the first optomechanical experiment to measure the gravitational constant, G [16]. In this experiment, schematically illustrated in Fig. 1.1, the torsion balance is made of two 0.73 Kg lead spheres attached to opposite ends of a 1.8 m wooden rod (red spheres in Fig. 1.1.b) and the entire system was suspended from the roof by a wire 51 mm in diameter. Then two 300 mm lead balls weighting 158 kg each, were positioned on the alternate sides of the resonator (gray spheres in Fig. 1.1.b). The gravitational attraction between the small and the large lead balls causes the arm to rotate, twisting the wire in the process. The arm would come to a resting angle where the twisting force of the wire balances the gravitational force between the balls. By measuring the rotation angle of the small spheres and calibrating the torsion coefficient [1] of the wire (by measuring

---

[1] Torsion coefficient is the equivalent of the spring constant for torsional modes in the angular form of the Hooke's law: $\tau = -\kappa\theta$, where τ is the torque, κ is the torsion coefficient and θ is the angle.

the natural resonance frequency of the torsion balance oscillator), Cavendish was able to measure G more than 3 centuries ago with amazing precision. His recorded value defers only by 1% from 2014 recommended value of 6.67408×10^{-11} m^3 kg^{-1} s^{-2} set by CODATA[2] [17].
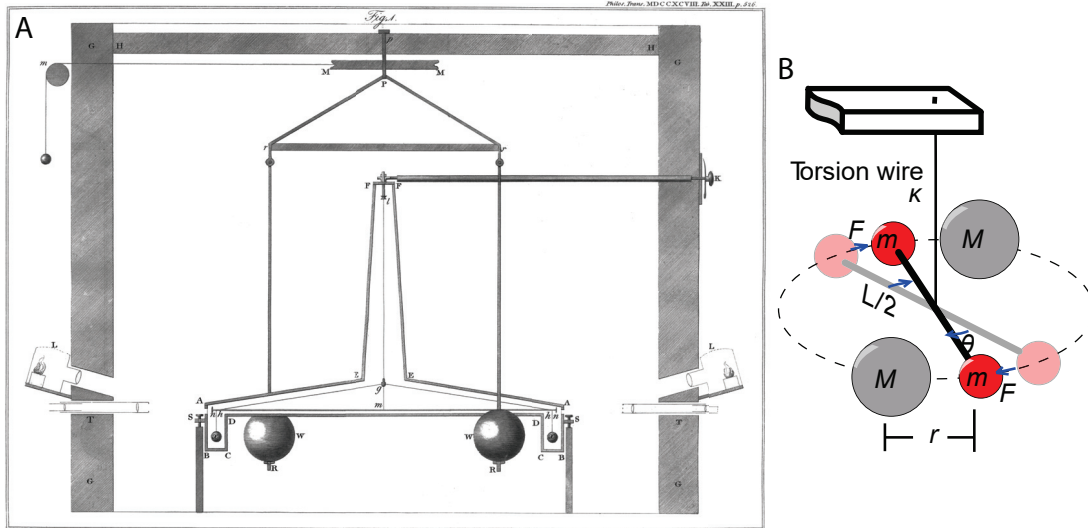
Figure 1.1 – **Cavendish's experiment for measuring the gravitational constant, G.** A) The original figure from Cavendish's 1798 paper [16] at Philosophical Transactions of the Royal Society of London. B) Schematic representation of the experiment (taken from [18])

There are several interesting facts worth noting about the Cavendish's experiment. An experimental apparatus built more than 300 years ago,which still bares interesting resemblance to today's modern optomechanical experiments:

1. To prevent air currents and temperature fluctuations from interfering with his measurements, Cavendish placed the entire apparatus in a closed wooden box with 61 cm thick walls and dimensions of 10m×3m×3m. This is similar to the vacuum chambers and temperature isolation stages used in modern experiments to isolate the system from gas damping and temperature fluctuations.

2. At its core, Cavendish's experiment was an optomechanical force sensor. With his setup, he was able to measure forces as small as 1.74×10^{-7}N equivalent to approximately 5×10^{-5} times smaller than the weight of his test masses [16], a remarkable sensitivity for its time. Cavendish measured the force by detecting the displacement of a mechanical resonator, a method still used in modern force sensors [6]. It is interesting to note that over the past 300 years and even today, mechanical oscillators, whether they are used in macro or micro dimensions, are among the best choices and transducers of force [6], acceleration [5], mass [2, 3], charge [4] and etc.

3. Similar to a modern optomechanical sensor, Cavendish used optical techniques to measure the displacement of his test masses. As illustrated in Fig. 1.1.a, he shined

---

[2]International Council for Science Committee on Data for Science and Technology

collimated light (analogous to the modern lasers) from one of the two holes in the walls and observed the displacement via a telescope mounted on the second hole on the other wall (analogous to the modern photodetectors, he used his eyes as the detector). With this technique he was able to measure displacements with accuracy better than 25μm, a record which stood for nearly a century until it was eventually beaten by Charles V. Boys in 1894 [19], [20].

After this "*golden era*" of the mechanical oscillators as an essential instrument in the scientific community in 18th and early 19th centuries, simultaneously by the discovery of electricity, electromagnetism, relativity and quantum mechanics, mechanical oscillators slowly lost their importance in the frontier scientific research. It would be decades in the future before the technology is advance enough to allow the control of dimensions at micro and nano-scales paving the way to fabrication of the first [21] *micro-electro-mechanical systems* (MEMS), a new golden age for mechanical oscillators in which dozen of different mechanical based sensors, clocks, RF filters and switches are used in our smartphones, laptops and other electronic products. One exception to this trend (dark age of mechanical oscillators) was the watch industry, which continued to rely on the stable resonance frequency of the mechanical resonators for time keeping purposes. Quartz crystal oscillator were invented at Bell labs in 1918 [22], and have ruled the time keeping industry for decades including today. This is mainly due to two factors: **I)** their intrinsically high quality factor ($\sim 10^6$) at room temperature [23] which leads to low phase noise. **II)** small long term drifts achieved with specific cut angles. Over the course of many years, engineers in the quartz industry have learned to cut crystals in specific angles such as AT-cut (temperature-compensated) [24] or SC-cut (stress-compensated) [25] where the resonance frequency has the minimum susceptibility to temperature and other environmental fluctuations. Quartz oscillators creates a platform not for stable time keeping, but also for studying the physics of mechanical loss. In deed, it should be emphasized that to the best of our knowledge, the highest quality factor that has ever been reported for an engineered mechanical oscillator at any temperature is 8×10^9 at 204 MHz, achieved for the 65th overtone of a SC-cut commercial planoconvex quarts oscillator measured at 3.75 K [26].

Continuing with the history of high Q mechanical oscillators, after this period of down fall of mechanical oscillators from the frontiers of scientific research, in an interesting turn of events, it was again *gravity* which brought mechanical oscillators back to the fore front of the scientific community. In the mid-20th century through their efforts to detect the gravitational waves [1], predicted by Einstein's theory of general relativity [27] that researchers turned their eyes back on high Q mechanical oscillators as precision measurement tools. From the first proposals on gravitational wave detectors, whether in the form of resonant bar gravitational antenna such as Weber bars [28] (Fig. 1.2.A) or in the form of kilometer- long laser-interferometer-based detectors [29] [30], such as the LIGO[3] experiment (Fig. 1.2.B), these detectors rely on massive high Q mechanical oscillators in their detection schemes. One fundamental difference between the modern gravitational wave detectors and Cavendish's experiment, is

---

[3]Laser Interferometer Gravitational-Wave Observatory

Figure 1.2 – **Two generation of gravitational wave detectors.** A) Joseph Weber with one of his aluminum cylinder resonant bar gravitational detector known also as Weber bars [Photo courtesy of AIP Emilio Segrè Visual Archives] B) Long interferometric gravitation wave detector such as LIGO [Photo courtesy of Caltech/MIT/LIGO Lab]

that due to the extremely small nature of the displacement caused by gravitational waves, the thermal Brownian motion [31] of the mechanical oscillator poses a fundamental limit on the detection sensitivity. Since the environmental noise scales as $\frac{1}{Q}$ [9], high Q mechanical oscillators had to be used in order to reduce the thermal noise. This led to an extensive study of dissipation mechanisms in different materials and designs in pursuit of ultra-high-Q mechanical oscillators conducted in 1960s and 1970s. This journey still continues today and is the basis for this thesis.

The first experimental attempts to study the dissipation mechanisms in materials (especially in the 1950s) were based on measuring the acoustic absorption of ultrasonic waves launched in different materials [32], [33], [34]. Due to technical difficulties in calibrating the coupling efficiency from the source to the resonator, as well as the issues associated to back reflections and scatterings of traveling waves, these measurements were not sensitive enough accurate to measure 10 ppt level required to measure dissipation for ultra-high-Q resonators ($Q > 100 \times 10^6$). Therefore, starting in the early 1960s, scientist became favoring resonance-based techniques to measure losses. In this technique, a mechanical resonator, made out of the material of interest is excited at its natural resonance frequency and upon reaching a certain amplitude, the drive is then turned off and the amplitude of the free running resonator is observed as it rings down. Due to various dissipation mechanisms, the oscillator loses a fraction of its energy with every oscillation and its motional amplitude decreases exponentially over time. Figure 1.3 shows an example of a typical ringdown. By measuring the time constant of its decay, one can infer the quality of the resonator and thereby the lossiness of the material. In appendix A.I, we discuss the physics of simple harmonic oscillator in details, where we drive the ringdown equation as time-domain solution to the equation of the motion of a mechanical oscillator eq. (A.I.32):

$$x(t) = x_0 e^{\frac{-\Gamma_m}{2}t} \sin(\Omega_m t) u(t) \tag{1.1}$$

Here Γ_m and Ω_m are the damping rate and resonance frequency of the oscillator, respectively, expressed in angular frequency units, and x_0 is its initial amplitude. In appendix A.I, we demonstrate that the amplitude of a free-ringing oscillator decays with the rate of $\Gamma_m/2$ and its energy decays with Γ_m. Therefore, Γ_m is commonly also known as the "energy decay rate". We define the quality factor of a resonator to be the ratio of its natural resonance frequency to its energy damping rate:

$$Q \equiv \frac{\Omega_m}{\Gamma_m} \tag{1.2}$$

The ringdown technique circumvent numerous technical challenges faced by the traveling wave approach. In particular, it does not rely on knowledge of input/output coupling efficiencies. it is also well-suited to measurements of low-level loss.
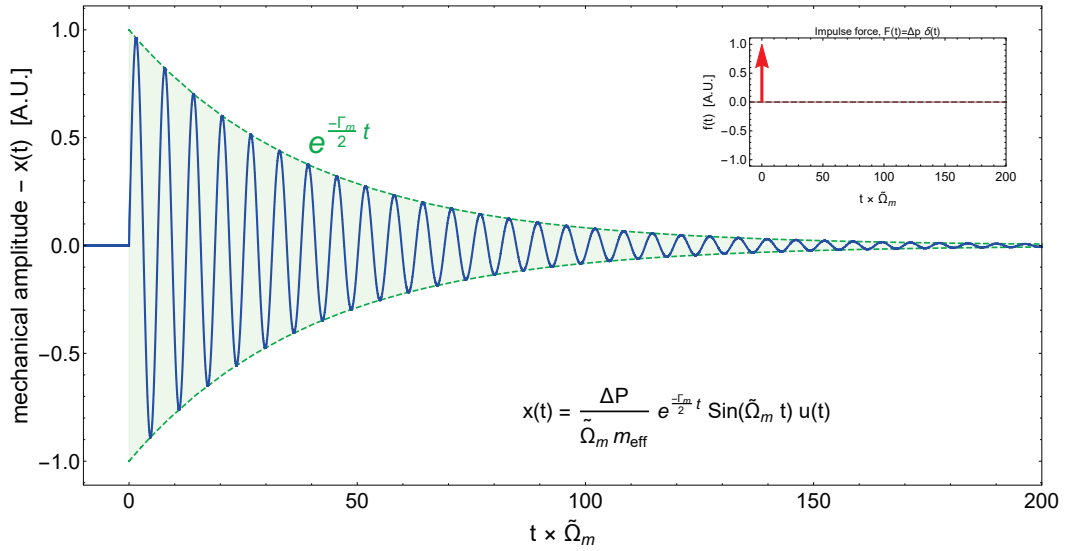
Figure 1.3 – **Impulse response of a simple harmonic oscillator with $Q = 20$.** Dashed green lines show the exponential decaying envelope of the damped oscillation. Inset shows the delta Dirac impulse force applied at $t = 0$ to the oscillator.

Russian scientists were among the first to extensively use the ringdown technique to study the mechanical losses of different materials, in 60s and 70s. They observed quality factors above 10 million in the 1960s [35] , [36] at room temperature and over 1 billion at 70s at cryogenic temperatures [37], [38]. This is equivalent of detecting less than 1 part per billion (ppb.) energy loss per oscillation. Ringdown is the only reliable measurement technique that can offer the sensitivity required to measure such a small mechanical loss.

It should be noted that an alternative approach to ringdown is to use the frequency domain

techniques in which the line shape of the resonance is measured either in a driven response measurement where the frequency of the driving force is swept cross the resonance or by detecting the power spectral density of thermo-mechanical motion [39]. In appendix A.I we demonstrate that for a high Q resonator, lineshape can be approximated with a Lorentzian lineshape where the "*Full Width Half Maximum*" (FWHM) of the lineshape is equal to the energy damping rate:

$$Q = \frac{\Omega_m}{\Delta\Omega} \quad , \quad \text{FWHM} = \Delta\Omega = \Gamma_m \tag{1.3}$$

To choose which technique is the best choice for measuring the Q, it depends largely on the damping rate of the mechanical oscillator and the speed of the measurement instruments. As a general rule of thumb, we normally choose the method that give us more points for the fitting (either an exponential or a Lorentzian). For large damping rates (usually larger than 10-100 Hz) the frequency techniques are favored as the lineshape of such a resonator is broad. For example for a mechanical oscillator with $\Gamma_m/2\pi =$10 KHz, depending on the settings of the spectrum analyzer for the span and the number of points and RBW[4], there could be 1000s of data points in the frequency response that forms the Lorentzian lineshape and statistical errors for fitting are minimized. On the other hand, ringdown of such resonator will only take about $\tau = 1/\Gamma_m = 100~\mu$s. Even with a 100 KHz sampling rate, the time domain response will only contains few 10s of data points which increases the fitting errors if the time domain techniques are used. But when we are dealing with a mechanical oscillator with for example $\Gamma_m = 10$ mHz, even the best spectrum analyzers with RBW=1 Hz cannot resolve its lineshape. Ringdown time of such an oscillator however, will last for several minutes and provides 1000s of data point for an excellent fitting to an exponential. Putting this technical fact aside, in general, ringdown is considered to be more reliable than frequency domain techniques as they are less sensitive to frequency fluctuation of the oscillator. In case of presence of frequency fluctuations, the spectral broadening of the lineshape can occur which lead to underestimation of the quality factor.

Going back to the history of high Q mechanical oscillators, the pioneering efforts were mostly tailored around the studying of the mechanical dissipation in crystalline materials which were considered as a candidate for massive mirrors in gravitational detectors; as well as low loss clamping strategies for mirror suspensions. Figure 1.4 shows examples of experimental apparatuses where cylindrical shape resonators were hanged via suspension wires (normally Tungsten wires as they proved to have less losses [40], [41]). Different materials such as silicon [38][41][42], sapphire [15][43][44][45], quarts [35] [37][36], fused silica [46] [47][46][48][49] , CaF$_2$ [50][51], MoS$_2$ [40], Spinel [52], YAG [52], aluminum [53] [54] and tungsten [40] have been studied over that last 60 years. It is important to emphasize a fundamental assumption behind all these experimental efforts that the intrinsic material losses are frequency- and, to a large extent, geometry-independent. We will revisit this assumption in later sections where

---

[4]Resolution Band Width
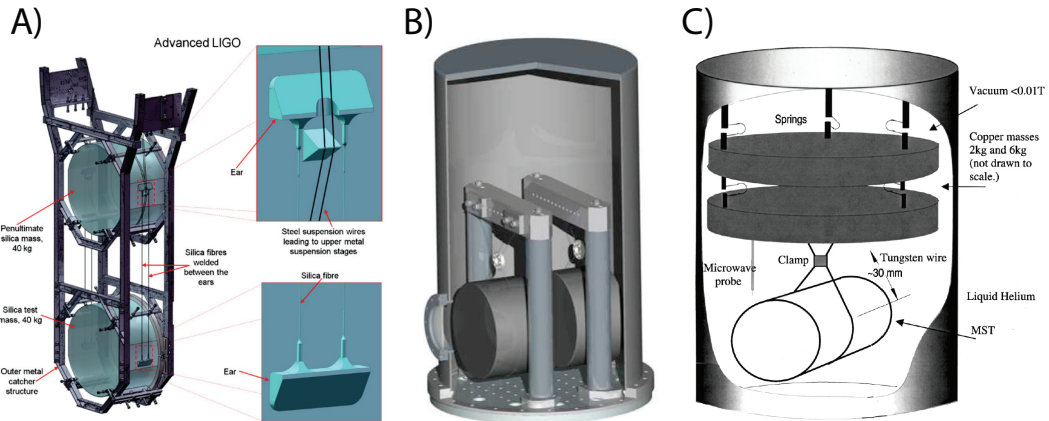
Figure 1.4 – **Examples of experimental apparatus to measure high Q suspended cylindrical shape substrates.** A) The 40 Kg mirrors and the suspension system for advance LIGO. Mirrors are made of fused silica and suspended by fused-silica wires. The image is taken from [55]. B) 3D design of a measurement setup used to study the mechanical losses of different materials. These setups are built in way to resemble the LIGO suspension structure in A. Image taken from [41], C) Schematic of measurement apparatus used to study the mechanical losses of different materials. Image taken from [43].

we discuss different loss mechanisms and the role of geometry in reducing the dissipation of mechanical resonators. In the framework of an elastic theory, intrinsic material losses can be written as the ratio of the real to the imaginary part of the material's Young's modulus:

$$Q = \frac{E_{\text{real}}}{E_{\text{imag}}} \qquad (1.4)$$

It has been experimentally demonstrated as early as 1920s [56] that both real and imaginary parts of the Young's modulus are weak functions of the frequency and could be considered frequency independent constants for a wide range of the frequency band. This means that researchers didn't need to reconstruct the expensive setups of LIGO with 40 kg mirrors [55] in order to study mechanical losses (figure 1.4.A). Assuming that the intrinsic Q is frequency independent, material losses could be studied in smaller and cheaper samples (figures 1.4.B, 1.4.C) and the results could be extended to the size and frequency of the actual LIGO mirrors. In the next section, we will observe that such an assumption holds even for mico- and nano-mechanical oscillators and that the intrinsic Q, to a large extent, remains frequency- and geometry-independent for bulk resonators. We will also observe one exception to this seemingly in-dependency: the surface losses, which effects the thin film resonators for which the intrinsic Q scales linearly with the film's thickness [57]. However, even surface loss remains a frequency-independent parameter.

Alongside experiments, there have been extensive theoretical efforts in the last 60 years to understand the origin of mechanical dissipation. This accounts to modeling the micro-physics

behind the imaginary part of the Young's modulus (E_{imag}) in equation (1.4). There have been many theoretical proposal regarding the origin of mechanical dissipation. A summery can be found in chapter II of Vladimir Braginsky's celebrated book, "System with Small Dissipation" [15]. We also refer the reader to the review given in [58]. In this thesis we do not explore the micro-physics of mechanical losses but instead focus on the effect of elastic tensile strain on the enhancement of the Q (phenomenon known as dissipation dilution [59]). Therefore, without going into the details of micro-physics of losses, we have list the main dissipation models and relevant references:

- **Thermoelastic damping** ($Q_{\text{Thermoelastic}}$) [60][61][62][63].

- **Phonon-phonon scattering** (also know as Akhiezer loss-Q_{Akhiezer}) [64][65][66][67].

- **Two level systems (TLS-Q_{TLS})** [68][69][70][71].

- **Surface losses** (Q_{Surface}) [57], [48], [72], [73].

One of the challenges of studying the mechanical loss is that even by today, we do not have a proper quantum theory for material losses (a quantum theory of friction) that can fully describe all the physical observations in regards with high Q mechanical resonators (for example the Q-temperate curves of different materials [71]). Each of the above models can only explain a few observations and fails to predict the others. One of reasons behind this difficulty is the additive nature of mechanical dissipation that is the total loss (the quantity is measured in experiments), is in practice a sum of several different components:

$$Q_{\text{tot}}^{-1} = \sum_{n=i} Q_{\text{i}}^{-1} \approx Q_{\text{Material}}^{-1} + Q_{\text{Radiation}}^{-1} + Q_{\text{Evanescent}}^{-1} + Q_{\text{Gas}}^{-1} \tag{1.5}$$

As in customary, here we have approximated the loss as sum of four contributions Q_{Material} refers to the internal losses in the material, originated from the friction which is modeled phenomenologically by the imaginary part of Young's modulus. We will study this loss channel in section 1.3 of this chapter, $Q_{\text{Radiation}}$ refers to acoustic radiation into the substrate and becomes a dominant factor especially at high frequencies where the acoustic wavelength is comparable to the physical dimensions of the system. In this regime, acoustic energy starts to leak into the substrate as we move to higher frequencies. We will study this loss channel in section 1.6 and present techniques on how to fight it. $Q_{\text{Evanescent}}$ associates with the near field region of the acoustic field [74] (as opposed to radiation loss which is a far field phenomenon). We briefly discuss this type of loss at the end of section 1.6 and argue that it is responsible for relatively low Q of the fundamental mode of Si_3N_4 membranes [75]; Last but not least, Q_{Gas} is known as gas damping and refers to the viscous damping that an oscillator experiences in the presence of air molecules. We will discuss this type of loss in appendix A.II. A common technique to fight gas damping is to operate at low pressures in a vacuum chamber.

In appendix A.II we present the designs for a custom-made ultra-high vacuum (UHV) chamber with which we realized record-breaking Q values.

In practice, several of these loss channels are usually present at the same time, each accounting for a fraction of the dissipated energy. Often, some of these loss-channels have comparable traces and fingerprints which leads to an infamous confusion and misinterpretation among the scientists in the past [76], [77], [78]. Isolating a single channel to study it independently can be technical challenging. In this thesis, we try to study the different channels presented in equation (1.5) and discuss their scaling laws with frequency, geometry and other design parameters.

If external loss mechanisms are eliminated ($Q_{\text{Radiation}}$, $Q_{\text{Evanescent}}$, Q_{Gas}), the mechanical Q is ultimately determined by internal losses of materials, Q_{Material}, which macroscopically is caused by friction. As mentioned above, there is still a debate about the true origin of the micro physics of internal loss , Q_{Material} is therefore usually divided into multiple subcategories:

$$Q_{\text{Material}}^{-1} = Q_{\text{Surface}}^{-1} + Q_{\text{Thermoelastic}}^{-1} + Q_{\text{Akhiezer}}^{-1} + Q_{\text{TLS}}^{-1} + \cdots \tag{1.6}$$

It is important to note that studying the micro physics of losses is beyond the scope of my PhD research and for the completion of this review, I only provided few references for the interested reader with regards to each loss model. Instead, in this thesis we focus on the geometrical techniques and ideas on how to enhance Q_{Material} by taking advantage of elastic tensile strain. Our discussion and models in sections 1.2, 1.3 are completely material-independent. We implement them experimentally on high stress Si_3N_4 [78] because of its availability and our previous experience with the fabrication of Si_3N_4. However, our techniques can be used on any material under tensile stress. It is an opportunity for the next generation of PhD students to apply these techniques to new materials especially crystalline materials such as strained silicon [79], strained germanium [80], strained InGaP [81] which may lead to improved performance.

Continuing with the history of high Q mechanical oscillators: Experimental efforts to study the intrinsic material quality of different substrates led to the discovery of a new method to enhance the quality factor which later became known as "*dissipation dilution*" [82]. From our daily experience, stretching a guitar string not only increases its pitch (resonance frequency) but the time over which its sound can be heard (its coherence time). In the similar fashion, as illustrated in figure 1.4, under the heavy weight of LIGO mirrors, the suspension wires of the mirrors are under a high tensile stress. Researchers observed that the flexural ("violin") modes of these suspension wires[83] [84] [85], had larger quality factors compared to their unstressed intrinsic Q of the material that the wire was made of [86], [87]. Extensive theoretical studies [82], [13] on this "stress enhancement" effect took place in the 1990s. This led to the invention of the concept of dissipation dilution [82], in which the intrinsic quality factor of a material, Q_{int}, is enhanced by a unit-less number, D_Q:

$$Q^{\sigma}_{\text{Material}} = Q_{\text{int}} D_Q(\sigma) \tag{1.7}$$

where σ is stress in the material. We will explore the details of dissipation dilution in sections 1.2 and 1.3. It is important to note that studies by G. Gonzfilez and P. Saulson [82], [13] in the 90s are important landmark which form the backbone of our analysis in that chapter. However, it was not until about 15 years after these pioneering works, that dissipation dilution resurfaced again at a completely different scales (micro/nano scale), as a means to understand the mechanism behind the exceptionally high mechanical quality factor of strained micro- and nano-mechanical.

Since 1965 and the invention of the first "micro-electro-mechanical systems" (MEMS) [21], a new horizon for micro- and nano-mechanical oscillators has appeared. Micro-mechanical oscillators began to appear in our daily lives in the form of sensors, filters and switches used in our smart phones, cars, airplanes and other applications. Miniaturization of mechanical oscillators not only significantly reduced the foot print of these MEMS devices (to the point where they could fit in our handheld electronics such as tablets and smartphones), but also came with the added bonus of extra stiffness, k. In general, the stiffness of a mechanical objects scales inversely with its length scale, $k \propto L^{-1}$. Large stiffness is essential for portable applications where the device might experience more than 1000 g shock [88] if dropped on the ground. The extreme stiffness of MEMS devices enabled delicate and fragile mechanical systems of the past to be carried around in our watches, phones and other consumer electronics without the risk of breaking them.

Miniaturization of mechanical oscillators, however, came with a cost: lower quality factors. A graphical review by M. Imboden et al.[89] reproduced in figure 1.5, illustrates the problem beautifully. We believe this scaling might be attributed to the increase of surface to volume ratio for smaller devices and dominance of the surface losses [94][95].

In the early applications of MEMS however, mechanical Q was not a major concern and oscillators were typically limited by their intrinsic material losses. Few techniques were available to achieve higher intrinsic Q: for example, using different materials with higher intrinsic Q, surface treatments, annealing and operating at cryogenic temperature. The emergence of quantum electro/optomechanics in the early 2000s changed the landscape and pursuit of mechanical oscillators with ultra-low dissipation became a high priority, particularly for micro/nanoscale devices. In the past decade, we have observed a "Moore's law" for mechanical dissipation where by each year mechanical oscillators with higher quality factors and longer coherences are introduced. Today, the highest reported value of the mechanical Q (at room temperature) belongs to the work presented in this thesis , a value of Q 1 billion at room temperature. This record is likely be broken in the near future.

Another breakthrough in the field of high Q micro/nano-mechanical resonators was the development of high stress Si_3N_4 string resonators in 2006 by the group of Harold Craighead
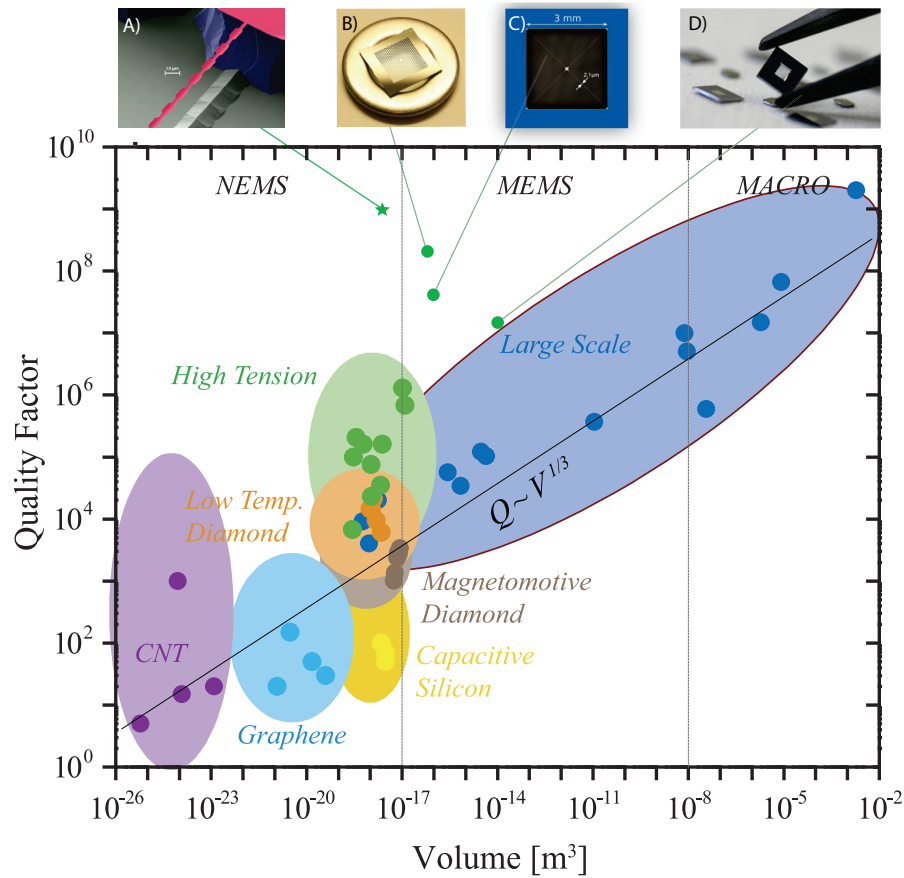
Figure 1.5 – **Q versus resonator volume taken from [89].** This plot, phenomenologically shows that mechanical Q reduces with resonator size. Overlaid, are the high stress Si_3N_4 resonators in the past 10 years, which have emerged as exceptions to this phenomenological scaling: A) Strain-engineered and soft-clamped beams [90], B) soft-clamped membranes [91], C) trampoline resonators [92][93], D) commercial Si_3N_4 membrane resonators [75]

[78] followed shortly by Si_3N_4 membrane resonators in 2008 and 2009 [96][75]. LPCVD[5] deposition of stoichiometric silicon nitrite (Si_3N_4) on silicon substrate results in relatively uniform ~ 1.2 GPa of tensile stress in the film [97] (Varying with deposition conditions such as temperature, pressures and etc.). As we will present in later sections, this initial stress is the key to our Q-enhancement techniques.

In the early days of high stress resonators in the micro/nano mechanics community, there was a confusion about the origin of the exceptionally high Q factor of Si_3N_4 resonators. In 2010 Q. P. Unterreithmeier et al. [98] presented a detailed explanation for the anomaly of Si_3N_4 resonators, and numerically demonstrated the concept of stress-induced dissipation dilution. Shortly thereafter, an analytical model for dissipation dilution was reported by S. Schmid et al. [99]. Schmid's formalism serves as an important building block theoretical discussion later in this chapter. Another important insight into the exceptional Q factor of Si_3N_4 resonators

---

[5]Low pressure chemical vapor deposition

was provided in 2014 by Villanueva et al. [57]. They phenomenologically demonstrated that such oscillators are limited by the surface loss, manifesting as an intrinsic quality factor which scales linearly with the device thickness, $Q_{int} \propto h$.

Schmid et al. [99] demonstrated that a major factor limiting the quality of high stress resonators is the sharp curvature of the mode shape near the clamping points. Therefore, the next big question in the field of ultra-high Q mechanical oscillators was that if there is a technique that allows us to engineer a smooth curvature near the clamping areas. In 2017, Tsaturyan et al. [91] demonstrated that by incorporating a carefully patterned phononic crystal [100],[101] into a high stress Si_3N_4 membrane resonator, the bending curvature at the clamping area can be strongly suppressed and this leads to a dramatic increase in the quality factor. Using this technique , which they named "soft clamping", Tsaturyan et al. [91] were able to realize a quality factor of 200×10^6 for a 770 kHz mode, operating at room temperature. In this thesis, we applied the soft clamping technique for the first time to a beam resonators, an object with ~1000 times smaller mass. In addition, we explored a new technique where we enhance the local stress via geometrical means [102][103] from a weak deposition stress of ~ 1 GPa to ~ 6 GPa, near the breaking point of Si_3N_4 (σ_{yield}). Especially, using a spatially non-uniform phononic crystal pattern, we co-localize the strain and flexural motion of a Si_3N_4 nanobeam. This combined strategy produces picogram-mass flexural modes with room-temperature Q factors in the excess of 800 million and $Q \times f$ products exceeding 10^{15} Hz both values are unprecedented values compare to any mechanical oscillator of any size and material at room temperature. These results signal a paradigm shift in the control of dissipation in nanomechanical systems, with impact ranging from precision force microscopy [6] to tests of quantum gravity [104]. Combining the reported approach with crystalline or 2D materials may lead to further improvement, of as yet unknown limitation.

In the following sections, we will walk through different aspects and challenges of design, implementation and characterization of ultra-high-Q nano-mechanical resonators. We start our analysis in section 1.2, by defining the dissipation dilution, D_Q, in abstract. We will observe its relation to the conservative and non-conservative parts of the stored energy in the oscillator. In section 1.3 we lay down the theoretical foundations of this chapter. We start with the basic theory of elasticity and show how dissipation dilution in a stressed mechanical resonator arises in general due to a "geometrical nonlinearity"[14]. Then we demonstrate that dissipation dilution is restricted to flexural modes of motion (in-plane and out of plane modes of beams) , whereas other mode classes such as torsional, breathing and longitudinal modes cannot be diluted by the stress. At the end of section 1.3 we specialize to a uniform doubly clamped beam which will be used to inform the designs of ultra-high Q resonators. In the section 1.4, we present three strategies to achieve enhanced Q and $Q \times f$ values. First we observe that by operating at the optimum mode order of a long beam, we can create "quantum enabled" mechanical oscillators with $Q \times f > \frac{k_B T}{\hbar}$. In our second strategy, the designs for the soft clamped beams and details of the phononic crystal and band structures are discussed which will be followed by the experimental demonstration of soft-clamped beams. Next we present our geometrical method for strain engineering in 1D objects and how to create regions

with locally enhanced stress by tapering the width of the resonator. Then we show how to combine the soft clamping with strain engineering using a special non-uniform phononic crystal as our third and most effective strategy and how to co-localize the displacement and the regions of high stress to achieve even further boost on the Q factor. Then we experimentally demonstrate the performance of these strained enhanced soft-clamped beams where we show case our record-breaking quality factor of 800 million for a megahertz oscillator at room temperature as the main experimental achievement of this thesis. In section, 1.5, we review an example where we apply our strain engineering method specifically to the clamping regions on a doubly-clamped beam and show how by removing mass at the clamping region can result in enhanced Q factors. Finally, in section 1.6, we study a form of loss which cannot be addressed by dissipation dilution: radiation loss. We demonstrate how radiation loss becomes dominant at frequencies above a certain threshold. We conclude this chapter by presenting a phononic crystal shielding technique to reduce radiation loss and realize intrinsic Q values for resonator modes at VHF and UHF frequencies.

1.2 Dissipation dilution[6]

The origin of dissipation dilution has been the subject of a long debate. When the phenomenon was first discovered in suspension wires of the test masses in the gravitational waves detectors, it was explained by an additional lossless gravitational potential "diluting" lossy elastic energy [82]. Surprisingly and in contrast to this picture, the same phenomenon was also found to enhance Q factors of suspended nanomechanical resonators made of highly-strained materials (most notably, silicon nitride resonators [98], [99]), where no external potential such as gravity is present. The quality factors of flexural modes of strained uniform beams [99] and membranes [105] were modeled and shown to be much greater than intrinsic material quality factor, $Q_{\text{int.}}$, in excellent agreement with experiments [98], [57], [105], [101]. These results established dissipation dilution to pertain to the domain of structural mechanics, but the understanding of this effect is still incomplete. Open questions include: (1) What is the physical origin of dissipation dilution due to tensile stress, (2) does it apply to mode families other than flexural modes, and (3) to what extent can it be optimized, for a particular mode family? Here we address these questions with a general and consistent theory of dissipation dilution in solid-state resonators. The main difference from the original work of Gonzalez [82][13], is that we do not resort to the concept of an a priori lossless potential and do not limit consideration to a pendulum-like geometry.

We start with a high-level definition of dissipation dilution and argue for its geometrical origin. In literature, dissipation dilution is commonly illustrated by a harmonic oscillator subjected to an external lossless potential [82], as in the case of optically-trapped mirrors [106] , [107] or massive pendula in a gravitational field [82]. In this thesis, we model material losses by the imaginary part in the spring constant (or imaginary part of Young's modulus for the case of continues material) in contrast to velocity dependent damping term known as viscous

---

[6]The content of this section is published at [14]

damping. It should be noted that one has to be careful when modeling the losses in this way and introducing the complex numbers in the equations of motion, as it could lead to the causality issues in such a model if the math is not properly done.

We begin by observing the effect of an external lossless potential on the mechanical oscillator. The equation of motion of structurally damped oscillator is given by:

$$\ddot{x} + \Omega_{\text{int}}^2 (1 + i\phi) x = \frac{F_{\text{ext}}}{m_{\text{eff}}} \tag{1.8}$$

It is much easier to solve the equation of motion in the frequency domain rather than time domain. Therefore, in this section and the following ones, we only work with the frequency domain version of the equations:

$$\left(\Omega_{\text{int}}^2 - \Omega^2 + i\phi(\Omega)\Omega^2 \right) = \frac{F_{\text{ext}}(\Omega)}{m_{\text{eff}}} \tag{1.9}$$

where Ω_{int} is the oscillator intrinsic natural frequency, ϕ is the oscillator loss tangent [108], m_{eff} is the oscillator's effective mass and F_{ext} is the external force applied to the oscillator. In appendix A.I, we argued that if damping is dominated by material elastic losses, the intrinsic quality factor of the oscillator —Q_{int}— is a frequency independent constant over a large frequency span and is equal to the inverse of the material loss tangent (an important phenomenological observation supported by many measurements [56] [109]); We define the approximately frequency-independent, intrinsic quality factor:

$$Q_{\text{int}} \equiv \phi^{-1} \tag{1.10}$$

Now we introduce a lossless potential of the form $U_{\text{dil}} = \frac{1}{2} m_{\text{eff}} x^2 \Omega_{\text{dil}}^2$ to the oscillator. Such a potential can be applied using optical trapping potential [106] , [107], gravity [13] or as we will see in section 1.5, via the static tensile stress in the elastic body. Since we assume this potential is lossless (with no imaginary part), it only changes the resonance frequency of the oscillator and modifies equation (1.9) to:

$$\left(\Omega_{\text{int}}^2 + \Omega_{\text{dil}}^2 - \Omega^2 + i\phi(\Omega)\Omega^2 \right) = \frac{F_{\text{ext}}(\Omega)}{m_{\text{eff}}} \tag{1.11}$$

The quality factor of the modified system is equivalent to the real part of it eigenfrequency divided by its imaginary part:

$$Q_{\text{dil}} = \frac{\Omega_{\text{int}}^2 + \Omega_{\text{dil}}^2}{\phi(\Omega)\Omega_{\text{int}}^2} = Q_{\text{int}} \frac{\Omega_{\text{int}}^2 + \Omega_{\text{dil}}^2}{\Omega_{\text{int}}^2} \tag{1.12}$$

we define to the dissipation dilution factor to be:

$$D_Q \equiv \frac{Q_{\mathrm{dil}}}{Q_{\mathrm{int}}} = \frac{\Omega_{\mathrm{int}}^2 + \Omega_{\mathrm{dil}}^2}{\Omega_{\mathrm{int}}^2} \qquad (1.13)$$

this simple analysis shows that adding a loss less potential to a lossy potential, will result in dilution of the quality factor of the oscillator. Intuitively, that the enhancement factor can be expressed as the ratio of the lossless potential to the lossy potential as:

$$\left. \begin{aligned} U_{\mathrm{int}} &= \frac{1}{2} m_{\mathrm{eff}} x^2 \Omega_{\mathrm{int}}^2 \\ U_{\mathrm{dil}} &= \frac{1}{2} m_{\mathrm{eff}} x^2 \Omega_{\mathrm{dil}}^2 \end{aligned} \right\} \implies D_Q = \frac{U_{\mathrm{int}} + U_{\mathrm{dil}}}{U_{\mathrm{int}}} \qquad (1.14)$$

For flexural vibrations of tensioned beams or membranes, the Q enhancement takes place in a way similar to (1.14) with the important distinction that in this case, unlike an external optical or gravitational potential, the potential energy is in elastic deformation. Instead of introducing an external potential, the elastic deformation potential is divided into lossy ("bending") and lossless ("elongation") parts, related to the curvature and gradient of the mode shape, respectively. It is not evident a priori, however, how to make this separation in a general case and under which conditions the lossless part of the energy is non-zero. In the following section, we answer both questions and show that effectively the lossless elastic energy emerges if two conditions are satisfied: a) static strain is non-zero in the resonator and b) the average of strain variation over the oscillation period is non-zero, i.e. the geometric nonlinearity of strain is significant. In the next section, we first derive the Q dilution for a the flexural modes and then for the a general complex geometry and mode flavor.

1.3   Material elastic losses and geometric non-linearity

In this section, we first start by driving the dissipation dilution of a specific example: flexural modes of a doubly clamped beam (same derivation can be applied to the case of a membrane). As we will show at the second part of this section, these modes experience a significant dissipation dilution compared to other mode flavors such as torsional and longitudinal modes, given a large enough initial stress in the film. Analyzing these modes gives useful insights into the geometrical nature of dissipation dilution in elastic bodies and the notion of geometrical nonlinearity. In addition, since we can analytically calculate the mode shapes of doubly clamped beams and square membranes, we will be able to analytically derive the dissipation dilution factors. These analytical solution will prove to be insightful when we present strategies to enhance the quality factor by soft clamping and strain-engineering also will help us to understand the source of loss in doubly clamped high stress beams.

Dissipation dilution of flexural mode of beam/plate type resonators

In order to calculate the dilution factor, we have to calculate the elastic energy stored in the material [63]:[7]

$$U_{\text{el}} = \int \frac{1}{2} E \varepsilon^2 \, dV \tag{1.16}$$

where E is the material's Young's modulus and ε is the strain. For an isotropic elastic material, strain is defined to be the relative length change of the material for a given applied stress, as illustrated in figure 1.6.

$$\varepsilon = \frac{\Delta L}{L}$$

$$E = \frac{\sigma}{\varepsilon}$$

$$\sigma = \frac{P}{A}$$
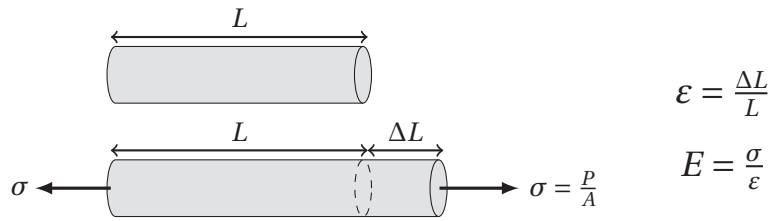
Figure 1.6 – **Definition of elastic strain**. ε in an isotropic elastic rod is defined as the fractional length change to the applied stress where E is material's Young's modulus, σ is the stress, P is the pressure applied to the rod , and A is the rod's cross section.

In the following, we will prove that the strain in the flexural modes of a beam is in the following form:

$$\varepsilon(u, z) = \underbrace{\varepsilon_0(x)}_{\text{pre-strain}} - \underbrace{u''_{xx} z}_{\text{bending strain}} + \underbrace{\frac{(u'_x)^2}{2}}_{\text{elongation strain}} \tag{1.17}$$

where $\varepsilon_0(x)$ is the pre-strain in the material at position x along the beam axis, $u(x)$ is the mode shape and z is the coordinate in the direction of motion. It should be noted that since a beam with non-uniform width $w(x)$, the pre-stress is not constant along the length of the beam and is inversely proportional to the local width $\varepsilon_0(x) \propto \frac{1}{w(x)}$. Will revisit this issue in the next section where we introduce our strain engineering strategy to locally enhance the stress by tapering the beam's geometry.

Proving equation (1.18) in not easy. First we show that for an infinitely thin beam, the elongation strain is induced as direct result of the mode curvature, $u(x)$. Then we derive its value to be equal to $\varepsilon_{\text{en}} = \frac{(u'_x)^2}{2}$, the third term in equation (1.18). Next we see that for a beam with a finite thickness, different parts of the thickness experiences different stretching and contraction

---

[7]Equation (1.16) is the continuum form of the stored energy in a simple harmonic oscillator:

$$U = \frac{1}{2} k x^2 \tag{1.15}$$

where k is the spring constant (equivalent to E in the continuum form) and x is the oscillator displacement (equivalent to ε in the continuum form)

(strain) due of the bending curvature of the beam which leads to the second term in equation (1.18).

Figure 1.7 illustrates the elongation strain for a beam with infinitely thin thickness and the mode shape of $u(x)$. It is illustrated in the figure that the elongation strain is equal to $\varepsilon_{\text{en}} = \frac{(u'_x)^2}{2}$. This shows that the relation between elongation elastic strain and the mode shape is nonlinear (quadratic). We will observe that this nonlinear relation will lead to a lossless potential and is responsible for the Q dilution in high stress beams and membrane resonators. This quadratic relation is what we refer to as "geometrical nonlinearity" in this text.
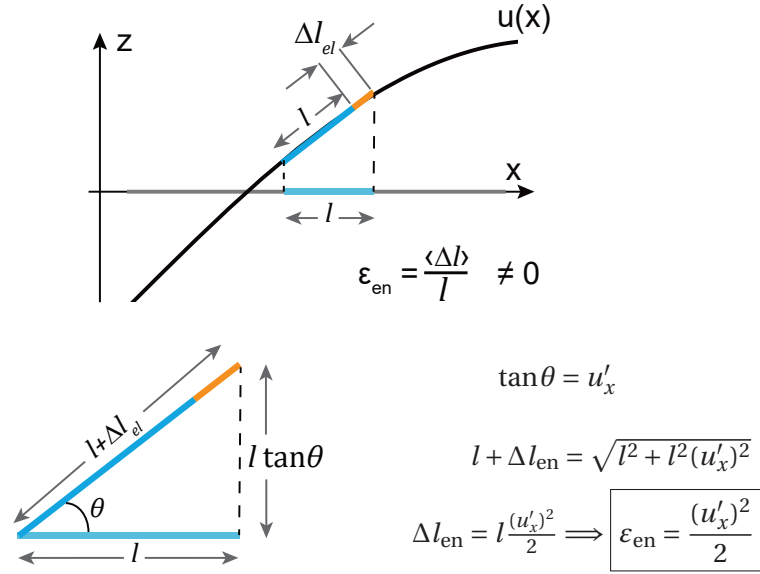
Figure 1.7 – **Derivation of elongation strain.** Mode shape curvature, $u(x)$ of an infinity thin beam, creates elongation of the beam (orange region). In this figure, we prove that the elongation strain is equal to $\varepsilon_{\text{en}} = \frac{(u'_x)^2}{2}$.

Calculating the bending strain however, is more challenging. Figure 1.8 shows that for a beam with a finite thickness, different parts of an infinitesimal volume element experience different strains because of the bending curvature. For example, in figure 1.8, due to continuity of the material, the red region above the so called "*neutral axis*" experiences an additional stretching and the orange region experiences compression. It is illustrated in the figure 1.8 that the strain induced at each z position, is inversely proportional to the local radius of curvature — ξ — of mode shape at each point.

It can be shown that for a smooth curvature of $u(x)$ with small bending radius, an assumption valid for most physical systems and beams, the inverse radius of curvature ξ, is equal to the second derivative of the mode shape [110] [63]:

$$\frac{1}{\xi} \approx -u''_{xx} \implies \boxed{\varepsilon_{\text{bn}}(z) = -u''_{xx}z} \tag{1.18}$$

17

$$l_0 = \xi\,\theta$$
$$\Delta l_{bn}(z) = z\,\theta$$
$$\left.\right\}\;\varepsilon_{bn}(z) = \frac{\Delta l_{bn}}{l_0} = \frac{z}{\xi}$$
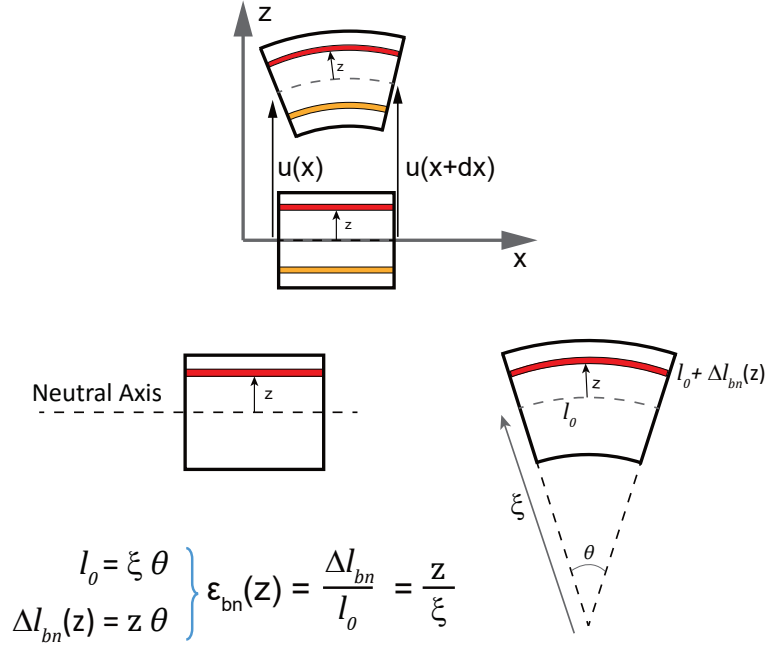
Figure 1.8 – **Bending strain for a beam with a finite thickness**. In a beam with a finite thickness, different parts along thickness, experience different stretch/contraction due to curvature. For example, the red region experiences an extra stretching compared to the neutral axis (dashed line) and the orange region experiences a compression. We show this extra strain which is known as the bending strain is inversely proportional to the bending radius, ξ.

Now after proving the equation (1.18), the rest of the derivation is downhill. First we have to calculate the elastic energy, eq. (1.16), using our formula for the strain in eq. (1.18), for a beam with the length of l and the variable width and thickness of $w(x)$, $h(x)$ respectively (our derivation is valid for an arbitrary geometry in a beam as long as it remains symmetric in with respect to two axial planes):

$$U_{\mathrm{el}} = \int_l dx \int_{-w(x)/2}^{w(x)/2} dy \int_{-h(x)/2}^{h(x)/2} dz \frac{E}{2}\left(\varepsilon_0^2 + (u_{xx}'')^2 z^2 + \left(\frac{(u_x')^2}{2}\right)^2 - u_{xx}''(u_x')^2 z - 2\varepsilon_0 u_{xx}'' z + \varepsilon_0 (u_x')^2\right)$$

$$= U_{\mathrm{el.0}} + \int_l dx \frac{E}{2}\left(\underbrace{I(x)(u_{xx}'')^2}_{\text{Energy stored in bending}} + \underbrace{A(x)\varepsilon_0(x)(u_x')^2 + A(x)\frac{(u_x')^4}{4}}_{\text{Energy stored in elongation}}\right) \qquad (1.19)$$

where $\int_l dx$ is the integral over the length of the beam, $U_{\mathrm{el.0}} = \int dV \frac{E}{2}\left(\varepsilon_0(x)\right)^2$ is the static part of the elastic energy due to the initial stress in the resonator and $I(x)$ and $A(x)$ are geometrical moment of inertia and cross-sectional area defined as the following:

18

$$A(x) = \int_{-w(x)/2}^{w(x)/2} dy \int_{-h(x)/2}^{h(x)/2} dz = w(x)h(x) \tag{1.20}$$

$$I(x) = \int_{-w(x)/2}^{w(x)/2} dy \int_{-h(x)/2}^{h(x)/2} z^2 dz = \frac{1}{12} w(x)h(x)^2 \tag{1.21}$$

Note that equation (1.19) doesn't require that the beam cross-section to be rectangular and would work equally well for a string with arbitrary cross-sectional shape which varies with position, as long as A(x) and I(x) are defined as (1.20), (1.21).

Lets summarize all the energy terms in equation (1.19). The first term is the energy stored in the bending deformation of the mechanical oscillator:

$$U_{\text{bending}} = \int_l \frac{E}{2} I(x)(u''_{xx})^2 \tag{1.22}$$

the energy stored in elongation:

$$U_{\text{elongation}} = \int_l dx \frac{E}{2} A(x)\varepsilon_0(x)(u'_x)^2 \tag{1.23}$$

and the last term is what we call it the energy term due to self-induced-stress.

$$U_{\text{self-stress}} = \int_l dx \frac{E}{8} A(x)(u'_x)^4 \approx 0 \qquad \text{(for small amplitudes)} \tag{1.24}$$

where this term is usually negligible for small amplitudes as it contains higher orders of $u'_x \ll 1$. This term only becomes important when the oscillator's amplitude is large. In that scenario, the large amplitude of the resonance creates a non-zero average stress in the oscillator which in turn, can dilute the Q similar to the static pre-stress of the beam. That is why we call this term self-induced-stress. In this thesis, we only work with the linear regime of mechanical oscillator where amplitudes are small and $U_{\text{self-stress}}$ can be safely neglected. In summary, the elastic energy stored in the material is given by:

$$U_{\text{el}} = U_{\text{bending}} + U_{\text{elongation}} \tag{1.25}$$

The next step is to calculate the lost energy in the resonator. In order to calculate the lost energy, it is easier to work with the phasor format. Where $\tilde{u}(x, t)$ can be written as the product of the vibrating part with the frequency of Ω_n and $u_n(x)$ being the mode profile for the nth mode:

$$\tilde{u}_n(x, t) = u_n(x)e^{i\Omega_n t} \tag{1.26}$$

The sign ˜ indicates that $\tilde{u}_n(x, t)$ is a complex number in the phasor domain. We can always retract the real-time domain values of our resonator by taking the real part of the phasor vector. The strain in phasor domain can be written as:

$$\tilde{\varepsilon}(t) = \varepsilon_0 + u_{xx}''ze^{i\Omega_n t} + \frac{(u_x')^2}{2}e^{i2\Omega_n t} \tag{1.27}$$

Similar to the last section (section 1.2) where we introduced the imaginary spring constant to model the material intrinsic losses, here we assume that (phenomenologically) our material has an imaginary part in its Young's modulus which is responsible for the losses:

$$\tilde{E} = E_r + iE_i \quad , \quad Q_{int} = \phi^{-1} = \frac{E_r}{E_i} \tag{1.28}$$

Therefore, the relation between the stress and strain becomes:

$$\tilde{\sigma}(t) = (E_r + iE_i)\tilde{\varepsilon}(t) \tag{1.29}$$

In other word, the imaginary part of Young's modulus creates a phase lag of ϕ between the stress and strain fields which is responsible for losses.

The dissipated energy per unit volume averaged over one period can be written as:

$$w_{diss} = \text{Real}\left\{\left\langle \tilde{\sigma}(t) \cdot \frac{d\tilde{\varepsilon}^*}{dt} \right\rangle_T \right\} \tag{1.30}$$

where $= \text{Real}\left\{\cdots\right\}$ is the real part operator, $\left\langle \cdots \right\rangle_T$ is the time average over the time, T (here it is equal to one mechanical period $T = \frac{2\pi}{\Omega_n}$) and * is the complex conjugate operator[8]. It should be noted that eq. (1.30) is the continuum form of the equation $\Delta W = \left\langle F\dot{x} \right\rangle_T$ which indicated the average worked done on the oscillator by the force F. The second term of equation (1.30) cab be written as:

$$\frac{d\tilde{\varepsilon}^*}{dt} = i\Omega_n u_{xx}''ze^{i\Omega_n t} + 2i\Omega_n\frac{(u_x')^2}{2}e^{i2\Omega_n t} \tag{1.32}$$

It is worth emphasizing that the pre-stress term, ε_0, vanishes in the derivative of the strain. This is the key factor for understanding the dissipation dilution of high stress resonators.

---

[8] When a ,b are real numbers, then:
$$(a + ib)^* = a - ib \tag{1.31}$$

As we saw in equations (1.16), (1.30), the stored energy is proportional to $U_{el} \propto \varepsilon^2$ and the dissipated energy is proportional to $w_{diss} \propto \varepsilon\dot{\varepsilon}$. Therefore, we observe the presence of the non-zero pre-strain in the stored energy as it has a non-zero average and appears as $U_{elongation}$ and increases the stored energy, but it vanishes in the derivative and does not play a role in dissipated energy. Therefore, the existence of a pre-stress in the beam, enhances the stored energy but does not contribute to the losses. Consequently, it acts as a lossless potential which in section 1.2 we demonstrate is responsible for Q dilution factor.

To simplify equation (1.30), we can use the lemma that the time average of the oscillatory parts over one period is zero[9] and only keep the non-oscillatory terms:

$$\left\langle \tilde{\sigma}(t) \cdot \frac{d\tilde{\varepsilon}^*}{dt} \right\rangle_T = -E_i\left((u_{xx}'')^2 z^2 + \frac{(u_x')^4}{2}\right) + iE_r\left((u_{xx}'')^2 z^2 + \underbrace{\frac{(u_x')^4}{2}}_{\approx 0 \text{ (small signal)}}\right) \tag{1.34}$$

we observe that the existence of the imaginary part of the young's modulus enables the (1.34) to have a non-zero real part. Equation (1.34) means that a negative work is done on the oscillator at each cycle due to the imaginary part of Young's modulus. On the other word, the oscillator is losing a fraction of its energy with each oscillation. By neglecting the non-linear self-stress term in equation (1.34), we can calculate the dissipated energy per unit volume to be:

$$w_{diss} = \text{Real}\left\{\left\langle \tilde{\sigma}(t) \cdot \frac{d\tilde{\varepsilon}^*}{dt} \right\rangle_T\right\} = -E_i(u_{xx}'')^2 z^2 \tag{1.35}$$

Now the total lost energy to be the volume integral of w_{diss}:

$$W_{diss} = \int w_{diss} dV = \frac{E_i}{2}\int_l dx I(x)(u_{xx}'')^2 \tag{1.36}$$

according to eq. (1.22) we have:

$$W_{diss} = \frac{E_r}{E_i} U_{bending} = \frac{1}{Q_{int}} U_{bending} \tag{1.37}$$

Therefore, the quality factor of the oscillator is the total elastic energy divided by the total lost energy per cycle:

---

[9]For n is an integer number:

$$\left\langle e^{in\Omega t} \right\rangle_T = \int_0^T e^{in\Omega t} dt = 0 \tag{1.33}$$

if $T = 2\pi/\Omega$

$$Q = \frac{U_{\text{el}}}{W_{\text{diss}}} = Q_{\text{int}} D_Q \quad , \quad D_Q = \frac{U_{\text{bending}} + U_{\text{elongation}}}{U_{\text{bending}}} \tag{1.38}$$

by comparing the equations (1.38) and (1.14), we realize that the initial stress in the materials acts as lossless potential for the oscillator. It increases its stored energy without adding losses to the oscillator. On the other word, the bending of an elastic body is a lossy process but the elongation is lossless. Here we have to emphasize that this argument is only valid if the loss mechanism is due to the imaginary part of the Young's modulus. In the general case, for non-isotropic materials, if the Poisson ratio also have an imaginary component, then elongation also becomes lossy. However, such cases are outside the scope of this thesis and we only work with the models where Young's modulus can be complex but the Poisson ratio is real.

In summary, the dissipation dilution of a flexural modes of a symmetric beam or membrane resonator is given by:

$$D_Q = 1 + \frac{\int_l dx A(x)\varepsilon_0(x)(u'_x)^2}{\int_l I(x)(u''_{xx})^2} \tag{1.39}$$

In order to calculate eq. (1.39) we only need to know the beam/plate's geometry (expressed in $I(x)$, $A(x)$) and its mode shape, $u(x)$. However, it is usually very difficult to find an analytical expression for the mode shapes of a resonator with arbitrary geometry except maybe for the case of a simple rectangular uniform beam or a rectangular membrane [13] [99] [105]. In the next section first we try to simplify the equation 1.39 for flexural modes of a high aspect ratio beam ($l/h \gg 1$ and $l/w \gg 1$ where w, h, l are beam's width, thickness and length respectively) for an arbitrary geometry using few simple assumptions. Then at the end, for completion of this chapter, we re-derive the dissipation dilution for a rectangular uniform beam as we believe this example illustrates important insights toward engineering of ultra-high Q mechanical resonators.

Equilibrium strain distribution in a suspended film and average stress

Until now we have considered beams of arbitrary variable transverse cross-section (both in width and thickness). In the following we impose one geometrical constraints: a constant uniform thickness. This is consistent with the fabrication methods where nano-mechanical resonators are fabricated by suspending a micropatterned thin film. Although qualitatively most of our conclusions are not affected by this assumption, it considerably simplifies the notations while allowing the theory to be directly applied to a very broad range of practical high-strain resonators. In particular, we assume that the yz cross section of the beam to be rectangular, and the width $w(x)$ to be, in general, x-dependent and the thickness to be constant (for example see the representative geometries shown in figure 1.9).
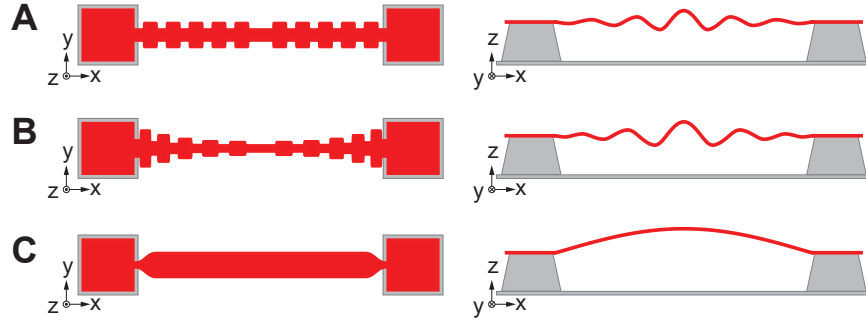
Figure 1.9 – **Examples of beam shapes with uniform thickness and non-uniform width that will be explored in the next sections.** A) Phononic crystal beam with "soft-clamped" localized mode, B) Tapered phononic crystal beam with soft-clamped mode and engineered local strain enhancement C) Beam with thin clamps and its fundamental mode.

Strain can be present in the thin film used for microresonator fabrication due to lattice mismatch [81][79] between the film and substrate in crystalline materials or by mismatch in their thermal expansion coefficients [111] in amorphous materials such as Si_3N_4. Although it should be noted that to the best of my knowledge, the true origin of high stress in Si_3N_4 are not completely understood and thermal stress only accounts for a portion of the observed stress in the experiments. On the other hand, another phenomenon that has to be taken into account is the anisotropicity of real materials modeled by Poisson's ratio. Upon suspension, the originally homogeneous strain inside the film is redistributed. The strain is locally enhanced in constrictions between voids and reduced elsewhere [102][112][103].

The analysis of the vibrational properties of a beam in this case requires the axial tension force T to be found first from the unsuspended deposition film strain $\varepsilon_{film} = \sigma_{film}/E$. This can be done by considering that (a) the total elongation of the beam $\int_0^l \varepsilon(x)dx$ is constant over the relaxation process, as it is defined by the separation of the beam clamping points (anchoring pads) before releasing the structure (this defined as the total beam's length of the resonator) and (b) that the balance of tensile force requires:

$$\varepsilon(x)w(x) = \text{const} = \frac{T}{hE} \tag{1.40}$$

It should be noted that equation (1.40), although very simple, plays a crucial role in the next sections where we present our methods on stress engineering to locally enhance the stress in desired regions. We will observe in the section 1.4 that by tapering the width of a suspended structure, we can locally increase the stress in that region and use it to enhance the quality factor. From the initial condition

$$\int_0^l \varepsilon(x)dx = \varepsilon_{film}(1-\nu)l \tag{1.41}$$

where ν is the Poisson's ratio and the factor $(1-\nu)$ accounts for transverse relaxation of the

strain due to anisotropicity of the materials. Equilibrium tension is thus given by:

$$T = \varepsilon_{\text{film}} E(1-\nu) h \left(\frac{1}{l} \int_0^l \frac{1}{w(x)} dx \right)^{-1}. \tag{1.42}$$

One other useful relation for the strain distribution follows from (1.40)

$$\varepsilon(x) = \frac{\varepsilon_{\text{avg}}}{\nu(x)} \tag{1.43}$$

where the $\varepsilon_{\text{avg}}, \nu(x)$ are introduced as:

1. Mean beam width

$$w_{\text{avg}} = \frac{1}{l} \int_0^l w(x) dx \tag{1.44}$$

2. The normalized width variation function

$$\nu(x) = \frac{w(x)}{w_{\text{avg}}} \tag{1.45}$$

3. The static average stress σ_{avg}, and strain ϵ_{avg}, is given by:

$$\sigma_{\text{avg}} = E\varepsilon_{\text{avg}} \tag{1.46}$$

$$\varepsilon_{\text{avg}} = \frac{1}{hw_0 l} \int_0^l hw(x)\varepsilon(x) dx = \frac{T}{w_0 h} \tag{1.47}$$

which it can be simplified to:

$$\varepsilon_{\text{avg}} = \frac{\varepsilon_{\text{film}}(1-\nu)}{\left(\frac{1}{l} \int_0^l \frac{1}{w(x)} dx \right) \left(\frac{1}{l} \int_0^l w(x) dx \right)} \tag{1.48}$$

However, based on Cauchy–Schwarz inequality [10]

$$\left(\frac{1}{l} \int_0^l \frac{1}{w(x)} dx \right) \left(\frac{1}{l} \int_0^l w(x) dx \right) \geq 1 \tag{1.50}$$

which means regardless of the geometry:

$$\varepsilon_{\text{avg}} \leq \varepsilon_{\text{film}}(1-\nu) \tag{1.51}$$

Equation (1.51) has crucial implications. It means that although we can locally increase the strain by narrowing down a region, the average strain can never be increased via the

---

[10] Based on Cauchy–Schwarz inequality [113] we have :

$$\left| \sum_{i=1}^n u_i \bar{v}_i \right|^2 \leq \sum_{j=1}^n |u_j|^2 \sum_{k=1}^n |v_k|^2. \tag{1.49}$$

geometrical manipulation. Also, the largest average strain belong to a uniform beams where $w(x) = $ const. It should be emphasized however, that for almost all the geometries investigated in this thesis, the average stress is very close to the stress of the uniform beam, $\varepsilon_{\text{avg}} \approx \varepsilon_{\text{film}}(1 - \nu)$.

Dissipation dilution of beams with rectangular cross section

In order to proceed with the explicit calculations of dissipation dilution, we first need to find eigenfrequencies Ω_n and vibrational mode shapes u_n of a beam. For a high aspect ratio ($l/h \gg 1$ and $l/w \gg 1$) elastic beam, eigenmodes can be found by solving the Euler-Bernoulli equation [63]

$$\frac{d^2}{dx^2}\left(I(x)E\frac{d^2 u_n}{dx^2}\right) - T\frac{d^2 u_n}{dx^2} - \rho_l(x)\Omega_n^2 u_n = 0 \tag{1.52}$$

where n is the mode index, $\rho_l(x) = \rho h w(x)$ is the linear mass density and $I(x)$ is the geometrical moment of inertia given by equation (1.21). In order to simplify the notation, it is convenient to introduce a new normalized coordinate $s = \frac{x}{l}$, taking values from 0 to 1, and transform (1.52) to a new form using eq.(1.21):

$$\lambda^2 \frac{1}{\nu(s)}\frac{d^2}{ds^2}\left(\nu(s)\frac{d^2 u_n}{ds^2}\right) - \frac{1}{\nu(s)}\frac{d^2 u_n}{ds^2} - \check{\Omega}_n^2 u_n = 0 \tag{1.53}$$

where $\check{\Omega}$ is the dimensionless frequency defined as:

$$\check{\Omega}^2 = \frac{\rho l^2 \Omega^2}{\varepsilon_{\text{avg}}E} \tag{1.54}$$

and λ is the stress dilution parameter defined as:

$$\lambda^2 = \frac{1}{12\varepsilon_{\text{avg}}}\frac{h^2}{l^2} \tag{1.55}$$

The high-stress/high aspect ratio regime corresponds to $\lambda \ll 1$.

For the case of a doubly clamped beam or a membrane, the equation of motion (1.53) is supplemented with these boundary conditions

$$\begin{cases} u(0) = u(1) = 0 \\ u'(0) = u'(1) = 0 \end{cases} \tag{1.56}$$

Now we can rewrite the dissipation dilution, eq. (1.39), using our normalized parameters

$(s, v(s), \lambda, \check{\Omega})$ for the n-th order mode:

$$D_{Q,n} = 1 + \frac{1}{\lambda^2} \frac{\int_0^1 \left(u'_n(s)\right)^2 ds}{\int_0^1 v(s) \left(u''_n(s)\right)^2 ds} \tag{1.57}$$

From this point, it is difficult to move forward without knowing the mode shape of the resonator which is typically very difficult to analytically calculate for an arbitrary geometry. Especially because of the boundary condition of $u'(0) = u'(1) = 0$, the eigenmodes of Euler-Bernoulli equation are not in the form of sinusoidal functions. However, we can use the perturbation theorem to approximate the dissipation dilution for the case of a high aspect ratio sdevice $\frac{l}{h} \gg 1$ which results in strong dilution ($D_Q \gg 1$). Although this is the second geometrical constrain that we are applying to our derivations, it is valid for a broad range of micro-mechanical oscillators especially the ones we are interest in this thesis. For this, we follow the method presented by S. Schmid et a. [99] where we separate the contributions due to distributed region at the center and the clamping parts of the mode. At the distributed region at the center, the mode shape approximately looks like a sinusoidal shape and exponential near the clamping points illustrated in figure 1.10.

Since we are interested in the high aspect ratio beams where $\lambda \ll 1$, we can neglect the first term in equation (1.53) for the regions far from the clamping points for our first perturbation approximation. The first term in (1.53) only represent the bending, which weakly perturbs the solution in the regions far away from the clamping points (see figure 1.10). Therefore, the normalized Euler-Bernoulli equation for the regions far from the clamping points, modifies to:

$$-\frac{1}{v(s)} \frac{d^2 u_n(s)}{ds^2} = \check{\Omega}_n^2 u_n(s) \tag{1.58}$$

For a fixed width, $v(s) = 1$, the solutions to equation (1.58) are sinusoidal as expected. However, it could be more complicated for an arbitrary $v(s)$. But the elongation and bending energy integrals in eq. (1.57) can be transformed to a new form using partition integrals:

$$U_{\text{elongation-central}} = \int_0^1 \left(u'_n(s)\right)^2 ds = u'_n u_n \Big|_0^1 - \int_0^1 \left(u'_n u''_n\right)^2 ds \tag{1.59}$$

$$= \check{\Omega}_n^2 \int_0^1 v(s) u_n(s)^2 ds$$

and

$$U_{\text{bending-central}} = \int_0^1 v(s) \left(u''_n(s)\right)^2 ds = \check{\Omega}_n^4 \int_0^1 v(s)^3 u_n(s)^2 ds \tag{1.60}$$

In addition to the distributed contributions (sinusoidal parts at the center), the bending energy includes a contribution from the clamping regions. In contrast, the elongation energy stored in these regions is negligibly small since $u'(s \to 0) \approx 0$ but the bending energy $\propto u''(x)$ is not. In fact, we will observe that due to sharp and exponential curvature near the clamping area,
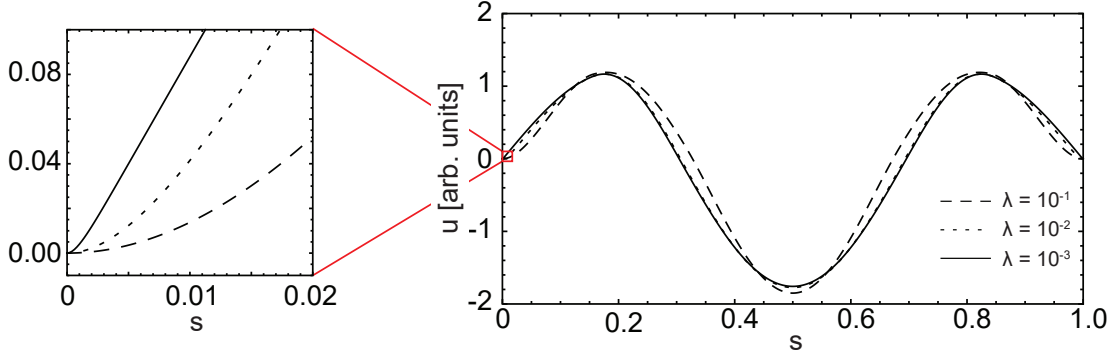
Figure 1.10 – **Demonstration of sharp bending curvature at the clamping points due to boundary condition.** Shapes of third order flexural modes of beams assuming the values of $\lambda = 10^{-1}, 10^{-3}, 10^{-3}$. The zoomed-in region shows the mode in the clamping regions, which illustrates an increase in bending curvature around the clamps with the reduction of λ.

majority of the bending energy comes from the clamping region.

Near the clamping points, the bending term in Euler-Bernoulli equation is significant due to the boundary condition $u'(0) = u'(1) = 0$, but, on the other hand, u is close to 0 so we can neglect the term $\check{\Omega}_n^2 u \approx 0$ in the equation (1.53). In the very small region around $s = 0$, to find a close form for dilution factor, we are assuming that the beam width is approximately constant and is equal to $v(s) = v_{\text{cl}}$, therefore (1.53) reduces to[11]:

$$\lambda^2 v_{\text{cl}} u''''(s) - u''(s) = 0 \tag{1.61}$$

The general solution is given by

$$u(s) = C_1 + C_2 s + C_3 e^{-s/(\lambda \sqrt{v_{\text{cl}}})} + C_4 e^{s/(\lambda \sqrt{v_{\text{cl}}})} \tag{1.62}$$

where the constants C_{1-4} can be found from the boundary conditions: $u(0) = 0$, $u'(0) = 0$ and $u'(s \gg \lambda \sqrt{v_{\text{cl}}}) = u'_{\text{cl},n}$, where $u'_{\text{cl,n}} = u'_n(0)$ in which u_n are the solutions to the wave equation given by (1.58), therefore it separately does not satisfy the boundary condition $u'_n(0) = 0$ per se. Instead the sinusoidal function has to asymptote to the exponential solutions at the clamping area given by (1.62). This ensures the continuity of our mode shape and that the two pieces of our solution (exponential term near the clamping and sinusoidal at the center) are smoothly connected. Explicitly for s around 0 the solution at (1.62) simplifies to:

$$u(s) = u'_{\text{cl},n} \left(s + \lambda \sqrt{v_{\text{cl}}} \left(e^{-s/(\lambda \sqrt{v_{\text{cl}}})} - 1 \right) \right) \tag{1.63}$$

---

[11] the same conclusions can also be reached if $v(s)$ is smooth and slowly varying function near the clamping where its derivatives can be neglected.

We emphasize that the length of the clamping region has an ambiguous definition but the high curvature region of the mode shape responsible to the majority of clamping losses is located at $0 \le s \le \lambda \sqrt{v_{\mathrm{cl}}}$ where the exponential term is dominant compare to the linear term in (1.63) (beyond this region, the exponential term in (1.63) approaches to zero and its contribution to the energy integral beyond $s > \lambda \sqrt{v_{\mathrm{cl}}}$ is negligible) . The contribution of the clamping region into the elongation and bending energy is found to be

$$U_{\text{elongation-clamping}} \approx 0 \tag{1.64}$$

$$U_{\text{bending-clamping}} = \int_0^\infty v(s) \left(u''(s) \right)^2 ds = \frac{1}{2\lambda} \sqrt{v_{\mathrm{cl}}} (u'_{\mathrm{cl},n})^2 \tag{1.65}$$

Note, that the clamping region is small $\Delta x_{\mathrm{cl}}/l = \lambda \sqrt{v_{\mathrm{cl}}} \ll 1$ and the bending energy stored here is proportional to the magnitude of the mode envelope at the beam boundaries ($u'_{\mathrm{cl},n}$).

Combining the energy at the clamping (assumed to be equal at both clamping points, $s = 0$ and $s = 1$) and at the distributed region (central parts away from the clamping) , we arrive at:

$$D_{Q,n} = \frac{1}{2\alpha_n \lambda + \beta_n \check{\Omega}_n^2 \lambda^2} \tag{1.66}$$

where

$$\alpha_n = \frac{\sqrt{v_{\mathrm{cl}}} (u'_{\mathrm{cl},n})^2}{2\check{\Omega}_n^2 \left(\int_0^1 v(s) u_n(s)^2 ds \right)} \tag{1.67}$$

$$\beta_n = \frac{\int_0^1 v(s)^3 u_n(s)^2 ds}{\int_0^1 v(s) u_n(s)^2 ds} \tag{1.68}$$

Equations (1.66)-(1.68) are our master equations for dissipation dilution engineering that we will use to design our ultra-high Q resonators and shows us the path for optimization of the dissipation dilution. Such an optimization can be performed by shaping $v(s)$ to reduce α_n (clamping losses) and β_n (distributed losses). We explore three of such a beam shaping strategies in sections 1.4 and 1.5.

For the completion of this section let us calculate the dissipation dilution, D_Q, for the canonical example of a uniform rectangular beam with the width of w, thickness of h, and length of l. In this scenario, our parameters simplifies to:

$$\begin{array}{c} \text{uniform rectangular beam} \\ \text{with dimensions of } (w, h, l) \end{array} \longrightarrow \begin{cases} v(s) = 1 \\ \check{\Omega}_n^2 = (\pi n) \\ u_n = \sqrt{2}\sin(\pi n s) \end{cases} \implies \begin{cases} \alpha_n = 1 \\ \beta_n = 1 \end{cases} \tag{1.69}$$

this reproduces the result reported by [13] [99] [105] [57]:

$$D_{Q,n}^{\text{rect.beam}} = \frac{1}{2\lambda + (n\pi)^2\lambda^2} \quad , \quad \lambda = \frac{h}{l}\sqrt{\frac{E}{12\sigma_{\text{avg}}}}$$

(1.70)

where σ_{avg} can be calculated from equation (1.41). For a uniform beam is given by:

$$\sigma_{\text{avg}} = (1-\nu)\sigma_{\text{film}}$$

(1.71)

Dissipation dilution in generic 3D mechanical resonator

So far we have only focused on the flexural modes of doubly clamped beams which are the modes that we are experimentally interested. However, for completion of the discussion, here we study the dissipation dilution in its most general condition for any mode flavor and any 3D geometry. Then, we apply the results of the generic solution, to numerically calculate the dilution factor for 3 different mode flavors (flexural, torsional and longitudinal modes) and observe that only dissipation of flexural modes gets diluted by the presence of an initial stress. The lack of geometrical nonlinearity in mode flavors other than flexural modes, prevents them from enjoying the lossless elongation energy and experience enhancement of the Q.

To derive the dissipation dilution factor of a generic vibrational mode, we have to use the generic form of Euler-Bernoulli equation where the relation between the strain field and the displacement field is tensorial product. This is in contrast to equation (1.18) which was only valid for flexural modes of a beam or a membrane . The time-dependent displacement field is denoted by $\tilde{U}_i(x, y, z, t)$, where $i = x, y, z$ is the coordinate index. The strain field is derived from the generalized Euler-Bernoulli equation [63]:

$$\tilde{e}_{ij} = \frac{1}{2}\left(\frac{\partial \tilde{U}_i}{\partial x_j} + \frac{\partial \tilde{U}_j}{\partial x_i} + \frac{\partial \tilde{U}_l}{\partial x_i}\frac{\partial \tilde{U}_l}{\partial x_j}\right)$$

(1.72)

where summation over repeating indices is implied. The last term in (1.72) is nonlinear in the displacement and can be identified as the geometric nonlinearity. We emphasize here that this nonlinearity is fundamental, it is not related to nonlinear stress-strain relation and is relevant even for infinitesimally small vibrations.

and the stress $\tilde{\sigma}_{ij}$ is related to strain via generalized Hooke's law in tensor form [63]

$$\tilde{\sigma}_{ij} = \frac{E}{1+\nu}\left(\tilde{e}_{ij} + \frac{\nu}{1-2\nu}\tilde{e}_{ll}\delta_{ij}\right)$$

(1.73)

where δ_{ij} is the Kronecker delta. We now assume that the deformation field consists of a static

part, $U_i(x, y, z)$, and a dynamic part, $\Delta U_{i,n}(x, y, z, t)$ which vibrates at the frequency of Ω_n. $\Delta U_{i,n}(x, y, z, t)$ can be written as

$$\Delta U_i(x, y, z, t) = \Delta U_{i,n}(x, y, z)e^{-i\Omega_n t} + c.c. \tag{1.74}$$

where $\Delta U_{i,n}(x, y, z)$ is the complex mode shape of the n-th mode and $c.c.$ refers to counter clockwise propagating terms. Strain, stress and elastic energy can be also separated into static and time-dependent contributions accordingly:

$$\tilde{e}_{ij}(t) = e_{ij} + \Delta e_{ij}(t) \tag{1.75}$$

$$\tilde{\sigma}_{ij}(t) = \sigma_{ij} + \Delta\sigma_{ij}(t) \tag{1.76}$$

$$\tilde{w}(t) = w + \Delta w(t) \tag{1.77}$$

The instantaneous elastic energy density is then given by [63]:

$$\tilde{w} = \frac{1}{2}\tilde{\sigma}_{ij}\tilde{e}_{ij} = \frac{E}{2(1+\nu)}\left(\tilde{e}_{ij}\tilde{e}_{ij} + \frac{\nu}{1-2\nu}(\tilde{e}_{ll})^2\right) \tag{1.78}$$

and the average of its variation, $\Delta w(t)$, which is the elastic energy stored by the vibrational mode, is found as:

$$\langle\Delta w(t)\rangle = \frac{1}{2}(\sigma_{ij}\langle\Delta e_{ij}(t)\rangle + e_{ij}\langle\Delta\sigma_{ij}(t)\rangle + \langle\Delta\sigma_{ij}(t)\Delta e_{ij}(t)\rangle)$$
$$= \frac{E}{2(1+\nu)}\left((2e_{ij}\langle\Delta e_{ij}(t)\rangle + \langle\Delta e_{ij}(t)\Delta e_{ij}(t)\rangle) + \frac{\nu}{1-2\nu}(2e_{ll}\langle\Delta e_{kk}(t)\rangle + \langle(\Delta e_{kk}(t))^2\rangle)\right) \tag{1.79}$$

We can then find the dissipated power density as:

$$p_{\text{diss}} = \left\langle\tilde{\sigma}_{ij}\frac{\partial\tilde{e}_{ij}}{\partial t}\right\rangle = \sigma_{ij}\left\langle\frac{\partial}{\partial t}\Delta e_{ij}(t)\right\rangle + \left\langle\Delta\sigma_{ij}(t)\frac{\partial}{\partial t}\Delta e_{ij}(t)\right\rangle \tag{1.80}$$

Here, the second term, $\langle\Delta\sigma_{ij}(t)\partial\Delta e_{ij}(t)/\partial t\rangle$, yields non-zero dissipated power if a delayed strain response to stress is introduced as a perturbation by the substitution $\Delta e_{ij}[\omega] \to (1 + i\phi)\Delta e_{ij}[\omega]$ and the average over time is found using the unperturbed Δe_{ij}. Unlike (1.79) for the stored energy, the extra term which arises in the presence of static deformation, $\sigma_{ij}\langle\partial\Delta e_{ij}(t)/\partial t\rangle$, is always zero as

$$\left\langle\frac{\partial}{\partial t}\Delta e_{ij}(t)\right\rangle = \frac{1}{T}\int_0^T \frac{\partial}{\partial t}\Delta e_{ij}(t)dt = \Delta e_{ij}(T) - \Delta e_{ij}(0) = 0 \tag{1.81}$$

where T is the oscillation period. Overall the dissipated power density is found as:

$$p_{\text{diss}} = \phi\omega_n\langle\Delta\sigma_{ij}(t)\Delta e_{ij}(t)\rangle = \phi\omega_n\frac{E}{(1+\nu)}\left(\langle\Delta e_{ij}(t)\Delta e_{ij}(t)\rangle + \frac{\nu}{1-2\nu}\langle(\Delta e_{kk}(t))^2\rangle\right) \quad (1.82)$$

We find the quality factor of the mode from the stored energy and dissipation rate as:

$$Q = \frac{2\omega_n\int\langle\Delta w(t)\rangle dV}{\int p_{\text{diss}}dV} \quad (1.83)$$

and then find the dissipation dilution ratio as:

$$D_Q = \frac{Q}{Q_{\text{int}}} = 1 + \frac{2\int(\sigma_{ij}\langle\Delta e_{ij}(t)\rangle + e_{ij}\langle\Delta\sigma_{ij}(t)\rangle)dV}{\int\langle\Delta\sigma_{ij}(t)\Delta e_{ij}(t)\rangle dV} = 1 + \frac{\langle W_{\text{dil}}(t)\rangle}{\langle W_{\text{lossy}}(t)\rangle} \quad (1.84)$$

where $Q_{\text{int}} = 1/\phi$ and the dilution and lossy energies are given, respectively, by:

$$\langle W_{\text{dil}}(t)\rangle = \int(\sigma_{ij}\langle\Delta e_{ij}(t)\rangle + e_{ij}\langle\Delta\sigma_{ij}(t)\rangle)dV \quad (1.85)$$

as an effectively lossless potential that generalizes the "elongation energy" in treatment of beams and membranes [13][99][105] and generalized equation (1.23). The lossy part of energy is given by:

$$\langle W_{\text{lossy}}(t)\rangle = \frac{1}{2}\int\langle\Delta\sigma_{ij}(t)\Delta e_{ij}(t)\rangle dV \quad (1.86)$$

which generalizes the "bending energy" [13][99][105] and corresponds to general case of (1.22). Unlike the toy model, W_{lossy} in general depends on the static strain. Therefore, the intuitive picture that tension increases stored energy without affecting dissipation is not correct in general.

(1.84) is the most general form of the expressions for dissipation dilution of non-zero Poisson's ratio (an-isotropic material). For a simple isotropic material with zero Poisson's ratio, equation (1.84) reduces to:

$$D_Q = 1 + \frac{\int 2e_{ij}\langle\Delta e_{ij}(t)\rangle dV}{\int\langle\Delta e_{ij}(t)\Delta e_{ij}(t)\rangle dV} \quad (1.87)$$

(1.87) reveals the peculiar effect of static strain e_{ij} on dissipation. If the static strain is zero then $D_Q = Q/Q_{\text{int}} = 1$ irrespective of the mode shape (we emphasize that corrections due to imaginary part of Poisson's ratio are here neglected). In contrast, D_Q can be higher (or lower) than unity if $e_{ij} \neq 0$ and $\langle\Delta e_{ij}(t)\rangle \neq 0$, the latter being possible due to geometric nonlinearity in (1.72).
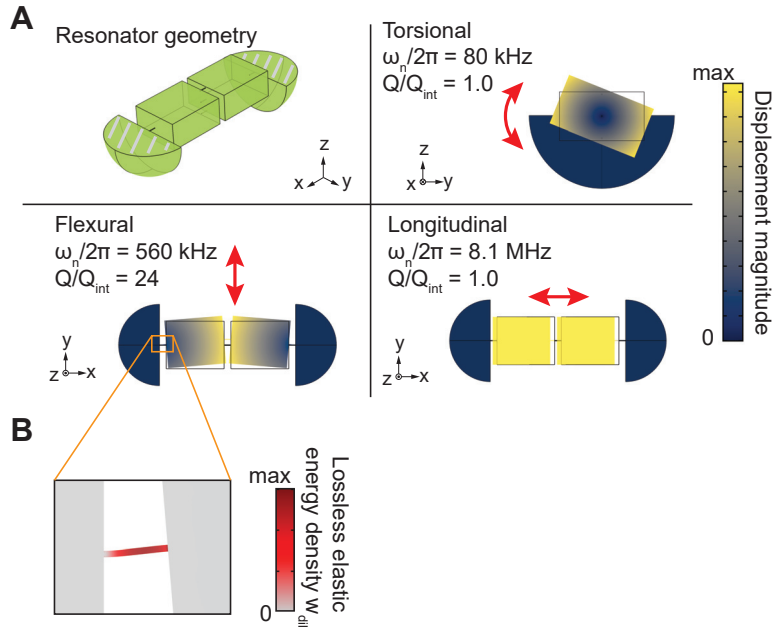
Figure 1.11 – **Dissipation dilution factors for vibrational modes of a 3D resonator** A) A doubly clamped beam with two quarter-sphere pads (hatched gray) and subjected to tension. The total length is 20 μm, the block size is $8.5 \times 7 \times 4$ μm, the bridge diameter is 100 nm and the material pre-strain is 0.4%. It shows that only flexural modes are subjected to dissipation dilution B) Distribution of effectively lossless elastic energy in a thin bridge during flexural vibration.

To give an example, we apply (1.87) to a doubly-clamped 3D resonator made of pre-strained material as shown in figure 1.11.A and calculate the dilution factors for a few representatives modes from different families. It can be seen that among these modes only the flexural one experiences dissipation dilution, whereas the torsional and longitudinal modes do not. Visualization of lossless energy density $\langle w_{\text{dil}}(t) \rangle$ in figure 1.11.B shows that it is concentrated in thin bridges between the blocks for the flexural mode. This is explained by a) static strain concentration in constrictions and b) relatively large geometric nonlinearity of strain in flexural deformations, which is not the case for torsional or longitudinal modes.

Strong dissipation dilution of flexural modes in high-aspect-ratio beams and membranes is thus due to the combination of tension and large geometrically nonlinear contribution in the dynamic strain.

Figure 1.12 provides another example of a geometry closer to the shapes we usually work with, in this thesis. Flexural modes (Figure 1.12A, C) of the beam resonator experiences enhancement of Q through the process of dissipation dilution but the torsional mode (figure 1.12.B) and the longitudinal mode (figure 1.12.D) do not experience such a dilution as the geometrical nonlinearity (elongation) is negligible for these modes.
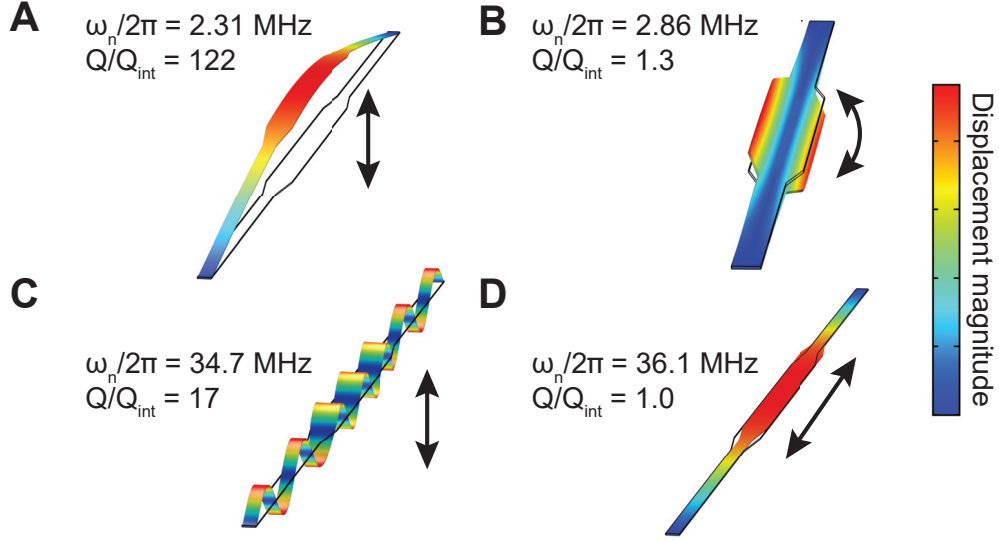
Figure 1.12 – **Simulated frequencies, mode shapes and dissipation dilution factors for different vibrational mode families of a doubly-clamped strained silicon nitride nanobeam (width = 1 μm, length = 100 μm, thickness = 100 nm).** A) fundamental out of plane mode, B) torsional mode C) 13-th order out of plane mode and D) the longitudinal mode.

Before we finish this section and present our strategies on how to design a geometry [$v(s)$] in order to enhance the quality factor, let's review two remaining unanswered questions about the theory of internal material losses and dissipation dilution. I) the ultimate limit of dissipation dilution and II) the role of surface losses versus the bulk losses.

Ultimate limit of dissipation dilution

Here we derive a rigorous upper bound for D_Q. This bound is set by the yield strain, material parameters, beam thickness and the frequency of vibration, but surprisingly does not depend on the beam length nor the mode order. From equations (1.40) - (1.47), we can derive our master equation for strain engineering which will be used in next sections:

$$\frac{\varepsilon(x)}{\varepsilon_{\text{avg}}} = \frac{w_{\text{avg}}}{w(x)} \tag{1.88}$$

Now we assume that the clamping losses are negligible ($\alpha_n = 0$) and evaluate the distributed loss coefficient β_n using the strain-width relation, eq. (1.88), and the condition that the maximum strain in the beam cannot exceed the yield strain $\varepsilon_{\text{max}} = \varepsilon_{\text{yield}}$. Using equation (1.88) we have:

$$v(x) = \frac{w(x)}{w_{\text{avg}}} = \frac{\varepsilon_{\text{avg}}}{\varepsilon(x)} \geq \frac{\varepsilon_{\text{avg}}}{\varepsilon_{\text{yield}}} \implies \int_0^1 v(s)^3 u_n(s)^2 ds \geq \left(\frac{\varepsilon_{\text{avg}}}{\varepsilon_{\text{yield}}}\right)^2 \int_0^1 v(s) u_n(s)^2 ds \tag{1.89}$$

Therefore using the definition of β_n in eq. (1.68) we obtain:

$$\beta_n \geq \left(\frac{\varepsilon_{\text{avg}}}{\varepsilon_{\text{yield}}}\right)^2 \tag{1.90}$$

and thus, the ultimate dissipation dilution bound is given by

$$\boxed{D_Q \leq \frac{12E\varepsilon_{\text{yield}}^2}{\rho h^2 \omega^2}} \tag{1.91}$$

This limit is formally equivalent to the dissipation dilution of a clamp free uniform beam strained to the yield strain of the material that is made of. On the other word, the ultimate limit of dissipation dilution is a sinusoidal curvature where the stress in the entire beam has reached it maximum value, $\varepsilon_{\text{yield}}$. This is regardless of the beam length and only depend on the frequency (wavelength) of the sinusoidal beam.

Surface losses in thin beams

The last theoretical topic that we are going to cover in this chapter is the effect of surface losses on the geometrical scaling of the mechanical Q. If the resonator's dissipation is dominated by its intrinsic material losses, the absolute mode quality factors can be calculated according to (1.38) from the intrinsic material quality factor Q_{int} and D_Q as

$$Q = D_Q \times Q_{\text{int}} \tag{1.92}$$

So far, we have only discussed the dissipation dilution and the role of geometry on its scaling. In the high-strain limit ($\lambda \ll 1$), D_Q depends only on the beam's geometry, mode order and the initial strain, but not on any of the material parameters. Dissipation dilution can therefore be understood without ever specifying a material. As a result, we argue that all of the techniques we are going to present for Q enhancement are material independent and can be used with any other strained materials.

On the other hand, in our derivation of dissipation dilution, we assumed that we are dealing with homogeneous materials in which the material parameters such as Young's modulus and Q_{int} are uniform across the entire geometry. This enabled us to summarize all the effects of the geometry into dissipation dilution factor. However, it has been shown by Villanueva et al. [57] that the real materials are not homogeneous. Especially the imaginary part of Young's modulus and Therefore, the Q_{int} seems to depends on the thickness of the resonator and reduces for thinner resonators [91].

This phenomenon is illustrated in figure 1.13, taken from a literature review performed by Villanueva et al. [57] . In this review, Villanueva et al. compiled a list of different Si_3N_4 resonators published over the past ~10 years, with different sizes and frequencies, extract
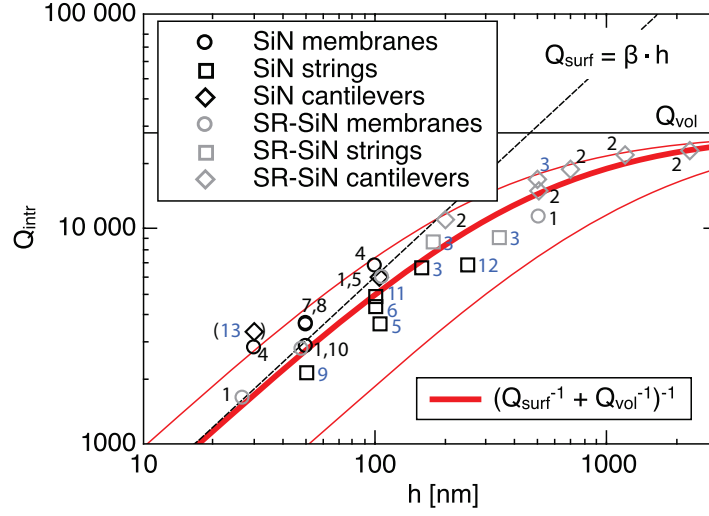
Figure 1.13 – **A literature review performed by Villanueva et al. [57] to determine the dependency of Q_{int} to the thickness (h).** The red line represents fitted to all values with $\beta = 6 \times 10^{10} \pm 4 \times 10^{10}$ m^{-1} and a volume loss related $Q_{vol} = 28000 \pm 2000$. The fine red lines represent the estimated error of β of $\pm 60\%$.

their dissipation dilution from the geometry and plotted their corresponding intrinsic quality factor versus the resonator's thickness. It is clear that the for thicknesses below 1μm, the intrinsic quality factor increases by thickness and eventually saturate to an upper bound (Q_{bulk}). Villanueva et al. argued that this is an evidence of surface losses and attribute the following phenomenological law to Q_{int} by fitting to this data:

$$Q_{int}(h) \approx 6000 \frac{h}{[100\,\text{nm}]}. \tag{1.93}$$

In this section, without going into the details of micro physics behind the surface losses, we try to derive this scaling law by using a toy phenomenological model with an inhomogeneous imaginary part of Young's modulus. We assume there are two phenomena responsible for friction. Friction at the surface which is much stronger than the friction in the bulk. Although the micro physics behind this observation is not completely understood, its evidence in the scaling of Q_{int} in thin mechanical resonators is apparent. We can attribute such a stronger friction at the surface to phenomena such as surface roughness, free dangling bonds or extra contamination on the surface. Regardless of the micro physics behind this effect, we can model the surface losses with two exponential functions with a very thin penetration depth (h_{PD}) of few nano meters. The in-homogeneous imaginary Young's modulus for a rectangular cross section can be written as:

$$E_i(z) = E_{i,B} + E_{i,S}e^{\frac{|z|-h/2}{h_{PD}}} \tag{1.94}$$

35

where $E_{i,B}, E_{i,S}$ are the imaginary components responsible for frictions in the bulk and at the surface respectively and h is the thickness of the resonator. Figure 1.14 shows the plot of equation (1.94) for the parameter fitted to figure (1.13) and assuming 1 nm penetration depths for the surface losses.
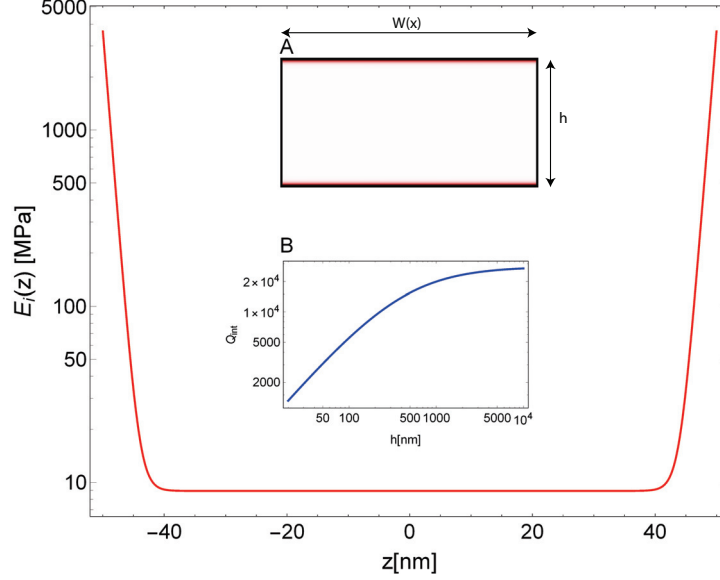
Figure 1.14 – **In-homogeneous imaginary part of Young's modulus according the phenomenological model of** (1.94) **with 1 nm penetration depth.** Inset A) Color coding of the dissipated energy as a function of position in cross section a rectangular beam. The extra surface losses induced by the top and bottom surface highlighted by darker color. Inset B) The calculated Q_{int} with the model in equation (1.98) corresponding to red fit in figure 1.13.

To derive the contribution of the surfaces losses, our calculations from equations (1.18) to (1.35) will remain exactly identical (as we assumed the real part of Young's modulus is still homogeneous). The difference between the homogeneous and in-homogeneous case appears at equation (1.36) where we calculate the volume integral of dissipated energy. In eq. (1.36), we assumed the E_i is a constant number and could be factorized from the integral. Now with z dependent imaginary Young's modulus, the equation (1.36) transforms to:

$$W_{\text{diss}} = \int w_{\text{diss}} dV = \frac{E_i}{2} \int_l dx I(x)(u''_{xx})^2 \longrightarrow W_{\text{diss}}^{\text{inhomog}} = \frac{1}{2} \int_l dx \int_{-h/2}^{h/2} dz z^2 E_i(z) w(x)(u''_{xx})^2 \tag{1.95}$$

therefore we have to calculate the integral of $\int_{-h/2}^{h/2} dz z^2 E_i(z)$ for a $E_i(z)$ which follows equation (1.94). In the condition where $h_{\text{PD}} \ll h$, we can approximate the integral to be:

$$\int_{-h/2}^{h/2} dz z^2 E_i(z) = \int_{-h/2}^{h/2} dz z^2 (E_{i,B} + E_{i,S} e^{\frac{|z|-h/2}{h_{\text{PD}}}}) \approx E_{i,B} \frac{h^3}{12} + E_{i,S} \frac{h^2}{2} h_{\text{PD}} \tag{1.96}$$

the in-homogeneous dissipated energy is then given by:

$$W_{\text{diss}}^{\text{inhomog}} = W_{\text{diss}}^{\text{homog}} \left(1 + \frac{6E_{i,S}h_{\text{PD}}}{E_{i,B}h} \right) \tag{1.97}$$

where for the $W_{\text{diss}}^{\text{homog}}$, the bulk imaginary Young's modulus is considered. Therefore, following our notation for the dissipation dilution, the equation (1.92) modifies to:

$$Q^{\text{homog}} = D_Q \times \frac{E_r}{E_i} \longrightarrow Q^{\text{inhomog}} = D_Q \frac{E_r}{E_{i,B} + \frac{6E_{i,S}h_{\text{PD}}}{h}} = D_Q \frac{E_r h}{E_{i,B}h + 6E_{i,S}h_{\text{PD}}} \tag{1.98}$$

we can further simplify (1.98) if we define the quality factors associated to the bulk and surface losses as the following:

$$Q_{\text{bulk}} = \frac{E_r}{E_{i,B}} \tag{1.99}$$

$$Q_{\text{surface}}(h) = \frac{E_r}{E_{i,S}} \frac{h}{h_{\text{PD}}} = \beta \cdot h \tag{1.100}$$

Equation (1.98) then simplifies to:

$$Q^{\text{inhomog}} = D_Q Q_{\text{int}}(h) \tag{1.101}$$

where

$$Q_{\text{int}}^{-1}(h) = Q_{\text{bulk}}^{-1} + Q_{\text{surface}}^{-1} \tag{1.102}$$

We reproduce the results from eq. (1.93) by separating the contributions from the surface and the bulk. It can be shown that for the very thin resonators ($h = 10 - 100$ nm) which is the range of thicknesses that have been fabricated for the experimental results of this thesis, $Q_{\text{bulk}} \gg Q_{\text{surface}}$ and the losses associated to bulk could be neglected. Therefore we assume a linear scaling for intrinsic quality factor, $Q_{\text{int}}(h) = \beta \cdot h$ for our resonators. At the end of section 1.4 we show the experimental demonstration of thickness scaling on our soft-clamped beams and experimentally confirm the same conclusion.

Surface losses has an interesting consequence for the fundamental mode of high aspect ratio uniform beams where $\lambda \ll 1$:

$$
\left.\begin{aligned}
f_1 &= \Omega_1/2\pi = \frac{1}{2\pi l}\sqrt{\frac{\sigma_{\text{avg}}}{\rho}} \\[2mm]
D_{(Q,1)} &= \frac{1}{2\lambda + n^2\pi^2\lambda^2} \approx \frac{1}{2\lambda} = \frac{l}{2h}\sqrt{\frac{12\sigma_{\text{avg}}}{E}} \\[2mm]
Q_{\text{int}} &= \beta \cdot h
\end{aligned}\right\}
\implies
\begin{cases}
Q_1 = \frac{\beta l}{2}\sqrt{\frac{12\sigma_{\text{avg}}}{E}} \\[3mm]
Q_1 \cdot f_1 = \frac{\beta\sigma_{\text{avg}}}{\pi}\sqrt{\frac{3}{4\rho E}} = \text{const}
\end{cases}
\tag{1.103}
$$

where f_1, Q_1 are the frequency and quality factors of the fundamental mode. Equation (1.103) shows that **I**) the quality factor of the fundamental mode is thickness independent and by thinning down the resonator, we do not gain on the quality factor. **II)** The $Q-$frequency product of the fundamental mode of a uniform rectangular beam is a geometrical independent constant. It means that regardless of the length, thickness and the width of the resonator, the $Q \times f$ product of the fundamental mode can be used as a standard candle to compare the resonators of different geometry and different fabrication methods. For Si_3N_4 and the measured deposition parameters [90] of $\varepsilon_{\text{film}} = 0.46\%$ (stress $\sigma_{\text{film}} = 1.14$ GPa), Young's modulus $E = 250$ GPa, Poisson's ratio $\nu = 0.23$ and density $\rho = 3100$ kg/m^3. and β calculated from (1.93), the $Q-$frequency product of the fundamental mode is:

$$
Q \cdot f \approx 10^{12} \text{ Hz}
\tag{1.104}
$$

Unfortunately this value is below the threshold of quantum coherency at room temperature where $Q \times f = \frac{k_B T}{\hbar} = 6.62 \times 10^{12}$ Hz [9]. As a result, the fundamental mode of Si_3N_4 beams regardless of their size, can never become "quantum enabled" [12][114] at room temperature and we need other techniques to achieve this goal. Based on the lessons that we learned about dissipation dilution in this section, we present 3 strategies that will enable us to cross this barrier and fabricate mechanical resonators that are quantum coherent at room temperature, in the next section.

1.4 Q-enhancement via high order modes, soft clamping and strain engineering [12]

In section 1.2, we described the concept of dissipation dilution where the quality factor of a mechanical oscillator is enhanced beyond its material's intrinsic quality factor due to a combination of initial stress and geometrical nonlinearity. We find out that in a general case, the dissipation dilution is in the form of equation (1.66) for thin film mechanical oscillators. In this section we present three strategies to enhance quality factor and $Q \times f$ product of a beam resonator to achieve quantum coherency at room temperature $Q \times f > \frac{k_B T}{\hbar}$ [12]. First we look at the higher order modes of a long uniform beam and will demonstrate how to achieve higher $Q \times f$ by operating at optimum mode order of longer beams. Then we present two geometrical micro-patterns (an especially designed $v(s)$) to further enhances the quality factor. In the first design, we try to reduces the clamping losses (reducing α_n in equation (1.66)) by placing the resonator in the bandgap of a phononic crystal to isolate the vibration from the clamping points; a technique known as "*soft clamping*" [91]. In the second strategy, we introduce a non-uniform phononic crystal pattern in which by tapering the central region of the beam, we locally create a region of enhanced strained, compared to the weak deposition stress of the film. Complementary to soft clamping, our second strategy consists of colocalizing the mode shape with a region of geometrically enhanced stress, making use of the tension balance relation $[\sigma(x) = T/[w(x)h]$. This approach allows us to cross the barrier of the soft clamping limit and reach a regime that has been inaccessible by any other oscillator in the past. Ringdown measurements at room temperature reveal string-like vibrational modes with Q factors as high as 800 million and $Q\times$ frequency exceeding 10^{15} hertz. These results illustrate, a promising route for engineering ultracoherent nanomechanical devices.

Strategy I: Q-enhancement via higher order modes of long uniform beams

To start our first strategy, let's review the quality factor and frequency of a uniform rectangular beam (presented in equation (1.70))

$$\text{uniform beam} \begin{cases} Q(\sigma, n) = Q_{\text{int}}\left(1 + \left(\underbrace{2\lambda}_{\text{supports}} + \underbrace{\pi^2 n^2 \lambda^2}_{\text{antinodes}}\right)^{-1}\right) \quad , \quad \lambda = \frac{h}{l}\sqrt{\frac{E}{12\sigma_{\text{avg}}}} \\ \\ f(\sigma, n) = \frac{n}{2l}\sqrt{\frac{\sigma}{\rho}} \cdot \sqrt{1 + n^2 \pi^2 \lambda^2} \end{cases} \tag{1.105}$$

where the frequency of the a high stress doubly clamped beam is taken from [115] and has been rearranged to fit to the notation in this thesis. The $\sqrt{1 + n^2\pi^2\lambda^2}$ term in frequency is often neglected in high aspect ration devices where $\lambda \ll 1$. The uniform beam model gives several rules of thumb for maximizing the Q or $Q \times f$ of a stressed nanomechanical resonator, namely, Q is typically highest for the fundamental mode ($n = 1$) and can be increased by increasing

---

[12]The content of this section is published at [101] and [90]

aspect ratio (l/h) or the stress. By contrast, $Q \times f$ is typically larger for high order modes. Both strategies have been explored for a wide variety of membrane-like geometries [76], [75]. In fact, it has been a mystery especially in the early years of the high stress nano-mechanics community on why Si_3N_4 membrane resonators had superior performance to their 1D counter parts [13] Although, both resonators enjoy similar initial stress and made of the same material. , the first-high stress beam shape Si_3N_4 mechanical resonators were invented and studied as early as 2006 [78] which predates Si_3N_4 membrane-like resonators by 2-3 years [116][75], their $Q \times f$ performance was limited to $Q \times f \approx 10^{12}$ Hz for many years (this limit is discussed in (1.103)). On the other hand, Si_3N_4 membranes resonators (although a latecomer to this field), were able to achieve $Q \times f > 10^{13}$ Hz as early as 2009 by Wilson et al. [75] and followed by impressive improvements over the next years and achieving $Q \times f$ as high as 10^{14} Hz in 2014 [76]. For many years, Si_3N_4 membrane resonators were considered the only platform that could reach the quantum coherency threshold at room temperature by operating at a regime where $Q \times f > \frac{k_B t}{\hbar} = 6.62 \times 10^{12}$ Hz.

It was only at 2015 that the first 1D objects could barely operate at the quantum coherency threshold [117]. This resonator was designed in the form of Si_3N_4 tuning fork and its higher performance wasn't completely understood at the time. Today with our dissipation dilution model [equation (1.66)] we hypothesize that in this work, Zhang et al. unknowingly took advantage of the strain engineering technique (similar to the method discussed in section 1.5) where an extra stress at the clamping points was achieved due to their specific geometrical design. It took until 2016 [118] that this discrepancy between the 1D and 2D objects were fully understood. The reason behind this discrepancy turned out to be a simple historical reason. Traditionally, people in the nano-beam community worked with the fundamental mode (a mode with highest quality factor) of relatively short beams (typically below 100μm long because of fabrication limitations). But researchers in the membrane community normally worked with higher order modes of a large membrane because **a)** the fundamental mode was significantly damped due to other damping mechanism (we revisit this issue in section 1.6) and the only way for them to achieve higher Q was to work with higher order modes. **b)** Because of the assembly of the optomechanical setups [39], membranes bigger than 1mm^2 were normally used. Beside millimeter size Si_3N_4 membranes were already commercially available.[14]

In the following analysis, we show that although the fundamental mode of a beam resonator has the highest quality factor, it is not the mode with the highest $Q \times f$. Figure 1.15.B beautifully illustrates this concept. We observe that even though the quality factor decreases in higher order modes, the frequency increases at a faster rate; but effectually Q takes over and we see a decline in $Q \times f$. In figure 1.15.B, we observe that $Q \times f$ rises at the beginning and then ultimately falls off because in very high order modes, $Q \propto 1/n^2$ drops faster than frequency

---

[13]This trend actually holds for nearly 10 years from 2008 [75] to 2018 [90] and was only broken by the work presented in this thesis.

[14]Because of their application as the vacuum windows for x-ray spectroscopy and as sample holders for transmission electron microscopy (TEM)[119]
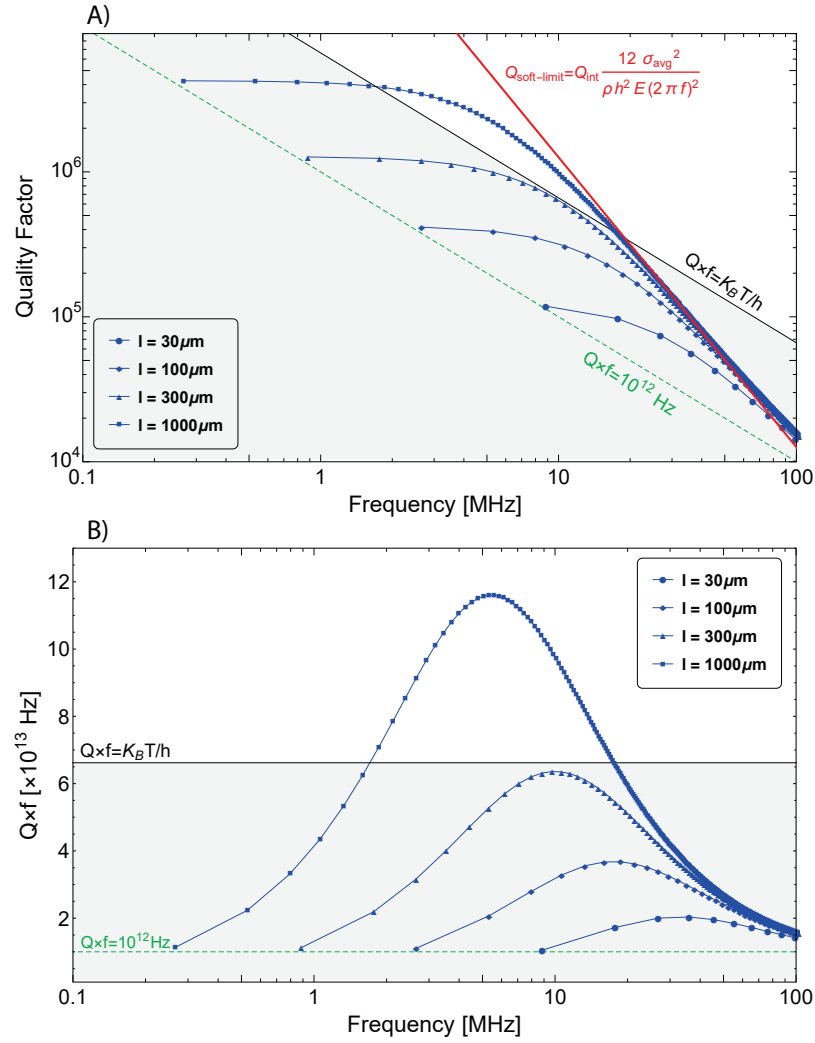
Figure 1.15 – Q **and** $Q \times f$ **of uniform rectangular beams.** A) Illustrates the quality factor of uniform rectangular beams at different mode orders and beam lengths according to equation (1.105). The quality factor of the fundamental mode, linearly increases by increase of the beam's length and roughly stays on the green dashed line representing the $Q \times f = 10^{12}$ Hz. Red curve represents the ultimate limit of soft clamping (clamp free beam) where the curvature at the clamping region is negligible. Very high order modes of a uniform beam, asymptote to this limit. B) $Q \times f$ plot for the same parameters used in A. It illustrates that there is an optimum mode order for each length that maximizes the $Q \times f$. The maximum value of $Q \times f$ increases with beam length and moves toward lower frequencies. The gray regions in both plots shows the regime where mechanical oscillator in not quantum coherent at room temperature. The parameters used in this plot: Young's modulus $E = 250$ GPa, density $\rho = 3100$ kg/m^3, thickness $h = 100$ nm, and $\sigma_{avg} = (1 - \nu)\sigma_{film} = 900$ MPa.

which is a linear function of n. This mean that there is an optimum mode order for each length that maximizes the $Q \times f$. Another observation from figure 1.15 is that the maximum value of $Q \times f$ increases with the beam's length. For lengths above $\sim 300 \mu$m, it is possible to operate a Si$_3$N$_4$ beam resonator in the quantum coherent regime at room temperature. In the following

we will present the quantitative description of this picture.

Assuming $\lambda \ll 1$ and treating n as a continuous variable in equation (1.105), the optimum mode order associated to the maximum $Q \times f$ product is given by:

$$\frac{d(Q(n) \cdot f(n))}{dn} = 0 \quad \cdots \Longrightarrow \quad n_{\text{opt}} \approx \sqrt{\frac{2}{(\pi^2 \lambda)}} \propto \sqrt{l} \tag{1.106}$$

the first observation from the equation(1.106) is that n_{opt} increases by going to longer beams. However, the frequency of the optimum mode order, decreases by going to longer beams:

$$f(n = n_{\text{opt}}) \approx \sqrt{\frac{\sigma}{\rho \pi^2 h l}} \sqrt{\frac{2\sigma}{E}} \propto \frac{1}{\sqrt{l}} \tag{1.107}$$

This is illustrated in figure 1.15 and is considered a weakness of this strategy as larger $Q \times f$ is only accessible at low frequencies. Operating at low frequencies (typically $\Omega_m/2\pi < 1$ MHz) could potentially creates technical issues for the optomechanical systems. For example existence of various technical noise sources at these low frequencies such as laser classical noise [120], $1/f$ noise of the photo-detectors and thermo-refractive noise [121]. The quality factor at the optimum mode order is:

$$Q(n = n_{\text{opt}}) \approx \frac{1}{4\lambda} \propto l \tag{1.108}$$

it shows that the Q of the optimum point is only half of the Q of fundamental mode $Q(n = n_{\text{opt}}) = Q_0/2$. The linear scaling of the Q_{opt} with the length means that the $\frac{Q}{m}$ of this resonator is fixed and we do not gain on the Q/m parameter. Finally, the $Q \times f$ at the optimum mode order is given by:

$$Q_{\text{opt}} \times f_{\text{opt}} \approx \frac{f_0 Q_0}{\sqrt{2\pi^2 \lambda}} \propto \sqrt{l} \tag{1.109}$$

where f_0, Q_0 are the frequency and quality factor of the fundamental mode. Although equation (1.109) shows us a path on how to increase the $Q \times f$ without any apparent limitation, the scaling is very week. If we decide to increase the $Q \times f$ by one order of magnitude from the highest in figure 1.15, $10^{13} \rightarrow 10^{14}$ Hz, we have to fabricate a beam with 100 times the length of device in figure 1.15 (10 cm). Fabrication of such a beam is impractical. Also as we discussed in chapter 3, there are two figures of merit for a mechanical oscillator that we are interested in optimizing: $Q \times f$ and Q/m. Our first strategy only allows us to enhance the $Q \times f$ but does not provide any improvement on Q/m ratio. In our next strategies, we present alternative approaches such as soft clamping and strain engineering which are significantly more efficient as they provide much faster scaling for $Q \times f$. In addition they offer enhancements of Q/m as our second figure of merit.
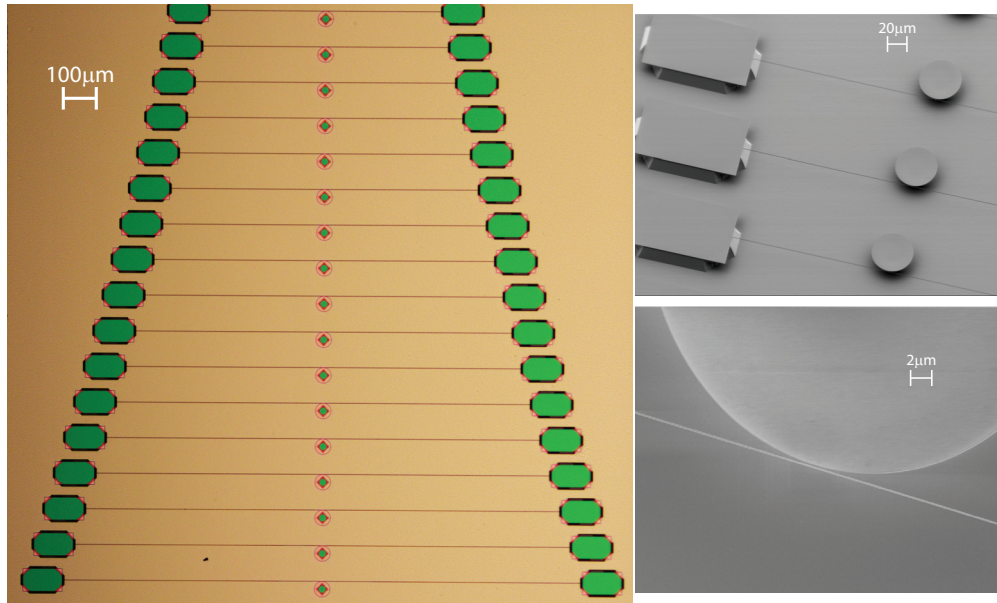
Figure 1.16 – **Optical and SEM images of a series of mechanical beam resonators with varying lengths.** In this sample we have fabricated beams (black horizontal stripes) from $l = 100$ μm to 1.5 mm. The two green regions at the two ends of each beam are the Si_3N_4 pads that solidly clamps the resonators to the silicon substrate. The circles at the center are optical micro-disk cavities monolithically fabricated from the same Si_3N_4 layer and used as an efficient readout sensor for the vibration of the mechanical resonator. In this work, we considered only in-plane flexural modes because of their compatibility with our displacement readout. The beam are made of a 400 nm thick Si_3N_4 and have a width of 100 nm (For in-plane modes, the thickness in the direction of motion is the beam's width). The micro-disks are separated by a gap of $\sim$ 80 nm from the beams. The near-field interaction between the beam and the micro-disk [122], [123] provide a displacement readout with an imprecision of ~ 1 fm/$\sqrt{\text{Hz}}$ capable of resolving the thermal Brownian motion of the oscillator with more than 70 dB signal to noise.

As the first experimental study presented in this thesis, we decided to experimentally explore the predictions made in equations (1.106) -(1.109). For this purpose, a series of beams with different lengths were fabricated from high stress stoichiometric Si_3N_4. Figure 1.16 shows a small fraction of this "harp shape" sweep of resonators (black horizontal stripes) where the lengths is varied from $l = 100$ μm up to 1.5 mm. Details of the fabrication is presented in chapter 2 but in summary, the devices are made from a 400 nm high stress LPCVD Si_3N_4 layer. The green areas in figure 1.16 are the regions that Si_3N_4 is attached to the underneath silicon substrate and the pink regions are the suspended parts of Si_3N_4 as the underneath Si layer has been etched away in the KOH bath during the undercut step. The Si_3N_4 beams are clamped to the silicon substrate using the two rectangular pads at each ends. In order to detect the vibrations of Si_3N_4 nano-beams, an optical micro-disk cavity is monolithically fabricated from the same Si_3N_4 layer with a separation gap of $\sim$ 80 nm from each beam and used as an efficient readout sensor for the vibration of the mechanical resonator. Since the nano-beam is positioned at the evanescent optical field of the micro-disk, the near-field interaction between

the beam and the micro-disk [122], [123], [124], [125], [126] modulates the effective optical path and results in phase modulation of the laser light sent on-resonance with the micro-disk cavity. Phase fluctuation of the transmitted light is detected on homodyne interferometer [7][9] with imprecision of ~ 1 fm/$\sqrt{\text{Hz}}$ at only few of μW of input power, capable of resolving the thermal Brownian motion of the oscillator with more than 70 dB signal to noise. The laser light is coupled in and out of the optical micro cavity using a tapered optical fiber [127][128][129].

We measured the quality factor of these resonators using a ringdown technique described in appendix A.I. To perform a ringdown, the beam were resonantly excited using a piezo located beneath the sample chip; the drive is then shuttered off, while displacement is continuously recorded using a network analyzer (with bandwidth $RBW \gg \Gamma_m$). It is important to note that in our real experimental apparatus, we record the demodulated signal at the output of the network analyzer which correspond to the envelope of the signal presented in figure 1.3 (the green dashed line). An example of such a ringdown measurement is presented at the inset of figure 1.17 (the exponential decay appears linear in logarithmic scale). Mechanical linewidths are measured by fitting an exponential function to these ringdown curves (black solid line in the inset). The experiments are perform in a high vacuum chamber operating at pressure $P \sim 10^{-4}$ mbar. Details of the setup and the vacuum chamber is discussed in appendix A.II.
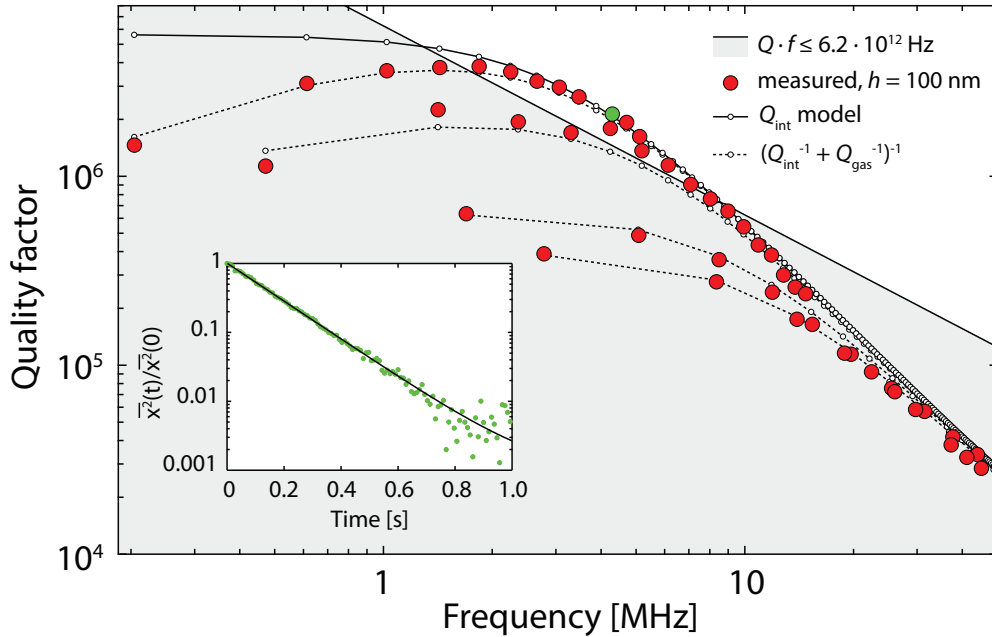
Figure 1.17 – **Measured quality factor versus mode order for long high-stress SiN nanobeams**. Q versus frequency for the odd-ordered flexural modes of nanobeams with lengths $L = 1.28, 0.55, 0.15,$ and 0.095 mm. Gray shading indicates $Q \cdot f < k_B \cdot 300 \, \text{K}/h = 6.2 \times 10^{12}$ Hz. Black dashed lines correspond to models for Q including internal loss (1.105) and an estimated gas damping rate of $\gamma_{\text{gas}} = 0.15$ Hz ($Q_{\text{gas}} = f/(0.15 \, \text{Hz})$). Inset: Ringdown measurement used to obtain the green point, $Q \times f \approx 9.0 \times 10^{12}$ Hz

The results of Q spectrum measurement for some representative beams is plotted in figure

1.17. For the longest beam, $L = 1.28$ mm, we observe a maximum of $Q \cdot f \approx 9.0 \times 10^{12}$ for $n = 21$ ($f \approx 4$ MHz). We compare this against a model curve for $Q(n)$ vs $f(n)$ (solid black line) based on a value of $\lambda = \frac{h}{l}\sqrt{\frac{E}{12\sigma_{\text{avg}}}} \approx 5 \cdot h/L$ estimated by fitting the dispersion relation $f(n)$ (1.105) and consistant with our deposition values for E, σ_{film}. The model predicts $Q(n_{\text{opt}}) \cdot f(n_{\text{opt}})$ to within 10%, but qualitatively overestimates Q for lower frequencies. This discrepancy is due to gas damping which contributes a systematic additional damping of $\gamma_{\text{gas}} \approx 0.15$ Hz. This shows the importance of ultra-high vacuum (UHV) chambers for these measurements. Especially in the next section, we present two techniquesin order to enhance the mechanical Q to 1 billion at 1MHz equivalent of mechanical linewidth of $\Gamma_m \sim$ 1mHz. In-order to measure these ultra-high Q mechanical resonators, we built a custom made UHV chamber with operating pressure of $\sim 10^{-8}$ mbar for this experiment as a major part of this thesis. The details of design, blue prints and mode of operation of this UHV chamber is presented at appendix A.II.

In summary, in our first strategy, we theoretically and experimentally studied the possibility of using the higher order modes of a long beam as a method to enhance the $Q \cdot f$ beyond the threshold for quantum coherency at room temperature, $Q \times f > 6 \times 10^{12}$ Hz. We also demonstrate these findings by measuring the Q spectrum of beams with different lengths and achieved $Q \times f = 9.0 \times 10^{12}$ Hz. Although this is on par with the membrane resonators with similar aspect ration and stress, nano-beam resonators have 100-1000 time smaller mass which could lead to higher optomechanical coupling strength. We observe that the general scaling laws of the main figures of merit for this strategy are :

$$\text{Higher order modes of rectangular uniform beam:} \begin{cases} Q \times f \propto \frac{1}{\sqrt{l}} \\[2mm] \frac{Q}{m} = \text{const.} \end{cases} \tag{1.110}$$

The main disadvantage of this method to enhance the quality factor are:

- weak scaling of $Q \times f$

- no improvement on Q/m

Strategy II: Q-enhancement via soft clamping

An alternative approach that recently has been demonstrated with a patterned Si_3N_4 membrane resonator [91], is to use periodic micropatterning of a phononic crystal (PnC) to localize the mode shape away from the supports. By this "soft clamping" approach, the leading term in (1.105) can be suppressed, giving access to the performance of an ideal clamp-free resonator (red line in figure 1.15).

The core of the idea behind the soft clamping technique is illustrated in figure 1.18. Since the sharp curvature near the clamping points is responsible for majority of losses, if (by some geometrical design) we manage to create a mode shape where its derivative, approaches to

$$u(x,t) = A_0 \sin(\Omega_m t) \sin(2\pi x / \lambda_m) e^{-|x|/\lambda_{\text{PnC-PD}}}$$
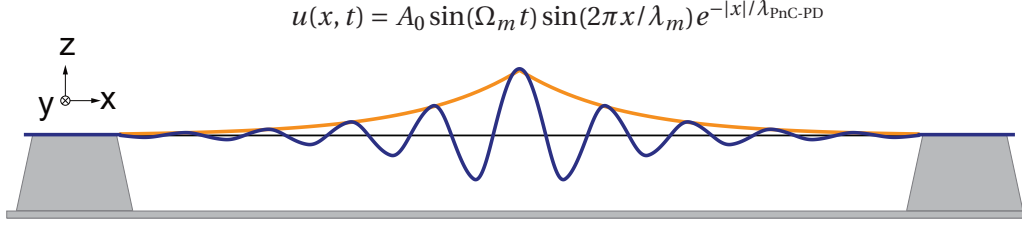
Figure 1.18 – **Localized mode shape of a soft-clamped beam.** The core of the idea of soft clamping is to create a medium where motion is localized at the center and slowly damps as it approaches the clamping points. The blue curve is an example of such a mode shape, localized sinusoidal with exponentially damped envelope (orange curve). The displacement and its derivative asymptote to zero ($u(0,l) = 0, u'(0,l) = 0$) and matches the boundary conditions. With this "soft clamping" method, there won't be a need for a sharp curvatures at the clamping regions to match the mode shape to the boundary conditions as is the case for uniform beams.

zero near the clamping region, we diminish the contribution of the clamping losses as $\alpha_n \to 0$ in equation (1.66). Figure 1.18 illustrates one example of such mode shape; A resonator which its amplitude exponentially drops as it moves away from the center toward the clamping points. Given enough length for the exponential drop, the amplitude and its derivative asymptote to zero ($u(0,l) \to 0, u'(0,l) \to 0$). Such a condition provides a soft clamping for the resonator as there won't be a need for a sharp curvature to match the mode shape to the boundary condition ("hard clamping"). The main question however, is how we can engineer a beam geometry ($v(s)$) that results in a mode shape similar to figure 1.18. It has been recently proposed by Y. Tsaturyan et al. [91] that placing a defect membrane resonator at the center of a 2D phononic crystal, creates a localized mode shape similar to figure 1.18. With this technique Y. Tsaturyan et al. were able to enhance the mechanical quality factor of a Si_3N_4 resonator to about 200 million at 777 KHz, a new record Q for the membrane community. In this section we try to apply this idea to 1D geometry.

A phononic crystal consists of an infinite chain of a periodic structure (see figure 1.19), a concept that has been widely used in nano-mechanics community [130] [131]. The figure 1.19 shows a canonical example of such a periodic structure made of masses and springs used as a toy model to understand the vibration in solid crystals [132][133]. In appendix A.I.1 we analytically calculate dispensation relation of this canonical example to be:

$$\Omega_\pm = \sqrt{(\Omega_1^2 + \Omega_2^2) \pm \sqrt{(\Omega_1^2 + \Omega_2^2)^2 - 4\Omega_1^2\Omega_2^2 \sin^2(k/2)}} \qquad (1.111)$$

where Ω_+ and Ω_- are the frequencies on the upper and lower branch in figure 1.19 and $\Omega_1 = \frac{k_s}{m_1}$, $\Omega_2 = \frac{k_s}{m_2}$ are the natural resonance frequency of individual parts of the "unitcell" and k is the special angular frequency in the direction of propagation. If $m_1 \neq m_2 \implies \Omega_1 \neq \Omega_2$, equation (1.111) shows that by cascading two pieces with different masses that are connected via a series of identical springs, we can create a region in the frequency domain known as
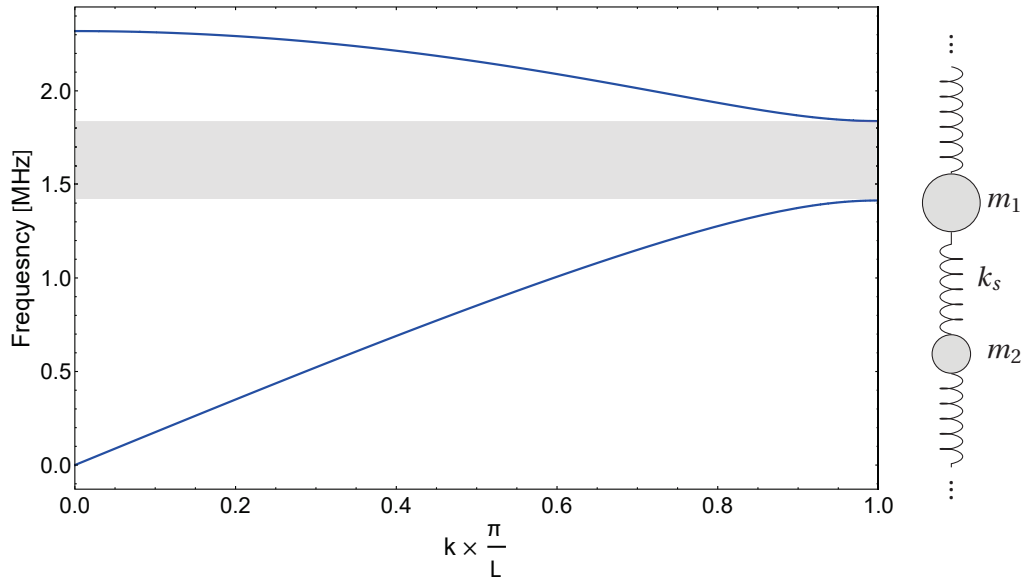
Figure 1.19 – **A canonical example of a phononic crystal** The bandgap (gray band) created by cascaded chain of connected masses and springs with two different mass elements in the chain. The upper and lower frequency branches are calculated using (1.111) where $\Omega_1 = 1$ MHz , $\Omega_2 = 1.3$ MHz. k is the special angular frequency and L is the length of the unitcell.

"*bandgap*" (gray area in figure 1.19), that there are no modes in the PnC chain to support these frequencies. On the other word, if we drive a part of this infinite periodic chain at a bandgap frequency, the oscillations cannot propagate in the structure and it gets exponentially damped as it penetrates inside the phononic crystal. Therefore, if we position a resonator at the middle of a PnC chain which its natural resonance frequency coincides with PnC's bandgap, its vibration will be localized at the center and its amplitude drops exponentially as it penetrates into the PnC, creating a mode shape similar to figure 1.18.

The width of the bandgap for this canonical case is given by (see appendix A.I.1):

$$\Delta\Omega_B = \sqrt{2}|\Omega_1 - \Omega_2| \tag{1.112}$$

This means that the larger the mass difference between the two pieces is, the larger the bandgap is. We will use this simple conclusion in section 1.6 to design our PnC shield to stop the radiation losses.

In fact, the unitcells we use to construct our phononic crystals in 1D, looks very similar to the canonical example of figure 1.19. In our PnC design, we create a mass difference by patterning alternating regions of wide and narrow on a high stress Si_3N_4 film. A schematic illustration of our PnC design is shown in figure 1.20. Before we proceed with the design details and experimental results, it is important to emphasize that phononic crystals are not a new concept and has been widely used in nano-mechanics community especially in 1D geometry [134][135][136][137][138][139]. However, in most of these works, the phononic crystals were used as an "acoustic shield" to stop the acoustic radiation loss at VHF-UHF frequencies. We

will study the concept of ration losses and our means to stop them via PnC shields in section 1.6, but in summary radiation losses are dominant at very high frequencies, $f > 100$ MHz. However, for the frequency range that we are interested in this section, $\Omega/2\pi < 10$ MHz, the radiation losses are negligible.
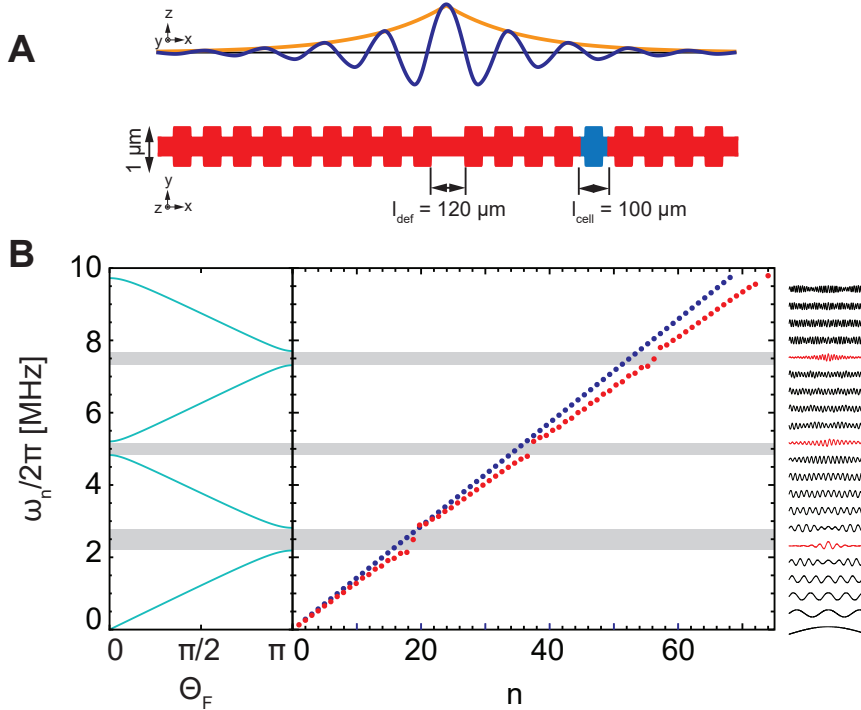
Figure 1.20 – **Schematic illustration of PnC design, bandgap calculations and mode spectrum.** A) Top: localized flexural mode shape $u(x)$ (blue) and its exponential envelope (orange). Bottom: Schematic of geometry of a corrugated beam for soft clamping (red). PnC unit cell is highlighted in blue within the beam. B) On the left: The band diagram of a phononic crystal for the unitcell highlighted in panel A illustrates the fundamental bandgap and higher order bandgaps of the PnC. In the middle: Red dots: spectrum of the out-of-plane flexural vibrations of the corrugated beam shown in panel A. Blue dots: spectrum of a uniform rectangular beam with same l, h as the PnC beam plotted for the reference. The sparse mode spectrum near the bandgap is a unique and important feature of the corrugated beams. On the right: The mode shapes for few selected modes where red mode shapes belong to the localized modes.

Our proposal to use phononic crystals to enhance the quality factor via soft clamping, is fundamentally different than the traditional applications of PnC shields. Here we propose to use phononic crystals as a "mode shaping medium" in order to engineer a specific mode shape that has a smooth transition between the sinusoidal region and the clamping parts. A major consequence of these two approaches to phononic crystals (PnC as shield versus PnC as mode shape engineering device) is the difference in design targets and goals, which has deep impact in the final geometrical design. When we design PnCs for an acoustic shield, we normally prefer to create as large of a mass mismatch between the two pieces of unitcell as possible to create a larger bandgap in order to shield wider range of frequencies. In addition, the larger

the mass mismatch between the two pieces is, the faster a bandgap oscillation is damped in the phononic crystal. Therefore, one of the main design parameters for PnC shields is to create a large mass difference in order to achieve a more effective and broadband shield. However, in the case of soft clamping, if the exponential drop is too fast, it creates additional curvature due to its sharp transition, which leads to reduction of the quality factor. On the other hand, if the mass ratio is too small, then the oscillation won't be damped in finite number of unitcells that we can fabricate and we won't achieve suppression of the clamping losses. Therefore, there is a sweat spot in the middle which creates a smooth exponential without additional curvature but fast enough so that the entire length of the structure is not too long. Through different numerical optimizations, we realized that the width ratio of $1.9 < \frac{w_{max}}{w_{min}} < 2.3$ for a fish-bone design (figure 1.20.A) is the optimum choice.

Fig. 1.20 shows an example of a 1D PnC nanobeam featuring a soft-clamped vibrational mode for which the clamping losses is suppressed. A defect resonator with the length of l_{def} and typically with the width of the small piece w_{min}, is encapsulated between two PnC barriers with n_{cell} on each side (10 in figure 1.20). The localized mode shape of the defect presented in 1.20.A shows the desired exponential damping for soft claiming. The band diagram for out-of-plane (z-direction) modes of the unitcell is plotted in figure 1.20.B, showing the frequencies of the bandgaps (gray bands). It is important to note that the unitcell in figure 1.20.A, unlike our toy mass and spring example in figure 1.19, is multi-mode object that could result in higher order bandgaps. For soft clamping, we mainly focus on the fundamental bandgap of the unitcell as our numerical simulations showed that the fundamental bandgap leads to the highest quality factors. It is equally important to point out that in our example in figure 1.20, we work with the fundamental mode of the defect as $l_{def} \sim l_{cell}$. We could also imagine working with higher order modes of defect in the same fundamental bandgap.

Among the different higher order defect modes, we find that the second order defect mode is especially interesting as its mode shape is an odd function with a node at the center of the beams. In our experiments (which will be followed shortly), we find out that the second order defect mode has the highest quality factor (even slightly higher than the fundamental mode of the defect) and is more robust. In fact, our record value for the $Q = 800$ million, was achieved on a sample designed to localize the 2nd order mode of the defect with $l_{def} \sim 2.2 l_{cell}$. Besides offering higher quality factors, 2nd order defect modes have another positive aspect: we can take advantage of the node at the center of geometry and clamp the structures at the center. We experimentally checked this idea which will be presented at the end of this section and it seems that such a clamping doesn't affect the Q of localized mods significantly. On the other hand, having the beams clamped at the center, solves one of major technical challenges of fabricating these extremely high aspect ratio devices.

The frequency versus mode order plot of the corrugated beam from panel 1.20.A is shown next to the band diagram in 1.20.B. First observation from this plot is that the frequency dispersion of the corrugated beam (red dots) is not significantly different than of a uniform beam (blue dots). The major difference between the two is the sparse mode spectrum of the corrugated

beams near the band gap frequencies. We can observe this sparse spectrum, more visibly in our experimental data in figure 1.27. The sparse spectrum of the localized modes, is another differentiating feature of our design which becomes very essential for the future quantum optomechanic experiments. One of the major limitations of laser cooling schemes for these mechanical oscillators is the off resonant tails of the neighboring modes interfering with our measurements [10]. As a bonus, the issue of neighboring modes is automatically solved in soft clamped beams.
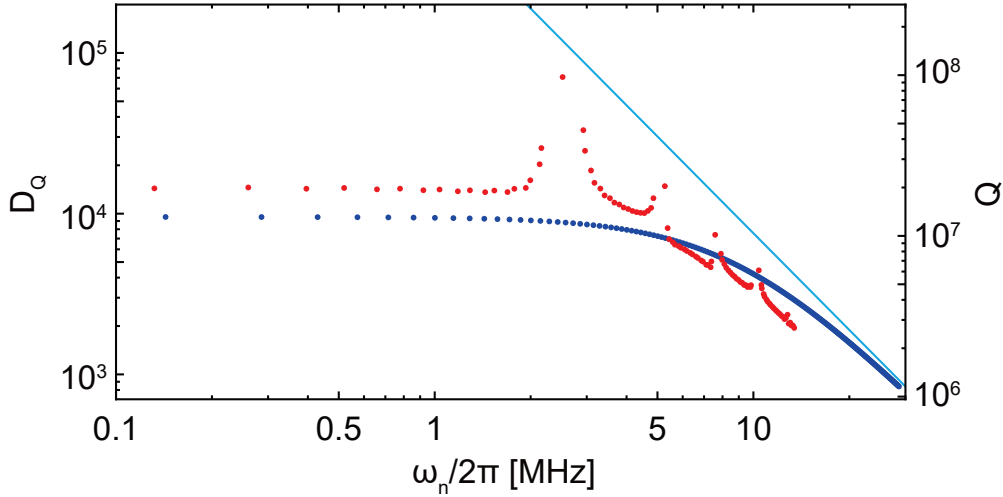
Figure 1.21 – **Dissipation dilution of PnC beam** for different modes (red dots) compared to the modes of a uniform beam (blue dots) plotted for the reference. The solid blue line represents the quality factor of clamp-free resonator as an ultimate limit of soft clamping (discussed in equation (1.113)). We observe an enhancement of the quality factor for the modes near the band gap with a celebrated mode (highest in among the red data points corresponding to the localized mode) in which the quality factor approached that of the soft clamping limit.

The most interesting part of the discussion about the soft clamped beams however, is the performance of their quality factor. Figure 1.21, illustrates the Q spectrum of the geometry presented in figure 1.20 (red dots) as comparison to the Q spectrum of high order modes of a uniform beam of the same length (blue dots), plotted for the reference. Outside of the bandgaps, the Q spectrum of the corrugated beam closely follows the trend of the uniform beam. However, as we approach the bandgap, mechanical Q increases and it finally peaks at the middle of the bandgap. The solid line in figure 1.21, represents a clamp free resonator as the ultimate limit of soft clamping technique:

$$Q_{\text{soft-limit}} = Q_{\text{int}} \frac{1}{\lambda^2} = Q_{\text{int}} \frac{12\sigma_{\text{avg}}2}{\rho h^2 E \Omega^2} \quad , \quad \sigma_{\text{avg}} = (1-\nu)\sigma_{\text{film}} \tag{1.113}$$

The mechanical Q of the mode in the middle of the bandgap approaches to this limit, which means that the clamping losses for localized modes are significantly suppressed ($\alpha_n \approx 0$ in equation (1.66)). However, the localized mode in figure 1.21 doesn't exactly reach the soft

clamping limit presented in equation (1.113). The reason for this is that the integral for β_n in equation (1.66) does not approach to unity for all localized mode shapes. However, if $\frac{w_{\max}}{w_{\min}} = 2$, we can show [15] that $0.44 < \beta_n < 1.77$ which means:

$$Q_{\text{soft-limit}} \times 0.56 < Q_{\text{localized}} < Q_{\text{soft-limit}} \times 2.25 \qquad (1.117)$$

we can modify β_n by changing the defect length and optimizing for the mechanical Q. In fact, in the experiment, we fabricate 10s of soft clamped beams on one chip (illustrated in figure 1.24) where we sweep the defect length to observe localized mode travels through the bandgap as we observe the quality factor. We experimentally observe that by optimizing the defect length, localized modes can asymptote to $Q_{\text{soft-limit}}$.

So far we demonstrate that by employing a phononic crystal, we can engineer a medium where the oscillations of the localized mode exponentially drop as it penetrates to the phononic crystal. This leads to a smooth transition to the clamping points. We observed that if we have enough number of unitcells, we can diminish the contribution of the clamping losses by making $\alpha_n = 0$ in equation (1.66). Now the main unanswered question is that how many unitcells are enough number of unitcells? On the other word, how many unitcells do we need to make the clamping losses negligible? It is very difficult to analytically answer this question. In figure 1.22 we try to numerically simulate Q for different number for unitcells and beam lengths. To understand the figure 1.22 lets only focus on data points for the longest beams, $l = 10$ mm. The dark blue data points represent the Q spectrum of a uniform beam with the same length plotted for the reference. Dark red data points, represents the Q of the localized mode, corresponding to the peak value in figure 1.21. To generate the dark red data points, we sweep the number of unitcells while fixing the total length of the beam and maintaining the ratio for $l_{\text{def}}/l_{\text{cell}} = $ const and $w_{\max}/w_{\min} = $ const. In this way, we make sure that the localized mode stays at the same position with respect to the bandgap. By increasing the number of unitcells in a fixed length, we shorten the length of the unitcell. As a result, the bandgap and the localized modes shift to higher frequencies. Now if we have many unitcells (the points to the right side of the curve), the Q of the localized mode asymptotes to the soft clamping

---

[15]In our integral for β_n, if the lengths of the thick and the thin parts the unitcell are equal, we have $v_{\min}(s) = \frac{2w_{\min}}{w_{\min} + w_{\max}}$, $v_{\max}(s) = \frac{2w_{\max}}{w_{\min} + w_{\max}}$ according to equations (1.44). therefore:

$$\left(\frac{2w_{\min}}{w_{\min} + w_{\max}} \right)^2 < v(s)^2 < \left(\frac{2w_{\max}}{w_{\min} + w_{\max}} \right)^2 \qquad (1.114)$$

this translates to:

$$\implies \left(\frac{2w_{\min}}{w_{\min} + w_{\max}} \right)^2 \int_0^1 v(s) u_n(s)^2 ds < \int_0^1 v(s)^3 u_n(s)^2 < \left(\frac{2w_{\max}}{w_{\min} + w_{\max}} \right)^2 \int_0^1 v(s) u_n(s)^2 ds \qquad (1.115)$$

equation (1.115) is only valid because $v(s$ and $u_n(s)^2$ or even positive functions with respect to the center of the beam. From eq. (1.115) we can conclude:

$$\beta_n = \frac{\int_0^1 v(s)^3 u_n(s)^2}{\int_0^1 v(s) u_n(s)^2 ds} \implies \left(\frac{2w_{\min}}{w_{\min} + w_{\max}} \right)^2 < \beta_n < \left(\frac{2w_{\max}}{w_{\min} + w_{\max}} \right)^2 \qquad (1.116)$$

51
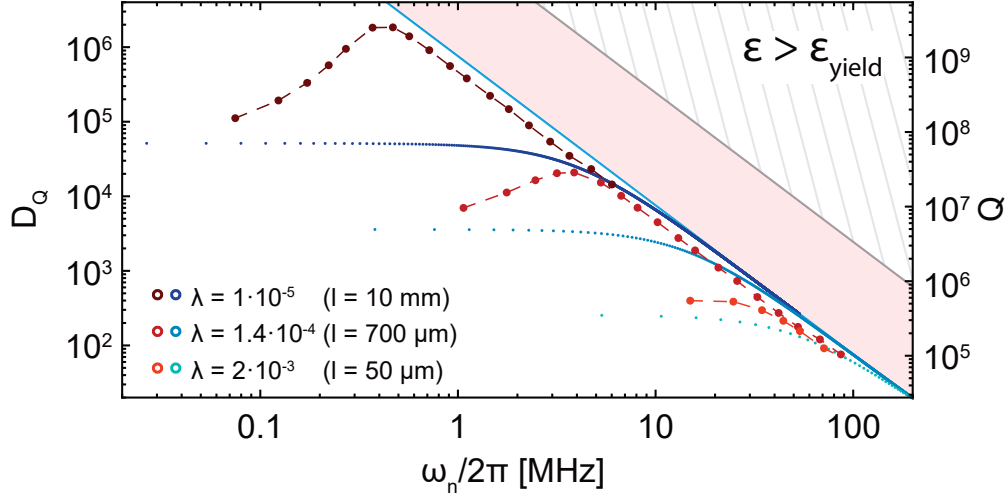
Figure 1.22 – **Optimization of number of unitcells for soft clamping technique.** Red dots: Quality factor of the localized mode (peak data point if figure 1.115) as we vary the number of unitcells for fixed total beam length while maintaining the ratio of l_{def}/l_{cell} and w_{max}/w_{min} constant. Blue data pints: Q spectrum of uniform beam of the same lengths (plotted for comparison). Beam thickness for this simulation is $h = 20$ nm. For high number of unitcells, the Q of the localized mode follows the clamp-free beam (blue solid line). For low number of unitcells, the quality factor declines due to additional losses at the clamping as the PnC is not effective for low number of unitcells. The hatched region represents the forbidden zone for a mechanical resonator according to equation (1.91) as the strain has to be larger than the yield strain of the material. Light red region represented by equation (1.118), in theory is accessible via dissipation dilution but is beyond the reach of soft clamping technique.

limit (the solid blue line corresponding to eq. (1.113)). However, as we lower the number of unitcells, below a threshold, we no longer climb on $Q_{soft-limit}$ and the Q of the localized mode starts to decline. This is because below this threshold, the phononic crystal is not efficiently damping the mode shape and the clamping losses starts to dominate. Therefore, the optimum position to operate a PnC beam is with the number of unitcells that maximizes the Q for a fixed beam length, $n_{soft-max}$. Fabricating more unitcells than $n_{soft-max}$, will not improve the performance of the soft clamping technique as the clamping losses are already negligible. In figure 1.22, we illustrate that $n_{soft-max}$ changes by changing the total length of the beam (light red and orange data points). However, it should be pointed out that the dependency of $n_{soft-max}$ to the total length of beam is logarithmic and very weak. For the lengths that we explore in this thesis, $n_{soft-max}$ is in the range of $6 < n_{soft-max} < 9$. It is important to point out that the maximum value of Q in figure (1.22) is only proportional to the total length of the mechanical oscillator. This means that the recipe to achieve higher quality factors using the soft clamping approach is to fabricate longer beams.

The hatched region in figure 1.22 illustrates the "forbidden zone" for a mechanical resonator with the yield strain of ε_{yield} according to equation (1.91). It is impossible to achieve a Q in this region as the mechanical oscillator would breaks before reaching this regime. Red region

in figure 1.22 however, illustrate the region were:

$$Q_{\text{int}} \frac{12\sigma_{\text{avg}}2}{\rho h^2 E\Omega^2} < Q < Q_{\text{int}} \frac{12\sigma_{\text{yield}}2}{\rho h^2 E\Omega^2} \tag{1.118}$$

This region is accessible in theory with dissipation dilution, but is beyond the reach of soft clamping method. This regime remains unexplored with both of the strategies we presented so far. As we will see in the following, we can enhance the mechanical Q and $Q \times f$ of the soft-clamped resonators by geometrical scaling, but we can never cross the barrier of $Q_{\text{soft-limit}}$ with this technique. In order to cross the soft clamping barrier, we have to increase the average stress, σ_{avg}. One difficult and unfruitful method of pursuing such goal is to find new deposition recipes that results in higher initial stress in the film, σ_{film}. However, in the next chapter we introduce our third and most efficient strategy, where we use geometrical tricks to locally enhance the stress in the localized region of the beam and be able to cross this barrier for the first time.

Before we present our experimental results on soft-clamped beams, let's review the geometrical scaling laws associated with our 2nd strategy. The dissipation dilution factor scales as $D_Q^{\text{soft-clamped}} \approx \frac{1}{\lambda^2} \propto \frac{l_{\text{cell}}^2}{h^2}$ (we use l_{cell} because it determines the frequency of the bandgap and thus, the localized mode). As we discussed in previous section, that intrinsic Q of the materials scales linearly with the thickness due to surface losses, $Q_{\text{int}} \propto h$. Therefore, the Q of the soft clamped modes scales as:

$$Q_{\text{soft-clamped}} \propto \frac{l_{\text{cell}}^2}{h} \tag{1.119}$$

This scaling is completely different compared to the scaling for the fundamental mode of a uniform beam (eq. (1.103)) or optimum mode order of a uniform beam (eq. (1.110)). One major difference of the soft-clamped resonators is that the performance of the resonator improves as we fabricate thinner samples. Y. Tsaturyan et al. [91] experimentally observed similar scaling for the thickness of the soft-clamped membrane oscillators. In addition, Q scales quadratically with length which means the scaling of the $Q \times f$ is linear ($f \propto \frac{1}{l_{\text{cell}}}$); a much faster scaling than our first strategy of using the optimum higher order mode of uniform beam. Also, the mass scales linearly with the length of the unitcell, going to longer devices improves the Q over mass ratio ($\frac{Q}{m}$), which is our second figure of merit for a mechanical resonator. In summary:

$$\text{soft-clamped beams} \begin{cases} Q \times f \propto \frac{l_{\text{cell}}}{h} \\[2ex] \frac{Q}{m} \propto \frac{l_{\text{cell}}}{h^2} \end{cases} \tag{1.120}$$

If we compare this scaling with the historical scaling of mechanical resonators presented in figure 1.5, we observe an opposite trend as higher quality factors are achieved by using smaller mode volumes (by going thinner). This gives us fundamentally new toolbox in design and opti-

mization of optomechanical systems. Now only by proper design of the mechanical oscillator (regardless of the optical subsystem), we can achieve better optomechanical performance and longer coherency at the same time.

Experimental demonstration of soft-clamped beams

In order to put this idea into the test, many devices were fabricated and several sweeps set in place to experimentally understand the different physical aspects of these soft-clamped resonators. Most important sweeps that we performed were: **I)** Sweep of the defect's length (l_{def}) which was normally performed between the samples of each chip (figure 1.24) as a method to observe the effect of the bandgap on the quality factor of the localized mode. As we see in figure 1.28, with this method, a single defect mode appears to move in and out of the band gap as the defect length is varied. **II)** Number of the unitcells where we could experimentally observe the behavior described in figure 1.22. **III)** The total length of the beam in order to achieve higher quality factors. **IV)** All the samples were fabricated in 3 thicknesses (20 nm, 50 nm and 100 nm) in order to observe the thickness scaling described in (1.119),(1.120). Observing $1/h$ scaling for Q_{int} with these ultra-high Q samples, is a direct and unambiguous experimental proof for surface losses.

The details of the fabrication process of these beams is discussed in chapter 2. However, it is important to emphasize few aspects of the fabrication process. Apart from the thickness scaling experiments where thickness of 50 nm and 100 nm were employed, our main devices were patterned on 20 nm-thick films of high-stress Si_3N_4 with nominal parameters of $E = 250$ GPa, $\sigma_{\text{film}} = 1.2$ GPa, $\rho = 3200$ kgm^{-3} grown by low-pressure chemical vapor deposition on a 100mm double sided polished 700 μm thick silicon wafers. Since the scaling of the quality factor for soft-clamped beams is given by $Q \sim \frac{1}{h}$, we choose $h = 20$ nm for the thickness of our main devices as it is the minimum thickness that we can still grow and control the fabrication in a deterministic way. In order to achieve extreme quality factors, a multistep release process was used to suspend beams as long as 7 mm, enabling aspect ratios as high as 3.5×10^5 and dilution factors in excess of $\lambda \approx 3 \times 10^4$. To the best of our knowledge this is among the highest aspect ratio devices of any size and any kind that has ever been made. Even higher than high aspect ratio carbon nano-tubes [140]. Such an extreme aspect ratio, made the fabrication of these ultra-high Q beams the most challenging part of this thesis which it took almost 1.5 year to master the techniques required for successful fabrication of these samples. One of the aspects of this complexity is the thickness of Si_3N_4 layer. With 20 nm thickness and typical width between 300 nm to 5 μm for different parts of the beams, the choices for undercut process are limited. With these aspect ratios for the width and the thickness, we required an etching selectivity better than $1:10,000$ between $Si_3N_4 : Si$ in order to successfully release the structures without damaging the nitrite layer. This means the dry Si etching chemistries for undercutting (such as SF_6 or XeF_2) are not suitable as they both have selectivity lower than $1:1000$. The only reliable solution that is accessible in our fabrication facility is Potassium hydroxide (KOH) solution which has near infinite selectivity between Si_3N_4 and Si (Silicon
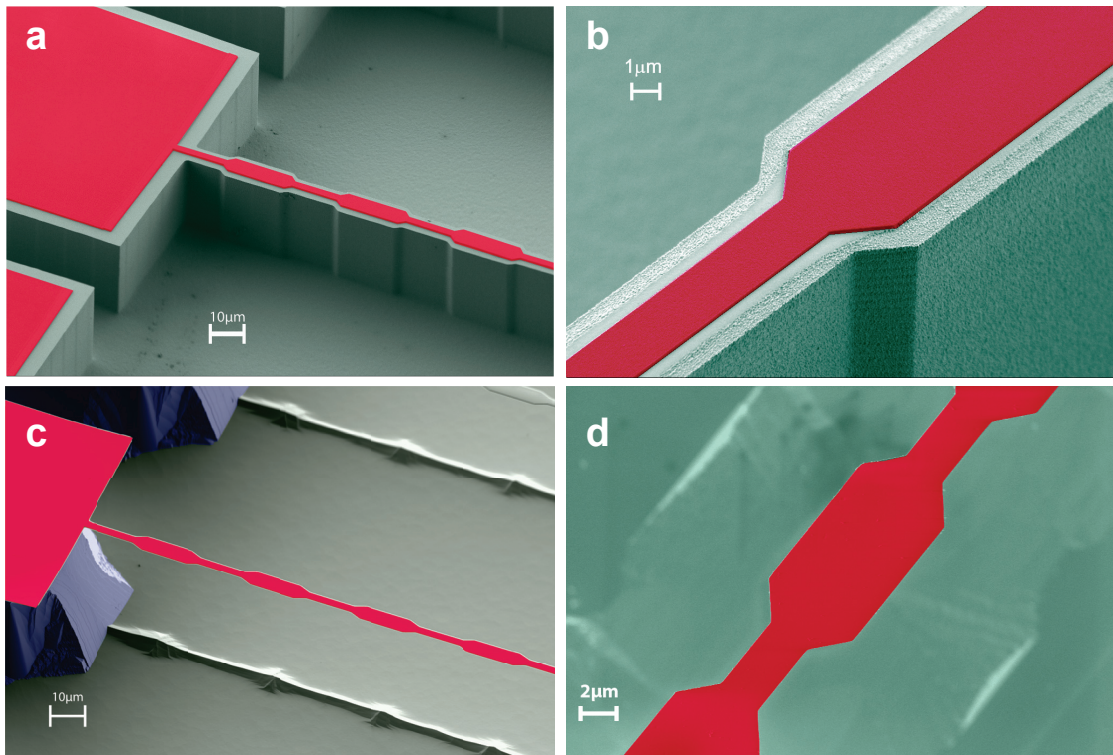
Figure 1.23 – **False colored SEM images of the beams before and after releasing.** (a) and (b) are right before the KOH undercut and highlights the up-scaled masked that has been etched deep into silicon substrate to expose the fast etching facets of Si. Focusing on (a) , (c) is the region near the clamping pads and (b) , (d) illustrates the actual geometry of one unitcell. The smoothed transition between the wide and narrow regions of the unitcell helps with stress relation in the film and avoid buckling at the corners. (c) and (d) shows the beams after the KOH undercut and CPD drying. Red: Si_3N_4, Blue: Silicon pillar, Green: Silicon substrate

etch rate depends on the temperature of the bath, KOH concentration and its density but the etch rate of Si_3N_4 in KOH bath is so small that is practically unmeasurable!). For this project we undercut our samples using 40% concentrated (weight concentration) VLSI grade KOH at 60°C while we maintain the bath density at 1.37. KOH bath, solves the selectivity issue and allows us to work with the thinnest possible Si_3N_4 layers, but it comes at cost of few major challenges in the process:

- **(a)** Using a liquid undercut step requires delicate drying procedure especially when dealing with extreme aspect ratios presented in this work. Because of the extreme aspect ratios of our samples, drying in the open air would result in either breaking or collapsing of the structures. This is due to the strong surface tension of water. While the water droplets under the beam are shrinking due to evaporation, they pull the beams down with them. On the other hand, since our beams are very long and thin at the same time, they are very soft springs that can easily be bent with smallest forces. To

avoid phase transition and surface tension[16], critical point drying (CPD) was used to avoid structural collapse where we used the critical point of CO_2 at 31°C and 1072 psi, performed in a high-pressure chamber to dry our samples. In fact, it should be note that the liquid undercut and drying process turned out to be the most challenging part of the fabrication process where we had an extremely low yield at the beginning. However, overtime we learned how to carefully handle our samples in liquid and control the CPD parameters and gas flows in order to achieve better than 95% yield at the end.

- **(b)** The second major problem of KOH undercut is the anisotropicity of silicon etching in a KOH bath. Different crystalline surfaces etched with different speeds in KOH solution. For example, <111> planes are etched ~200 times slower than <100> planes [142]. As illustrated in chapter 2, if we attempt to undercut Si_3N_4 beams immediately after transferring the mask to Si_3N_4 layer, we will face a "pyramid" shape structures under the beams (the slow surfaces) where it will take a very long time to etch and release the beams. The problem we observed was not just the length of the process, but more importantly, the fact that the silicon underneath the clamping pads would get etched away before we consume all the silicon material underneath the beams. To solve this problem, an up-scaled version of the beams were patterned using e-beam lithography and etched deep in silicon substrate (depth of $10 - 30 \ \mu$m) using Bosch process . This is illustrated in figure 1.23.A and 1.23.B). With this technique, the fast surfaces of silicon on the sides are exposed and KOH can quickly etch the silicon underneath the beams. Since the angle between slow surface (<111>) and the fast surface (<100>) in silicon crystal is $\theta = 54.74$ degree, the minimum depth for the Si etching should be a bit longer than $w_{\max} \cdot \tan\theta \approx 1.5 \times w_{\max}$ where $w_{\max}$ is the maximum width in our design. Another positive advantage of introducing the Si etching step is that we can independently control the distance between the Si_3N_4 layer and the surface of the substrate. With an extreme aspect ratios reported in this thesis, by experience we realized that a gap of 10-30 μm between the surface of Si_3N_4 and silicon substrate is required to avoid the structural collapse during the CPD drying.

- **(c)** Another difficulty of working with KOH undercut step is the issue of handling these fragile structures in liquid medium. These high aspect ratio beams acts like an efficient sail's boat in liquid and could be dragged and often break because of the turbulence in the water. To answer this challenge, an especial chip holder was designed and made from Teflon (see chapter 2) which solidly clamps our chip while keeping them in the horizontal position. It is important that we let water remains on surface of the chips while transferring them from one bath to the next (for example from KOH to water for cleaning). In our experience, careful handling of the chips in the liquid and especially during the bath transfer is the most crucial step of the fabrication that may lead to extremely low yield if it is not done properly.

---

[16]If we go from the liquid phase to the gas phase without passing through a phase transition surface, we can avoid surface tension. This is done via going around the critical point of the liquid, via the super-critical phase where due to high temperature and high pressure, the difference between the gas and liquid cannot distinguished via a surface.[141]

During the measurements, we realized cleanness of the samples are crucial to achieve ultra-high quality factors. Therefore, in this process we went through a number of cleaning steps to ensure the contamination is kept at the minimum level. These cleaning steps includes N-methyl-pyrrolidone (NMP) bath (used to strip photoresists), Piranha bath (to remove organic residues), BHF bath (to remove ebeam resist and silica particles), KOH bath (for undercut and removing Si particles) and finally a HCL bath which neutralizes the potassium leftovers from KOH undercut step.

Figure 1.23 illustrates the actual shape of the unitcells that was used in our experiment. We realized that unitcells with rectangular shapes as shown in the schematic design of figure 1.20, results in upward bending of the corners due to stress relaxation after the release. This leads to lower quality factors. Therefore, the masks were changed to adapt a smooth transition between the wide and narrow regions of the unitcell. Our numerical simulations show no significant difference between the two geometry. It is important to note that all the models and fittings for the measured data are based on the exact geometry extracted from SEM images.
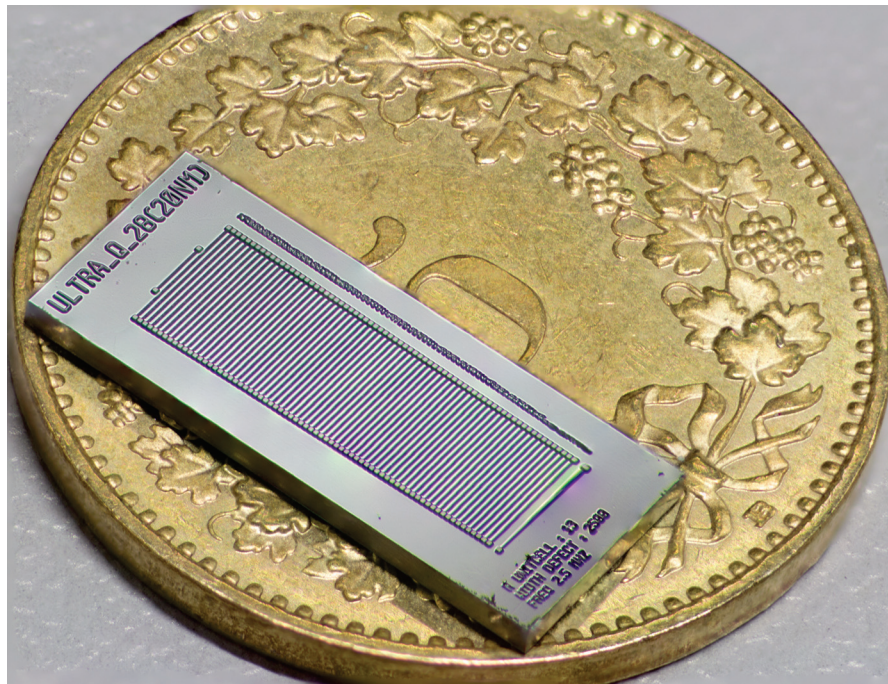
Figure 1.24 – **Optical image of a sample chip.** Dimensions of the chip are 12 mm×5 mm. On this chip there are 75 beams, each with a different defect length; photographed on top a 5cent Swiss coin as a reference for the scale. (this images is creased by superimposing 60 individual photos taken from the same angle with different focal depths in order to create a fully focused photo)

For this experiment, silicon wafer was diced into 12 mm×5 mm chips (we could effectively fit up to 65 chip on a 100 mm wafer for each run). Figure 1.24 shows the optical image of one of these samples where 75 devices fabricated on each individual chip. One of the advantages of working with 1D objects compare to 2D membrane resonators is their extremely

small footprint. Many devices can fit into a small area and different parameters can be experimentally swept. In our design, we usually sweep the length of the defect from $0.5l_{\text{cell}}$ to $2.5l_{\text{cell}}$ in extremely fine steps over the samples inside each chip. This allows us to observe the localized mode in different parts of the bandgap and unambiguously observe the effect of bandgap on the mechanical Q. Normally we swept the other parameters (such as the total beam's length and number of unitcells) from one chip to another. The reason behind this choice is that we would like to fix the parameters of the bandgap (namely its frequency as well as mode spectrum of the beams) for every time that we load a new sample in our vacuum chamber. In this way, we can quickly characterize and test many samples for each pump down as the geometry doesn't change a lot between the neighboring devices. It is important to emphasize that we normally place two calibration uniform beams at each end of our chips. One with the fixed length of 1 mm and width of 2.5 μm (the top beam in figure 1.24) and one uniform beam with the same length of the corrugated beams but with a fix width of 2.5 μm (bottom device in figure 1.24). These two beams were used at the beginning of each measurement campaign as a calibration devices to **a)** check the Q_{int} on a simple geometry that we understand its spectrum **b)** to vertically align our fiber interferometer with the chip.

To characterize these devices, we carried out thermal noise and ringdown measurements in vacuo ($< 10^{-7}$ mbar) using a lensed-fiber interferometer. Based on our numerical model, we are expecting to observe mechanical Qs approaching 1 billion for our highest aspect ratio for frequencies close to $\Omega_m/2\pi \approx 1$ MHz. This means that the expected mechanical linewidth would be around $\Gamma_m/2\pi \approx 1$ mHz. Such an extreme linewidth together with the fact that thickness of our devices is very small (~ 20 nm) means[17] that gas damping could become a limitation for our resonators. Our analysis (see appendix A.II) shows that we need a vacuum below 10^{-7} mbar in order for the gas damping to be negligible. This pressure is an order of magnitude below the all of the previous operational vacuum chambers in our lab. Therefore, as one the major projects of this thesis we construct a custom made UHV chamber and measurement apparatus to characterize ultra-high Q mechanical resonators. We discuss the details of the design and operation of this UHV chamber in appendix A.II but here we only review few major aspects of it. In figure 1.25 we can find the 3D rendering and an optical image of our vacuum chamber designed in SolidWork [143] . All the previous experiences of vacuum chamber designs and experiment setup in our lab was put into making this setup most suitable and easy-to-use for our experiments, with lots of flexibilities to host future upgrades. One of these experiences was the fact that in the field of optomechanics we change samples very often compare to for example ultra-cold atom experiments. In our previous chamber designs, the entire chamber had to be vented to load a new chip and pumped again. This process could even take up to several days before the pressure of the chamber is low enough that the gas damping becomes negligible. This made the process of sample characterization very long and inefficient, In addition, this practice could damage the ion pumps in the long run. In the UHV

---

[17]Gas damping scales as [95]:

$$Q_{\text{gas}} \propto \frac{\Omega \times h}{P} \qquad (1.121)$$

where P is pressure. Therefore, the thinner the device is, higher the gas damping becomes.
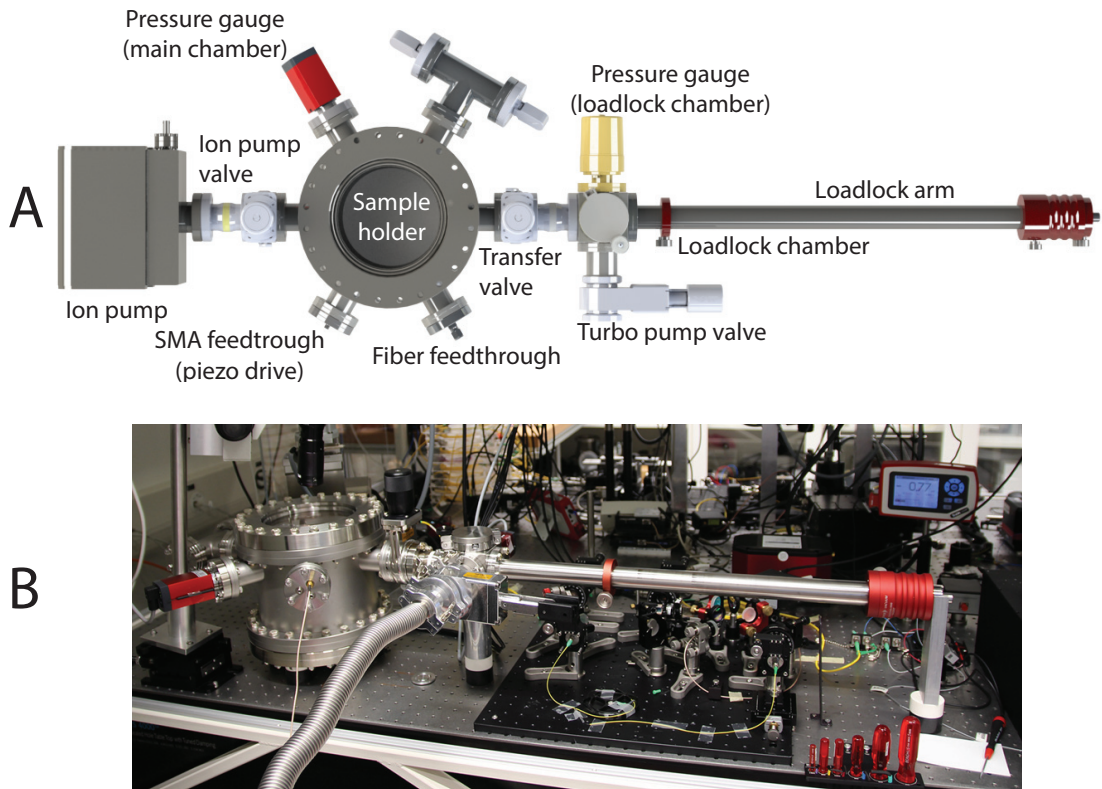
Figure 1.25 – (A) the 3D SolidWork rendering and (B) the image of our completed custom made vacuum chamber. The samples are transferred to the main chamber through a lock chamber via the magnetically coupled load lock arm. The loadlock enables samples to be loaded from ambient pressure into 10^{-8} mbar vacuum in less than 5 minutes which significantly increases the speed and efficiency of our measurements. The main chamber is always pumped via the ion pump and could reaches the pressure of 9×10^{-9} mbar without backing. The 3-axis nono-nanopositioning stages that controls the position of the sample, the fiber lens, piezo drive, and sample chip are housed together in the vacuum chamber. The laser light and electrical signals are transmitted in and out of the chamber via especial UHV compatible fiber and SMA feed-throughs. The pressure of both chambers is constantly monitored via the pressure gauges connected to each chamber. An optical microscope is setup on the top of the view point and used for alignment procedure.

chamber illustrated in 1.25, in order to over come this obstacle, a small load lock was designed with separate vent and pumping valves. To operate the system, the main chamber is always kept under high vacuum ($\sim 10^{-8}$ mbar) by opening the ion pump valve which constantly pumps on the main chamber. In order to load and unload samples, the small load lock is pumped via a turbo pump and the samples are transfered to the main chamber by opening the transfer valve and using the magnetically coupled load lock arm. We normally keep the loadlock chamber also in vacuum to avoid contaminating the load-lock. In our experimental setup, the samples are sitting on a 3D stage UHV compatible nano-positioning systems. An

automated program was written to position the sample holder in front of the load lock during the loading and bring it close to the tip of the fiber interferometer during the measurements. The load-lock enables samples to be loaded into $\sim 10^{-8}$ mbar vacuum in less than five minutes.
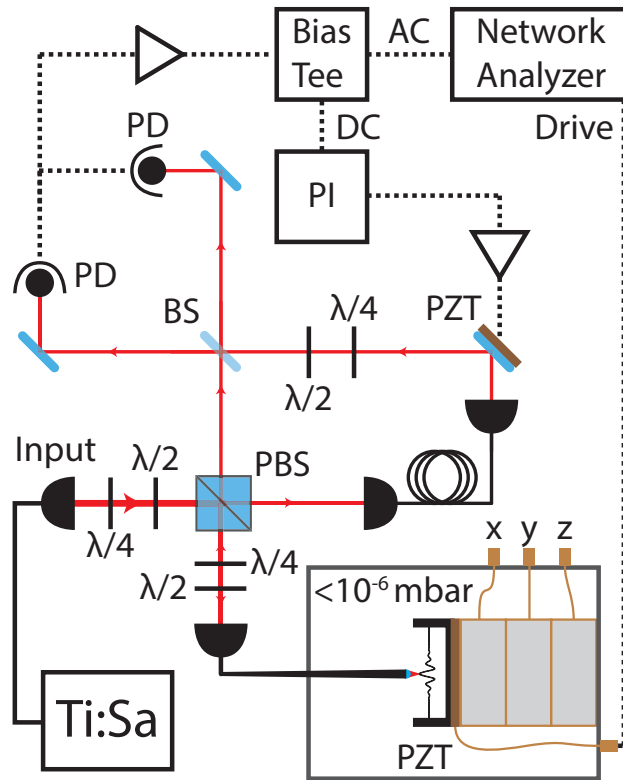
Figure 1.26 – **Schematic of measurement setup.** The reflected light from the facet of the beams is collected by the lensed fiber and the mechanical induced phases shift is detected on a double balanced Mach-Zehnder homodyne interferometer. $\lambda/2$: Half-wave plate. $\lambda/4$: Quarter-wave plate. PBS: Polarizing beamsplitter. BS: 50/50 beamsplitter. PZT: Piezoelectric transducer. PI: Proportional-integral loop filter. PD: Photodiode.

In our experiments, nanobeams were characterized using a custom, balanced Mach-Zehnder interferometer whose signal arm is terminated with a lensed fiber where the focal spot radius of the lens is $r \approx 1.4$ μm and focal distance of ~ 3 μm. Figure 1.26 illustrate the schematic design of our setup. To align a nanobeam to the interferometer, the sample chip is maneuvered in the focal plane of the lens using a 3-axis nanopositioning stage. For the measurements reported, a signal (reference) arm power of $0.1 - 10$ (1) mW was used. The reference arm length was served with a piezo-actuated mirror in order to stabilize the interference fringe at its inflection point. Despite alignment inefficiency (typically 0.1% of the power incident on the beam was retro-reflected into the fiber), thermal motion of the nanobeam could be observed in the power spectrum of the photocurrent at frequencies as high as 10 MHz.

Ringdown measurements were initiated by resonantly exciting the nanobeam (at frequency f)

using a thin piezo-electric plate attached to the sample holder. After turning off the drive, the slowly-varying amplitude of the beam was monitored by demodulating the photocurrent at f with a bandwidth BW > 100 Hz $\gg \Gamma_m/2\pi$. The large demodulation bandwidth was used to mitigate the influence of resonance frequency drift (typically 1 Hz/s in steady state with laser on) on ringdown measurements.

We start our experiment demonstration of soft-clamped 1D nanomechanical resonators by studying 2.6 mm-long devices with unit cells of length $L_{\text{cell}} = 100 \ \mu$m and width $w_{\text{max}}/w_{\text{min}} = 2$ and $w_{\text{min}} = 500$ nm fbricated on 20 nm high stress Si_3N_4 layer. There are 12 unitcellls at each side of the defect in this samples (slightly higher than the optimum number of unitcells studied in figure 1.22) and the defect length was varied between $0.5l_{\text{cell}}$ and $2.5l_{\text{cell}}$. In the first step, we measured the thermal noise spectrum of each device. An example of such a thermal noise is plotted in figure 1.27.B. Bandgap for this geometry is presented at figure 1.27 where in-plane and out of plane mode of the unitcell are highlighted. Since the aspect ratios of both in-plane and out of plane modes is extremely large, the fundamental mode bandgap for the two modes overlap. It is important to emphasize here that although all our measurements and designs in this section are designed for out of plane motion (as it is the mode that can be measured better with our interferometer), the same discussion can be held for in-plane modes. In fact, in the next section, we will observe the in-plane modes by off centering the fiber interferometer and measuring on the edge of our beams. Particularly one of the striking features of corrugated beams is the sparse mode spectrum inside the bandgap, visualized by compiling spectra of beams with different defect lengths (figure 1.27.C). As we discussed before, such a sparse spectrum is really beneficial for laser cooling experiments where the off-resonance tail of neighboring modes could pose a fundamental limitation for cooling. A single defect mode appears to move in and out of the bandgap as the defect length is varied.

This mode is expected to be localized and therefore have a reduced effective mass. One of the other important features of our localized modes compare to, for example higher order modes of uniform beam is that the effective mass of these resonators are extremely small. Much smaller than the physical mass of the oscillator since only a very small fraction of the beam is oscillating at the center of the resonator. The exponential damping of the amplitude in the PnC be is the form of $e^{-|n|/n_{PD}}$ were n is the unitcell number from the center of the beam and n_{PD} is the penetration depth of localized mode into the PnC. Based on our analysis in figure 1.22, we can numerically simulate the penetration depth to be $2 < n_{PD} < 3$ with a weal logarithmic dependency on total length of the beam. Therefore we can show the effective mass of the localized mode to $m_{\text{eff}}^{\text{localized}} \approx \frac{n_{PD}}{2} m_{\text{phys}}^{\text{defect}}$. On the other word, a soft-clamped mode has an effective mass approximately equal to the physical mass of the defect but with the quality factor of 100-1000 times larger. Comparing the area under thermal noise peaks and estimating the physical beam mass to be $m_0 = 100$ pg, we infer that indeed $m \approx 5$ pg $\ll m_0$. This value is in good agreement with the mode profile obtained from the Euler-Bernoulli equation, and is roughly 2 orders of magnitude smaller than that of an equivalent 2D localized mode.

The next step is to look at the quality factor of these soft-clamp resonators. The mechanical
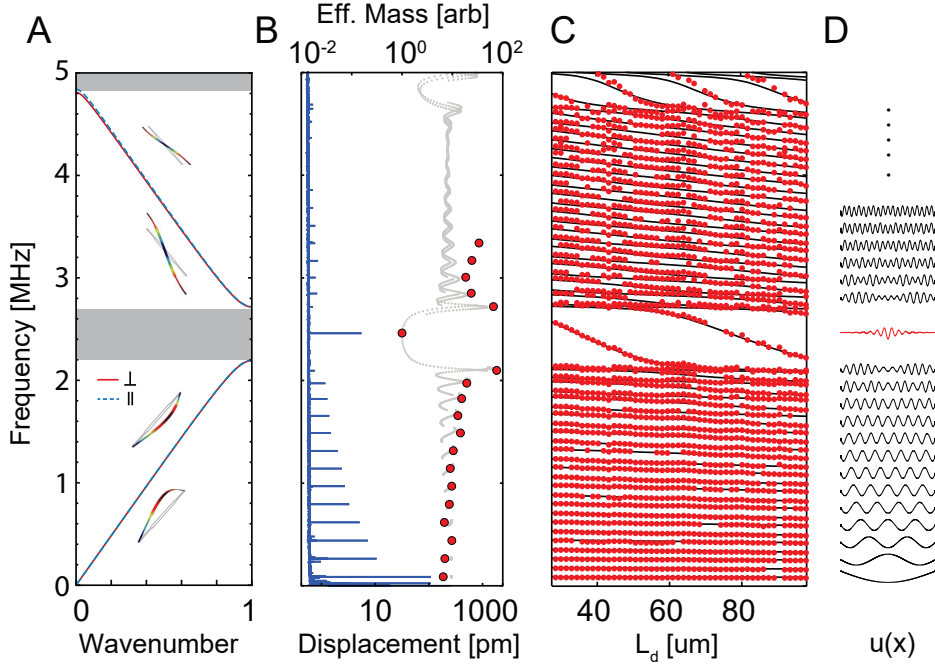
Figure 1.27 – (A) Band diagram showing in($\parallel$)- and out($\perp$)-of-plane normal modes of a unit cell for geometry presented in figure 1.20. (B) Displacement thermal spectrum (blue) of a single beam, scaled to the theoretical RMS thermal displacement of the defect mode, $\sqrt{k_B T / m_d (2\pi f)^2} \approx 6$ pm. Overlaid are effective mass coefficients m/m_{defect} (red circles) inferred from the area beneath noise peaks. Gray is a model based on mode shapes in (D), used to estimate $m_{\text{defect}} \approx 5$ pm (C) Frequency spectra of multiple beams with different defect length. Black lines are a solution to the Euler-Bernoulli equation. By sweeping the defect length, a localized mode can be tracked as it moved in and out of the bandgap. (D) Mode-shapes obtained from the Euler-Bernoulli equation where red illustrate the mode shape of the localized mode.

quality factors are several modes near the bandgap were measured using the ringdown technique. The results are illustrated in figure 1.28. In accordance with (1.66), we also observe a dramatic increase in the Q of localized modes. To visualize this enhancement, we compiled measurements of Q versus mode frequency for 40 beams of different defect length (figure 1.28.A). Outside the bandgap, we find that $Q(f)$ is consistent with that of a uniform beam, asymptoting at low mode order ($n \lesssim 20$) to $Q \approx 2 \times 10^7$, implying $Q_0 \approx 2\lambda Q \approx 1500$. Inside the bandgap ($n \approx 26$), Q approaches that of an idealized clamp-free beam ($Q \approx Q_0/(\pi n \lambda)^2 \approx 10^8$). The transition between these two regimes agrees well with a full model (blue dots) based on (1.66). In figure 1.28.A we highlight the 19-second ringdown of a 2.46 MHz defect mode, corresponding to $Q = 1.5 \times 10^8$ and $Q \times f = 3.7 \times 10^{14}$ Hz marked by the star in figure 1.28.B as the highest Q measured in this sample set. It is important to point out that our quality factor is on par with the best quality factors achieved with 2D soft-clamped membranes [91] at higher frequency which means higher $Q \cdot f$. This value is higher than any recorded value for $Q \times f$ of any mechanical oscillator of any size at room temperature is equivalent to about 60 coherent
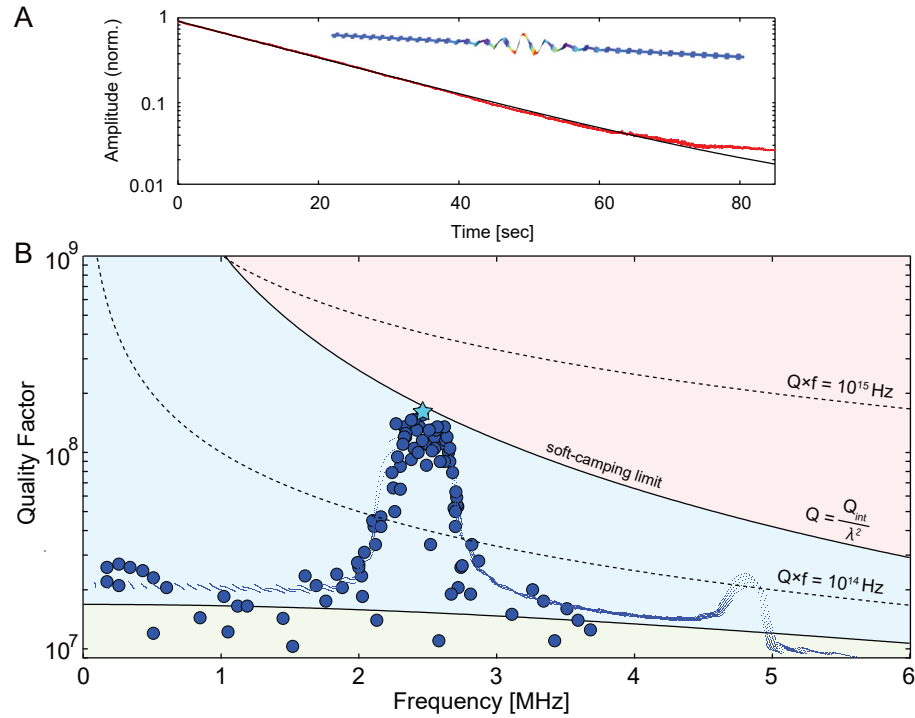
Figure 1.28 – (A) Interferometric ringdown of for the highest Q measured on 2.6-long, 20-nm-thick PnC nanobeam excited in its 2.46 MHz defect mode (cyan star). Black solid line is an exponential fit with a decay time of ∼ 20 seconds. (B) *Q* versus mode frequency of PnC nanobeams for different defect lengths and modes. We experimentally observe that the quality factor of localized modes approaches the limit of clamp free beam (solid black line). Green regions correspond to the area accessible via higher order modes of uniform beams, blue correspond to area accessible via soft clamping and red is the region beyond the access of soft clamping technique. The dashed lines correspond to constant $Q \times f$.

oscillation of the mechanical oscillator at room temperature. These results demonstrate the strength and validity of the soft clamping technique to create mechanical oscillator with extreme quality factors.

The last remaining piece of the puzzle in regard to our soft-clamped modes is two show that we surface loss limited and have $Q_{\text{soft-clamped}} \propto 1/h$ scaling for localized mode as discussed in (1.120). In order to experimentally verify this hypothesis, same geometry discussed in figure 1.28 where were fabricated on 50 nm and 100 nm high stress Si_3N_4 and measured in our vacuum systems. The results of this measurements can be found in figure 1.29. In figure 1.29.A. We observe that for other 50 nm and 100 nm thick resonators, the mechanical Q follows our numerical model (solid lines). Although as expected, the dissipation dilution factor is lower for thicker samples. In figure 1.29.B, we stack all the measurements of the figure 1.29.A into one line for each thickness. We observe the peak values of the quality factor which corresponds to the localized modes, follows a linear scaling with thickness as predicted by equation (1.100).
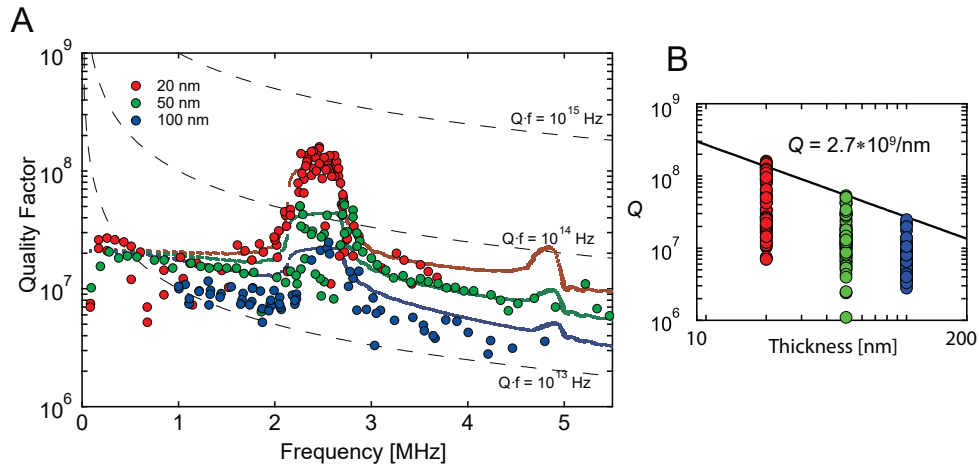
Figure 1.29 – (A) Measured Q (circles) versus frequency for corrugated PnC beams with different defect length and thickness of Si_3N_4 layer super imposed on the model for each thickness (solid lines). (B) All the measured Qs for each mode is stacked on top of each nitrite thickness. Overlaid is a model with $Q_0 = 6900 \cdot h/(100 \text{ nm})$, consistent with surface loss as the localized mode (the top Qs for each thickness) should follow a $1/h$ scaling law.

In conclusion, in this section we theoretically and experimentally discussed the idea of soft-clamped oscillator and show case its strength at engineering mechanical oscillators with extreme quality factors. Soft clamping technique enhances the quality factor by diminishing the extra curvature at the clamping points, while localizing the motion at the small portion of the beam that leads to reduce mass. This offers a unique and strong toolbox (summarized in equations (1.120)) for engineering optomechanical system that are capable of reaching the quantum ground state at room temperature. However, for the completion of this section, lets also briefly review the weaknesses of soft clamping approach. There are to major drawback we can think of while working with soft clamping beams. a) the performance of the soft clamping beams at best (if we succeeded in complete suppression of clamping losses) is limited by a clamp-free model presented in equation (1.113). This means the $Q_{\text{soft-clamped}} \times f \propto 1/\Omega$. Such a scaling for $Q \times f$ is one of the major limitation of soft clamping as the highest $Q \times f$ and operation frequencies are locked to each other. If for a certain experiment, we need to achieve $Q \times f$, we are forced to operate at lower frequencies. Considering all the technical noise at frequencies below 1 MHz (such as laser classical noise, thermo-refractive noise [121] and etc.), this could limit the ultimate performance of these oscillators. b) the second weakness as discussed in equation (1.118) is that the regions identified by light red bands in figure 1.28 and 1.22 in theory is accessible for mechanical resonators. However, the performance of soft-clamped resonators are bounded to the $Q_{\text{soft-limit}}$ and therefore, they can never be accessed with soft clamping technique. In other word, it seems that soft clamping cannot fully make use of all the potential capabilities of dissipation dilution. In the next section, we present a third strategy to that takes advantage of the geometrical strain engineering to locally enhances the strain at the region of the localized motion lives. We will observe that both of these two weaknesses can be addressed via our third strategy as with this strain engineering, we can

break the soft clamping barrier and explore the forbidden zone. Also our third strategy will offer a technique to independently engineer $Q \times f$ at any desired frequency for an operation which gives us a lot of degrees of freedom in the design of optomechanical systems.

Strain-enhanced soft-clamped beams

Having established near-ideal soft clamping of uniform PnC nanobeams, now we focus on our third and most efficient strategy to enhance dissipation dilution via geometrical designs. In the last section, we observe encapsulating a defect in the middle of a phononic crystal bandgap would result in a localized mode with near clamp-free quality factors that approaches $Q_{\text{soft-limit}}$ according to equation (1.113). But as we illustrate in figures 1.28 and 1.22, $Q_{\text{soft-limit}}$ is still far from the ultimate limit of dissipation dilution discussed in section 1.2. In this section, we present a new strategy that enables us to surpass the $Q_{\text{soft-limit}}$ barrier and make a nano-mechanical resonator with unprecedented performance. Lets start by reviewing our remaining degrees of freedom. According to equation (1.66), in its most general case, the Q of a clamped-free beam can be written as:

$$Q_{\text{clamp-free-general}} = Q_{\text{int}} \frac{1}{\beta} \frac{12\sigma_{\text{avg}}^2}{\rho h^2 E \Omega^2} \tag{1.122}$$

Assuming that we fabricated the thinnest possible resonator (smallest h), the only remaining degree of freedom is to design a geometry that enhances β. This is because, in equation (1.51), we demonstrated that unfortunately it is impossible to increase the average stress (σ_{avg}) via geometrical designs. However, the good news is that we do not need to increase the average stress across the entire beam. Especially in the case of the soft-clamped beams, we can use localized mode shape to our advantage. Due to their confined and localized nature, we only need to locally enhance the stress in the region where the localized mode exist which in turn lead to further enhancement of the dissipation dilution. It should be noted, however one difficult and fruitless path would be to find new deposition recipes that increase the σ_{film} which in turn could lead to higher average stresses. However, we are interested in perusing the enhancement of stress via geometrical means [102][103][144].

$$w(x) \times \sigma(x) = const$$
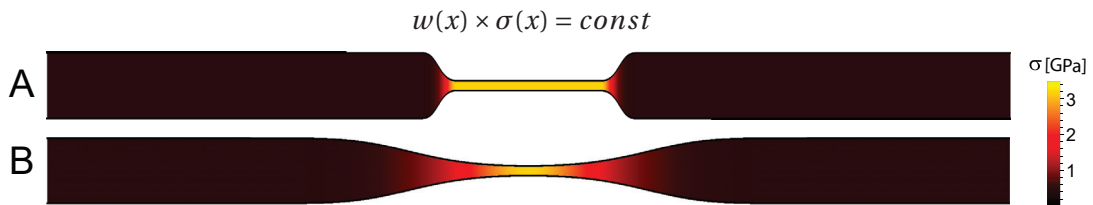
Figure 1.30 – Numerical simulation for geometrical strain engineering where by narrowing down the cross-section of a high-stress beam, we can locally concentrate the stress (Yellow regions represent the areas with higher stress.). (A) a sharp-step like transition with a constant narrow region. (B) Smooth transition via a Gaussian envelope.

Equation (1.88), shows the main principle behind the concept of geometrical strain engineering. By narrowing down a region of high-stress mechanical beams, we concentrate the entire tensile force on a small bottleneck and locally enhance the quality factor. Figure 1.30 beautifully illustrates the concept of strain engineering by color coding the stress in different regions of a non-uniform beam. It should be pointed out that geometrical strain engineering has a long history in solid-state community to realize unusual material properties [145]. For instance, stress can be used to enhance the electron mobility of a semiconductor, enabling more efficient solar cells [146] and smaller, faster transistors [147]. Here we want to use it for controlling the mechanical properties of elastic materials. Although Elastic strain engineering traditionally relies on extreme inhomogeneous stresses produced by nanoscale deformation [148] [e.g., by lithographic patterning [80] [102], or nano-indentation [149]], here the main challenge is how we use this powerful technique through the process of dissipation dilution to boost the performance of phonons with very large wavelengths that often approach several 100s of micrometer.

The main schematic design for the concept for strain enhanced soft-clamped beams is illustrated in figure 1.31. In our third strategy, if we will manage co-localized the mechanical mode shape with the of regions enhanced stress, this may lead to higher quality factors. To
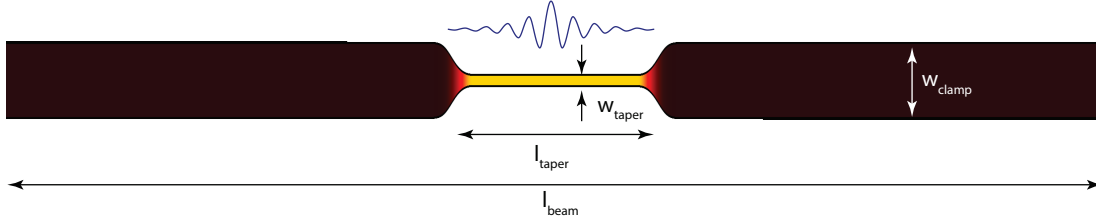
Figure 1.31 – Schematic design of the idea of strained enhanced soft-clamped beams. In this idea, the regions of high stress (yellow regions at the center) is created via tapering the width of the beam where a localized mode shape is created via phonoic crystals. The co-localization of high stress and the mode shape results in dramatic enhancement of the quality factor. It is also important to realize that for the tapered region to have higher stress, other regions of beam ends of have lower stress compare to a uniform beam. This results that the stress of the tapered region is a function of both $\frac{w_{\text{taper}}}{w_{\text{beam}}}$ and $\frac{l_{\text{taper}}}{l_{\text{beam}}}$ according to equation (1.127).

understand this further enhancement, let review the equation for β:

$$\beta = \frac{\int_0^1 v(s)^3 u(s)^2 ds}{\int_0^1 v(s) u(s)^2 ds} \tag{1.123}$$

where $u(s)$ and $v(s)$ are the mode shape and normalized width respectively. Now if we assume the tapered region of the is much smaller than the entire length of the beam ($l_{\text{taper}} \gg l_{\text{beam}}$), then we can assume that $w_{\text{avg}} \approx w_{\text{clamp}}$ and $\sigma_{\text{avg}} \approx (1 - v)\sigma_{\text{film}}$ based on figure 1.31 geometry. Now in such a situation if via PnC localization on the soft-clamped, the extent of $u(x)$ will be only limited to l_{taper}, then we can approximate the β factor to be:

$$\beta_{\text{tapered soft-camped}} \approx \left(\frac{w_{\text{taper}}}{w_{\text{avg}}}\right)^2 \tag{1.124}$$

which means that the Q of the strained enhanced localized modes can be derived to be:

$$Q_{\text{tapered soft-camped}} \approx Q_{\text{int}} \frac{12\sigma_{\text{taper}}^2}{\rho h^2 E \Omega^2} \tag{1.125}$$

where

$$\sigma_{\text{taper}} = \frac{w_{\text{avg}}}{w_{\text{raper}}} \sigma_{\text{avg}} \tag{1.126}$$

with this idea and via combining a strained engineering through taper and mode localization though, we achieve higher quality factors if $\sigma_{\text{taper}} > (1 - \nu)\sigma_{\text{film}}$. Here it is important that we understand the non-intuitiveness and complexity of strain engineering. Based on stress relaxation laws, in order for the tapered region at the center of figure 1.31 to have higher stress, other regions of beam ends of have lower stress compare to a uniform beam. In other word, the reason beside the enhanced stress at the tapered region is the other parts of the beam attempt to shrink and relax their stress and as result they pull the central region with them. For a small region to have enhanced stress, a large amount of mass has to shrink. As a result, if the length the tapered region in figure 1.31 is comparable with the length of the entire beam, we can no longer assume that $\sigma_{\text{avg}} \approx (1 - \nu)\sigma_{\text{film}}$ and in fact we reduce the average stress. Therefore we have to engineer our system in a way that local enhancement of the stress does not come at the cost of large reduction of the σ_{avg}. Lets calculate the σ_{taper} for geometry presented in figure 1.31 as it provides insights about our strategy on choosing the taper parameters. Based on equation (1.48), we can show:

$$\sigma_{\text{taper}} \approx \frac{(1 - \nu)\sigma_{\text{film}}}{\frac{l_{\text{taper}}}{l_{\text{beam}}} + \frac{w_{\text{taper}}}{w_{\text{beam}}}} \tag{1.127}$$

Equation (1.127) shows, not only we can change the stress of the tapered region by changing the tapering ratio, but also with the length of the taper. In fact, in our in our experiment, we sweep the stress of the tapered region by changing the length of taper rather than the width of the taper. This is because changing the width of the taper, requires some changes in the design of the PnC and technically changing the tapering length is much easier. Eq. (1.127) is useful not only for the evaluation of geometric strain enhancement in beams, but also in membranes. For example, it predicts that no significant enhancement of strain takes place in the tethers of a trampoline membrane with fillet radius smaller than the tether length. This contradicts with the claim from [92], [93].

It should be noted that for technical reasons, in our experiments we implement a smoother
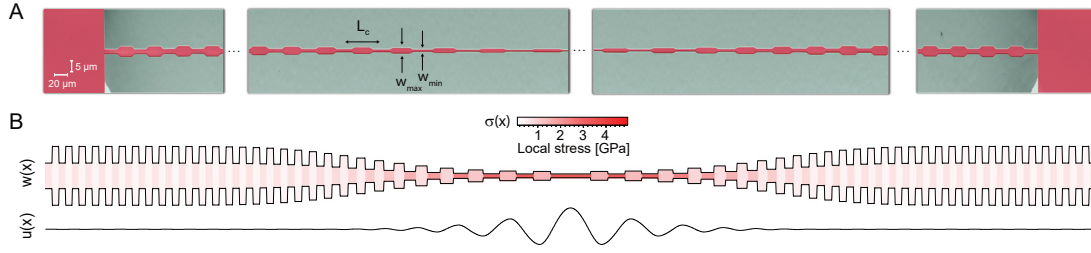
Figure 1.32 – **Geometry of strain-engineered 1D phononic crystals.** (A) A segmented scanning electron micrograph (SEM) of 1 4 mm fabricated tapered PnC nanobeam, vertically scaled for perspective (1:4). (B) Width/stress profile and defect mode shape of a device with 60 unit cells where a non-uniform tapered phononic crystal is used to co-localize the stress and mode shape at the same time (the image is not to scale and is vertically scaled for perspective). In this design we used a Gaussian tapering envelope according to equation (1.128).

tapering presented in 1.30.B. The Q factors of both two tapering geometries displayed in figure 1.30 simulated to be similar (within a factor of two). Figure 1.32 illustrated the actual geometry we used in our experiments. In this geometry, by weakly corrugating a prestressed nanobeam, we create a bandgap for localizing its flexural modes around a central defect. By tapering the beam, we colocalize these modes with a region of enhanced stress. Reduced motion near the supports (soft clamping) results in higher dissipation dilution, while enhanced stress increases both dilution and mode frequency. Leveraging a multi-step release process, we implement our approach on extremely high aspect ratio tapered beams (as long as 7 mm and as thin as 20 nm) made of pre-stressed (1.1 GPa) Si_3N_4, and achieve local stresses as high as 3.8 GPa.

In our proposed geometry in figure 1.32, unlike the toy model in figure 1.30, we implement the tapering by patterning a non-uniform phononic crystal. Colocalization of stress with these modes is achieved by adiabatically tapering the width of successive unit cells toward the defect according to a Gaussian envelope function. Implementation of the strain engineering in this way proves to be significantly less complicated than other geometries. However, designing a non-uniform phononic crystal comes with its complication. The chief among them is the fact that by increasing in the tapering regions, we are also changing the speed of the sound in the material ($v_s = \sqrt{\sigma/\rho}$). Therefore in return, we have to adapt the length of the unitcell in order to maintain the bandgap frequency at any given location of the non-uniform PnC beam.

The tapering geometry is displayed in figure 1.33. In our designs, we fixed the width ratio of the wide and narrow region of the unitcellls, $\frac{w_{\max}(n)}{w_{\min}(n)} = 2.3$. The transverse adiabatic tapering is applied to the beams cell-by-cell (see figure 1.33), with the widths of the unit cells following the Gaussian envelope:

$$w_{\max}(i) = 2.3 \cdot w_{\min}(i) \propto 1 - (1 - \alpha_w) \exp\left(-i^2/i_0^2\right). \tag{1.128}$$

Here $i = 0, 1, \ldots$ is the unit cell number counting from the central defect, α_w and i_0 respectively define the transverse and longitudinal sizes of the waist region. In out numerical simulations,
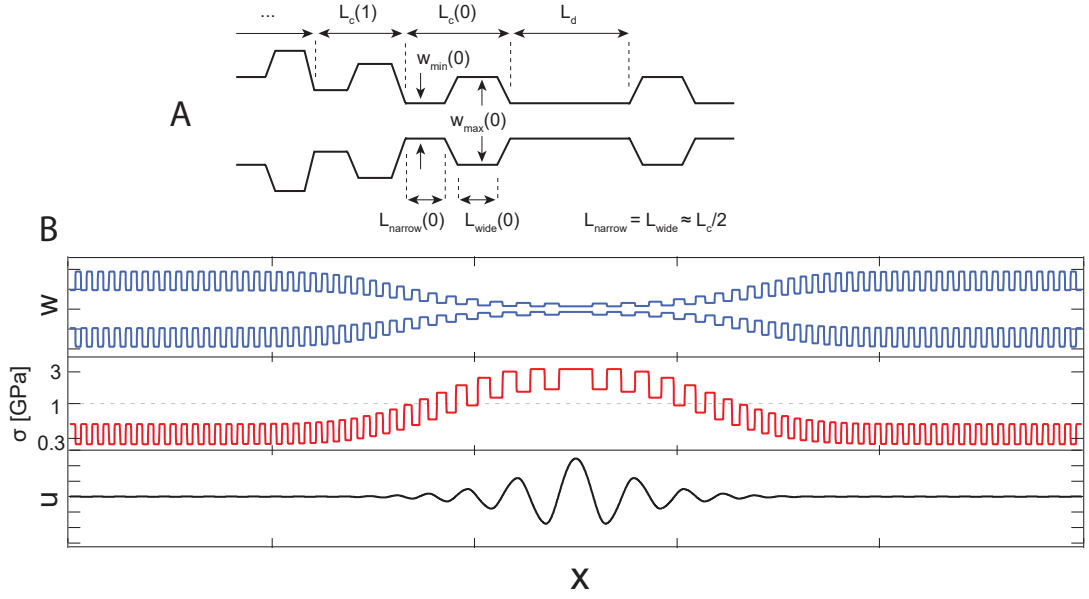
Figure 1.33 – **Design of tapered 1D PnC.** (A). Paramters of the tapered PnC that used for Gaussian envelope according to equation (1.128). (B) Details of the device shown in figure 1.32. Width profile $w(x)$, axial stress $\sigma(x)$, and out-of-plane displacement $u(x)$ of the first order localized mode, plotted versus axial coordinate along the beam, x. A deposition stress of $\sigma_{\text{film}} = 1.1$ GPa is assumed.

we realized that too sharp and narrow tapering (small i_0 and large α_w) although leads to higher stress in tapering regions according to eq. (1.127), it could lead to lower Q. This is because a sharp tapering, would lead to sharp curvature in the mode shape which results in lower dissipation dilution. Also to wide and long tapering is not effective as it does not produce a large σ_{taper}. Therefore, there is an optimum value for α_w, i_0.The values we used in our experiments, $\alpha_w = 0.15 - 0.2$, and $i_0 = 8 - 10$. were optimized by a random-search algorithm to maximize Q/Q_0. This means that our tapering ratio is $\frac{w_{\text{clamp}}}{w_{\text{taper}}} = \frac{1}{\alpha_w} = 5 - 6.6$. This mean by adjusting the length of the tapered region according to equation (1.127), we can tune the stress in the tapered region between 0.9 GPa $< \sigma_{\text{taper}} < 6$ GPa (note that the yield stress of the Si$_3$N$_4$ is about $\sigma_{\text{yield}} \sim 5$ GPa). On the hand, having $i_0 = 8 - 10$ which means that the length of the tapering region is roughly 8-9 unit-cell on each side. Considering the fact that in figure 1.22 we demonstrate the localize mode penetration depth into PnC is also about 6-8 unitcell, we observe that the localized mode is completely confined in the high stressed tapered region. Importantly, we also taper the unit cell length as $L_c(i) \propto 1/\sqrt{w_{\text{max}}(i)}$. This has the effect of matching the bandgap frequency of each cell, ensuring strong co-localization of stress and defect motion.

Similar to what we did in the case of soft-clamped beams, first we start our analysis by looking at the Q spectrum of a tapered PnC beams. In figure 1.34 we find the Q spectrum of tapered PnC beams (red dots) compare to a uniform beam of the same size (blue does). An interesting difference figure 1.21 and figure 1.34 is that a tapered corrugated beam, unlike a uniform PnC
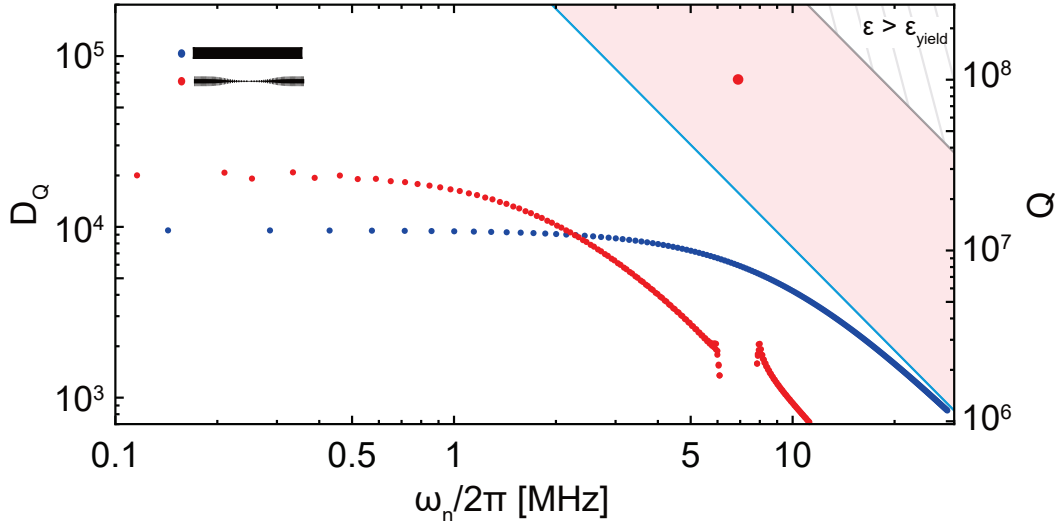
Figure 1.34 – Dissipation dilution spectrum of the modes of a PnC beam (red dots) $l = 3$ mm $h = 20$ nm beam with the shape described in figure 1.33 . Blue: modes of uniform beam with the same l, h plotted for the reference. The region with red background shows the range of D_Q values that exceed the D_Q (blue solid line) of an idealized clamp free beam, $Q_{\text{soft-limit}}$, but is allowed in theory by dissipation dilution theorem (eq. (1.66)). Localized mode of the tapered PnC beam can reach the quality factors of the red region. Hatched region is the forbidden region by dissipation dilution according to equation (1.91) as it requires stress beyond the breaking point of the material.

beam, does not behave like a uniform beam outside the bandgap. In fact, the Q factors of mode outside the bandgap usually fall below the Q of a standard uniform beam. This is because this mode has an extended mode shape which has non-zero amplitude outside the tapered area where the Q is reduced. On the other word, if the strain engineering is not correctly used and doesn't complement with our PnC localization technique, could even lead to lower quality factor rather than being beneficial. However, the most interesting data point in figure 1.34 is the Q of the localized mode which goes beyond the soft clamping limit (solid blue line) and enters a regime (red region) that wasn't accessible with any other technique we studied before. These results signal a paradigm shift in the control of dissipation in nanomechanical systems, with impact ranging from precision force microscopy [6] to fundamental quantum science [9] such as tests of quantum gravity [104]. Combining the reported approach with crystalline [150][81] or 2D materials [148] [149][151] may lead to further improvement, of as yet unknown limitation.

Having demonstrated the extreme quality factors of these resonators beyond the soft clamping limit, now the next task is to understand their scaling behavior and how does the Q and $Q \times f$ scale with the dimension. Equation (1.125) already shows the thickness scaling of the tapered localized beams are similar to the normal localized modes $Q \sim 1/h$ (we include the contribution of surface losses here as $Q_{\text{int}} \propto h$). However, the more interesting question is

the scaling with length. Similar to our analysis with uniform localized mode, we foxed the total length of the beam and change the band-gap frequency by changing the number of unitcells and keeping all the other parameters (such as α_w, i_0 and $\frac{w_{\max}(n)}{w_{\min}(n)}$) fixed. Since unitcell length determine the bandgap frequency therefore we have: $\Omega \propto 1/l_{\text{cell}}$. Also we assume for a small α_w, the stress in tapered region scales inversely with the length of the tapered resonator: $\sigma_{\text{taper}} \propto \frac{l_{\text{beam}}}{l_{\text{taper}}}$. Since in our designs we fix the taper length to be $l_{\text{taper}} = \eta i_0 \times l_{\text{unitcell}}$ (η is constant number that accommodate the fact that the length of unitcells are not equal in the tapering region), the quality factor of the taper soft-clamped beams scales as:

$$Q^{\text{ideal}}_{\text{tapered soft-camped}} \propto \frac{l^2_{\text{beam}}}{h} \tag{1.129}$$

This the most unusual scaling that we observe compare to uniform beams or uniform PnC beams. The quality factor of the localized mode in the ideal scenario is independent from the frequency and is only limited by the total length of the cavity. In contrast, in the last sections, we observe the Q of the fundamental modes (or the optimum higher order mode) of a uniform beam scales with $Q \sim \frac{1}{\Omega}$ or scaling of $Q \sim \frac{1}{\Omega^2}$ for the localized modes. For the tapered PnC beams however, Q is constant regardless of the geometry. This is because by putting more unitcell in the beam and decrease of the length of the unitcell, bandgap moves to higher frequency, we increase the bending curvature but its effect gets compensated by having higher stress. This scaling is for an ideal localized mode in the form of figure 1.31 in which the stress is uniformly enhanced through out the tapered region. However, for the real geometry we used in figure 1.32 where adiabatic taper of the PnC is used to enhance the stress, the stress in not uniformly enhanced throughout the tapered region. Therefore correctly calculating the Q scaling for our geometry in figure 1.32 will results in:

$$Q_{\text{tapered soft-camped}} \propto \frac{l_{\text{beam}}}{h l_{\text{cell}}} \tag{1.130}$$

Equation (1.130) means the $1/\Omega$ scaling for the mechanical Q and it means the $Q \times f$ is a fixed number independent of the frequency. This is beautifully illustrated in figure 1.35 where we numerically calculate the quality factor of the localized mode in a tapered geometry. Similar to our analysis of uniform soft-clamped beams (figure 1.22), here we also change the localized mode's frequency by changing the number unitcell for a fixed length of the beams. In figure 1.35.A we see that how the Q of the tapered localized mode goes beyond limit of soft clamping. The gap between the two grows stronger in higher and higher frequencies. In figure 1.35.B, we observe that the $Q \times f$ of the tapered localized modes (light red data points) is almost fixed regardless of the frequency. Decoupling the $Q \times f$ and frequency solves one of the major limitation we faced with uniform localized modes. With just soft clamping technique alone, we observe that the only way to achieve higher $Q \times f$ was to move to lower frequency. An option which could come at a cost of major technical challenges due to various noise sources at low frequencies. But with our third strategy, not only we can use the dissipation dilution to its full extent, but also we can engineer an ultra-high $Q \times f$ at any desired frequency.
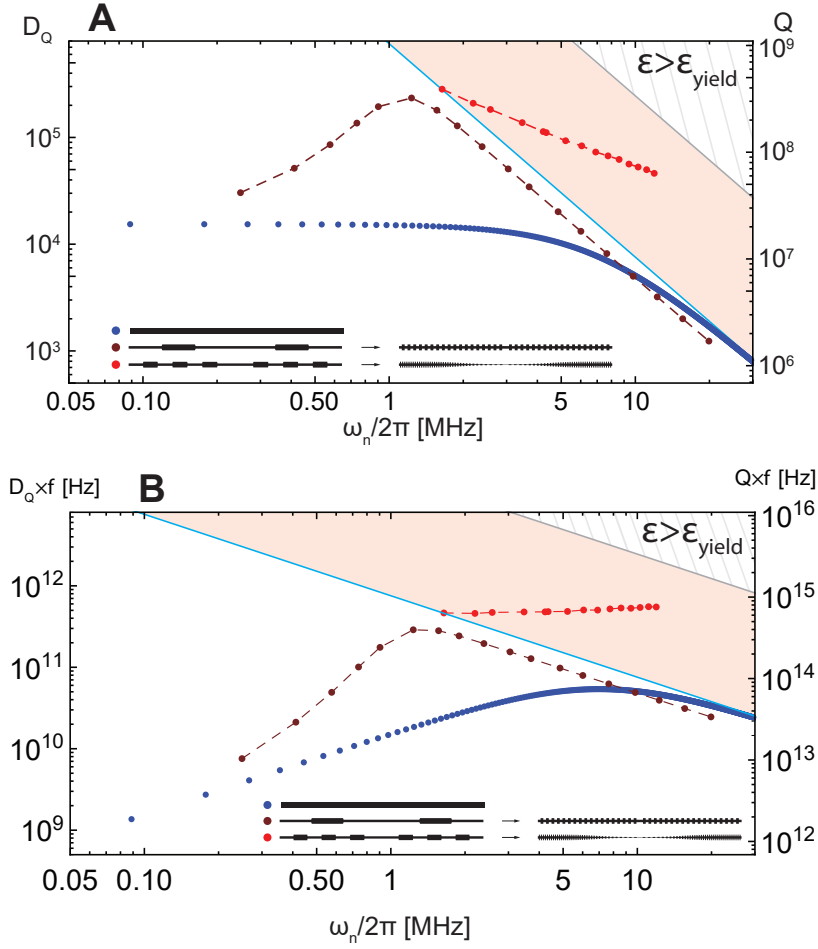
Figure 1.35 – Comparison of the Q in panel A and $Q \times f$ in panel B, between our three proposed strategies. These results simulated for a beam with a fixed length $l = 3$ mm and thickness $h = 20$ nm. The value of $Q_{int} = 1.4 \times 10^3$ is considered to calculate the Q factor. Blue circles correspond to modes of uniform doubly clamped beams (or first strategy) where highest $Q \times f$ is achievable at an optimum mode order. Dark red and red points correspond to localized modes of uniform PnC beams where we change the number of unitcells to go to higher frequencies. These soft-clamped modes have superior Q and $Q \times f$ compare to uniform beams but their performance is limited by the ideal limit for a soft-clamped beam $Q_{soft-limit}$, (blue line) and higher $Q \times f$ is achievable only at lower frequencies. Red circles represent our third strategy of strain enhanced soft-clamped beams where a non-uniform PnC is used to co-localize the stress and the modes shape to achive higher Qs. These tapered PnC beams, not only can achieve Qs beyond the access of the soft-clamped beams in the red region, they offer almost a constant $Q \times f$ for any given frequency. This give a lot of degrees of freedom in design of optomechanical systems to be able to independently choose the frequency of the system. Hatched region is the forbidden region by dissipation dilution according equation (1.91).

Equation (1.130) shows us the route to further increase the Q factor. In an interesting coincident, the ultimate performance of a beam is only limited by the total length of the beam

that we can fabricate. This actually turns the main fundamental question of how we design higher Q resonator to an engineering question of how we can fabricate longer and longer (higher aspect ratios to be precise) beams. With this in mind we tried to experimentally test this hypothesis. But before we review our experimental results, let summarize the scaling law for our two main figure of merit for a mechanical oscillator:

$$\text{Tapered soft-clamped} \begin{cases} Q \times f \propto \frac{l_{\text{beam}}}{h} \\[2mm] \frac{Q}{m} \propto \frac{l_{\text{beam}}}{l_{\text{cell}} h^2} \end{cases} \tag{1.131}$$

where l_{beam} is the total length of the released beam. This mean that by improving the aspect ratio of our beams and find new fabrication methods to fabricate longer structures, we can improve the performance of the mechanical oscillator.

In the next step, we tried to experimentally investigate the performance of these tapered PnC beams. Details of the fabrication of these devices is presented in chapter 2 but in summary, the process is very similar to our discussion about the uniform soft-clamped beams with the difference that by having the scaling law with the total length of the beam in mind, here went to the extreme of the aspect ratio we could fabricate, thickness of 20 nm and length of 7 mm. This as aspect ratio appear to be anomalously high for a suspended thin film, including 2D materials [140]. Due to the extreme aspect ratio of these devices, it is unfortunately very difficult to image them in one figure. However, a segmented SEM of these localized modes is shown in figure 1.32.A. Samples where measured on our UHV chamber (see appendix A.II) at pressures near 10^{-8} mbar to unsure gas damping is negligible. In our measurement, to speed up the process, we normally start to procedure by with finding the frequency of the localized mode via the thermal spectrum. Then the mechanical quality factors were measured using a ringdown technique where the vibrations of the mechanical resonator were detected using a fiber interferometer (described in figure 1.26)

In the first step, similar to our experiments with uniform PnC beams, we try to measure and understand the spectrum and the behavior of the bandgap. For this we measured the thermomechanical spectrum of the Brownian motion of the tapered PnC beams. In figure 1.36, we can find the thermal displacement spectrum of few selected 4 mm-long devices with different unitcell. As we can see, similar to uniform soft-clamped beams, our tapered ones also consist of a jungle of low order modes with relatively low Q and a sparse spectrum near the bandgaps (highlighted in orange). We can use the frequency of the band gap to indirectly measure the stress in the tapered region as illustrated in figure 1.37.

In figure 1.37, the yellow, orange and red squares are represent the three cases presented in figure 1.36 and correspond to 28, 60 and 118 unitcells respectively. As expected, the frequency of the bandgap increases by increasing the number of unitcells. A part of this scaling is due to reduction of the length of the unitcellls (the solid blue line in figure 1.37). However, what we

A

B
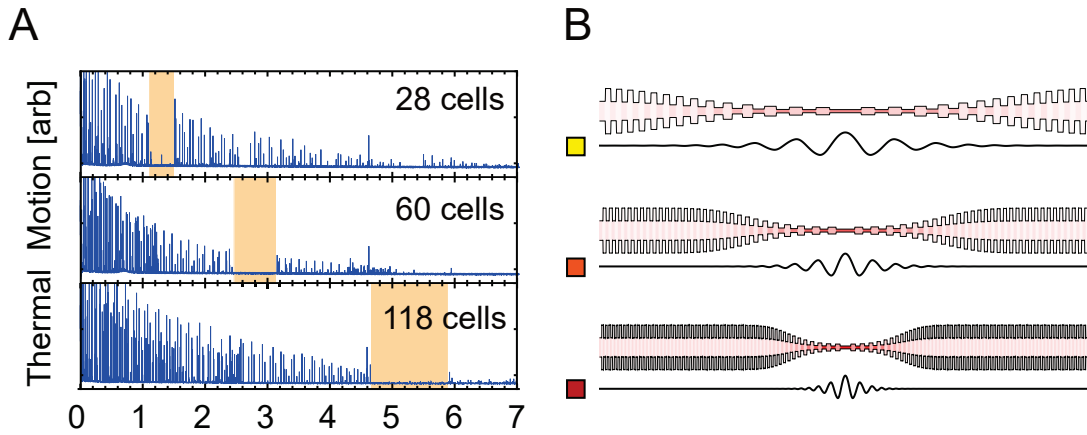
Figure 1.36 – (A) Thermal displacement spectrum of few selected 4 mm-long devices with different number of unitcells. Band gaps are highlighted in orange. (B) Width/stress profiles and the mode shape of each devices corresponding device in panel (A)

A

B
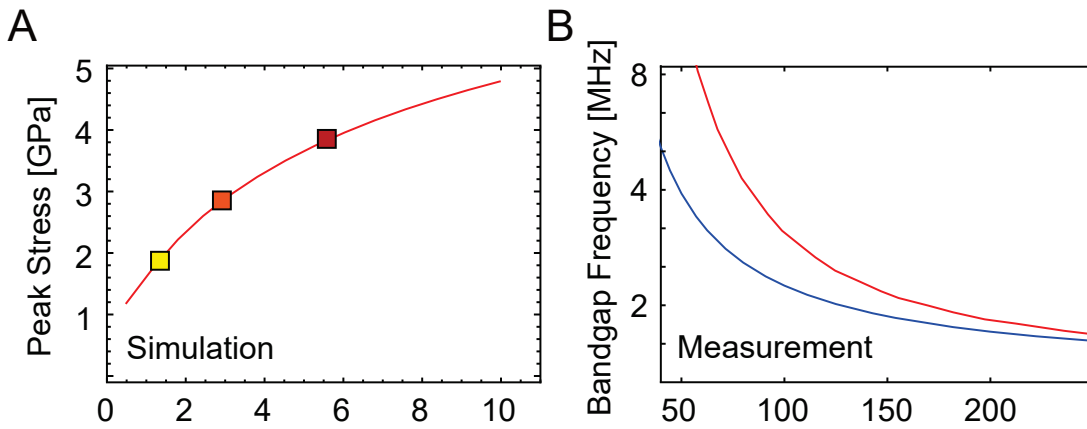
Figure 1.37 – (A) Simulation of peak stress versus band gap frequency for the devices shown in figure 1.36. (B) Measurements of bandgap frequency versus length of the central unit cell (parameterizing the taper length). Red and blue lines are models with and without accounting for stress localization, respectively.

observe in the experiment (red circles in figure 1.37) is that the frequency rises faster than of $1/l_{cell}$. This is because by increasing the number of unitcell and thus, decreasing the length of the taper compare to the total length, the stress in the tapered region also increases according to equation (1.127). The red solid line in figure 1.37.B is the model that account for stress localization. Fitting to this model to our data, we observe that we have increased the stressed in the tapered region from ~ 0.9 MPa to 3.8 GPa. In the next section, we measure the yield stress oft Si_3N_4 to be about 6 GPa. In that sense, we want to emphasize that even through in this thesis we broke the record for highest Q, $Q \times f$ and Q/m at room temperature, there is still a large room for further improvements for the next generation of students.

Now after understanding the spectrum and measured stress in these beam, the next step
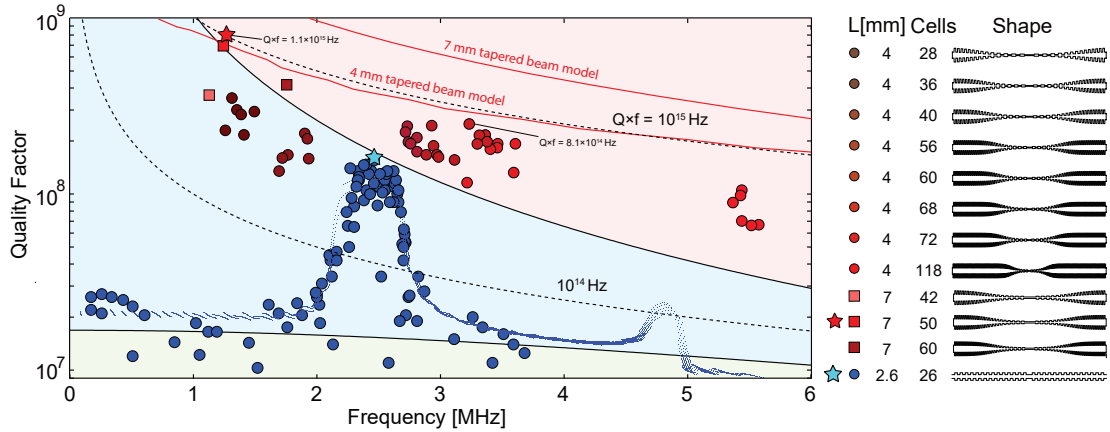
Figure 1.38 – **Compilation of the measured quality factors of tapered PnC beams** Measured quality factors of the localized modes of $h = 20$ nm $l = 4$ mm beams are shown as red circles, with different shades denoting geometries with different numbers of unit cells and, correspondingly, different localized mode frequencies. The corresponding beam profiles are shown to the right of the plot. The highest value recorded for 4 mm sample set is $Q \times f = 8.1 \times 10^{14}$ Hz. Quality factors of $h = 20$ nm $l = 7$ mm beams are shown as red squares, with the highest-Q sample denoted by red star. The two continuous red lines show theoretical quality factors, calculated for optimized localized modes in $l = 4$ and $l = 7$ mm beams. The experimental values show an unexplained factor of 3 reduction compared to the model. Blue circles are the quality factors of in- and out-of-the -bandgap modes of $h = 20$ nm $l = 2.6$ uniform PnC presented in figure 1.28 and plotted for the reference.

is to look at their quality factor. Results of the Q measured on the tapered soft-clamped beams are presented in figure 1.38 as red circles and squares. Blue data points represent the Q measurement for the uniform PnC beams kept for the reference. As the first measurement campaign, we tried to experimentally l observe that a) we can go beyond the soft clamping region and b) demonstrate the frequency independent $Q \times f$ we established in equation (1.131). Unlike the soft-clamped beams, instead of plotting Q for defect sweep, we only plotted the highest Qs (corresponding to the localized modes) for each length. The corresponding number of unitcells for each data groups and their schematic design is plotted on the right hand side.

Red circles are compiled for localized modes of 4 mm-long tapered beams with various peak stresses, corresponding to a bandgap frequency varied from $f_{bg} = 1 - 6$ MHz. According to a full model (eq. (1.66)), $Q(f_{bg})$ should in principle trace out a line of constant $Q \times f \approx 10^{15}$ Hz, exceeding the clamp-free limit of a uniform beam ($Q \times f \propto 1/f$) for sufficiently high frequency. We observe this behavior with an unexplained $\sim 30\%$ reduction compare to the red trace as theoretical expectation for 4 mm beams, with Q factors exceeding the clamp-free model by a factor of up to three and reaching absolute values high as 3×10^8. Although our data follows the expected Q from these beams, this factor of 3 reductions could be attributed the worse surface condition of our samples for these measurements. Another possible scenario could be attributed to the fact that E_{img} is a function of stress and increases by going to higher

stress. Further research has to be done in order to fully understand this factor of 3 discrepancy between the model and the measurements. Though theoretically this Q should be accessible by soft clamping alone at lower frequency, our strain-engineering strategy gives access to higher $Q \times f$, reaching a value as high as 8.1×10^{14} Hz for the 3.2 MHz mode of a 4 mm-long device.
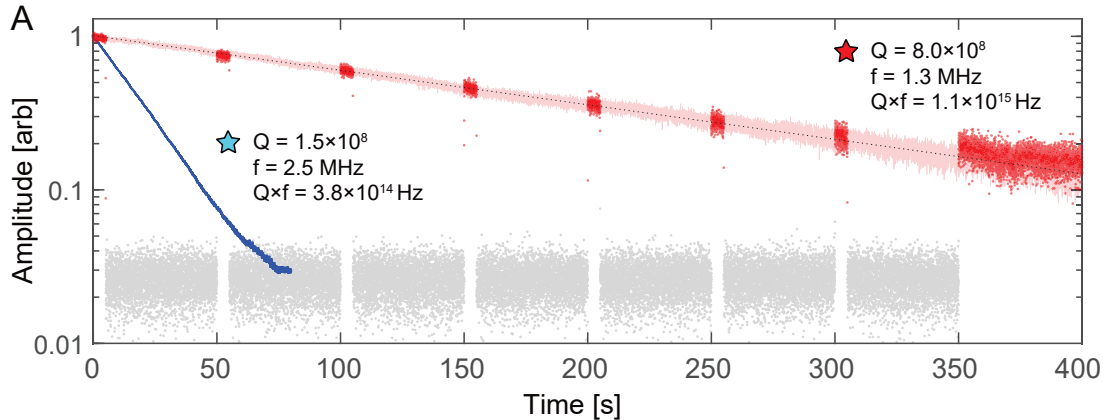
Figure 1.39 – Interferometric ringdown of a 7 mm-long, 20 nm-thick tapered PnC nanobeam excited in its 1.33 MHz defect mode (pink). Dotted line is an exponential fit with a decay time of 190 seconds. The inferred Q of 8.0×10^8 is indicated by a red star in figure1.38. Overlaid is a stroboscopic ringdown with measurement-on(off) intervals in red(gray). Fits to stroboscopic ringdowns yield the same Q to within 5%, suggesting that photothermal damping is negligible. Also shown in blue is a ringdown of the highest recorded uniform PnC nanobeam (cyan star in fig 1.38) plotted for the reference.

To investigate our finding in equation 1.131 that we can increase the $Q \times f$ by fabricating longer devices, longer beams were tested. Higher Q and $Q \times f$ factors were achieved using longer beams (red squares). In figure 1.39 we highlight the 190 second ringdown of a 7-mm-long device excited in its 1.33 MHz defect mode (pink)., corresponding to $Q = 8.0 \times 10^8$ and $Q \times f = 1.1 \times 10^{15}$ Hz as our record value (corresponding to red star if figure 1.38). Th blue data correspond to the highest Q we measured with uniform PnC beams in the previous section (blue star). We note that for the mechanical oscillators with such a high quality factor, damping date approaches the low mHz regime ($f/Q \sim 1$ mHz), During the experiments, we discover that laser light in some cases can affect these ultra-high Q beams and at certain conditions (depending on the power and position of the beam width respect to laser spot and focal point of the lensed fiber) , they can can induce damping or anti-damping which is at the same order of our linewidth (~ 1 mHz). Typically these effects are negligible in lower Q samples but it become a major challenge in the charachterization of ultra-high Q beams where the quality factor approaches 1 billion at room temperature. Figure 1.40 shows an exampled of a recorded measurement on one device the measured quality factor is different depending on the vertical position of the beam with respect to lensed fiber.

There are number of different physical mechanism which link the mechanical objects to
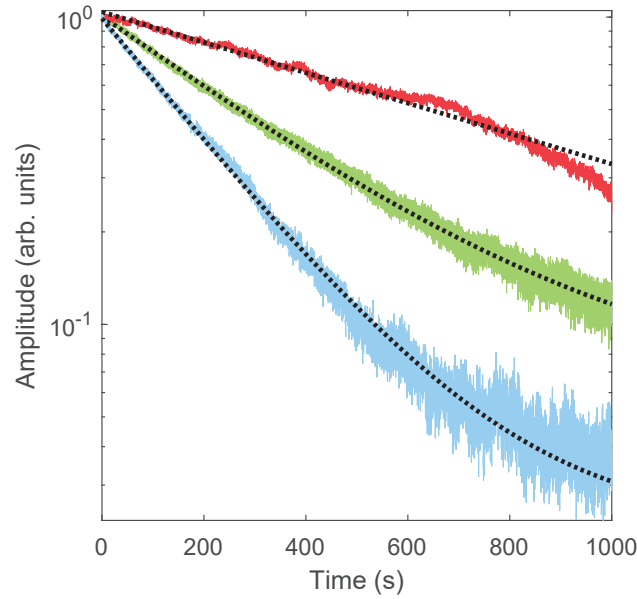
Figure 1.40 – **Position-dependent photothermal damping.** The plots show ringdown measurements of the same mechanical mode (a 1.06 MHz localized mode of a 7 mm tapered PnC beam) taken at different fiber positions. The damping rates vary from $f/Q = 0.35$ mHz (red) to $f/Q = 0.9$ mHz (green) to finally $f/Q = 1.5$ mHz (blue). The true quality factor of the beam was not determined.

optical fields such as radiation pressure or photothermal effects. We believe that the effect we are observing has some signatures of photothermal effect. Absorption of light can lead to photothermal forces including viscous damping, which can mask the intrinsic damping rate of the oscillator. The photothermal damping (or anti-damping) rate is proportional to the laser power, and thus may be detected by comparing the total damping rate of the oscillator measured different powers. For all but the lowest mechanical damping rates, ringdown times were found to be independent of laser power in the range $0.1 - 10$ mW, suggesting that photothermal damping was negligible. We found, however, that this effect may be non-negligible for the modes with the lowest observed mechanical linewidths $f/Q \lesssim 2$ mHz. For such modes we observed both photothermal damping and anti-damping approaching ~ 1 mHz, magnitude and sign being dependent on the position of the lensed fiber above the beam (see 1.40).

In order to make sure that we are measuring the intrinsic dissipation of the highest-Q 7 mm samples, "stroboscopic" ringdown measurements we performed (red data points in 1.39), where the laser is turned off between short (compared to the $\tau = 1/\Gamma_m$ of the oscillator) 'on' intervals. The laser pulse sequence is described in 1.41 and the data is shown in 1.39. Both the continuous and stroboscopic ringdowns shown here were performed using 1.2 mW of laser power incident on the beam. In figure (1.39), we can observe that the stroboscopic and the

continues ringdown measurement has an excellent agreement. For our highest Q, we actually took one step further to unambiguously prove the measured Q is the actual Q of the resonator and effect of laser light is negligible, we change the time between the strobes and thus the change the absorbed power by the beam. The results are presented in figure 1.42.
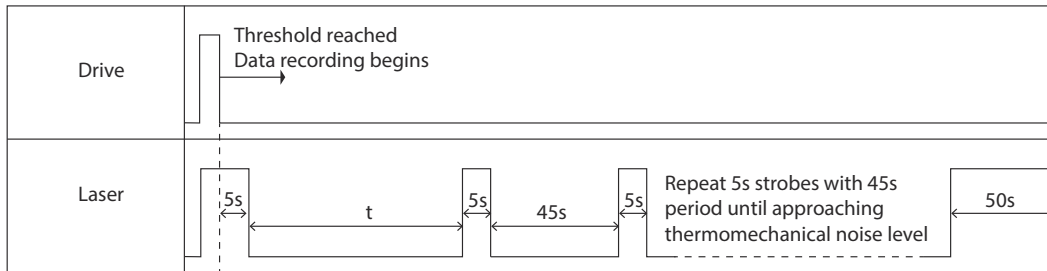
Figure 1.41 – **Stroboscopic ringdown sequence**. The figure shows the sequence of strobes used to perform a stroboscopic measurement of a mechanical mode quality factor. The length of each trace is kept constant. As t, the separation between the initial measurement and the first strobe is increased, the number of strobes is reduced to keep the total length of the trace constant. The 50 s long measurement at the end of the trace is used to measure the thermomechanical background of each trace in order to calibrate the alignment drift between traces.

In the first set of experiments, we sweep the gap between the strobes (figure 1.42). At the core of its logic, in the stroboscopic measurements, the idea is that during the dark periods of laser, the oscillator is losing its energy in the background even though we are not "looking" at it. Even if by the act of measurement each time we excite the beam by some amplitude, the stroboscopic ringdown should be different for different waiting times for the experiment. In figure 1.42.B we explore the sweeping time of the dark time in a different way. In this experiment step by step, we increase the time delay between the first two strops. Our observations is that there is an excellent agreement between the continuous measurement and stroboscopic measurement regardless of the time difference between two strobes. By separately fitting into each stroboscopic measurement, we confirm that photothermal damping contributes less than 5% uncertainty.

Before we conclude this section, let's review two more aspects of these localized beams (whether in the case of uniform or tapered nano-beams). The first question is regarding the robustness of the localized modes with respect to fabrication imperfections. In theory, the presence of ultrahigh-Q localized modes in high-strain phononic crystal beams is robust with respect to small variations in the beam parameters like unit cell geometry and the central defect size. The localized mode Q is a weak function of these parameters, attaining values close to those of a clamp free uniform beam (the ideal situation) even with the simple geometries used in this work. This is in contrast to photonic crystals, where minor changes in the unit cell pattern and/or fabrication imperfections can dramatically reduce the Q factor of a localized
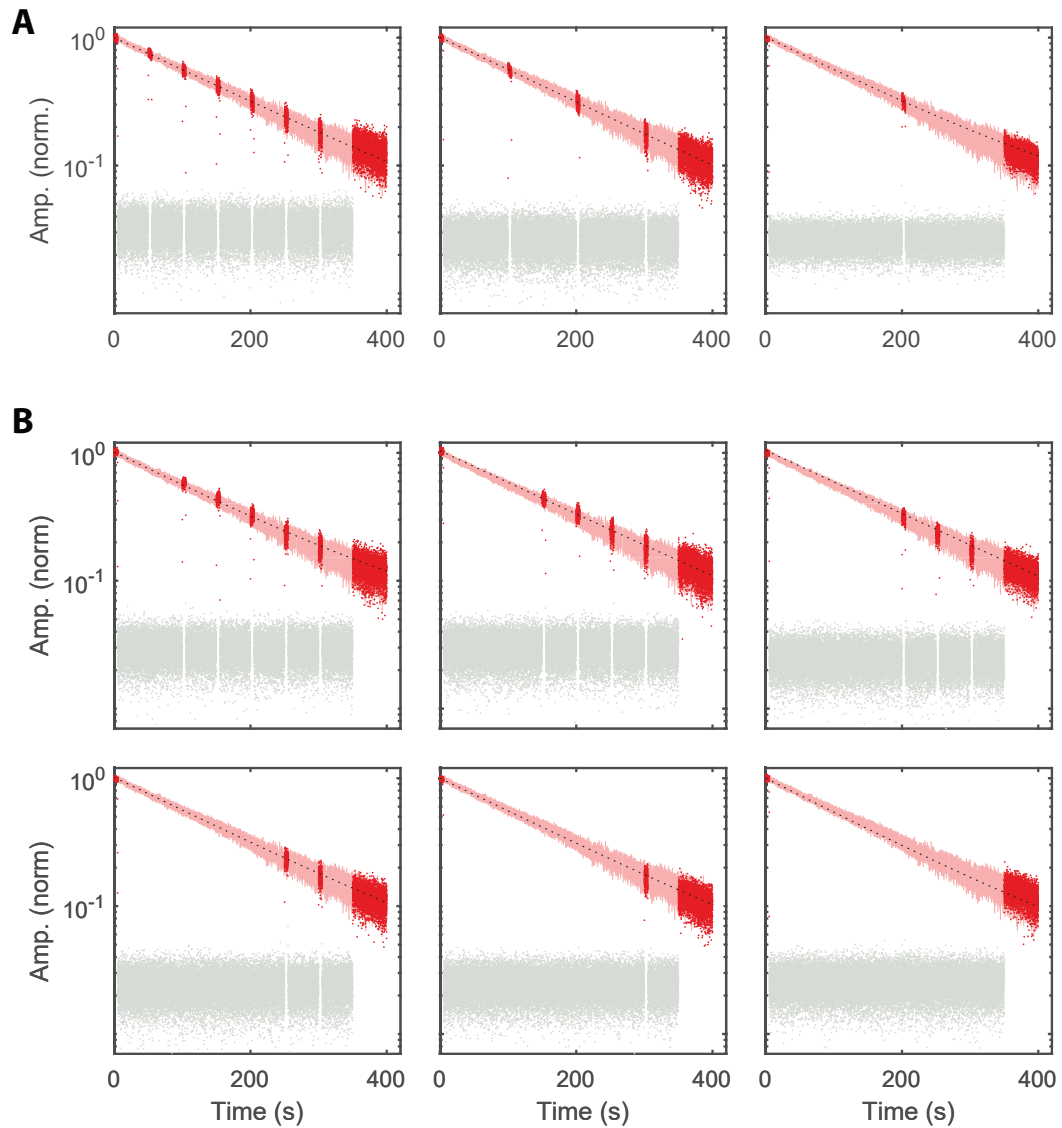
Figure 1.42 – **Stroboscopic ringdown.** Light red: data taken with light on throughout the ringdown. Red: Stroboscopic ringdowns. Gray: Data recorded with light off. **A:** The duty cycle was varied from left to right from 45 off/5 on to 95 off/5 on and finally to 195 off/5 on. **B:** The time t as described in 1.41 was varied in steps of 45 seconds from 45 seconds to 345 seconds. In both cases, no significant change in damping rates was observed. Fits to stroboscopic ringdowns with different duty cycles yield the same Q to within 5%, suggesting that photothermal damping is negligible.

mode. The robustness of phononic modes originates primarily from the fact that sound cannot irradiate energy into free space (in vacuum), which can constitute a major source of loss in photonic crystals (radiation losses). We believe at its core, the source of this robustness is the extremely large wavelength of these mechanical modes at MHz frequencies. With wavelengths

in excess of 100 μm, these modes are averaging out the nano-meter random imperfections and roughness.
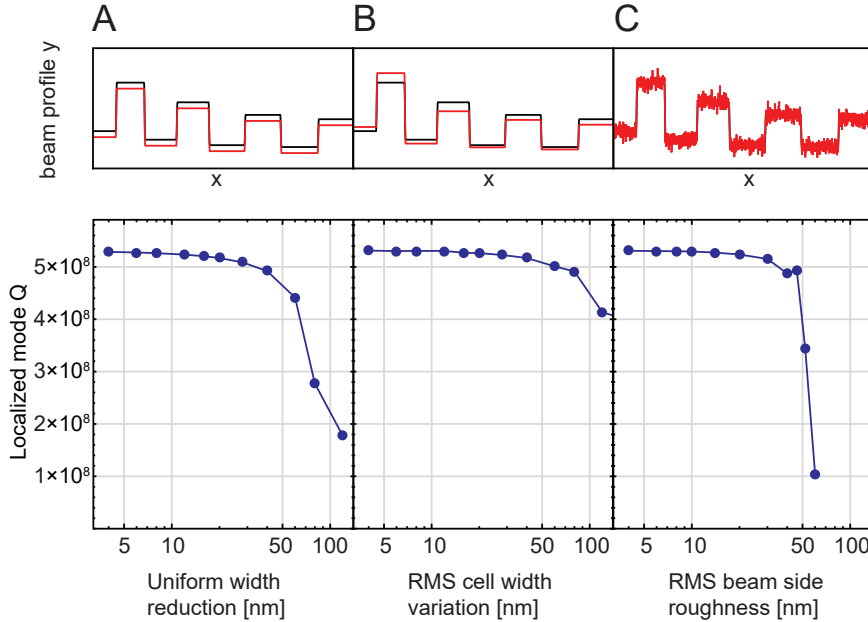
Figure 1.43 – **Impact of shape imperfections**. Bottom plots show the variation of the localized mode quality factor under different types of shape perturbations illustrated at the top as perturbed beam shapes (red) vs unperturbed (black). A) uniform beam width reduction — 1 in the text, B) random variation of the beam unit cell widths — 2, C) side-wall roughness of the beam — 3.

The typical fabrication resolution, limited by e-beam lithography to ~ 10 nm, is orders of magnitude below the acoustic wavelength in this work (50-200 μm). However, the thinnest part of the beams can be as small as a few hundred nanometers wide, raising concerns about the effect of random or systematic width imperfections. We theoretically model three types of sidewall-related fabrication errors: 1) uniform beam width reductions compared to the optimum design due to over-etching of Si_3N_4 during pattern transfer; 2) random variation of beam unit cell widths; 3) side-wall roughness of the beam. In 2) the width of each unit cell was perturbed by a Gaussian-distributed random number dw_{cell}, and in 3) a Gaussian-distributed random width perturbation $dw(x)$ was applied to the beam profile at each grid point, in both cases due to computational constraints, the perturbed beam shapes were assumed to preserve in-plane reflection symmetry and the Q degradation was calculated as the average of 30 realizations of random shape perturbations at each perturbation magnitude. The results are presented in 1.43 for a typical 38 unit cell tapered beam design from this work, with 4 mm beam length, 400 nm beam width in the narrowest part (center) and 20 nm Si_3N_4 thickness. The unperturbed design predicts a localized mode at 2.1 MHz with Q = 530 million. From 1.43 it follows that for none of the considered imperfection types with variations of order 10% of the minimum beam width results in more than 10% degradation in Q.

Another important imperfection, which arises during fabrication of tapered beams is transverse buckling of the wide unit cells (near the supports) due to stress relaxation in the y direction. The buckling increases the effective beam crossection, reducing the Q of the localized mode. This effect limits the maximum achievable frequency of localized modes ($\approx f_{bg}$) within a beam of given length and given minimum width in the center, as the length/width ratio of the widest unit cells near the beam clampings decreases as a function of f_{bg}. In our work buckling was observed with unit cell length/width<3 for 20 nm-thick beams.
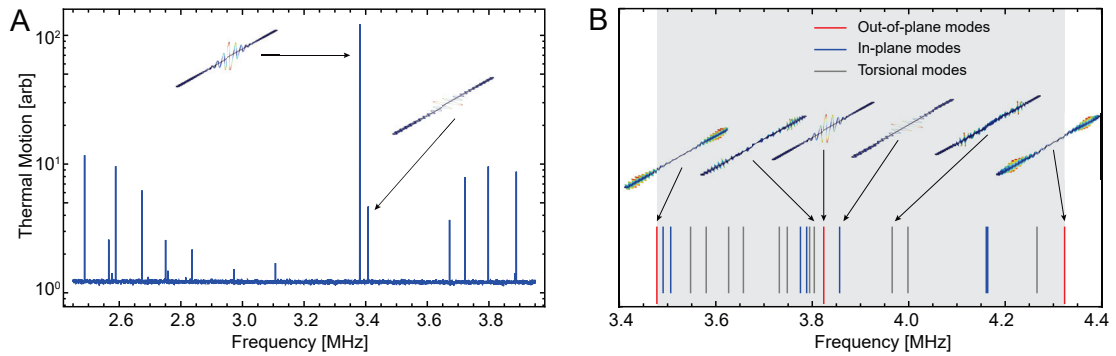
Figure 1.44 – **Presence of in-plane and torsional beam modes** A) Thermal spectrum around phononic bandgap taken with the lensed fiber positioned off the beam axis. An in-plane mode is co-localized with an out-of-plane one in a tapered beam with the parameters $l = 3$ mm, $h = 20$ nm, $N_{cells} = 52$. B) 3D finite element simulation of the spectrum of a $l = 3$ mm, $h = 100$ nm, $N_{cells} = 52$ beam. The phononic bandgap for out-of-plane modes is shaded gray with the modes nearest to the localized out-of-plane one annotated by their shapes. Unlike the pure soft clamping beams where the experimental and simulated frequencies agree very well (at % level), the measured localized mode frequencies for tapered beams are typically 10% lower than the results of simulations.

The last remaining topics in regard to the localized modes are the other flavors modes. So far in our discussion we were only focused on the out of plane flexural modes, but in reality, these oscillators have other type of modes such as in-plane, torsional, longitudinal and other types of modes. The structures investigated in this manuscript are optimized for high-quality factor out-of-plane modes. Therefore, the measurement setup is engineered to be more sensitive to the out-of-plane modes by using a lensed fiber positioned directly above the beam. The in-plane and torsional modes have much lower transduction. However, by displacing the lensed fiber perpendicularly to the beam axis, the in-plane resonances can be observed in the measured signal. While it is challenging to identify all modes outside the bandgap, a localized in-plane mode may be identified near the localized out-of-plane mode. This mode is shifted slightly higher in frequency than the localized out-of-plane mode (see 1.44 A). Also, to give an idea of what other modes except for the localized out-of-plane one can populate the bandgap, we perform a 3D finite element simulation of the vibrational spectrum of a 100 nm thick nanobeam (1.44 B). 3D simulations of the 20 nm structures used in this work were not performed due to the large problem sizes for such extreme aspect ratios.
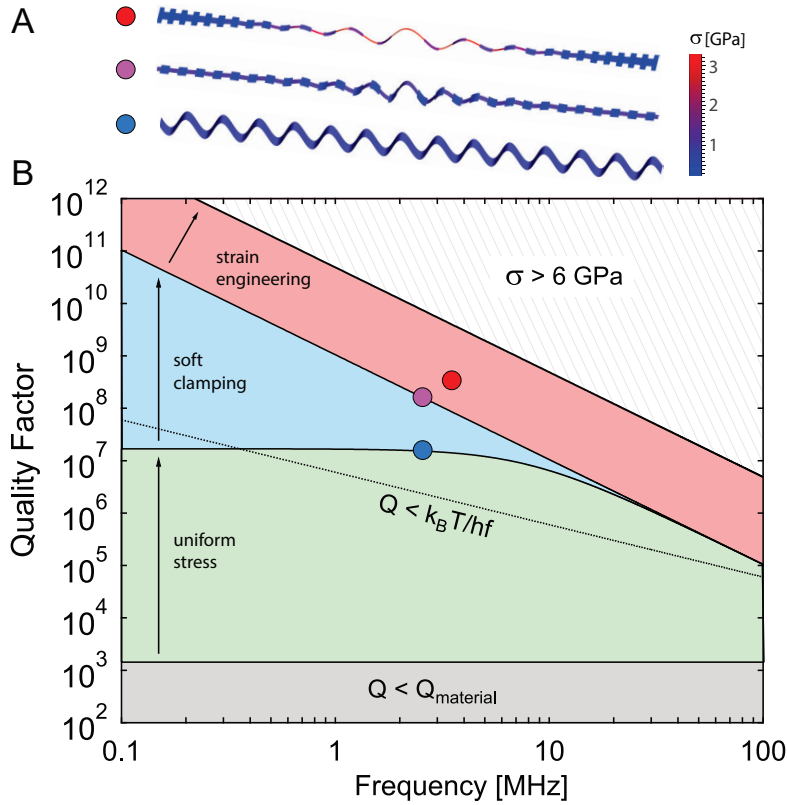
Figure 1.45 – **Ultra-high-Q nanobeams through dissipation dilution.** (a) Mode shapes representing three strategies to enhance the Q of a nanobeam via dissipation dilution. From bottom to top: uniform stress, soft clamping, and geometric strain engineering. Color-coding represents axial stress, σ. (b) Q versus mode frequency (f) accessible for a 20 nm-thick Si_3N_4 nanobeam, following (1.66). Gray region: $Q(f)$ of an unstressed beam, limited by material loss. Green region: $Q(f)$ of a 3 mm-long uniform beam with $\sigma < 1$ GPa. Blue region: $Q(f)$ accessible by soft clamping. Red region: $Q(f)$ accessible by soft clamping and strain engineering. The hatched region is forbidden by the material yield strength. Solid circles correspond to measurements described by equation (1.91).

In summary, in this section, we introduce 3 strategies in order to enhance the quality factor: I) Using the higher order modes of uniform long beam at it optimum mode order. II) Reducing the contribution of the clamping losses (soft clamping) by localizing the mode shape in bandgap phononic crystal and isolating it from the clamping regions III) Using the strain engineering techniques to boost the stress to near the yield stress of the material and combine it with non-uniform tapered PnC that co-localizes the mode shape and the regions of the enhanced stress at the center of the cavity. All of these strategies are visualized in figure 1.45. In this plot, we start from the gray region at the bottom. This region shows the extent of a Q of an unstressed beam, limited by material loss (no dissipation dilution effect). Above the gray section, an limited by the forbidden zone (hatched area) is the region that we can access by the means of dissipation dilution technique. Green, is the area that can be achieved using uniform stress in uniform standard beams and their higher order modes. Most of the work

around high-stress nano-mechanical resonators were only exploring this limited region of dissipation dilution. By taking advantage of the recently introduced soft clamping technique and diminishing the clamping loses, we can access the blue region. In this thesis, for the first time we introduced the strained enhanced localized modes that let us cross into the red area and use the dissipation dilution with its maximum capability.

In conclusion, realization of $Q \times f \sim 10^{15}$ in a $m \sim$ pg mechanical oscillator has numerous intriguing implications. First, such an oscillator is an exquisite force sensor. For example, localized modes of the beam outlined in figure 3 are limited by thermal noise to a sensitivity of $\sqrt{8\pi k_B T m f / Q} \approx 3 (\mathrm{aN}/\sqrt{\mathrm{Hz}})$ at $T = 300$ K. This value is on par with a typical AFM cantilever operating at 100 times lower frequency and temperature [152], creating new opportunities for applications such as high-speed force microscopy (MRFM) [153] . Of practical importance is that the reported devices also exhibit an exceptionally strong thermal displacement of $\sqrt{k_B T Q / (4\pi^3 m f^3)} \sim \mathrm{nm}/\sqrt{\mathrm{Hz}}$, accessible by rudimentary detection techniques such as deflectometry. Indeed, their zero-point motion $\sqrt{\hbar Q / (2\pi^2 m f^2)} \sim \mathrm{pm}/\sqrt{\mathrm{Hz}}$ is orders of magnitude larger than the sensitivity of modern microcavity-based optical interferometers [9], offering possibilities in the field of quantum measurement and control [10]. A fascinating prospect is to use measurement-based feedback to cool such an oscillator to its ground state from room temperature [154]. A basic requirement is that the oscillator undergo a single oscillation in the thermal decoherence time $\hbar Q / k_B T$. The devices reported are exceptional in this respect, capable of performing $\frac{2\pi Q \times f}{k_B T / \hbar} > 100$ coherent oscillations at room temperature.

Remarkably, the performance of our devices seems far from exhausted. First, the dilution factors we have achieved are still an order of magnitude below the limit set by the breaking stress of Si_3N_4. Our results may thus benefit from more aggressive strain engineering. (For example, 30-nm-wide Si microbridges have been fabricated with geometric stresses as high as 7.6 GPa [102].) We also emphasize that higher aspect ratio devices offer a direct route to higher Q. The aspect ratios of our longest beams ($L/h = 3.5 \times 10^5$) appear to be anomalously high for a suspended thin film, including 2D materials [140]; however, a recent report has demonstrated high-stress Si_3N_4 membranes with cm-scale dimensions [155], hinting at a trend towards more extreme devices. Interestingly, the $Q \propto \frac{l_{\mathrm{beam}}}{h l_{\mathrm{cell}}}$ scaling of strained enhanced soft-clamped resonators preserves the advantage of thinner and longer devices without any apparent limitation. The performance of our devices seems far from exhausted. First, the dilution factors we have achieved are still an order of magnitude below the limit set by the yield stress of Si_3N_4. Our results may thus benefit from more aggressive strain engineering. (For example, Si microbridges have been fabricated with local stresses as high as 7.6 GPa [102].)

Looking forward, several directions seem promising for realizing yet higher Q. One route is to fabricate mechanical resonators from strained 2D materials. Extreme aspect ratios as high as 3×10^5 have been demonstrated for suspended graphene sheets [140], matching the highest values realized in the present work. These materials can moreover have yield stresses well in excess of 10 GPa [156], and are currently being widely explored in the field of elastic strain engineering. Another route is to reduce intrinsic loss, for instance by improved surface

conditioning [57][157] or by employing cryogenic temperatures [158][159] or using crystalline thin films [160]. The latter approach is intriguing because pre-stresses of $\sigma_0 \sim$ GPa are in fact readily accessible by lattice mismatch in epitaxial growth (for critical thicknesses of $h \sim 10$ nm). To give an example: engineering the reported devices out of a 1%-strained InGaP film ($\sigma_0 \approx 1$ GPa, $E_0 \approx 100$ GPa) [81] and operating at 4 K should in principle enable $Q_0 \sim 10^5$, $Q \sim 10^{11}$ and $Q \times f \sim 10^{17}$ Hz, corresponding to zepto newton force sensitivities and a thermal decoherence rate of $k_B T / hQ \sim 1$ Hz. This value sparks the imagination, as it exceeds even the performance of trapped ions [161]. The crystalline platform moreover dovetails handsomely with proposals for hybrid quantum systems based on strain-coupled defect (e.g. NV diamond) centers [162], inviting speculation that such systems may one day serve as a realistic platform for solid state quantum sensing [163].

Outlook for UHQ beams (I): challenges of integration

In the previous sections, we study three different strategies to achieve ultra-high Q resonators and we observed that the strained enhanced soft-clamped beams have the best performance among the three. Besides all these positive aspects of these strategies especially in terms of interesting scalings laws for $Q \times f$ and Q/m, the major downside and challenge of these ultra-high Q beams are their incredible aspect ratio. In order to achieve quantum enabled devices ($Q \times f > \frac{k_B T}{\hbar}$) with Q factors in excess of 100 million, we usually require beams that are several mm long and few 10s of nano-meter thick. A beam with such dimensions is an extremely soft spring that can bend with tinniest forces. By experience, we learn that fabricating such structures is a very delicate and challenging task. For example, during the release process, these beams can easily stick to abject around them including the underneath substrate and it is very difficult and almost impossible to unstick them. For examples for many of the devices measured in the last section, we had to push down the underneath substrate by more than 10μm during the Bosch process in order to create a gap that is large enough and beams won't collapse into the substrate. This "softness" and aspect ratio pose a major limitation and challenge on integrating these mechanical beams into any optomechanical systems especially near field based optomechanical systems [123], [125], [126] where the optical cavity and mechanical oscillator often are required to be as close as 100s of nm from each other.

Our solution to this challenge is surprisingly simple: anchoring the beam at it nodes of the mode shape. For example figure 1.46 illustrates an example of a beam where the second order mode of the defect is localized. For this geometry, the length of the defect is designed to be $l_{\text{def}} = 2.2 \times l_{\text{cell}}$ where l_{cell} is the neighboring cell of the defect. The performance of these second order localized modes have no major difference between the first order modes presented in 1.33. In the measurement we observed that the second order modes have even better performance compare to the fundamental defect modes and we observe consistently more reliable samples fabricated to operate at their second order mode of the defect. In fact, our highest ever recorded Q in figure 1.39, is achieved on second order defect mode of a 7 mm

beam with the geometry similar to figure 1.46.A. Beside being more reliable, the second order modes also have a node at the center of the beam as illustrated in figure 1.46.A.
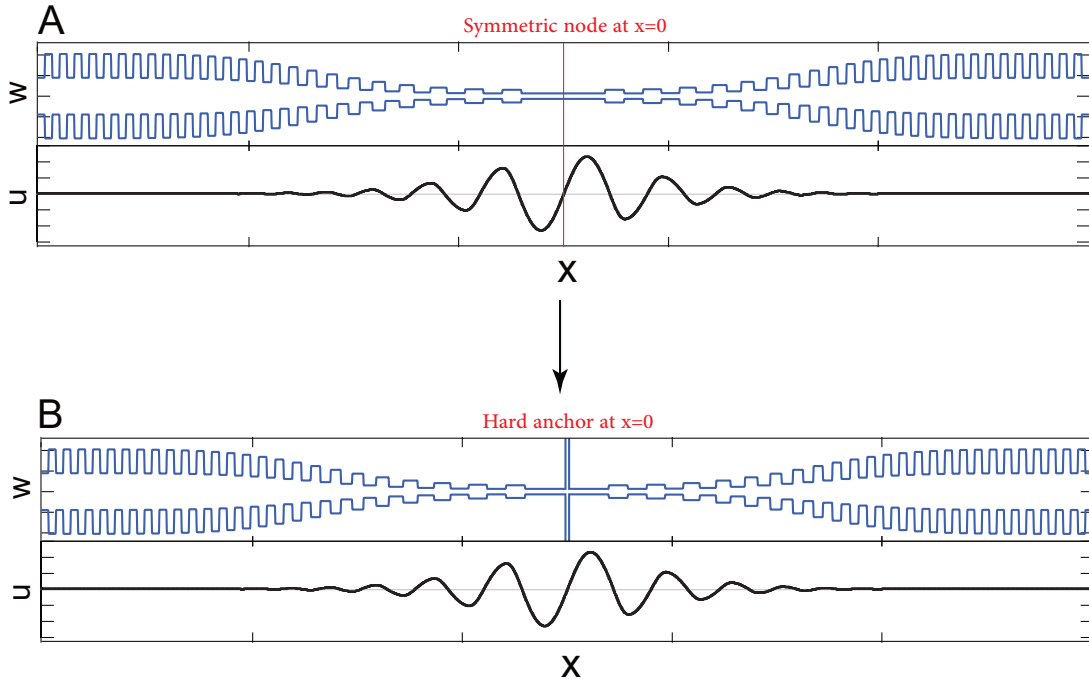
Figure 1.46 – Schematic of the proposed geometry for anchored localized beams where a solid anchor is used at the node of the mode shape to fix the beam during release process without affecting its quality factor. (A) Schematic and mode shape for a second order mode of the defect with a symmetric node at the center of the beam. For this mode $l_{\mathrm{def}} = 2.2 \times l_{\mathrm{cell}}$. (B) Schematic and mode shape after adding a thin clamp at the center of the beam. Fo infinity thin clamp, the mode shape does not get affected by the clamps.

According to dissipation dilution and Euler–Bernoulli theorem, if now we clamp the beam at the node of its geometry, the dynamic response of the system does not change (figure 1.46.B). Meaning that if the width of the anchor is infinitely small, the mode shape and the quality factor of this beam will be the same as the free standing beam. However, in reality the smallest anchor we can fabricate is limited to beams as small as 40-50 nm . It should be noted that if the anchors are wider than the threshold the motion of the beam creates a torsional motion in the anchoring beams. We have shown in figure 1.11 that the Q of torsional motions do not dilute via the dissipation dilution and remains low Q. Therefore, we predict the Q of the beams would reduce for wide anchors. On the other hand, anchoring the beam at its weakest point (at the center) could completely change the static behavior of the beams. Now from the static point of view, these beams are very solid and stable near their center (anchoring point) where the amplitude of the motion is largest and we normally prefer to integrate an optical cavity.

Recently we attempted to test this idea. Figure 1.47 shows the SEM image of an anchored localized beams where in red we see the central defect of the beam attached to a thin anchor
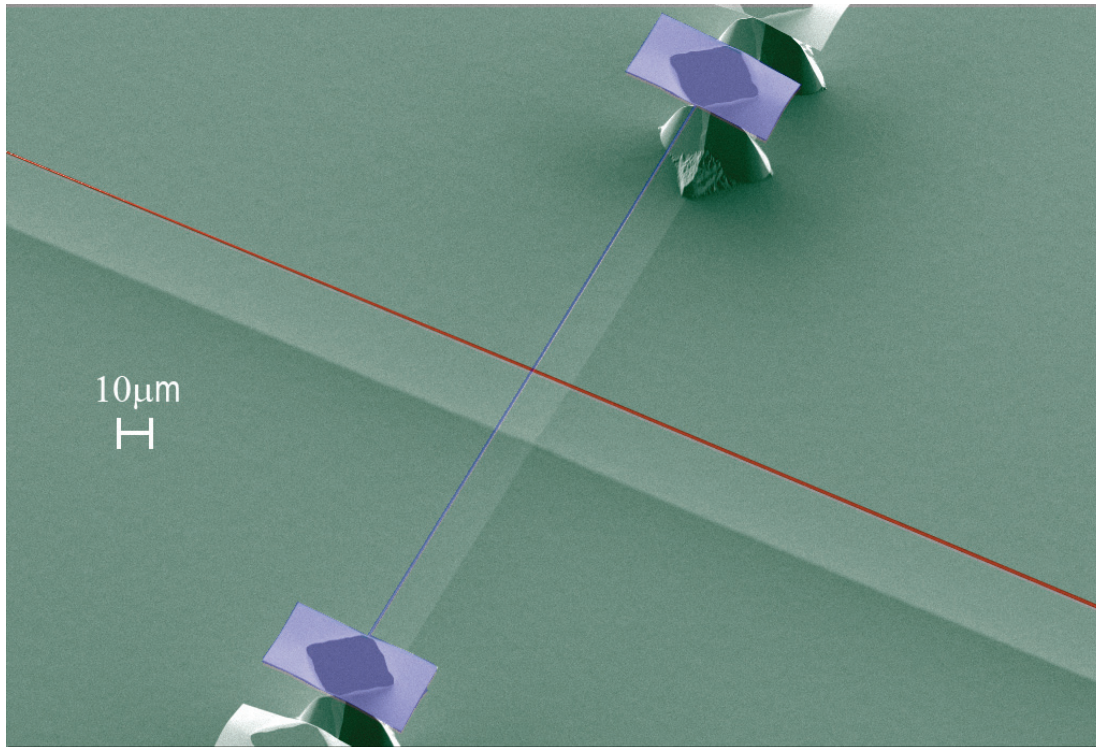
Figure 1.47 – False color SEM image of released 4 mm long taper PnC beams (red) with anchored at the center by 50 nm wide beams (Blue). Green represent the silicon substrate.

(blue). In these samples we fabricate defects as thin as 50 nm which is near the limit of lithography resolution at EPFL fabrication facilities. We have tested these devices and recently we were able to measure Qs as high as 100 million for the anchored geometry. This is about a factor of 3-4 lower than the free standing beams of the same geometry we measured in previous section. Although more measurement has to be performed to confirm that if such a reduction is systematic and is due to the anchoring and is not just statistical fluctuations of the quality factor due to other causes such as poorer surface conditions of the particular sample that we measured. As an outlook and next steps of this project, I believe the anchored beams has to be studied more systematically to understand the effect of the anchor beams on the quality factor of these resonators. Such an anchoring strategy will be at the core of any future integration of these devices even if it comes with the cost of an order of magnitude reduction in the quality factor.

If such an anchoring strategy proves to work as expected, one can think of putting more anchors at other nodes along the beam. With this approach, extreme aspect ratios and lengths beyond several cm is within a reach. Although anchoring the beam at any other point except its symmetric point at the center will create further complication for our strain engineering strategy. As we discussed in the previous section, the enhanced stress in the tapered region is created as result of shirking of the outer parts of the beam. Anchoring the device at several points would complicate such a stress redistribution process and more complex anchoring

may be needed in such a case. It should be also noted that the anchoring the beam at its central point, also removes odd order modes (such as 1st, 3rd and other odd modes) from the spectrum. This could be very beneficial for any future optomechanical systems as these modes have an anti-node at the center which results in their small effective mass. But such an anchoring strategy, we remove all these modes from our spectrum and make sure only the localized mode have the strongest optomechanical coupling to the optical cavity.

Outlook for UHQ beams (II): Process flow for strained silicon beams

All the theoretical and experimental studies including all the strategies we present in this thesis to enhance the quality factor of materials are pure geometrical designs and fundamentally material independent. We applied those techniques to resonators made of high stress Si_3N_4 only because Si_3N_4 is widely available and established material to reliably achieve high stress. However, Si_3N_4 is an amorphous materials with relatively low intrinsic quality factor. All of our techniques could be applied to other strained materials. We can draw insights from the field of elastic strain engineering (ESE)[145], in which extreme stresses (approaching the material yield strength) are routinely achieved in nano-scale structures made of crystalline and/or 2D materials. An important example of ESE is the use of epitaxial strain to enhance the mobility of silicon in modern transistors [164]. Indeed, strained silicon-on-insulator (sSOI) is now a commercial wafer-scale technology, which has yet to be explored for nanomechanics. As is a broad zoo of compound semiconductors and/or 2D materials routinely subject to epitaxial or deformation-based stress in the context of ESE, ranging from germanium microbridges [80] (7 GPa) to nano-indented graphene [156] or MoS2 sheets (~10 GPa). To give a realistic example, applying our techniques to a nanostring released from a 20 nm film of strained silicon should enable, at an operating temperature of 4 K, an intrinsic quality of $Q_{int} > 10^5$, a diluted quality factor of $Q > 10^{11}$, and an enhanced $Q \times f$ product of $> 10^{17}$ Hz, corresponding to a thermal coherence time of $hQ/k_B T \sim 1$ second and an astounding $hQf/k_B T \sim 10^6$ quantum coherent oscillations. As an initial testing ground, these devices hold particular promise in the field of measurement-based quantum optomechanics, making long-established goals, such as room temperature ground-state cooling using active feedback [10]Measurement-based quantum control of mechanical motion, a realistic endeavor.

Viewed more broadly the ability to increase the mechanical coherence by several orders of magnitude – achieved via combining insights from elastic strain engineering, 2D or crystalline thin films and phononic bandgap engineering – can provide a rich new scientific setting for exploration. It can provide impetus to a wide range of applications that already make use of mechanical systems for storing, interconversion or processing of signals and information. Likewise it can catalyze devices for sensing of force, mass, acceleration, electrical or magnetic fields with exceptional sensitivity. Extremely coherent mechanical systems can therefore serve as the technological basis for a wide range of future or already existing hybrid devices.

For the next steps of this project, we propose to utilize commercially available crystalline thin-

film materials, in particular strained silicon-on-insulator (sSOI) wafers (from SOITEC, used for high speed micro-electronics) to fabricate exceptionally high quality factor nanobeams or membranes. soft clamping and strain engineering will be used to engineer the dissipation dilution of the resonators. These techniques have never been used to enhance mechanical oscillators in crystalline thin-films. The main challenge in the fabrication of strained silicon nanobeams is, of course, the fabrication. The commercially available sSOI wafers only have a thin 10 nanometer layer of oxide separating the strained silicon from the silicon substrate. In our work with Si_3N_4, gaps as large as 10μm were created in order to release the beams from the substrate without collapse. The commercially available wafers therefore require modification of the fabrication techniques previously used for Si_3N_4.
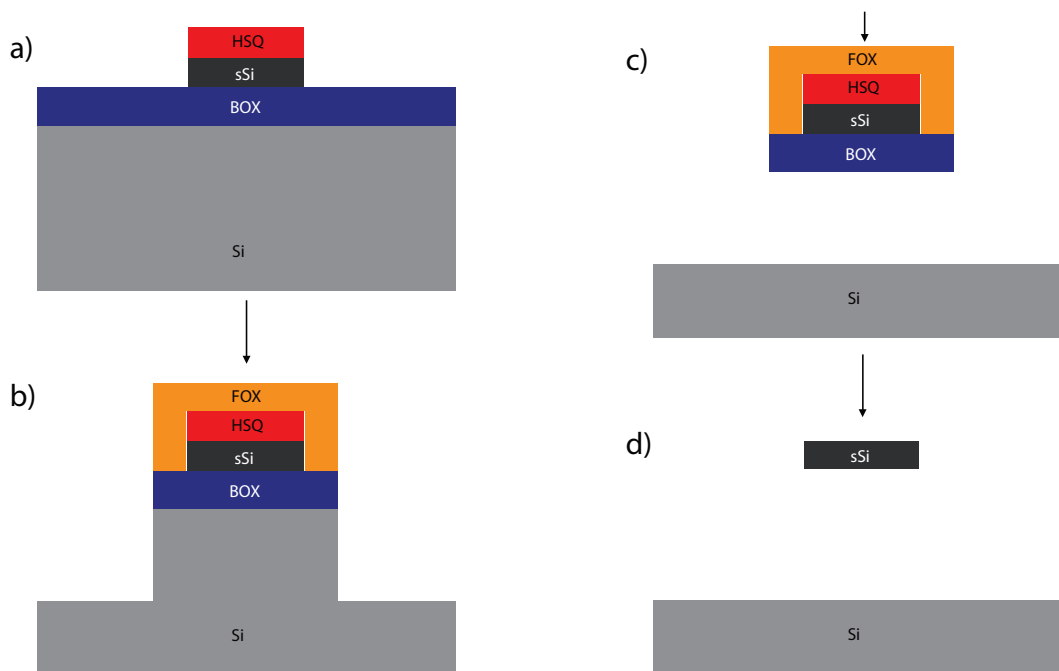
Figure 1.48 – The proposed fabrication process flow for high aspect ratio devices made from strained silicon on insulator.

In figure 1.48 we propose a process flow that could possibly allow fabrication of high aspect ratio beam in sSOI platform. With Si_3N_4 deposited on a silicon substrate, the different chemical composition of the beams and the substrate allow the use of highly selective etching processes. In the case of sSOI wafers, both the substrate and the devices will be made of silicon and a different technique must be used where the beams are encapsulated for protection during the etching process. The proposed process in figure 1.48 is optimized for fabrication of high aspect ratio (10^5) strained silicon beams. The process starts by pattering the nano beams using electron beam lithography on hydrogen silsesquioxane resist (HSQ). A reactive ion-etching (RIE) step follows for pattern transfer from the HSQ mask to the strained silicon (sSi) (figure 1.48.a). In order to protect the 20 nm sSi layer from the following Si undercut steps, a second

electron beam lithography layer is incorporated using a thick flowable oxide resist (FOX). As illustrated in figure 1.48.b, the sSi beam will be encapsulated in FOX and the buffer oxide (BOX) layer which is resistive against the fluorine chemistry used for etching the Si substrate. The BOX layer outside the beam region is RIE etched and the second beam mask is used as the mask for deep etching of the substrate using the Bosch process. This step is essential for high aspect ratio beams – a large gap between the beam and the substrate must be created to avoid the collapse of the structures during the undercut step. In the next step, the silicon pillar underneath the BOX layer is undercut using isotropic SF_6 plasma etching (figure 1.48.c) or using XeF_2 undercut step. Finally, the protective FOX and BOX layer around the beam is stripped in a vapor HF etching step and the beams are released (Fig 1.48.d).

1.5 Strain engineering and tapered clamping

In the previous section, we focused on implementing geometrical designs that enabled us to achieve record-breaking value for quality factor and to use the dissipation dilution to its full capability. However, one main drawback of all the strategies that we proposed in the previous section is that they all require extremely long and thin devices to achieve high $Q \times f$. As we observed this aspect ratio could present a technical challenge for integration of these devices. In this section, we would like to turn our attention to a simpler alternative that enables us to enhance quality factor via the lessons we learned in strain engineering and without requiring a long beam. However, it should be noted that with this technique, we will only can maximum up to a factor of 3 for out of plane modes. This may seem negligible compared to our previous methods but still could be interesting for applications where the length of the structure is limited to few 100s of μm.
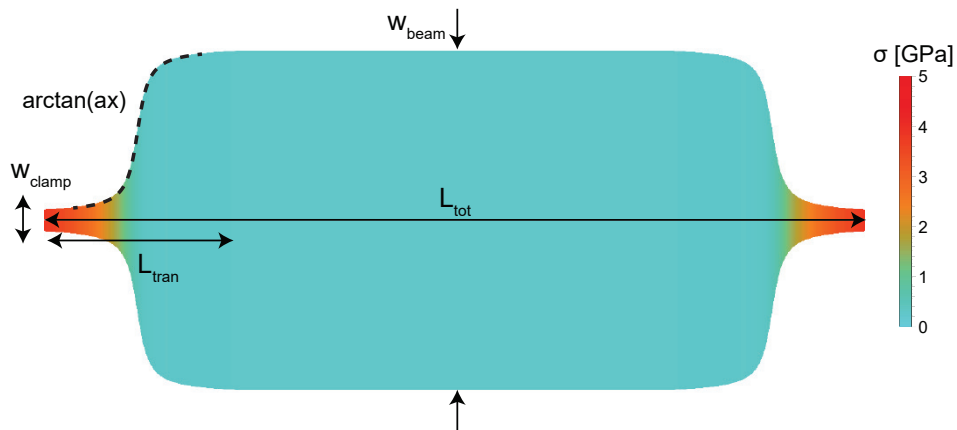
Figure 1.49 – **Pinched beam geometry**. L_{tot}: total beam length, L_{tran}: transition length, w_{clamp}: beam width at the clamping point, w_{beam}: beam width after the transition region. The color coding corresponds to the stress profile for the following design parameter: $\frac{w_{clamp}}{w_{beam}} = 0.2$, $a = 20$ and $\frac{L_{tran}}{L_{tot}} = 0.2$.

Our proposed geometry is illustrated in figure 1.49 where we apply the stress engineering

technique to the clamping area. In this approach by enhancing the stress at the clamping point we increase the quality factor. To understand this effect, let's look back at the generalized dissipation dilution of a mechanical oscillator (equation (1.66)):

$$D_{Q,n} = \frac{1}{2\alpha_n \lambda + \beta_n \check{\Omega}_n^2 \lambda^2} \tag{1.132}$$

In the previous section we tried to diminish the first term by forcing $\alpha_n \to 0$ via localizing the mechanical mode at the center via a PnC. We observe that in return, soft clamping requires a long beam (to host enough number of unitcells so that amplitude approaches to zero at the clamping points). In contrast, in this approach instead of diminishing α , we try to reduce it by tapering the width at the clamping area and concentrating the stress in this region. Here we consider reduction of the beam widths of $v_{cl} = w(0)/w_{avg}$, in order to create local strain enhancement in clamping regions (see 1.49). (1.67) shows that α_n is proportional to $\alpha_n \propto \sqrt{v_{cl}}$ and thus can be reduced by thinning down the clamps. It should be noted that for a device in the shape of figure 1.49 where the tapering is localized around the clamping area (where $\frac{L_{tran}}{l_{tot}} \ll 1$ we can assume that $u'_{cl,n}$ and Ω_n are almost unaffected by v_{cl} and still have sinusoidal mode shape. In this case the α can be calculated to be:

$$\alpha_n \approx \sqrt{v_{cl}} = \sqrt{\frac{w_{beam}}{w_{avg}}} \tag{1.133}$$

This can be interpreted as an effective decrease of λ over the clamping region to

$$\lambda_{cl} = \alpha_n \lambda = \frac{h}{l}\sqrt{\frac{\sigma_{avg} \times \frac{w_{beam}}{w_{avg}}}{12E}} = \frac{h}{l}\sqrt{\frac{\sigma_{clamp}}{12E}} \tag{1.134}$$

using λ_{cl} we can rearrange the dissipation dilution for the tapered clamped beams in the shape of fig 1.49 to be:

$$D_{Q,n} \approx \frac{1}{2\lambda_{cl} + (n\pi)^2 \lambda^2}. \tag{1.135}$$

In contrast to the PnC approach, tapered-clamped beams are predicted to have improved quality factors for low-order beam modes, including the fundamental mode. However, the improvement the maximum enhancement will be limited to $\sqrt{\frac{\sigma_{yield}}{\sigma_{avg}}} \approx 2.5$ in which the clamps are thinned until we reached the breaking point of the material (σ_{yield}).

Figure 1.50.B shows the simulated stress for width, respect to the ratio of $\frac{w_{beam}}{w_{avg}}$. If the length of the tapering region is much smaller than the total length of the beam, the stress increases linearly with the tapering ratio and reaches values close to yield strength for tapering ratio of 0.1. In figure 1.50 we also considered a negative tapering (fillet) because it has been suggested by Norte et al [93] that a fillet clamping can lead to an increase of the quality factor. Figure 1.50.c shows the Q spectrum for the three illustrated situations. Red data points correspond to the positive tapering scenario where the enhancement of Q is observed. Compare to the blue
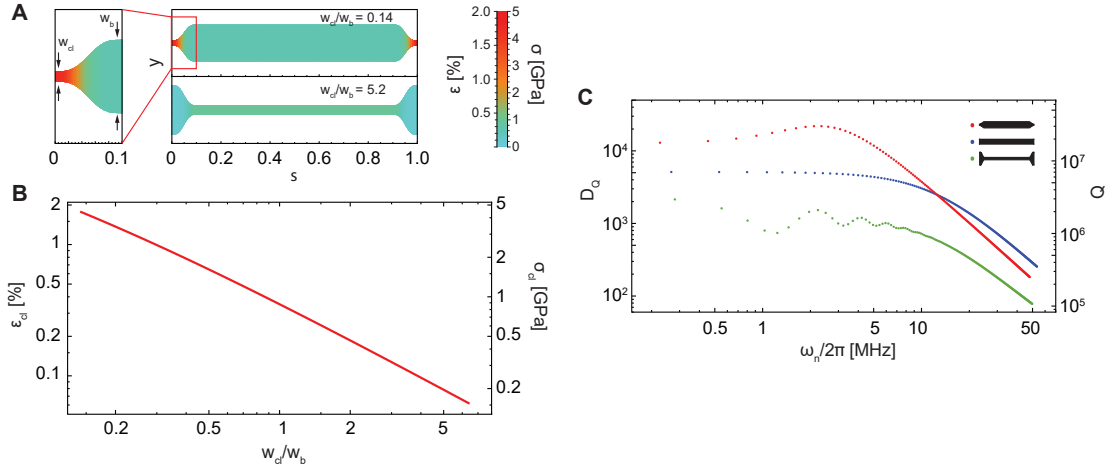
Figure 1.50 – **Dissipation dilution for a tapered clamped resonator** (A) geometry and color-coded strain distribution in beams with thin (top) and thick (bottom) clampings. (B) Variation of the strain in the clamping region as a function of clamp width w_{cl} relative to the beam center w_{b}. (C) Dissipation dilutions and quality factors of modes of a thin-clamp beam (red), a uniform rectangular beam (blue) and a thick-clamp beam (green). Here $l = 1$ mm, $h = 20$ nm.

data points (regular uniform beam), we see a factor of 2 enhancement for the fundamental mode and in the difference rises to the factor of 4 for the optimum higher order mode. However, for very high order modes (soft clamping limit) the Q of the tapered-clamped beams falls below the uniform beams. This is because the average stress in tapered beams is lower than of the stress in uniform beams as discussed in equation (1.51). The Q factor of the fillet beams sees a reduction for all the modes of a beam. This reduction is not only because we reduce the stress at the clamping point which lead to more losses (less dilution) at the clamping point, but also we reduce the average stress for the rest of higher order modes. Therefore, our finding is in the exact contradiction with the claim by Norte et al [93] for trampoline shape resonators.

In the next step, we put this idea to the test. For this purpose, we choose an *arcTan* shape for our tapering (see figure 1.49). This is because with arcTan function, we can independently control the length, the width and the slope of the tapering region. In our simulations, we realized that the optimum length of the tapering length is $\frac{L_{\mathrm{tran}}}{l_{\mathrm{tot}}} \approx 1\%$. Tapering length larger than this, will reduce the average stress and does not benefit the clamping losses. Also if the tapering length is smaller than 1%, our high stress region becomes smaller than the sharp curvature near the clamping, thus our method won't be efficient. In regards to the slope, if the slope is large (mean a sharp transition from wide to narrow region), then due to stress relaxation, we observe a buckling at there corners which leads to lower quality factors. Therefore, in this experiments we choose a very smooth tapering (in our simulations, we did not observe a significant difference when the slope is lower than 1 in normalized unit, s).

For this experiments, samples are fabricated on a chip where $\frac{w_{\mathrm{clamp}}}{w_{\mathrm{total}}}$ is swept from 10 to 0.05 in 80 steps using the $w(x) \propto \arctan(x)$ for two different lengths (L = 250μm, 150μm). This allows
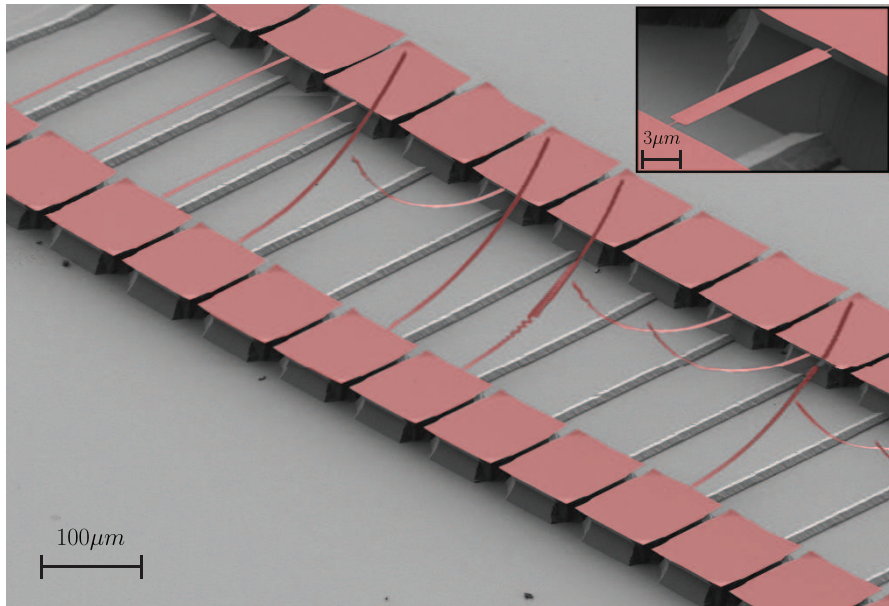
Figure 1.51 – **Yield stress breaking of** Si_3N_4 **nanobeams.** Fabricated devices start to break after reaching the clamp to beam width ratio of 0.16 which corresponds to 6.3 GPa stress. Inset shows a false colored image of a device with tapered geometry. Apparent wave pattern on some of the beams is due to excitation of cantilever modes during electron microscope imaging.

us to access to stress from 90 MPa to 19 GPa. Many samples with $\sigma_{cl} > \sigma_{yield}$ will break at their clamping point. In fact, another purpose of this experiment is to experimentally determine the yield stress of the material. Figure 1.51 shows the SEM of the fabricated tapered beams. For both lengths it is observed that after reaching $\frac{w_{clamp}}{w_{total}} \geq 0.16$ which corresponds to $\sigma_{clamp} \geq 6.3$ GPa, no working device was survived and it is shown in figure 1.51 that all the devices break after reaching this point (corresponding to the bent beams after beam number 3 from the top). Based on this observation, we use $\sigma \sim 6$ GPa to calculate the forbidden region for the figures in the previous section.

In the next step we measured the frequency and Q of the tapered beam. Frequency and quality factor of the devices are measured using lensed-fiber-based homodyne interferometer at $\lambda = 780$ nm . Frequencies are determined by measuring the thermal Brownian motion of the nanobeams. Measurements are performed in a high vacuum chamber (P = 10^{-8} mbar) to avoid gas damping of the modes. The Q factors are determined using ringdown spectroscopy. Mechanical modes are driven using a piezoelectric slab attached to the bottom of the chip holder on which samples are clamped. The piezoelectric slab is driven using UHF lock-in amplifier [Zurich Instrument] with a frequency swept tone to drive a desired mode on resonance and measuring the ringdown. Figure 1.52 shows the measured frequency of tapered beam as a function of the tapering ratio. We observe that the quality factor of these beams follow the predicted trend from the theory where frequency reduces as we tinning down the clamps.
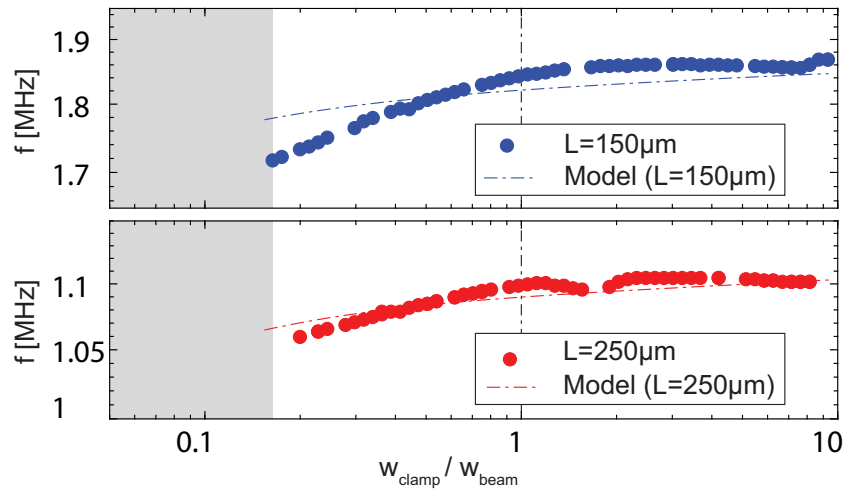
Figure 1.52 – **Frequency of the fundamental out of plane mode for different clamping widths.** Frequency of fundamental out of plane mode for a 150 μm (blue dots), 250 μm (red dots) with theoretical model fit in dashed lines for 150 μm (blue) and 250 μm (red). The vertical black dashed line indicates the normal beam geometry ($\frac{w_{\text{clamp}}}{w_{\text{beam}}} = 1$).
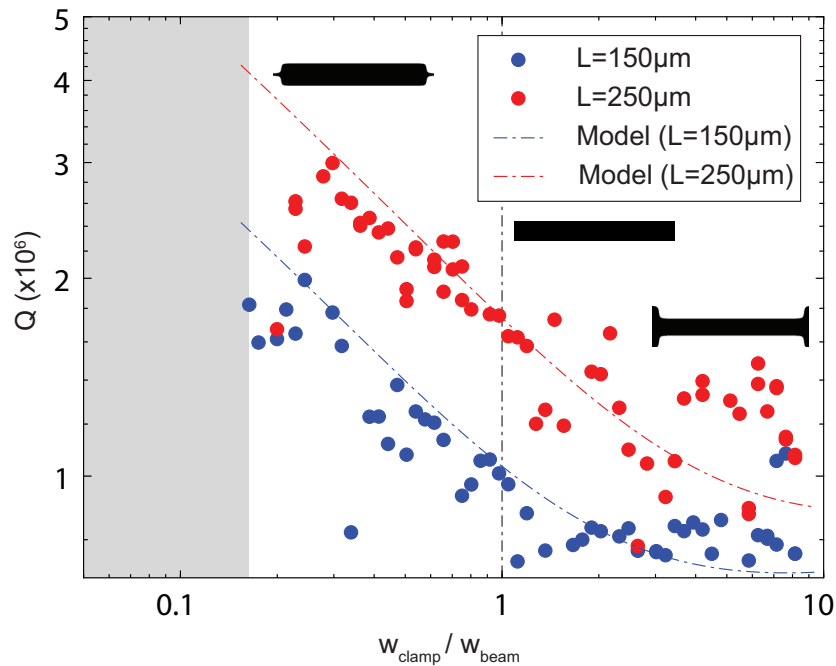
Figure 1.53 – **Quality factor for different clamping widths.** Quality factors of fundamental out-of-plane mode for a 150 μm (blue dots), 250 μm (red dots) with theoretical model fit in dashed lines for 150 μm (blue) and 250 μm (red). The vertical black dashed line indicates the normal beam geometry ($\frac{w_{\text{clamp}}}{w_{\text{beam}}} = 1$). Gray region corresponds to stresses above the yield strength. Schematic beam geometries are plotted in black for tapering, normal and filleting designs.

However, the interesting observation is the Q measurements illustrated in figure 1.53. We observe a geometric enhancement of the Q factor by changing from a fillet design to a tapered clamping geometry. The experimental data in Figure 1.53 and 1.52 are whithin 10% agreement with the fit using semi-analytic model for the solutions of Euler-Bernouli equations with the deposition stress assumed to be 1.1 GPa. We believe similar mechanism was responsible for high $Q \times f$ in the previous design of tuning fork resonators [117]. It has been observed that a tuning fork design with neck has higher Q factor compared to a uniform beam. In this design, necking geometry is essentially equal to tapering of the clamping point. This increases the stress at the clamps and results in enhancement of the Q factor which supports our results shown in Figure 1.53.

In conclusion we showed a technique to enhance the quality factor of the fundamental and lower order modes for Si_3N_4 nanobeams by geometric tapering its clamping points which allow us to enhance the quality factor by $\sqrt{\frac{\epsilon_{yield}}{\epsilon_{avg}}}$ depending on the deposition and yield stress of the thin film. Enhancement of the fundamental mode quality factor by even a factor of 2.5 is of great interest for optomechanical systems. Since this method can be applied to short beam lengths, it has been used for relatively easy integration with optical microcavities [123]. Finally, by varying the taper width, we are able to estimate the yield stress of Si_3N_4 at about 6.3 GPa.

1.6 Acoustic radiation losses at VHF and UHF frequencies and PnC shield[18]

In last few sections we focused on studying the internal material losses of high stress materials. These losses coming from the intrinsic friction force between different nano-scale pieces of the materials and although we did not present a model to describe the micro-physics these sort of losses, we phenomenologically model it by the imaginary parts of Young's modulus. Then we observe the existence of initial stress in the material together with the concept of geometrical non-linearity in deformation, give rise to boost of the mechanical quality factor for few specific more flavors such as flexural modes. A process know as dissipation dilution. Then in the next step we developed a theoretical model to analytically calculate dissipation dilution for any arbitrary geometry. Based on our modeling of dissipation dilution, we studied four strategies to enhance the quality factor and $Q \times$ freqeuncy product via I) optimum mode order of a long uniform beam. II) soft clamping by using and PnC to reduce the effect of clamping losses III) strained enhanced localized mode technique in which in a non-uniform tapered PnC design we localized the region of high stress and the mode shape to achieve record-breaking quality factors IV) and finally tapered clamped beams where stress engineering techniques were directly used to reduce the clamping losses. In this section, we would like to switch our attention to a completely different source of losses and the means to reduce it. Although this new channel of loss seems at the beginning to be unrelated to the story of this chapter, the methods that we use to fight it, have very close similarities with the soft clamping approach.

---

[18]The content of this section is published at [101]

Beside, studying the losses in high frequency mechanical oscillators have a also a practical use. I) mechanical frequencies studied in previous section are all below 10 MHz. Although they offer extremely high quality factors their frequencies are typically below 10 MHz. On the other hand the optical micro cavities such as optical micro disk cavities [165][166][123] and photonic crystal defect cavities [167][168] have optical linewidth of 100s of MHz, we have to work with VHF-UHF mechanical frequencies [169] if we are interested in creating a resolved side band optomechanical system [9] with these mechanical resonators and access to resolved side band toolbox [170][171][172]. On the other hand, going toward higher frequency oscillator means lower masses which is advantages for applications such as mass [173], charge [4] and force [174] sensing applications.

For the mechanical frequencies in the mid range frequencies (MF and HF range) from few 100s of KHz to 10s of MHz, we have observed that the internal losses are dominant. The internal model predicts that for high frequencies mechanical resonators where the aspect ratio becomes very small, dissipation dilution approach to 0 and Therefore, the internal losses asymptote to a constant given by intrinsic quality factor of the material, $Q_{\text{int}} = \frac{E_{\text{real}}}{E_{\text{img}}}$. In sections 1.1 and 1.2 we argued that a major assumption behind all of our analysis is that $E_{\text{real}}, E_{\text{img}}$ are frequency independent constants (or at least they are extremely weak functions of frequency). This assumption seems to hold for many experiments performed by us and many researchers in the past 50 years of research in the field of high Q mechanical resonators. Although or expectation from internal model is that the Q factor asymptote to a constat number, many researchers have repeatedly observed that the quality factor deviates from this model and reduces at VHF and UHF frequencies [175] [176][177][140][178].

Such a deviation from the internal loss model drives the scientist to propose a new channel of loss which is particular dominant at very high frequencies: acoustic radiation losses [179][77][180][181][182][183]. A form of phonon tunneling in to the substrate. According to this picture, at very high frequencies. the mechanical wavelength become so small that is comparable to the size of our system and we cannot use the lumped model approximation. In this regime, the object surrounding the mechanical resonator (pillars, anchors and the substrate) are no longer solid objects that every part of the system modes with the same phase. In another word, so far in our calculation we assume a boundary condition of $u(x = 0, l) = 0$, $u'(x = 0, l) = 0$ for our mechanical oscillators. However, in reality this just an approximation valid for low frequency modes. At high frequencies, However, we have to rely on wave picture and impedance mismatch. In the wave picture to the mechanical oscillators, the energy confinement in an string is due to its impedance-mismatch between the beam and the clamping pads. At low frequencies, since the acoustic wavelength is much larger than the lateral dimensions of the beam, the confinement is near ideal and reflection at the clamping are near 100%. However, as we increase the frequency of the system and the acoustic wavelength becomes comparable with the lateral dimensions of the oscillator (namely the width and thickness for rectangular cross section). This leads to reduction of the impedance mismatch and leaking of the energy into the substrate.
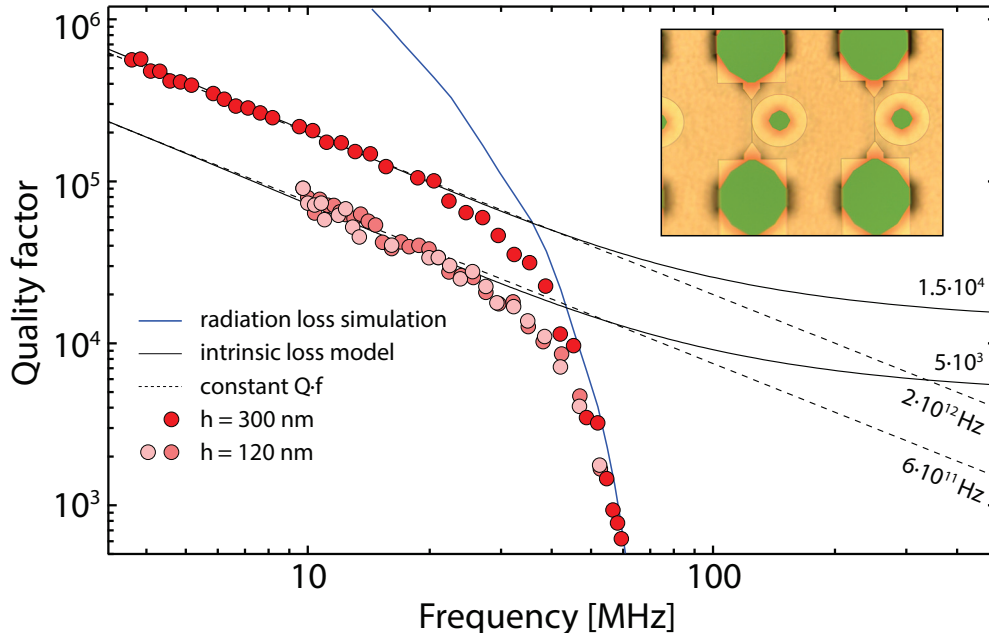
Figure 1.54 – **Quality factor of nanobeams for beam length sweep**. Q versus f for the fundamental mode of nanobeams of various lengths ($L \approx 5 - 1000\,\mu$m). Solid black lines are a single parameter fit to the internal loss model in (1.70), using Q_{int} as the fit parameter. Dashed black lines indicate constant $Q \cdot f$. The solid blue line is an FEM simulation of radiation loss for the unshielded beams. The inset shows a sample chip containing a typical set of devices with different beam length, in this case without a PnC.

In order to investigate such a scaling, we fabricate and measured mechanical oscillators with decreasing length in an attempt to observe a deviation from the internal loss model. Inset of 1.54 shows an array of such resonators. In this section we follow the path we present in figure 1.16 and will use optical micro disk cavities as our displacement sensor in contrast to lensed fiber reflectometry used to measured UHQ resonators in the previous section because will need better sensitivity for the measurements in this section compared to the last sections. We believe it is useful to the scope of this thesis to understand why it is more difficult to make measurements at higher frequencies. First complication in regard with high frequencies, is the driving the mechanical oscillator becomes increasingly more difficult. On fact, in our system with a thin piezo drive glued under the chip holder, we could not drive the resonances above 20 MHz. This is because, in high frequency, we have look at the wave picture again. In VHF-UHF frequencies, driving a piezo does not mean that the chip is going up and down in phase with the drive (as it is the case for low frequencies). But instead we have to consider the piezo driving the as lunching ultra-sonic VHF mechanical waves into the system. As we move to higher frequencies and the acoustic wavelength reduces, leakage of these modes to the other part of the system (sample holder, nano-positioners, the chamber and optical table and etc.) increase as transferring energy to mechanical resonator become less and less efficient. n order to drive a mechanical oscillator at VHF and UHF frequencies, the actuator (whether in the form of piezo [184][185] or electro-static [186] drive) has to be fabricated next

to the resonator due to added complication that these methods would have on the Q of the resonator, we avoid this path. If we want to study the pure isolated mechanical oscillator, the other option is to work with its thermo mechanical Brownian motion (on the other word, we use the broad band thermal random force for our drive). Here we will show that the thermo-mechanical signal reduces in an accelerative rate as we go to higher frequencies. In a cavity based optomechanical displacement detection scheme, the power spectral density of frequency fluctuations induced by thermal motion of the mechanical oscillator is given by [9]:

$$S_{\Omega\Omega}^{\text{th}}(\Omega) = n_{\text{th}} g_0^2 \mathcal{L}(\Omega - \Omega_m, \Gamma_m) \tag{1.136}$$
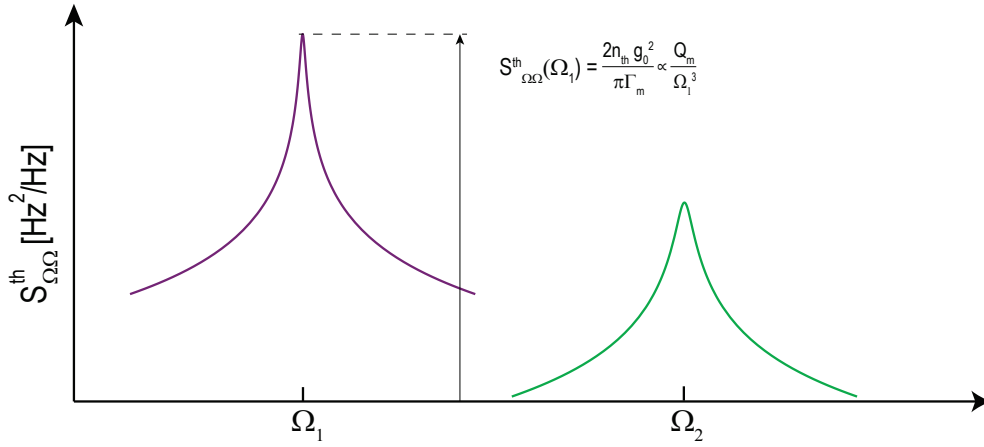
Figure 1.55 – Lorentzian lineshape of the power spectral density of the thermo-mechanically induced frequency fluctuation in the optical cavity. The peak of the Brownian motion in unit of frequency fluctuations Hz^2/Hz is calculated to be $S_{\Omega\Omega}^{\text{th}}(\Omega_m) = \frac{2n_{\text{th}} g_0^2}{pi\Gamma_m}$ [9].

where $n_{\text{th}} = \frac{k_B T}{\hbar\Omega}$ is the average thermal phonon occupation, g_0 is the optomechanical vacuum coupling rate and $\mathcal{L}(\Omega, \Gamma)$ is the Lorentzian function defined in (A.I.29). The vacuum coupling rate [9] is given by $g_0 = G\sqrt{\frac{1}{2m_{\text{eff}}\Omega_m}}$ where G is the frequency pulling factor of the mechanical oscillator. For the simplicity, we assume G is a frequency indipendent parameter and is purely a function of the distance between an optical disk and the mechanical resonator [122]. For the 1D mechanical oscillators, the mass is a linear function of the oscillator's length and therefore inverse function of its frequency. In Summary, the peak of the thermo-mechanical signal in the units of cavity frequency fluctuations is given by:

$$\left. \begin{aligned} g_0^2 &\propto \frac{1}{m_{\text{eff}}\Omega} \\ L(0, \Gamma_m) &= \frac{2Q}{\pi\Omega_m} \\ n_{\text{th}} &= \frac{k_B T}{\hbar\Omega} \end{aligned} \right\} \implies S_{\Omega\Omega}^{\text{th}}(\Omega_m) \propto \frac{Q}{\Omega_m^3} \tag{1.137}$$

Equation 1.137 illustrate why making measurement at higher frequencies becomes accelera-

tively more difficult. If we assume we are in the regime where quality factor is fixed, the peak of the signal reduces 30 dB per decade. In reality the signal scales even faster than this rate. This because for high stress doubly clamped uniform beams. at the beginning, due to dissipation dilution we are in the regime that $Q \propto \frac{1}{\Omega}$ (see equation (1.103)) which means we lose the signal with $S^{\text{th}}_{\Omega\Omega}(\Omega_m) \propto \frac{1}{\Omega_m^4}$ or 40dB per decade. In the other word, making measurements at 200 MHz for example is 8 orders of magnitude more difficult than it is at 2 MHz. We realized that our fiber interferometer is not sensitive enough to resolve such a weak signal. Towards this end, we employ a microcavity-based near-field sensor [122] capable of non-invasive thermal noise measurements with $\text{fm}/\sqrt{\text{Hz}}$ resolution and provide the sensitivity required to make these measurements. In this regard, in this study, we consider only in-plane flexural modes because of their compatibility with displacement readout (using an in-plane microcavity-based sensor shown in blue in figure 1.54).

To probe mechanical displacement, an elliptical microdisk cavity is patterned next to each beam, separated by ~ 80 nm. Whispering gallery modes of the microdisk are excited with a detuned 1550 nm laser field using a tapered optical fiber, enabling evanescent displacement readout [122] with an imprecision of ~ 1 $\text{fm}/\sqrt{\text{Hz}}$. All measurements were performed in a vacuum chamber at 10^{-4} mbar (as these higher frequencies and lower Q, we do not need a UHV pressure) in order to reduce gas damping. In conjunction with the relatively large cavity linewidth of ~ 1 GHz (mitigating radiation pressure effects), this enables non-invasive thermal noise measurements for beams as short as 4 μm with frequency as high as 207 MHz.

Coming back to the Q measurement illustrated in figure 1.54 we have made a comprehensive study of Q vs f for unshielded beams (red data points) of various lengths, using thermal noise measurements. These results correspond to unshielded uniform beams with lengths of $10.5 - 90.5$ μm, comprising a total of 121 independent devices. The back solid lines correspond the dissipation dilution model from equation (1.70). At low frequencies, it seems to be an excellent agreement between the measurement and the dissipation dilution model. The most striking feature in figure 1.54 is a sharp transition at $f_0 \sim 50$ MHz, corresponding to $L \sim 10$ μm, at which the Q of unshielded beams changes from $Q \propto f^{-1}$ to a $Q \propto e^{-\alpha(f-f_0)}$. Such a sharp deviation is an indication that a new channel of loss is activated at these frequencies.

To confirm that the deviation from the internal loss model in Figure 1.54 is indeed due to acoustic radiation, we have conducted a no-free-parameter finite element simulation using COMSOL [187] where the geometry of the beam and PnC are determined from SEM imaging and used in the finite element simulation (blue solid line in figure 1.54). Although there haves been several attempts in the past to find an analytical model for radiation losses [179][77], in these models many assumption and geometrical simplification had to be taken into account which at the end makes these analytical models useless for our geometry. Due to complexity of the wave nature of the radiation losses and different reflection from complex surfaces, we believe finite element simulation using perfectly matched layers (PML) is the best approach to model radiation losses [188][189][190][182].
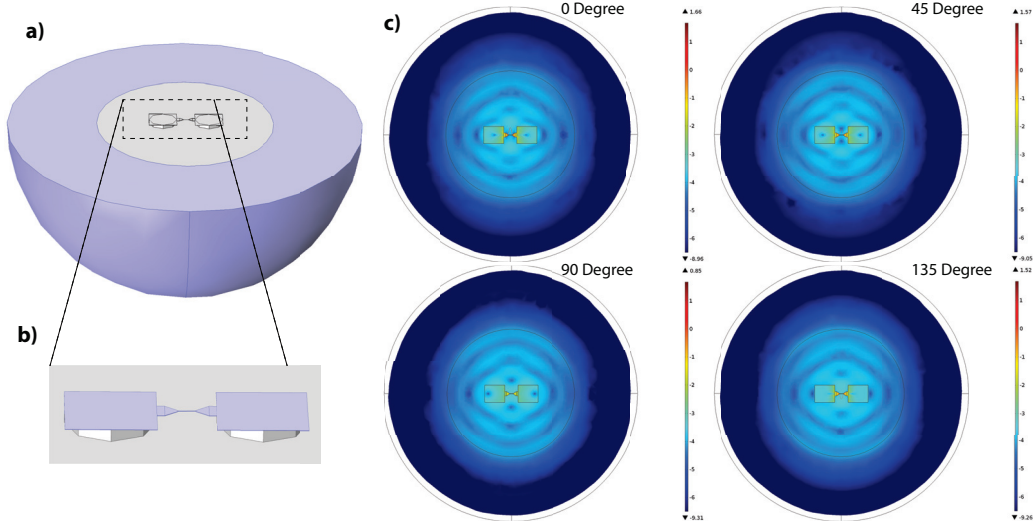
Figure 1.56 – **FEM simulation of radiation loss.** (a) Geometry of the simulated device. The gray volume indicates the mechanical structure and the blue volume is a PML. (b) Magnified image of the mechanical structure, including the SiN beam and PnC shield, SiN support pads, Si pillars beneath the support pads, and a portion of the underlying Si substrate. A stress relaxation simulation is performed in order to determine the stress profile of this structure before solving for eigenmodes. (c) Visualization of acoustic waves propagating into the Si substrate and being absorbed by PML. The amplitude of the mechanical strain field is illustrated by logarithmic color-coding.

The radiation loss model ((blue solid line in figure 1.54)) was obtained by computing the complex eigenfrequency spectrum of the mechanical structure surrounded by numerically implemented PML (perfectly matched layer, corresponding to a perfectly impedance matched and absorbing boundary). We used the COMSOL Structural Mechanics Finite Element Analysis software package for this simulation. The modeled structure is shown in gray in figure 1.56.a, and includes the SiN defect beam, SiN support pads, the Si pillars beneath the pads, a half-spherical transect of the Si substrate and finally the blue shell in figure 1.56.a corresponds to the PML layer. By placing the PML far from the nanobeam, we ensure that reflection of acoustic waves from the supports is accounted for in the simulation. We also ensure that the size of the PML is large enough that its own reflection coefficient is negligible. Visualization of acoustic radiation into the PML is shown in figure 1.56.c. Radiation loss manifests as an imaginary component of each numerically computed eigenfrequency, Ω_{m}. The eigenfrequency of the defect mode is identified based on its mode shape. Radiation-loss-limited Q-factors (blue curve in figure 1.54) are obtained from the formula:

$$Q_{\mathrm{rad}} = \frac{\mathrm{Re}[\Omega_{\mathrm{m}}]}{2 \cdot \mathrm{Im}[\Omega_{\mathrm{m}}]}. \tag{1.138}$$

The location of the knee point in the model of Q_{rad} versus f in figure 1.54 depends on the dimensions of the extended mechanical structure, in particular that of Si pillars and the

clamping structures and shape of the pads. The blue curve shown in figure 4 of the main text employs dimensions obtained from SEM imaging and uses no fit parameters. Amazingly our free-fitting-parameter FEM model for radiation losses has an excellent agreement with the measured Q factors in figure 1.54.
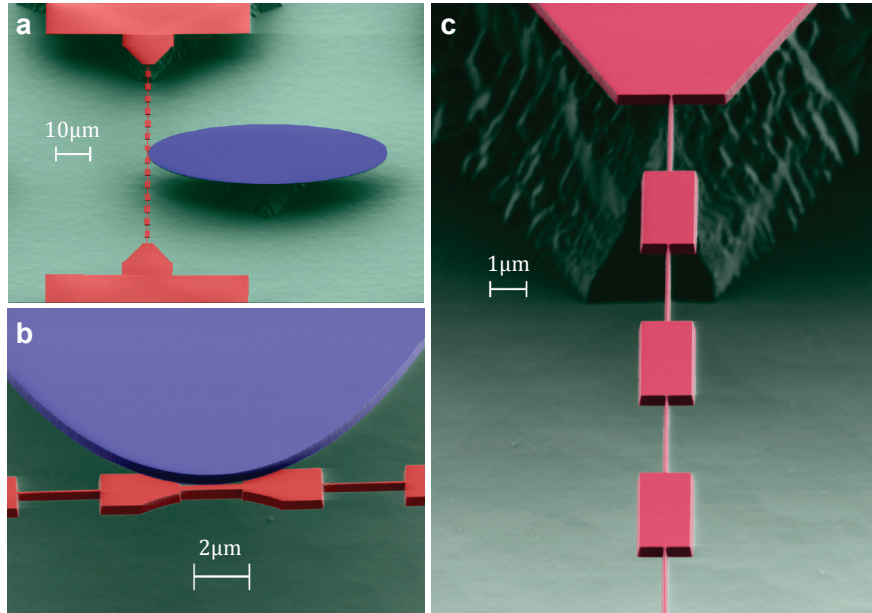
Figure 1.57 – **A nanobeam embedded in a 1D phononic crystal**. SEM images of the device. False-coloring is used to distinguish the Si substrate (green), the micro-patterned SiN nanobeam (red) and a SiN microdisk (blue). The microdisk is used to optically probe the beam's displacement [122].

Having established the effect of radiation losses for mechanical frequencies above 50 MHz, the next question is how to shied our resonators against this type of losses. It has been suggested by many groups that a phononic crystal shield can significantly improve the quality factor of the mechanical resonators in VHF and UHF frequencies [191][192][193][194][137][136][195][134][175]. In fact, one of to most monumental optomechanical system (phoxonic crystals from the grou pf Dr. Painter) were made possible using 2D PnC shields at 3.6 GHz [167] [196]. To this end we employed 1D phononic crystals in order to shield our resonators against radiation losses. Figure 1.57 shows the SEM image of our corrugated beams. Here a high-stress Si_3N_4 thin film has been patterned into a 1D PnC with a beam-like defect at its center. From the standpoint of the beam, the crystal acts like a radiation shield, the performance of which is determined by the band structure of the box-shaped unit cell. As discussed in the soft-clamped beams, our application of phononic crystals here is different to their use in the soft-clamped beams. In the frequency regime that we are interested to use this shields, the dissipation dilution is negligible and Therefore, the curvature of the modes shape is not important. However, the shielding efficiency (reflection from each unitcell) of these PnCs is determined by the mass ratio of each unitcell. Therefore in this experiment, unlike the soft-clamped beams where $\frac{w_{max}}{w_{min}}$ 2 − 2.3 was used, here the width ratio of 15 is chosen. With this ratio, only few unitcells are
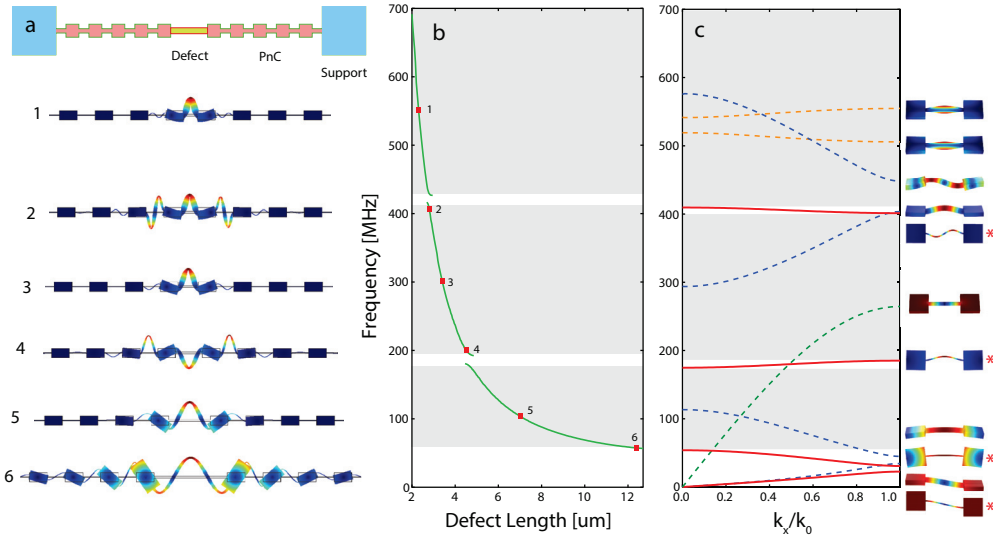
Figure 1.58 – **Simulation of defect modes and the phononic crystal bandgap.** (a) Schematic diagram of the device (top view), consisting of a nanobeam (green) patterned as a defect in a 1D phononic crystal (pink). Unit cell dimensions used in this work are (h_1,L_1)=(100 nm,3 μm) for the short segment and (h_2,L_2)=(1.5 μm,3 μm) for the long segment. The SiN thickness of all devices is 400 nm. (b) Simulated fundamental eigenfrequency of a defect beam with in-plane thickness $h = 100$ nm and length $L = 2 - 16\,\mu$m. Gray regions indicate bandgaps for in-plane flexural modes. Six representative modes are highlighted; their FEM-simulated modeshapes are plotted on the left. (c) Dispersion diagram of the phononic crystal. Curves represent different modes of the unit cell, color-coded according to symmetry (red, blue, green, and orange correspond to in-plane, out-of-plane, breathing, and torsional modes, respectively). Gray regions correspond to pseudo-bandgaps for in-plane modes.

required to stop the ration losses of the defect resonator.

A simulation of the dispersion diagram of the unit cell is shown in figure 1.58.c, with lines of different color corresponding to modes of the cell with different symmetries. In this work, we consider only in-plane flexural modes because of their compatibility with displacement readout (using the microcavity-based sensor shown in blue in figure 1.57). Pseudo-bandgaps for in-plane symmetry are indicated by gray shading in figure 1.58c. The presence of a bandgap implies strong reflection of waves from the PnC. It also implies the support of localized defect modes. To illustrate this concept, a simulation of the fundamental flexural mode of a beam embedded in a 14-element PnC is shown in figure 1.58b. Dimensions of the beam and unit cell are given in the caption. The beam's length is varied to span the frequency range of the three bandgaps shown in figure 1.58c. Qualitatively, it is evident that modes which are well-centered in a bandgap (1,3,5) exhibit strong confinement. Conversely, modes near the edge of a bandgap (2,4,6) penetrate deeply into the PnC. This is because the defect modes start to hybridize with the in-plane modes of the unit cell, shown as red curves in figure 1.58c. Our central claim is that localized defect modes will exhibit reduced radiation loss and similar effective mass relative to unshielded beams.
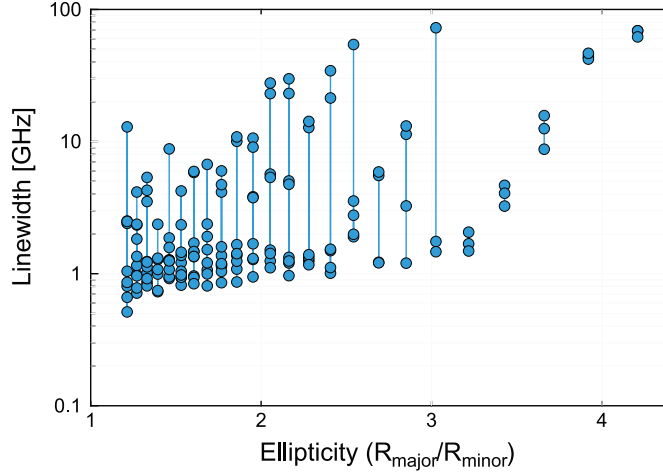
Figure 1.59 – **Optical Q of the elliptical microdisk cavities.** Measured WGM linewidth for microdisks with a fixed circumference of 31 μm and ellipticity (ratio of the major and minor radii) varying from 1 to 4. WGMs of different polarization and radial order were measured, giving rise observed variation in optical loss for each ellipticity.

Before we present the experimental results in regard with the shielded nano-beams, it is worth mentioning that due to small form factors of these defect nano-beams ($L_{\text{defect}} = 12.2 - 4.1 \ \mu$m), we had to use elliptical micro disks in order to fit to the small dimensions of our resonator and achieve closes proximity needed to create a ~ KHz g_0 needed to make measurements at VHF frequencies. For this purpose a new amorphous silicon hard-mask process follow was developed and optimized with two goals in mind: (1) to minimize the in-plane gap (x_{gap}) between the nanobeam and the microdisk and (2) to minimize the sidewall roughness of the microdisk. Small x_{gap} is desirable as it gives rise to a large parametric (optomechanical) coupling G. We also realized that the optical quality factor of the elliptical disks are a function of their ellipticity. This is illustrated in our measurements of optical quality in factor in figure 1.59. We discovered for ellipticity ratio larger than 3, the optical linewidth exponentially increases due to share bending curvature at the two ends of the ellipse where the Si_3N_4 refractive index is not large enough to confine optical light in such a sharp bending.

The next step is the measurement of these PnC beams. As a demonstration of spatial mode confinement, the thermal displacement noise spectrum of a 5 μm-long defect embedded in a 100 μm-long, 14-cell PnC is presented in figure 1.60. The fundamental in-plane mode of the defect appears at 74 MHz, situated within a large, spectrally quiet window coinciding with the pseudo-bandgap of the PnC. The small effective mass of the defect mode manifests in the relatively large area beneath the thermal noise peak $\langle x^2 \rangle \approx k_B T / (4 m \pi^2 f^2)$. Comparing $(\langle x^2 \rangle f^2)^{-1}$ for the defect mode to that of adjacent peaks (green points) reveals a 1000-fold decrease in m relative to the fundamental in-plane mode of the extended structure. Quantitative agreement of this scaling with an FEM simulation (red points, assuming a point-like probed at the mid-point of the defect) corroborates an estimated effective mass of $m = 0.3$ pg for the localized mode. The corresponding fitted mechanical linewidth is $\gamma / 2\pi = 5.1$ kHz ($Q \equiv f/\gamma = 1.4 \cdot 10^4$),
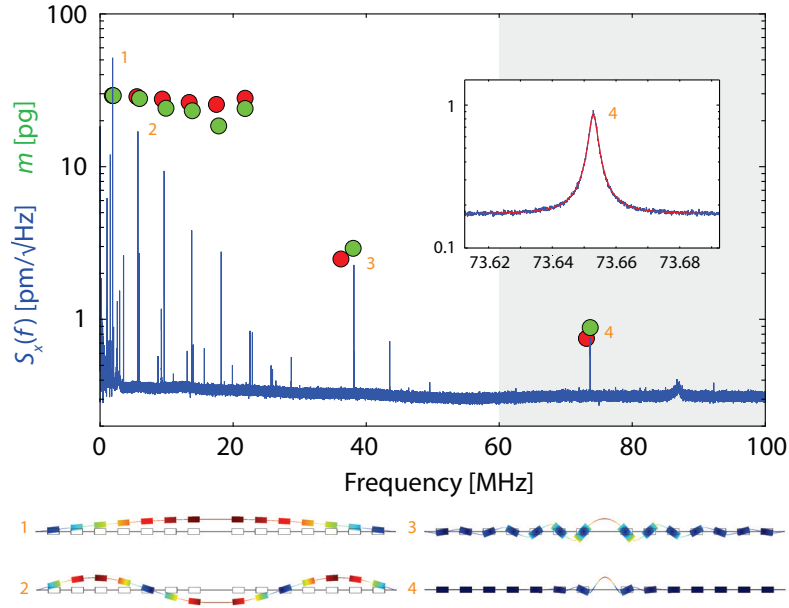
Figure 1.60 – **Broadband displacement spectrum of a PnC-shielded nanobeam**. A beam length of 8.25 μm is shown. FEM-simulations of four representative mode shapes are plotted below. Green points above selected peaks indicate the inferred effective mass. Red points are obtained from an FEM model. The absolute magnitude of the displacement spectrum and the effective mass is estimated by bootstrapping the latter to an FEM model (red points) of the effective mass for mode #1. Shaded regions correspond to the PnC bandgaps in figure 1.58. Inset: Magnified displacement spectrum of the localized (defect) mode, fitted to a Lorentzian.

giving access to a low thermal-noise-limited force sensitivity of $8\pi k_B T m\gamma = (0.38\,\mathrm{fN}/\sqrt{\mathrm{Hz}})^2$. This value is within a factor of 10 of state-of-the-art VHF nanomechanical oscillators at room temperature [176].

The results of the Q measurement of the localized shielded mode are presented as the grren data points in figure 1.61. Remarkably, the Q of shielded beams (green points) recovers to the expected internal loss scaling for $f \sim 50 - 200$ MHz ($L \sim 4 - 12\,\mu$m), suggesting that with this technique we suppressed the radiation losses.

In summery, in this section we present an alternative channel for the mechanical losses which in contrast to material losses is dominant at higher frequencies. Then we experimentally studied the scaling law of the dissipation dilution theorem where we observe a sharp deviation for frequencies above 50-100 MHz corresponding to length of $l_{\mathrm{beam}} < 10\mu$m. We observe such a deviation follows the predictions of a finite element model for acoustic radiation. In the last part of this section, we observe that by encapsulating the resonator at the center of a phononic crystal shield, we can stop the radiations and recover the quality factor to the level expected from internal material losses. In this study we unambiguously the effects of radiation losses. Our shielding method could be used as a platform for ultra small mass-high Q resonators operating in VHF-UHF regime.
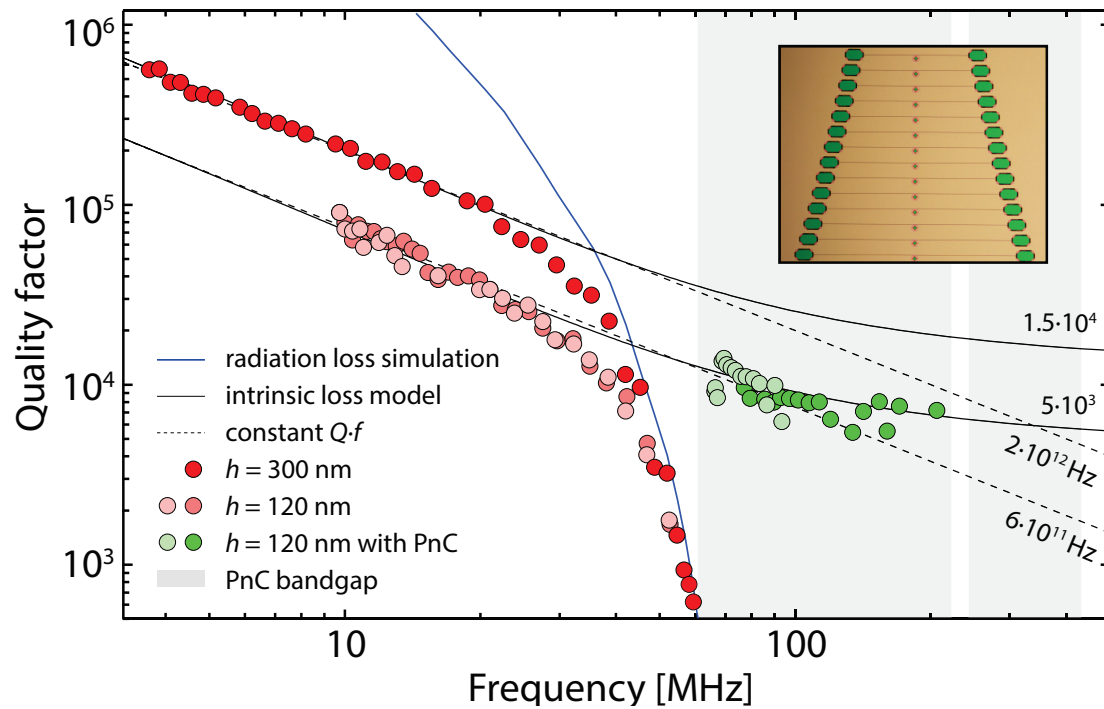
Figure 1.61 – **Quality factor of nanobeams with and without PnC shield**. Q versus f for the fundamental mode of nanobeams of various lengths ($L \approx 5 - 1000\,\mu$m). Green (red) points correspond to beams with (without) a PnC shield. Solid black lines are a single parameter fit to the internal loss model in (1.70), using Q_{int} as the fit parameter. Dashed black lines indicate constant $Q \cdot f$. The solid blue line is an FEM simulation of radiation loss for the unshielded beams. Shaded regions correspond to the PnC bandgaps in figure 1.58. The inset shows a sample chip containing a typical set of devices with different beam length, in this case without a PnC.

2 Fabrication

Indeed there is plenty of the room when we enter the wonders of nano-world. The "room" that Feynman had envisioned is much bigger than just ability to fit more transistors into an smaller area. Of course, the main the driving force behind success of the nano-technology and micro-electronics of the past 40 years was to shrink the size of the transistors where could fit more of them into an small area an achieve higher computational performance. But beyond the mundane geometric scaling, going smaller bring new physical phenomena and possibilities into the games. One these "new kinds of effects" is the fact that "smaller is stronger"[198]. Generally the stiffness of mechanical object increases as we scale down the size. This means miniaturized delicate mechanical oscillator can be used in our daily life as building block of our smartphones and other consumer electronic devices without the risk of breaking under even large shock forces such as falling on the ground. In addition, "smaller is stronger" also means that nanomaterials can experience much larger stress than a traditional material [145]. This become a key for engineering mechanical oscillators with unprecedented quality factor as we show in chapter 1. In the previous chapter we experimentally observed that a 20 nm thick Si_3N_4 can systematically experience up to $\varepsilon_{yield} \approx 2.5\%$ strain before it reaches the unset of fracturing. In comparison, traditional macroscopic materials usually cannot sustain tensile strain exceeding $0.2 - 0.3\%$ before inelastic relaxations (fracture for example) sets in. [145]

Another important consequence of working at micro/nano scale is the ability to engineer extremely high aspect ratios. In chapter 1 we studied the dissipation mechanism in high Q mechanical oscillators. We observed that through a pure geometrical process known as

dissipation dilution [199], the quality factor of mechanical oscillators under tensile stress experience an enhancement compare to their intrinsic quality factor. We then studied different aspect of dissipation dilution and its scaling laws with the geometry. An important out come of our analysis was the fact that in order to achieve higher quality factors, we have to fabricate higher aspect ratio devices. We show case our method by achieving a quality factor near 1 billion on a $\Omega/2\pi \sim 1\mathrm{MHz}$ Si_3N_4 resonator with thickness of 20 nm and length of 7 mm. This is equivalent of and aspect ratio of $\frac{l}{h} \sim 3.5 \times 10^5$. We have even successfully fabricated devices as long as 10 mm (although the Q factor of these devices were not high due to contamination issue) with equivalent aspect ratio of 3.5×10^5. This a aspect ratio is among the highest man-made object of any size and any type, even compare to high aspect ratio carbon nano-tubes [140]. If we try to scale up this aspect ratio to our humane scales to better understand its implications, a bridge of the size of Golden Gate bridge in San Francisco[200] would have the length of approximately 5000 km to achieve an aspect ratio equivalent of $\sim 5 \times 10^5$. That is roughly the distance between the New York city and London. In addition, such bridge had to be hold with noting but its to ends.

It seems that we can only achieve such an extreme aspect ratio in mico/nano scale and we are unable to achieve it in smaller (atomic scale) or larger (macroscopic scale) dimensions Although we still do not completely understand what fundamentally makes micro/nano scales so unique among all other physical scales, it is probably because in ultra small dimensions (atomic scale for example for carbon nano-tubes), the electromagnetic force are too strong to be reliably controlled. Manipulating dimensions of a suspended nano-structure in atomic scale dimensions becomes an extremely challenging task. In macroscopic scale on the other hand, the elctromagnetic forces cancel out in massive scales and gravity becomes a new challenge. In micro-nano scale however, devices are small enough that gravitational forces are negligible but large enough that we can still control the electromagnetic force. This is combined with unique lithography techniques developed for these scales that allows us to control the dimensions and shapes with an unprecedented precision compare to other scales. Having said that, still making micro mechanical resonators with this aspect ratio is a difficult challenge that required years of process development and experimentation.

In the following section, we review the details of our developed fabrication process to fabricate high aspect ratio devices made from high stress LPCVD Si_3N_4 thin films.

2.1   High level over view of the process flow and its challenges

Figure 2.1 shows a highly condensed process flow we used to fabricate these high aspect ratio beams. Before we start by reviewing the details of the step by step process flow, I believe it is important and useful to first discuss at high level, the logic behind such a specific process flow. The first ingredient we need to have to create dissipation dilution is a high tensile stress material. Although there are number of tensile-stressed crystalline thin films available in the market such as strained silicon [79], strained germanium [80] and strained InGaP [81] , to the

Figure 2.1 – **Schematic of fabrication process flow.** Summary of the main steps of the fabrication process of high aspect ratio Si_3N_4. Layers: Si (gray), Si_3N_4 (orange), HSQ [1]layer (blue) for the main mask, the FOX[2]layer (green) for up-scaled mask.

best of our knowledge none of these materials have been extensively studied as a platform for making ultra high Q mechanical resonators. On other hand, stoichiometric high stress Si_3N_4 since 2006 [78], has been the major driving force behind the success of strained micromechanical oscillators. Although Si_3N_4 is an amorphous material, its standard low pressure chemical vapor deposition (LPCVD) recipe (developed initially for the CMOS industry), offers a reliable and deterministic tensile stress of $\sigma_{film} \approx 1.2$ GPa (or $\varepsilon_{film} \approx 0.5\%$) when deposited on a silicon wafer at ~ 800 °C. Because of its reliability and our previous experience with fabrication of Si_3N_4, it will be our material of choice for this project. As an extra bonus, Si_3N_4 is a low loss dielectric [201][202][203] that can be also used in optical circuits, which is beneficial for future integration of an optomechanical systems[123]. Fixing the thin film material would automatically set the chemistries that we can use for etching and determines majority of our strategy for fabrication. Among the different steps of fabrication summarized in figure 2.1, most challenging for us is the undercut step (step 6 in fig 2.1). So our strategy for fabrication of these resonators is tailored in a way to make sure that we will have a successful release of the structures at the end of the process with as little as possible sample contamination. As we will see, we have to perform few extra steps ahead, to make sure that samples won't collapse during the undercut and drying procedure afterward (steps 4,5 in figure 2.1). For

---

[1]Hydrogen Silsesquioxane
[2]Flowable oxide: an beam resist. It is the non-diluted version of HSQ

Si_3N_4 deposition we have two general options as illustrated in figure 2.2. I) Directly depositing Si_3N_4 layer on silicon or II) deposition Si_3N_4 layer on a SiO_2 buffer layer so we can undercut using HF[3] chemistry.

Left diagram:

| Si_3N_4 |
| Si substrate |

Dry undercut

Process	Selectivity (Si : Si$_3$N$_4$)	Isotropic
XeF$_2$	~100:1	yes
RIE enhanced isotropic SF$_6$	~400:1	yes

wet undercut

Process	Selectivity (Si : Si$_3$N$_4$)	Isotropic
KOH	~∞	No
TMAH	~1000:1	No

Right diagram:

| Si_3N_4 |
| SiO_2 buffer layer |
| Si substrate |

Dry undercut

Process	Selectivity (SiO$_2$: Si$_3$N$_4$)	Isotropic
Vapor HF	~10:1	yes

wet undercut

Process	Selectivity (SiO$_2$: Si$_3$N$_4$)	Isotropic
BHF	~100:1	yes

Figure 2.2 – **Si$_3$N$_4$ deposition strategies and selectivity of different undercut options**. Left: Direct LPCVD disposition on silicon substrate. Dry Si undercut options: XeF$_2$ or SF$_6$. Wet Si undercut options: TMAH[4]or KOH. Right deposition on a buffer oxide layer to use: vapor HF (dry) or BHF[5] (wet) for undercutting. Only KOH has the selectivity required for this project.

Choosing between the options in figure2.2, depends on the selectivity that we need in the undercut process. To determine the selectivity, we need some information about the geometry. In chapter 1 we observe that $Q \propto \frac{1}{h}$ for the localized modes. Therefore to achieve the highest quality factor, we try to work with the thinnest possible Si_3N_4 layer that we can still comfortably fabricate and control. After few experimentation and release tests, we choose $h = 20$ nm for the thickness of our devices. Thickness below 20 nm becomes too fragile to survive the release and drying process (we tested 10 nm samples but achieved disappoint low yields of survival). On the other hand, the width of our tapered localized mode at its thinnest part in the center is 300 nm and increases via a Gaussian envelope to ∼ 5 μm for the largest piece. Measurements of samples below the width of 300 nm with our fiber interferometer becomes challenging as the reflected light off the surface of the beam reduces dramatically. In summary, with our undercut chemistry, we have to be able to etch silicon below a 5μm $\times$ 20 nm Si_3N_4 beam. That means we have to etch stripes with vertical aspect ratio of ∼ 250. The rule of thump for the undercut is to have selectivity at least ∼ 10 − 100 time better than the aspect ratio we are going to release. In this way we consume the underneath substrate without damaging our active layer. Therefore, we have to choose the deposition strategy that will eventually enables us to achieve an etching selectivity better than 1 : 10, 000 between Si_3N_4 : Si in order to successfully release the structures without damaging the nitrite layer. Figure 2.2 shows two deposition strategies, our options for undercut chemistry and our calibrated selectivity. Unfortunately dry undercut chemistries for Si etching(such as SF$_6$[6] or XeF$_2$[7]) or for SiO_2 etching (such as

---

[3]Hydrofluoric Acid
[4]Tetramethylammonium Hydroxide
[5]Buffered Hydrofluoric Acid
[6]Sulfur Hexafluoride
[7]Xenon Difluoride
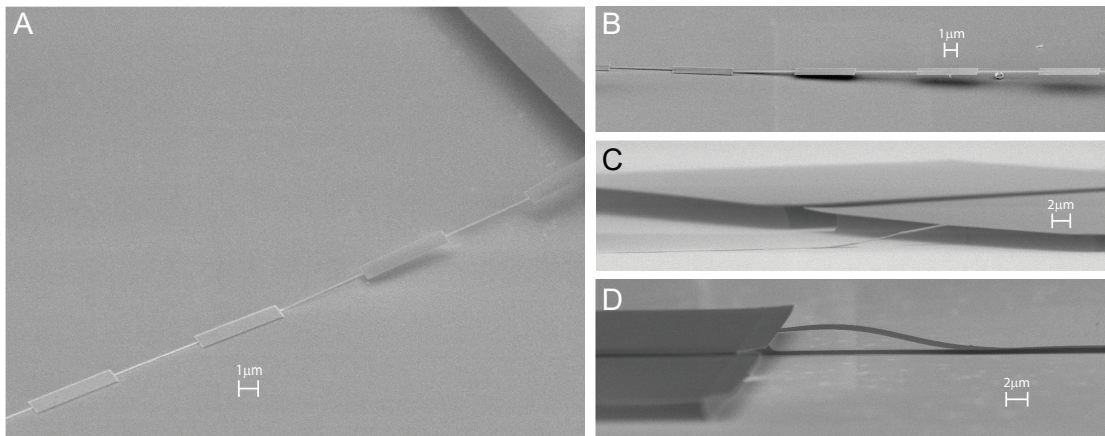
Figure 2.3 – **Examples of SEM images of collapsed Si$_3$N$_4$ beams**. If the CPD is not used (or CPD process does not reach critical point) beams would collapse to the underneath substrate due to the surface tension of the water droplets underneath that pulls the beams down as they evaporate.

vapor HF) are not suitable as they all have selectivity lower that 1 : 1000 and nitride layer will be consumed if any of these techniques are used.

The only reliable solution that is accessible in our fabrication facility is Potassium hydroxide (KOH) solution which has near infinite selectivity between Si$_3$N$_4$ and Si (Silicon etch rate depends on the temperature of the bath, KOH concentration and its density but the etch rate of Si$_3$N$_4$ in KOH bath is so small that is practically unmeasurable!). For example we have tested backside release of 20 nm Si$_3$N$_4$ membranes by etching $\sim 700\mu$m of underlying Si without any measurable thickness change in the nitride layer. For this project we undercut our samples using 40% concentrated (weight concentration) VLSI grade KOH at 60° degree while we maintain the bath density at 1.37. KOH bath. This solves the selectivity issue and allows us to work with the thinnest possible Si$_3$N$_4$ layers, but it comes at cost of few major challenges in the process. In the following we briefly review these challenges that determine many aspect of our process flow:

Drying issue with liquid undercut techniques.

Using a liquid undercut step requires delicate drying procedure especially when dealing with extreme aspect ratios presented in this work. Because of the extreme aspect ratios of our samples, drying in the open air would result in either breaking or collapsing of the structures. Figure 2.3 illustrates SEM[8] image of a few such a collapsed structures. This is due to the strong surface tension of water, while the water droplets under the suspended beam are shrinking due to evaporation, they pull the beams down with them. On the other hand, since our beams are very long and thin at the same time, they are very soft springs that can easily be bent with smallest forces.

---

[8]Scanning electron microscope
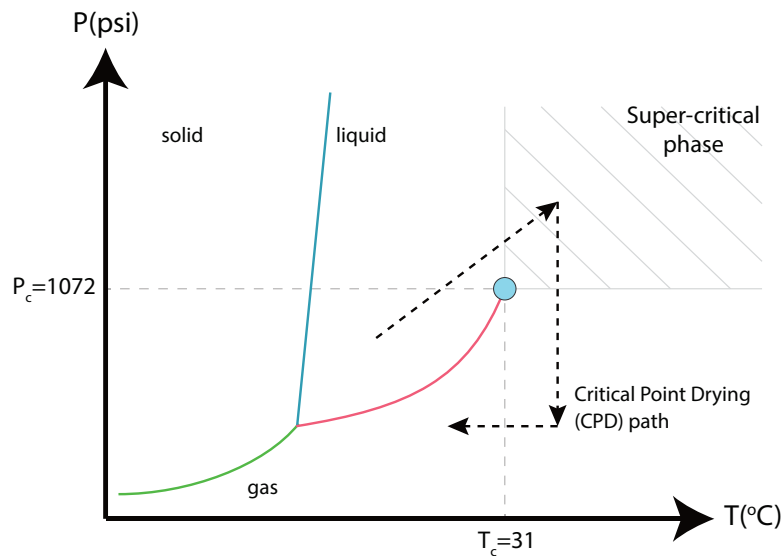
Figure 2.4 – **Schematic plot of critical point drying**. With CPD technique, we dry the samples without passing trough the phase transition surface (red curve) by going around the critical point (cyan circle) though the super-critical phase (hashed region). The path for CPD is illustrated with the dashed lines.

This problem happens at the surface of two the phases (surface of the gas and liquid) and the solution is to avoid going through a phase transition surface. In other words, to dry our objects, we have to bring our samples from water to air without actually going though the surface of the water. Such a seemingly impossible task is done via a process called critical point drying (CPD) [141]. Figure 2.4 illustrates the concept of critical point drying. We avoid the surface transition by going around the critical point (cyan circle) of the material and through the "super-critical phase" [9]. For our purposes, usually the critical point of CO_2 is used as it is a non-polarized molecule with low surface tension. In addition it has relatively low temperature critical point at at T31° degree and P= 1072 psi. The CPD procedure is illustrated in figure 2.4 by dashed lines. First we increase the pressure in a high pressure chamber, then we increase the temperature to go to super-critical phase and slowly vent the chamber at 40° to go back to the gas phase.

It should be emphasized that the liquid undercut and drying process turned out to be the most challenging part of the fabrication process for which we had an extremely low yield at the beginning. However, over time we learned how to carefully handle our samples in liquid and control the CPD parameters and gas flows in order to achieve better than 95% yield at the end. One important consideration is that since the water has the highest surface tension, any water droplets left in the chamber could prevent the system from properly reaching the critical point. Therefore, we used 99% pure VLSI grade ethanol as a intermediate liquid (ethanol has the an

---

[9]In this phase and high pressure and high temperature, the liquid, the evaporation and condensation are happening instantly at the same time at every point of the material. In other words, liquid and gas are converting back and forth at every location. Therefore the gas and liquid are indistinguishable via a border surface.
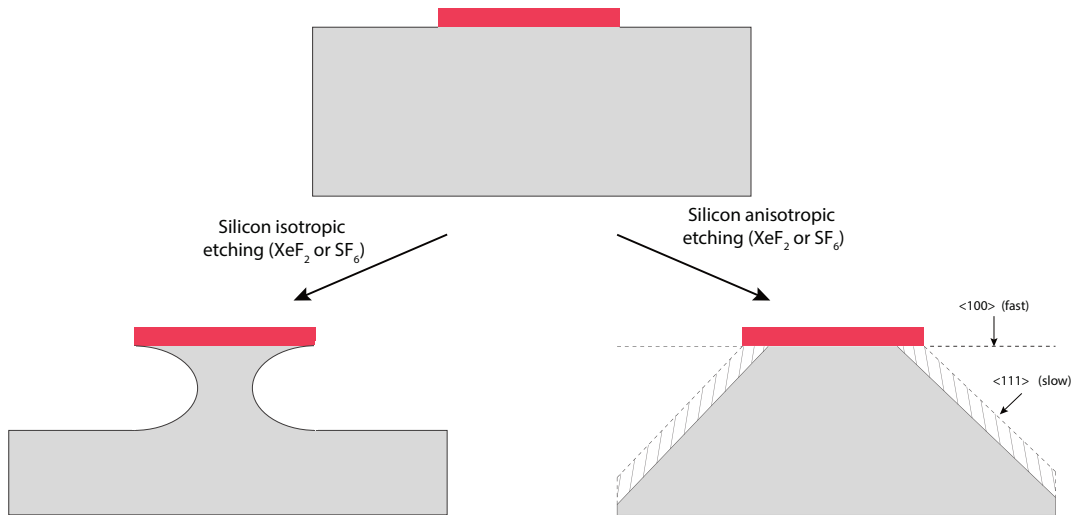
Figure 2.5 – **Isotropic versus an anisotropic silicon undercut.** In isotropic etching, substrate is etch with relatively similar rate in all direction. For the anisotropic etch different crystalline angles etch with different rate. For KOH etching of silicon, <111> planes are etched ~200 times slower than <100> planes[142]. After several minutes, the <100> planes will be etched away and we left with triangular shape structures under Si_3N_4 beams.

extremely small surface tension)[10]. Then ethanol was purged for 15 minutes with CO_2 until no ethanol was left in the charmer. Another important point is that because of the extreme aspect ratios of our devices, they are very fragile structures and turbulence in the liquid can cause them to break (figure 2.9) or collapse. Therefore the CO_2 flow was kept at minimum during the filling and purge steps to avoid strong turbulence in the liquid in high pressure chamber.

Anisotropicity of silicon etching in KOH and undercut using KOH

The second major problem of KOH undercut is the anisotropicity of silicon etching in a KOH bath as illustrated in figure 2.5. Different crystalline surfaces etch with different speeds in KOH solution. For example, <111> planes are etched ~200 times slower than <100> planes[142]. if we attempt to undercut Si_3N_4 beams directly with KOH, immediately etching Si_3N_4 layer, we will produce a "pyramid" shape structure under the beams (see figure 2.6.A and 2.6.B) and it will take a very long time to etch and release the beams. We performed an experimental test for KOH undercut as illustrated in figure 2.6. Arrays for 50 nm Si_3N_4 beams where fabricated on a standard silicon wafer where we sweep the width of the beams from 100 nm to 5 μm. The wafer was cleaved from the center in-order to view the cross section of the beams. In fig. 2.6.A step by step increase the wafer exposure time to KOH. This experiment was performed using 40% concentrated (weight concentration) VLSI grade KOH at 60° degree while we maintain

---

[10]In summary the drying process is:

$$\text{water} \rightarrow \text{ethanol} \rightarrow CO_2 \text{ (liquid)} \xrightarrow{\text{CPD}} \text{air} \qquad (2.1)$$
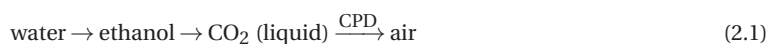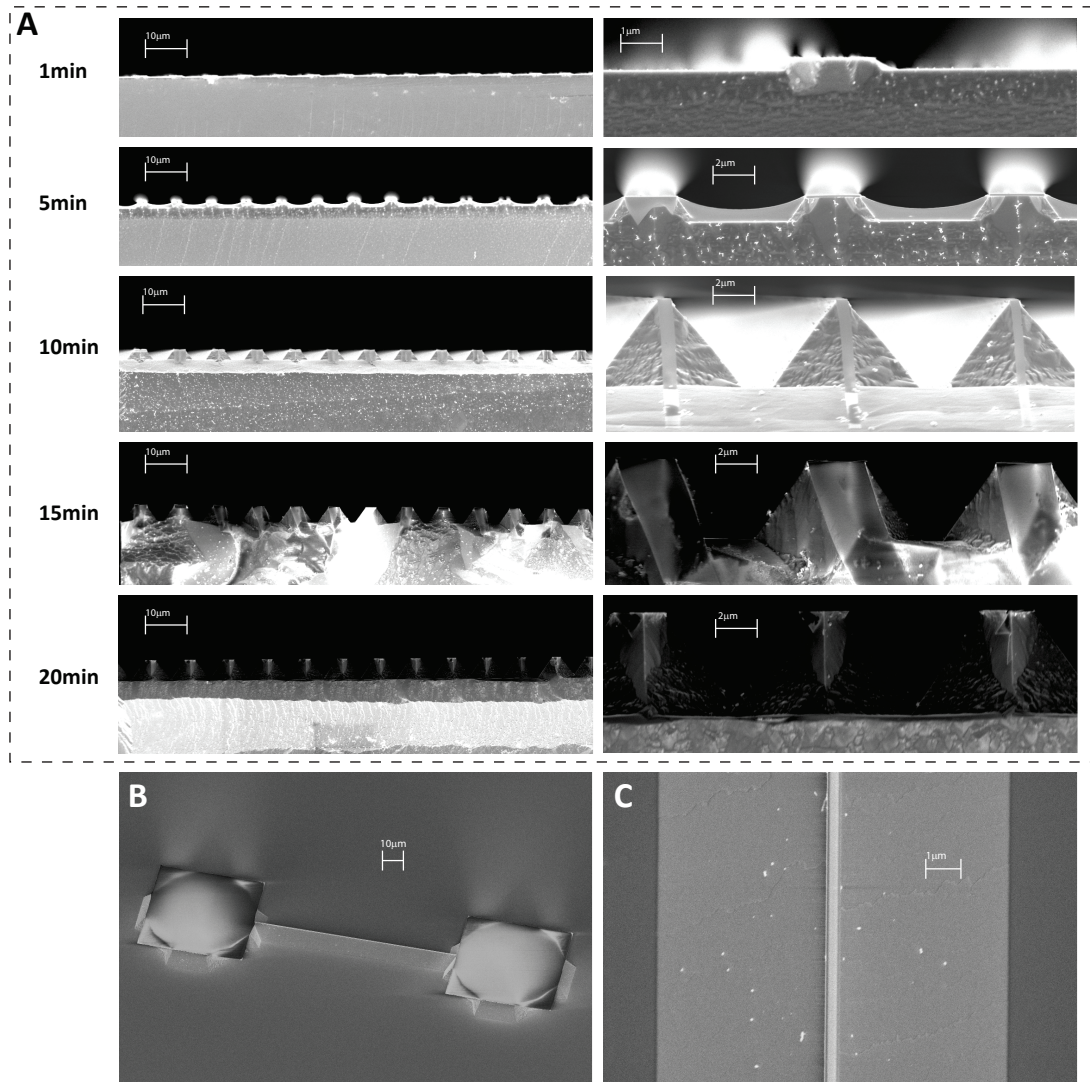
Figure 2.6 – **Experimental demonstration of anisotropicity KOH etching.** A) Shows the cross sectional SEM image of arrays of Si_3N_4 beams on silicon exposed to different KOH etching time. The formation of triangular shape structures in silicon due to slower etching speed of <111> planes is clear. B) The SEM image a beam and its anchor pars after 30 min KOH etching. If the process continues, the pads will be released before the silicon under the beams is consumed. C) SEM of the beam section in B from the top view.

the bath density at 1.37. We experimentally observe the formation of triangular structures that are extremely slow to etch. It will be matter of hours to be able to fetch those <111> planes and consume the silicon underneath the beams. The main problem however, is not just the length of the process. More importantly, the fact that the silicon underneath the clamping pads would get etched away before we consume all the silicon material underneath the beams. This is illustrated in figure 2.6. This is because of the asymmetric geometry of width respect to crystalline planes, where KOH and always find fast angles for different locations.
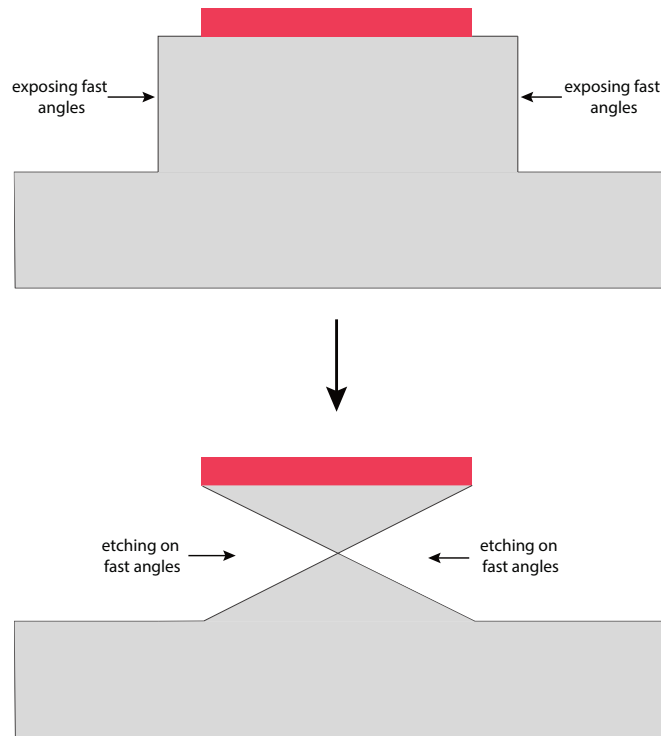
Figure 2.7 – **KOH undercut by via etching from the sides.** In order to undercut Si_3N_4 beams via KOH, we first create an upscale version of the mask and etch deep into silicon via the Bosch process to expose the fast etching surfaces from the side. The depth of the silicon groove is equal has to be ~ 1.5 times deeper than the width of the beam.

Our idea to solve this problem is to go deep in silicon and attack from the sides by exposing the fast angles as illustrated in figure 2.7. For this, an up-scaled version of the beams was patterned using e-beam lithography and etched deep in a silicon substrate (depth of $10 - 30 \mu$m) using the Bosch process . Since the angle between the slow surface (<111>) and the fast surface (<100>) in a silicon crystal is $\theta = 54.74$ degree, the minimum depth for the Si etching should be a bit longer than $w_{max} \cdot \tan\theta \approx 1.5 \times w_{max}$ where w_{max} is the maximum width in our design.

Another positive advantage of introducing the Si etching step is that we can independently control the distance between the Si_3N_4 layer and the surface of the substrate. For the extreme aspect ratios reported in this thesis, by experience we realized that a gap of 10-30 μm between the surface of Si_3N_4 and silicon substrate is required to avoid the structural collapse during the CPD drying. We have experimentally tested this idea. Figure 2.8 shows the results of our method for KOH undercut. In left-top we can see the silicon grooves before etching where an up-scaled version of the beam mask is etch ~ 10 μm into silicon. The 50 nm Si_3N_4 layer is clear in the top-right zoomed version. Similar to our experiment in 2.6, here we sweep the time we exposed the chips to KOH and imaged the cleaved chips from the side. In a strong contrast to direct KOH undercut (fig. 2.6), the silicon underneath the Si_3N_4 beams layered is almost consumed in only 5 min. Panel right-down shows that few narrower beams are already

released after only 5 min. With this method, not only we significantly reduce the etching time, but also make sure the pads are not etched and we won't suffer from over-hanging.
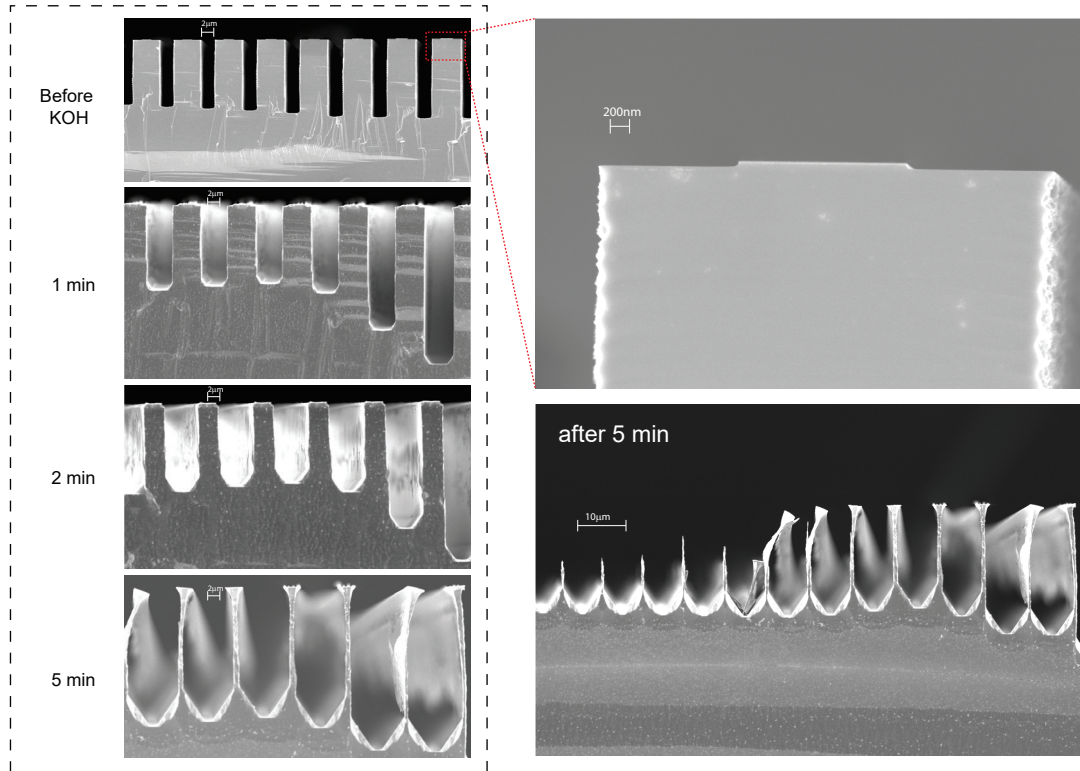
Figure 2.8 – **Experimental demonstration of KOH undercut via etching from the sides.** On the left: Shows the cross sectional SEM image of up-scaled ~ 10 μm silicon grooved etched via the Bosch process, exposed to different KOH etching time. After only 5 minutes, underneath silicon is almost completely consumed. In the top right, show the zoomed view before KOH undercut where the 50 nm Si_3N_4 beam on top is clear. Bottom right SEM shows that few Si_3N_4 beams are already released (since we cleaved through the beams, we lose the beams after their release.)

Another positive advantage of introducing the Si etching step is that we can independently control the distance between the Si_3N_4 layer and the surface of the substrate. With an extreme aspect ratios reported in this thesis, by experience we realized that a gap of 10-30 μm between the surface of Si_3N_4 and silicon substrate is required to avoid the structural collapse during the CPD drying.

Handling of chips in liquid bath

We process almost all of our fabrication recipe on a wafer scale and rarely we perform a chip scaled processing. Even if our active area is less that 1% of the entire silicon area. The reason behind this is that is since we use standard cheap silicon substrates, material cost for our

structures are completely negligible (1-5% of total cost) compare to the processing cost (95-99% of total cost). Working with wafer scale however, come with advantage of using commercial reliable solutions for wafer handling and waver carriage. Most machines (automatic coaters, mask aligners, dry and wet etchers and etc.) in at EPFL fabrication facility are compatible with 100 mm wafers. This makes the fabrication process very reliable and repeatable. On exception to this is the KOH undercut. We perform only this step in the chip scale instead of wafer scale. In other words, we first dice the wafers into the 12 mm × 5 mm chips and then proceed with releasing the beams in the KOH solution. The logic behind this order is that after undercut, the beams are extremely fragile and would break during any harsh post processing such dicing. In our previous generation of devices in our group [204][205], we used to dice the wafers halfway through and create cleaving trenches 200-300 μm deep (similar to a chocolate bar). In this method, the KOH undercut was perform in wafer scale where there are commercial reliable solutions to handle the wafers in liquid, and then the wafer was manually broke into little chips in through the cleaving trenches. However, such a breaking process creates thousands of silicon particles that could randomly land on our ultra-high Q beams and lead to significant reduction of the quality factor. Our solutions to this problem was to reverse the order and first dice the wafer into small chips and perform the KOH undercut on chip scale. The issue main issue with chip processing in KOH however, is their handling in liquid as they will fly off because of liquid current. So we have to clamped the beams in a chip holder.
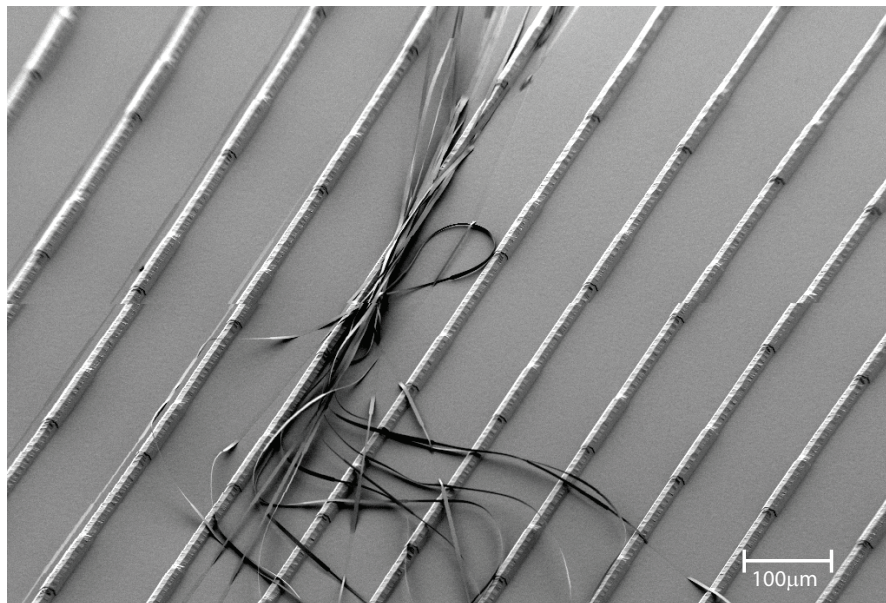
Figure 2.9 – **SEM image of few broken beams due to liquid turbulence.** One of the major difficulties in the fabrication is that if one of the beams break during undercut process, because of their long length, they can strangle to neighboring beams and cause them to also break.

Another difficulty of working with KOH undercut step is the issue of handling these fragile structures in liquid medium. These high aspect ratio beams acts like an efficient sail's boat in liquid and could be dragged and often break because of the turbulence in the water. Figure 2.9

shows an example of several broken beams that are tangled to each other. It is important to note here that one of the major difficulties we faced in the fabrication is that if one of these beams breaks during undercut process, because of their long length, they can strangle to neighboring beams and cause them to also break.
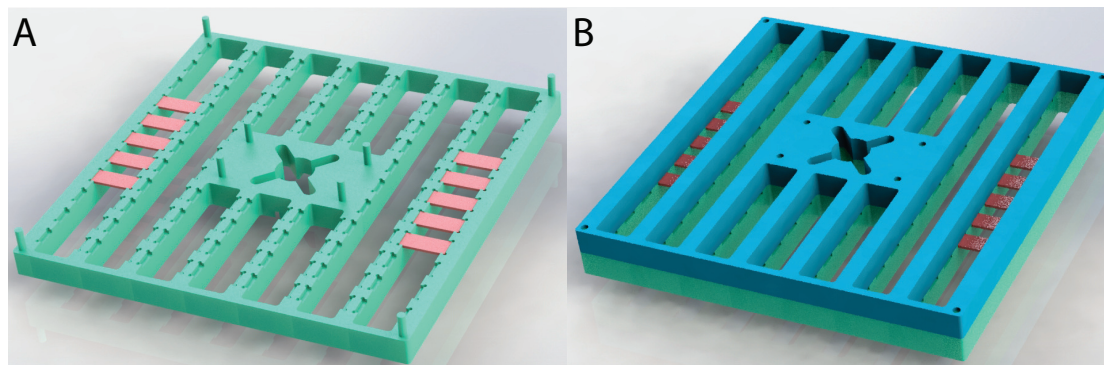
Figure 2.10 – **3D rendering of Teflon chip holders for KOH etching.** (A) Shows the 3D rendering of the bottom piece of the chip holder (green) where 64 slots are available to host our 12 mm × 5 mm chips (red). Chips are mounted horizontally (face up) in-order to keep the water on the surface of the chips and keep the samples in liquid during bath transfer. (B) Blue illustrates the top cap on the chip holder which prevents the chips from flying away during to liquid current normally coming from the bottom. The wall of the chip holder protects the beam from strong turbulence in the liquid.

To answer this challenge, an especial chip holder was designed and made of Teflon (it was fabricated by milling on a 1 cm thick Teflon plate). Figure 2.10 shows the 3D rendering of the chip holder. It is designed to solidly clamps our chip while keeping them in the horizontal position . It is important that we let water remains on surface of the chips while transferring them from one bath to the next (for example from KOH to water or water to ethanol). This ensure that the high aspect ratio beams will remain submerged in liquid during entire process before CPD. In our experience, careful handling of the chips in the liquid and especially during the bath transfer is the most crucial step of the fabrication that may lead to extremely low yield if this is not done properly.

General overview of the process flow

Based on our discussion regarding the choice of chemistry for the undercut and our etching method, we can now briefly review the summarized process flow (fig. 2.1) before going into the details of each step. The fabrication process starts with LPCVD deposition of stoichiometric Si_3N_4 on a Si substrate (fig. 2.1.1). The main processing steps are as follows: first, patterning the beams atop the Si_3N_4 layer using electron beam (e-beam) lithography on a HSQ006 (6% HSQ) resist (fig. 2.1.2), second, transferring the patterns to the Si_3N_4 layer by reactive ion etching (RIE) using fluorine chemistry (fig. 2.1.3) and third, releasing beams from the underlying Si substrate in KOH bath (fig. 2.1.6). Intermediate steps relates mainly to the challenge of preventing released nanobeams from collapsing due to their extreme aspect

ratios. The most important step, carried out prior to undercut step, involves recessing the Si substrate by ~10-30 μm from the Si_3N_4 layer using the Bosch process(fig. 2.1.5). During the Bosch process, beams are protected using an upscaled version of the first e-beam mask (fig. 2.1.4) patterned on a thicker (~ 800 nm) FOX-16®resist. The final step is also crucial, in which critical point drying (CPD) is used to avoid structural collapse due to surface tension in the process of drying the released structures. Undercut takes place on individual $5 \times 12 \, mm^2$ sample chips diced from 700μm double sided polished Si wafer after step (fig. 2.1.5). The wafer is coated with a protective photoresist before dicing, and to remove this protective layer and other organic contaminants prior to undercut, sample chips are cleaned by NMP [11] and a piranha bath.

2.2 Details of the fabrication process flow and related mask designs

In the following section, we will review the details of each of these process steps as well as the masks designs.

Wafer preparation and alignment marks

Silicon substrate is used for this process are 100 mm (diameter) wafers cut from a Cz grown silicon ingot in thickness of $700 \pm 25 \, \mu$m. These wafers were purchased from SVM Co.[206] with the following specs:

- TTV[12]: <5 μm

- Bow < 30 μm

- P-doped (Boron)

- Resistivity: 1-100 ohm-cm

- Orientation: <100>

- Double-side polished

The first processing step we perform on these wafers is the alignment mark definition. In our fabrication method, we align all the other masks to the alignment master mask (figure 2.11) that contains many alignment for different lithography techniques.

- Electron beam lithography global alignment mark (pre-alignment mark)

- Electron beam lithography chip alignment mark

---

[11] 1-methyl-2-pyrrolidon
[12] Total Thickness Variations
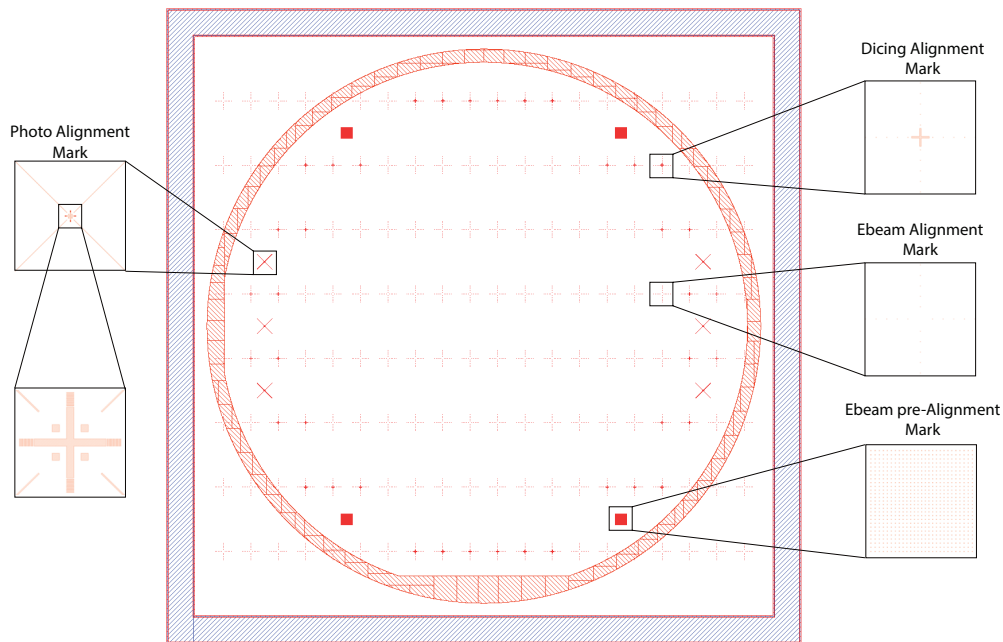
Figure 2.11 – **Alignment mark master mask** Different alignment marks are patterned on the silicon wafer and all other layers are aligned to this mask. The orange shape determine the borders of 100 mm wafer and purple square determines the borders of a 5" chrome mask.

- Photo lithography alignment marks

- Dicing alignment marks

The ebeam alignment in this process is the most crucial alignment which we implement it in 3 stages for maximum accuracy: **I)** First stage is to find the coordinates of a reference point on the wafer with regards to the wafer holder (usually the Faraday cup). The center of pre-alignment markers (see figure 2.11) are used for this task. The pre-alignment marks consist of 27×27 squares with dimension of 10 μm × 10 μm. The spacing between the squares is increased from the center to the edge: $(x_i, y_j) = ([75 + i] * i, [75 + j] * j$ where (x_0, y_0) is the coordinates of the central square. We can program the ebeam tool (Vistec EBPG5000 100 keV electron lithography machine) to search and find the center of this pattern irrespective of where it lands initially. This reduces the chance of not finding the first alignment mark (the scan range of ebeam machine is a radius of 30 μm. Without the pre-alignment mark pattern, we are forced to measure the position of the first marker with resolution better than 30μm. Any inaccuracy larger than that, would cause alignment procedure fails and wafer had to be unloaded and re-aligned). **II)**The second stage is to find 5 more points across the wafer to globally align the axis parameters ((x,y) offsets, rotation, non-orthogonality and scaling of each axis). At this stage we reach alignment accuracy better than 50 nm. **III)** In the 3rd stage, before writing each chip, the ebeam tool locally re-aligns again to the 4 chip alignment markers next to each chip. This procedure repeats for every 65 chips. With this 3 stage alignment mark
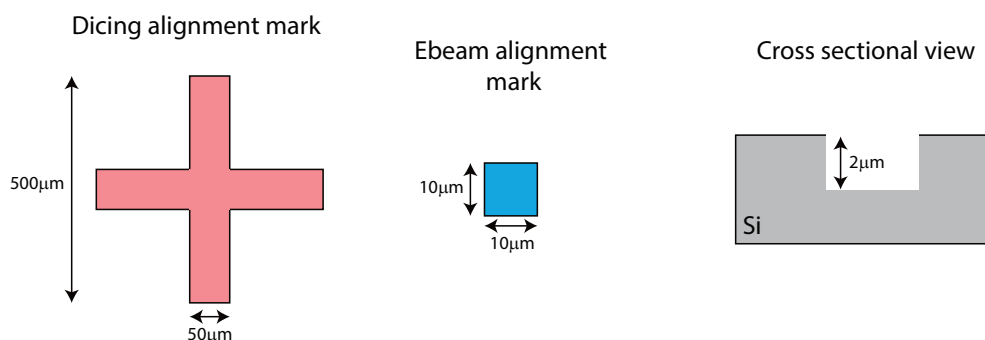
Figure 2.12 – **Ebeam and dicing alignment marks** Alignment ebeam alignment marks are 10 μm × 10 μm squares that have to be etched at least 2 μm into silicon substrate to create a visible contrast.

procedure, we reliably achieve alignment accuracy below <10 nm.

The ebeam alignment marks are 10 μm × 10 μm squares etched 3 μm into silicon substrate (see figure 2.12). One important design considerations we applied to the alignment mask in figure 2.11 is that we remove the "cross pattern" alignment mark from the central regions of the wafer. This is because these cross shapes (used to align the dicing step) are massive structures that creates large topography on the surface. This results in a shadowing effect in the spin coating of ebeam resist. Therefore, the crosses removed from the center parts (active region of the wafer) to allow a smooth and uniform coating in these regions.

The alignment marks are patterned and etched into the Si substrate using photo-lithography and RIE etching. Wafers are coated with 2 μm AZ1512 photo-resist using ACS200 GEN3 automatic coater (an HMDS[13] layer is first applied to increase the adhesion of the resist to the silicon substrate.). The alignment mark/mask is exposed with Suss MA6-Gen3, double side mask aligner with 70 mJ/cm^2 of i-Line UV light spectrum exposure. The wafers are then developed using ACS 200. In the next step the alignment pattern is then etched into the Si wafer using Florine chemistry with high verticality. For the this Si-Opto recipe on Alcatel AMS 200 SE, dry etcher, was used with etching time of 3 minutes. This recipe is used because of its slow and accurate etching with smooth sidewalls. It offers the selectivity of ~1:10 for photo-resist. The photo resist is then stripped using a 5min oxygen plasma perform via the "resist high strip" recipe on Tepla GiGAbatch dry etcher.

Thin film deposition

Before deposition, wafers are cleaned using the standard RCA process[207]. In the RCA cleaning procedure is used to clean the wafer from organic contaminant, thin oxide layer and ionic contamination. In this process the surface of the wafer is oxidized (few nano-meter) and the thin oxide layer is then removed using HF to etch and undercut any possible particles on

---

[13]Hexamethyldisilazane
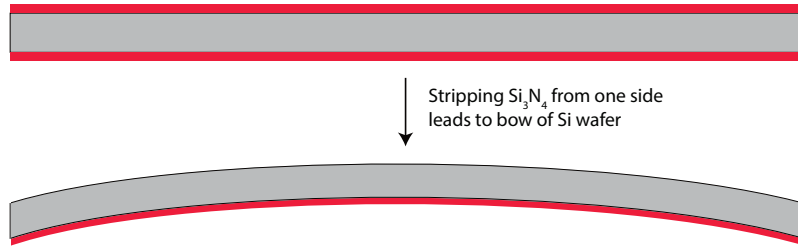
Figure 2.13 – **Stress measurements via the induced bow of the wafer.** Removing the Si_3N_4 layer (red) from one side of the silicon wafer (gray) causes the bending of the wafer due to tensile stress in the film (exaggerated view and dimensions are not to scale). By laser interferometric measurement of the bow of the wafer before and after the deposition, we can measure the deposition stress in Si_3N_4 layer.

the wafer in order to have a clean wafer before entering the deposition furnace.

Wafers are then put in low pressure chemical vapor deposition (LPCVD) furnace and the deposition happens at very high temperature. The reaction initiates with the thermal decomposition of dichlorosilane (SiH_2Cl_2) reacting with ammonia (NH_3) in the temperature of ~800 degrees centigrade. This leads to high stress stoichiometric silicon nitride with the following chemical reaction:

$$3SiH_2Cl_2 + 4NH_3 \xrightarrow{700^oC\ -\ 840^oC} Si_3N4 + 6HCl + 6H_2 \tag{2.2}$$
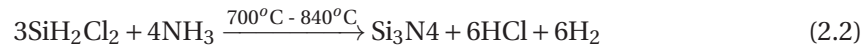
The thickness the thin film (usually 20 nm for this process) is then measured using a Sopra GES 5E, spectroscopic ellipsometer. The next step is the measurement of the film stress. The film stress (σ_{film}) is measured via measuring the bowing induced in the wafer because of the nitride layer before and after the deposition. Wafer's bow is measured by laser interferometry (via Toho Technology FLX 2320-S - Thin Film Stress Measurement tool). With this technique we measured the film stress to be about $\sigma_{film} \approx 1.1$ GPa.

Electron beam lithography

The first major of the fabrication starts with the patterning the geometry of the beam. In chapter 1, we show that the dissipation dilution is independent of the width of the mechanical oscillator. Therefore, the minimum feature size of our structures can be selected independently. However, the wider the structure become, it is more difficult to undercut the structure. We choose 400 nm for the minimum width of our structure at the center of the tapered region (it means the widest part of our beam will around 6.1 μm). Also we observe that the localized mode design is very robust against roughness and geometrical changes. Therefore these beams can be written with photo-lithography as well. But for this project we write all masks using ebeam-lithography. This is not only to achieve nano-meter resolution and alignment
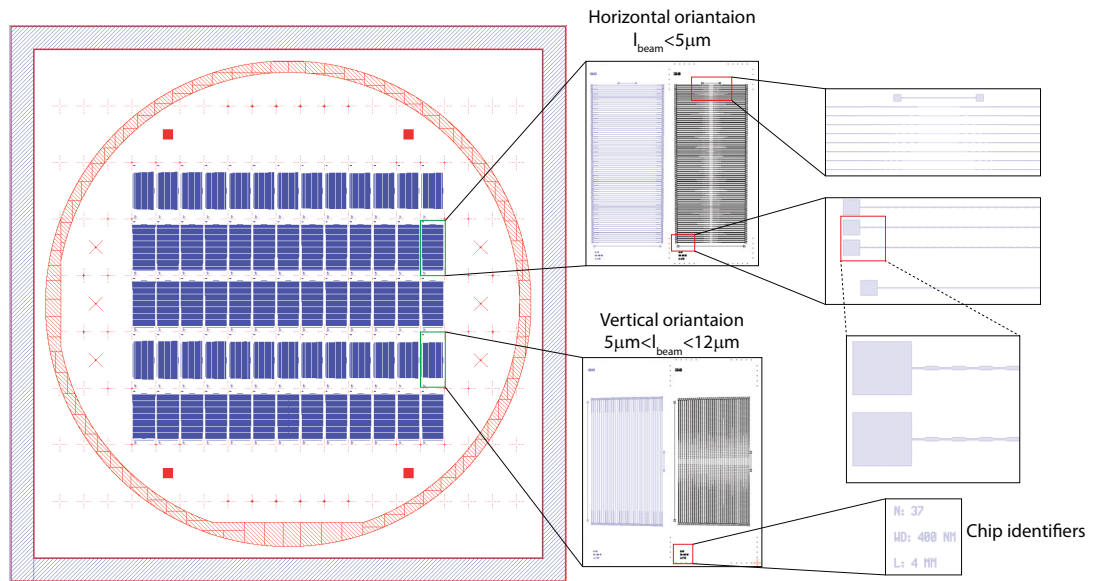
Figure 2.14 – **First ebeam mask: definition of beam geometry**. The orientation of the beams could be vertical or horizontal depending on the beam length is longer or shorter than 5 mm. The wafer can host up to 65 chips (13 columns and 5 rows) with dimensions of 12 mm× 5 mm. We normally sweep the length of the defect across the samples of each chip and other parameters are swept between the chips (such as number of unitcells and the length of the beam). Each chip also contains a unique identifier that helps to find the parameters of the chip during the measurement. The entire mask is generated via a C++ code.

accuracy but also the flexibility and fast prototyping capability we can achieve with ebeam. In addition, by experience, we realized our beams are very sensitive to organic contamination are burnt photo-resist residues were a major problem for us. Using ebeam, we can rely on non-organic resist such as HSQ and its non-diluted versions such as FOX.

An example of the fist ebeam mask is illustrated in figure 2.14. It this mask we observe 65 chips with different beam lengths and different designs were many sweeps were implemented to experimentally observe the behavior of the quality factor (for example changing the position of the localized mode with respect to the bandgap by sweeping the length of the defect.). Since the dimensions of our chips are fixed at 5 mm × 12 mm, as illustrated in figure 2.14, the orientation of the beams could be vertical or horizontal if the beam length is longer or shorter than 5mm. It is important to note that we generate all the masks for this project via c C++ code that automatically draws the geometry and all the sweeps. The code is compiled in L-edit mask drawing software[208].

The wafer is coated with HSQ using the manual coater. Prior to the coating there is a pre-bake step for 5 minutes at 180ºC to dehydrate the surface from possible water molecules on the surface, followed by a nitrogen air flow. Dehydration is required for the adhesion of the resist to silicon substrate. After resting on a clean cloth tissue for 10 seconds to cool down, the
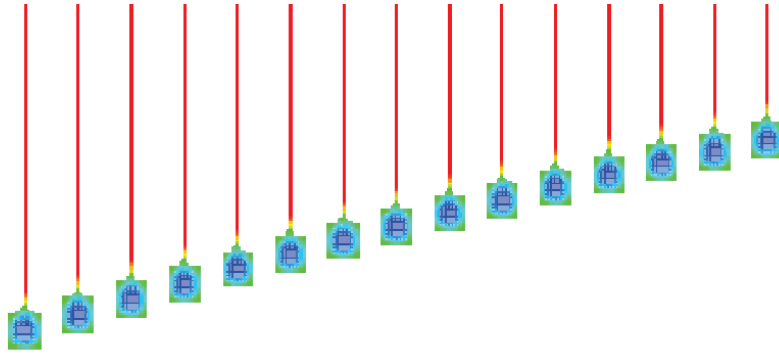
Figure 2.15 – **Proximity correction**. The proximity factor is color coded in the design. The region illustrated by red will receive an enhancement in the doze because of their sparse surrounding but the blue regions experience a reduction of the doze due to back scattering of the electrons from the surrounding pattern. These proximity corrections are calculated using proximity factor of $\eta = 1.7$.

ebeam resist layer is spin coated using 2000 rpm speed for 1 minute with dispensing of 2ml of HSQ06 (6% HSQ) solution. With the recipe will coat about 200 nm of ebeam resist atop of silicon nitride film. The wafer is then placed on the ebeam holder. First we perform a height measurement on the entire wafer using a laser interferometer to check the height. The magnetic lenses on the beam machine can adjust the focus in the range of 0-50 μm and therefore height of the wafer has to be in this range. At this stage we use two distant alignment marks on two distant edges of the wafer to manually align the rotation of the wafer by adjusting the adjustment screws on the holder. This step is carried out in multiple iteration steps by fixing the position on one side and compensating for the possible rotation misalignment on the other side of the wafer until the rotation of the wafer is minimized.

After this alignment, we set the reference position of the holder to zero at the Faraday cup that is located on the corner of the holder. This is the zero point of the coordinate system used by ebeam tool. We then measure the position of the center of the pre-alignment mark pattern with respect the Faraday cup and use it to start our alignment procedure as explained in previous section.The wafer is then loaded into the ebeam load-lock and transferred to the main stage after pumping to high-vacuum (5×10^{-5} mbar). For this project we use automatic alignment procedure as it offer high alignment accuracy compared to manual alignment.

To achieve minimum fillets and the corners, we perform a proximity correction [209] to calculate a non-uniform doze across the pattern. Near the regions with high a dense structures in the surrounding, we reduce the doze to account for the background doze coming from the back reflected electrons and enhances the doze the region with no surrounding structures and therefore no back-scattered electrons. Figure 2.15 shows an example of proximity correction calculations perform using GenISys layout beamer [210] where the value for the doze correction is color coded at each point (red means doze adjustment factor higher than one and blue beam lower than one). At the center of the beam the doze has to be enhanced
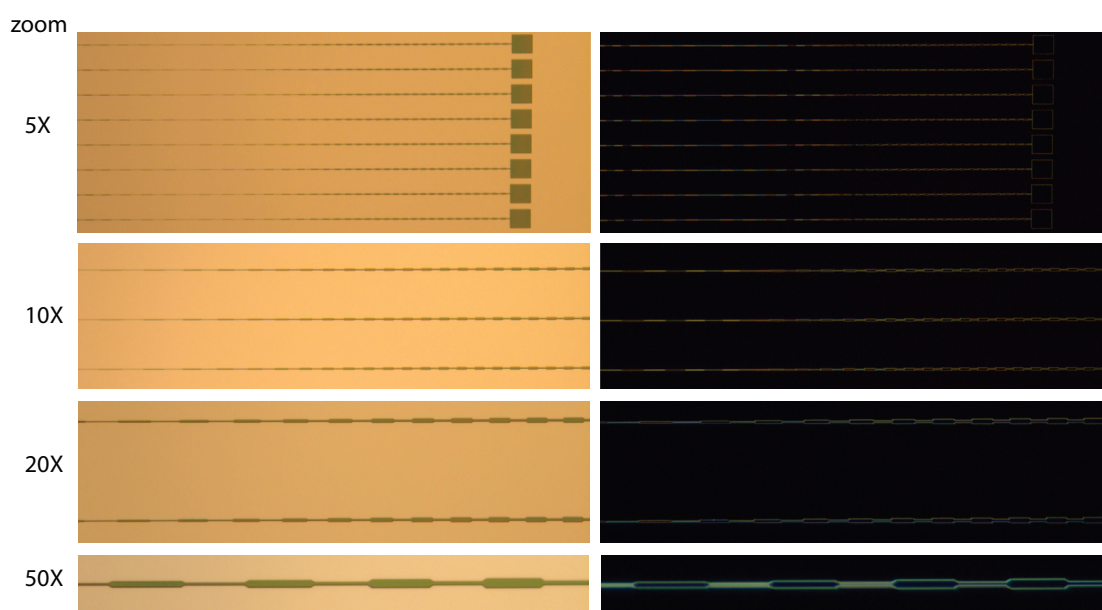
Figure 2.16 – **Optical image of the 1st ebeam mask.** On the left is the bright field and on the right is the dark field image of the tapered corrugated beams in different zooms.

because of their sparse surrounding and in the middle of the pads, doze has to be reduced due to surrounding of each point. Through an independent test, we have calibrated the proximity parameter to be $\eta = 1.7$ and the base doze of 1500 μC/cm^2. As we do not have round structures in this mask and are not sensitive to roughness, we choose the grid resolution of 30 nm for our ebeam fracturing and the electron current of 200 mA. This gives us the maximum writing time. With these settings, normally it would take about 4-5 hours to write a similar mask to the one presented at figure 2.14. To reduce sidewall roughness with no additional costs, we perform a double path writing in which we write every part of the mask two times with half the doze. The random drifts because between the two paths would lead to reduction of the sidewall roughness.

Finally after ebeam writing, the samples are developed in 25% TMAH solution for 2 minutes and rinsed in DI water[14] until the resistivity of the bath is above 15 MΩ. The samples are then air dried using the nitrogen gun and inspected under optical microscope (see figure 2.16).

Pattern transfer to Si$_3$N$_4$ using RIE etching

The ebeam pattern is transferred into the Si$_3$N$_4$ layer via ICP-RIE[15] etching. In order to achieve selective etching of Si$_3$N$_4$ used fluorine chemistry dry etching with a mixture of CHF$_3$/SF$_6$ gases. This mixture is used in "Si$_3$N$_4$ Smooth" recipe in SPTS APS Dielectric Etcher. We have calibrated the etch rate of Si$_3$N$_4$ to be around ~200 nm/min which is pattern dependent.

---

[14]Deionized water
[15]Inductively Coupled Plasma - Reactive Ion Etching

We normally use 15 seconds of etching for 20 nm thin films that account also for ~ 10 sec over etching. Over etching helps in the undercut process as it exposes the sidewall of silicon underneath the Si_3N_4 layer. Since the selectivity between Si_3N_4 and HSQ is about 1:1, the over etching process results in etching of 50 nm of 200 nm resist. Also over etching helps to avoid any uneven etching of the top film. Figure 2.17 shows the false colored SEM image after the pattern transfer to Si_3N_4.
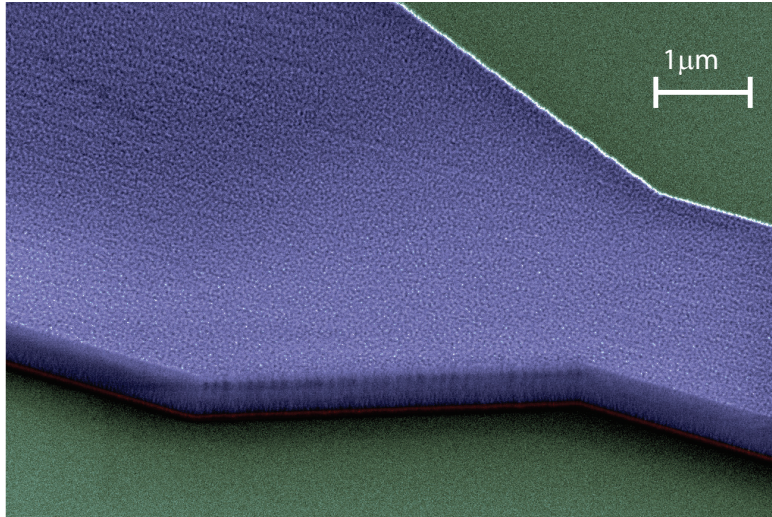
Figure 2.17 – **False color SEM image of** Si_3N_4 **etching.** Blue is the HSQ ebeam mask, red is the Si_3N_4 layer and green is the silicon substrate.

We do not remove the HSQ resist atop of the Si_3N_4 until the end our process. This is because this non-organic resist layer will protect the surface of the nitride beams through the remaining of the aggressive processing steps such as deep Si etching, photo-resist coating, and dicing. This HSQ layer will be only removed in BHF, right before the KOH undercut step. Also KOH dissolves HSQ and FOX layers. Therefore if any resist is left over the beams, they will be etched in the final KOH undercutting step.

E-beam lithography of up-scaled mask for deep Si etching

Based on our discussion in previous section in regard to our strategy for KOH etching, the next step is to pattern an-upscale version of the beam layer for the deep Si etching to expose the fast angles on the side. The reason that we are using the up-scaled version of the beam instead of using the same mask is that because Bosch process for Si etch is an aggressive etching process that creates a lot of sidewall roughness. If the same mask is used, Si_3N_4 beams will be damaged by the Bosch process. Therefore an upscale masked is designed to encapsulate the beams and protect them in the next processing steps.

The 2nd up-scaled mask is illustrated in figure 2.18.B where a uniform increase of 1.5 μm from each side is implemented in this mask. The patterning procedure for this mask is very similar
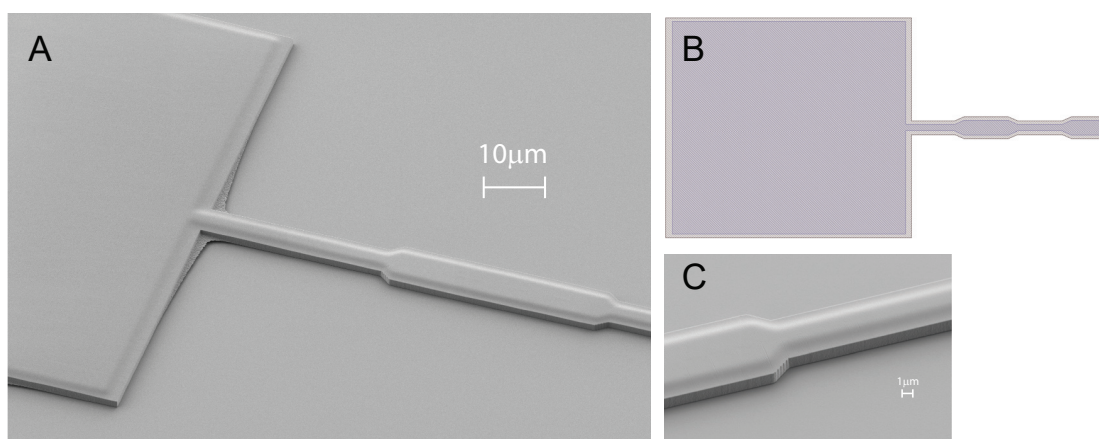
Figure 2.18 – **The upscale mask used to protect the** Si_3N_4 **for deep Si etching.** (A,C) The SEM image of the 2nd beam mask (FOX) after development. The effect of the 1st mask is clear in the topography of the 2nd mask. B) The upscale second mask where the mask is increased by 1.5μm from each side.

to the first mask. With the difference that here we use FOX-16®resist spin coated with 4000 rpm for 1 minutes. This creates a FOX-16®layer with thickness of about 600 nm. We choose a thick resist to completely encapsulate the first layer and protect it throughout the rest of the processing steps. The pre-backing recipe, the alignment procedure and ebeam parameters (base doze, proximity correction, grid resolution, the beam current and the development recipe and time are all similar to what we described for the 1st mask.). SEM images of the 2nd mask after development can be found in figure 2.18. In figure 2.18 first we observe the perfect alignment between the two layers and second striking feature is that effect of the first mask (which we did not striped) on the topography of the 2nd mask.

Deep etching of up-scaled mask into silicon substrate

As discussed in previous section, our strategy for KOH undercut is to expose the fast angles from the side by etching deep into the silicon substrate. As mentioned before, another advantage of this deeps Si etching steps is that we can independently determine the gap between the Si substrate and Si_3N_4 beam. Depending on the design and length of the beams, this gap can be between 10-30 μm. Therefore the etching time of the for this step could be varied depending on the target gap.

To perform the deep etching step, we used the Bosch process, in which, by applying pulses of SF_6 followed by passionating pulses of C_4F_8 that creates a polymer thin coating on the side walls of the structures to enable deep and high aspect ratio etching with more that 1:100 selectivity between Si and HSQ [211]. This etching was perform on Alcatel AMS 200 SE, dry etcher. For this process we used the recipe of SOI accurate for usually 12 minutes (associated with ~ 20μm depth).
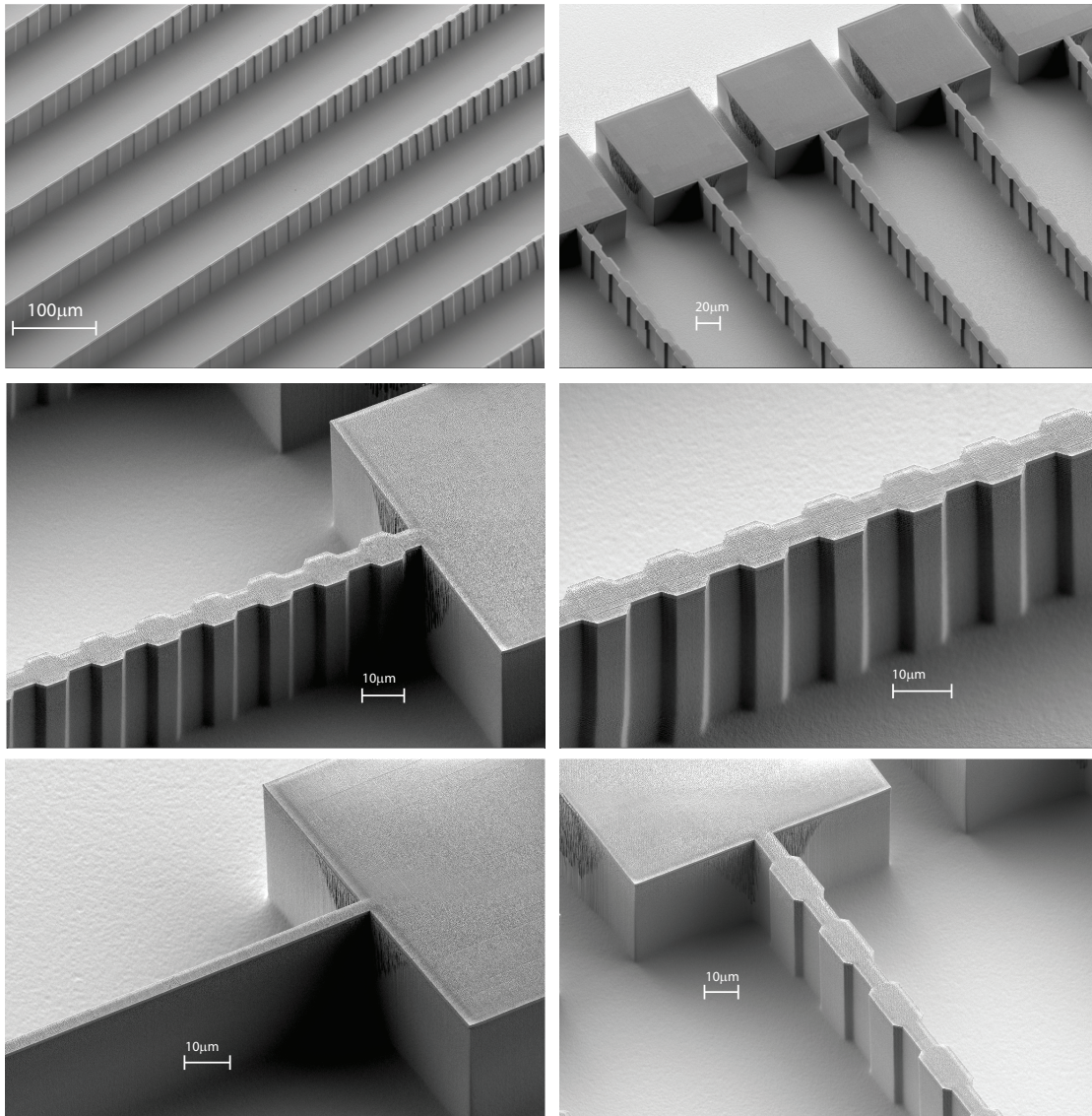
Figure 2.19 – **Few SEM images after the Bosch process.** The tapering of the width of the resonator is illustrated in top-left image.

Figure 2.19 shows the SEM image of several samples after 12 minutes of Bosch process. An interesting feature in the top-left corner figure is that the tapering of the resonator is visually observable in the silicon shadow of the beams.

Removing the passivation polymers using O_2 plasma

One important step after the Bosch process is to strip the passivation polymer using O_2 plasma. We observed by experience that this passivation layer does not remove in our cleaning steps such as acetone bath, IPA bath, Piranha bath or BHF. It only goes away in O_2 plasma and if it is not removed at this stage, will be left on Si_3N_4 beams and leads to dramatic reduction of
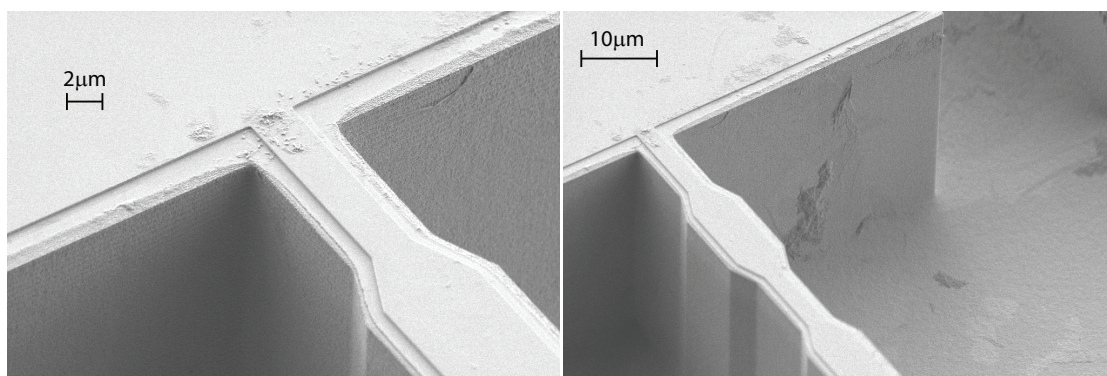
Figure 2.20 – **Contamination regarding the passivation polymer during the Bosch process.** This polymer layer can only be removed by O_2 plasma and has survived Piranha, BHF, IPA and acetone bathes, KOH and HCLbathes. This layer leads to significant reduction of Q if the O_2 plasma cleaning after Bosch process is not performed.

the quality factor. Figure 2.20 shows the SEM images of such a polymer contamination which does not dissolve in either of our cleaning bathes.

For this stripping we performed 5 min oxygen plasma "resist high strip" recipe on Tepla GiGAbatch dry etcher.

Thick photo-resist coating for protection during dicing step

Since the dicing process creates enormous amount of contamination (silicon particles and organic oil from the sawing and others) and it is even performed outside of the cleanroom we coat our wafers with a thick (100> μm) photo-resist to protect and cover our structures. The photo-resist will later be striped in the cleaning stages. For this protective layer, the wafer is coated by a thick layer of AZ9260 photo resist. Before the coating, wafer is dehydrated using a baking step at ambient pressure at 105 degrees temperature hot plate for 5 minutes. The coating is done using a manual coater by dispensing photo resist all over the wafer manually and spinning for 1 min using 500 rpm speed to make the coating uniform. After the coating is done the wafer is transferred to a hot plate at the temperature of 105 degrees for a post bake to solidify the resist. This procedure lasts for 3 minutes. After this stage wafers are transferred to the dicing tool for dicing.

Dicing the wafers into 5 mm × 12 mm chips

Dicing is performed using a Disco DAD321, automatic dicing saw. For this dicing, we use "Nickel 100" dicing blade with 30000 rpm spindle speed. This blade has a thickness of 120μm. The alignment is done using dicing alignment marks (see figure 2.11). The wafer is taped to a UV sensitive tape on to a dicing chuck. The wafer is diced into 65 individual chips. The dicing is performed all the way through the wafer and even for 100 μm into the tape to make sure
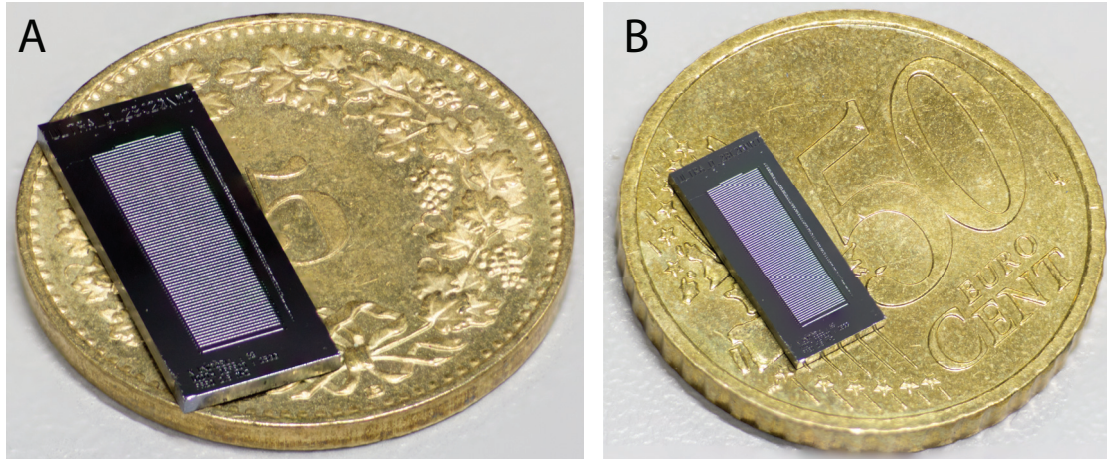
Figure 2.21 – **5 mm × 12 mm chips after dicing** A) shows the optical image of the chip after dicing and cleaning on 5 cent Swiss coin as the size reference. B) the same chip of a 50 cent Euro coin. The sweep of the central defect is clear in (A). Both of these images are a super-imposed combination 35 images with different depth of field to create a sharp image.

all the chips are properly released. The height of the blade is 0.8 um from the reference tape thickness which makes the cuts through the wafer. After the dicing, the UV tape is exposed with a UV lamp for 5min. This helps the tape to loses its adhesion and the chips are removed from the tape using a tweezer.

Figure 2.21 shows the optical image of the diced chips (after cleaning). They are imaged on top of 5 cent Swiss and 50 cent Euro coins for the sense of the scale.

Cleaning procedure before undercut

One of the major obstacles we experimentally observe is that since our UHQ resonators are very thin and surface losses are dominant, they are extremely sensitive to contamination. Specially we observe that they are very sensitive to organic contamination. Figure 2.22 shows false color SEM image of few examples of organic contamination on the beams. We experimentally observed that the a reduction of one order magnitude (from expected Q of ~1 billion to measured value of ~100 million) in quality factor could be expected if the sample is not properly cleaned.

Chips are transferred from the dicing tape into a our custom design chip holder that we described in previous Section. We have made the chip holder from Teflon because Teflon is among the few materials that does not interact with neither the bases nor acids that we will use to clean our sample. Therefore we can use the same holder for all the following cleaning steps. At this stage the main contamination sources and their cleaning bath are:

- Si particles (from dicing): Cleaned in KOH during the final Si undercut
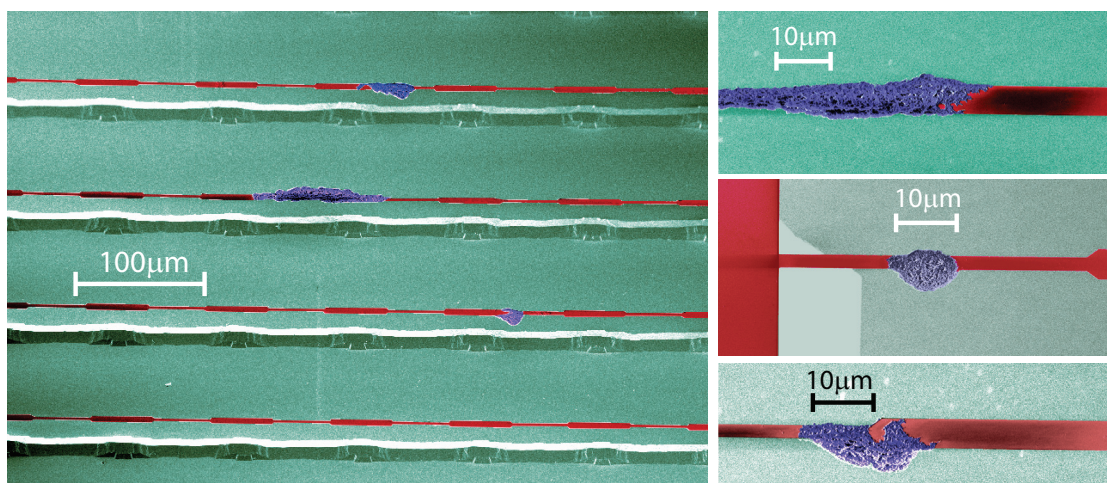
Figure 2.22 – **False color SEM image of organic contamination of the corrugated beams** Red : Si$_3$N$_4$ beam, green : Si substrate and Blue is the organic contamination. The UHQ beams are extremely sensitive to contamination and establishing a rigorous cleaning procedure was the key to achieve Q factors as high as 800 million.

- Photo-resist: Cleaned using NMP (Shipley 1615) resist stripper

- Organic contamination from photo resist or oil in the dicing process and other unknown sources: Cleaned using Piranha solution

- HSQ and FOX resist and silica particles: Removed via a 15 sec dip into BHF.

The samples are cleaned in a high temperature photo resist stripping solution at 70 degrees using NMP (Shipley 1615) for two cycles of 5 min. In the first cycle the overall photo resist will be removed in a not-clean bath and then the patterned details would be removed using second cycle in a clean solution. Next step would be cleaning the samples in the Piranha solution at 100 degrees. This happens for two cycles of 10 minutes at high temperature. Piranha solution consist of 95% sulfuric acid (H$_2$SO$_4$) that is activated by 100 ml H$_2$O$_2$ at 100 ^{o} C. This is a very strong acid that dissolve most of the organic chemistry.

The last step is to clean the original ebeam resists (HSQ and FOX) with BHF in order to clean the surface of the beams as well as stripping the ebeam resist. Another advantage of BHF dip is to remove the oxynitride layer that form in the oxidation steps in the past (Piranha and O$_2$ plasma) that has been observe to reduce the stress and thus the Q factor f the oscillator [212]. We use buffered HF for 30 seconds to remove the FOX and oxynitrid layer.

Figure 2.23 shows several SEM images after described cleaning procedure. As we can see the Si$_3$N$_4$ samples look visually very clean (no organic or polymer contamination and the HSQ-FOX resist are dissolved in BHF) before we enter the KOH undercut process. However it should be noted that other contamination could come in the next stages for example from a contaminated KOH bath or contaminated CPD chamber. The reason we did not performed
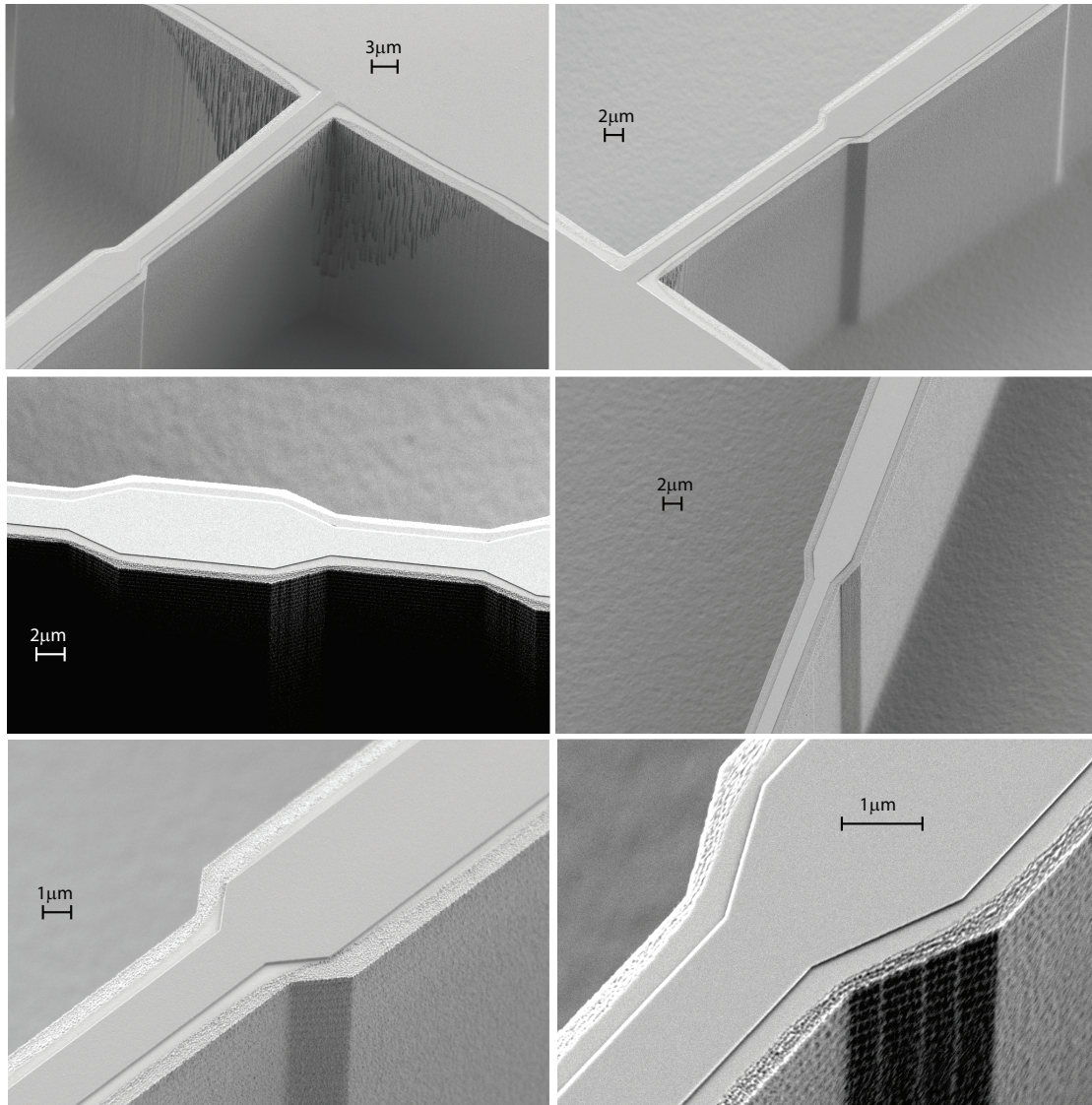
Figure 2.23 – **Few selected SEM image of devices after the decontamination phase.** After dicing, samples are cleaned in NMP resist striping bath, Piranha solution and BHF dip for 30 second. The images show that the samples as visually clean before the undercut process.

out cleaning procedure after the undercut process is that after KOH undercut, the samples are released and therefore very fragile. Changing these many bathes with a released beam, would significantly increase the risk that the samples get broken during bath transfers. Therefore, as we will discuss, we try to minimize the risk of contamination in the next steps by working with a costume made KOH and HCL bath and a cleaning the chamber of CPD before every run.

KOH silicon undercut

In the previous section, we discussed different methods of undercut and concluded that the KOH is the only solution for this project as it has the etching selectivity that is required from this undercut step. The we reviewed the challenges of silicon undercut with KOH such as the anisotropicity of the etching and the drying issue. However, as we discussed, solution were put in place in advance (such as the deep Si etching and chip holder design) to assist the undercut process. KOH undercut reaction is as the following:

$$Si + 2OH^- + 2H_2O \xrightarrow{60^oC} SiO_2(OH)_2^{2-} + 2H_2 \tag{2.3}$$
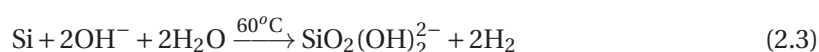
This shows that the hydroxide ions are the main etcher of Si and not the potassium. In fact removing the potassium salts that automatically will be deposited on the surface of the resonators is one of the other challenges of KOH etching. In the next section we will discuss about how to neutralize the potassium leftovers in a HCL bath . One of the main important features of the KOH etching step is the release of the H_2 bubbles from the surface. Therefore, an important consideration during the design of the chip holder as to create as much as open space for the bubbles to come out of the medium. One experience we observed in the previous generations of our chip holders is that the small opening if Teflon tends to be hydrophobic and leads to accumulation of the air bubbles. If the opening is the chip holder are not wide enough, the air can be trapped in different parts of the chip holder and could leads to the breaking of the beams due to surface tension of the air bubble that is formed on top of the chips. Therefore the chip holder is re-designed to accommodates a lot of openings for the air bubbles to escape and each the surface of KOH bath.

It should be emphasized that KOH is an aggressive substance that attacks many materials and most of the organic and non-organic contamination can not survive in KOH. However, there are still few exceptional polymers such micro structures of Teflon that can survive in a KOH solution. Since our UHQ beams are extremely sensitive to contamination, by experience we observed that the shared KOH bath at EPFL cleanroom facility is contaminated which leads to lower Q oscillators. Therefore, the key to achieve clean samples with quality factors near 1 billion was to perform the KOH undercut in a costume bath in a beaker. For this we used a VLSI grade 40% concentration (weight concentration) KOH and the temperature of the bath was actively kept at 60 degrees Celsius. This was done via a thermometer and a heater with PID controller. As the silicon etch rate is a function of the density of the bath, in order to have a stable and repeatable process, density of the bath was kept at 1.37 gr/cm^3. This was done by floating a density meter in the KOH bath and adding water to the bath until we reach the proper density.

We calibrated the etch rate of the fast planes of silicon to be ~ 25 μm/hr at this temperature and density. We also calibrated that we need 25 minutes consume all the silicon underneath Si$_3$N$_4$ beams. The KOH timing has to calibrated for different designs depending on the maximum
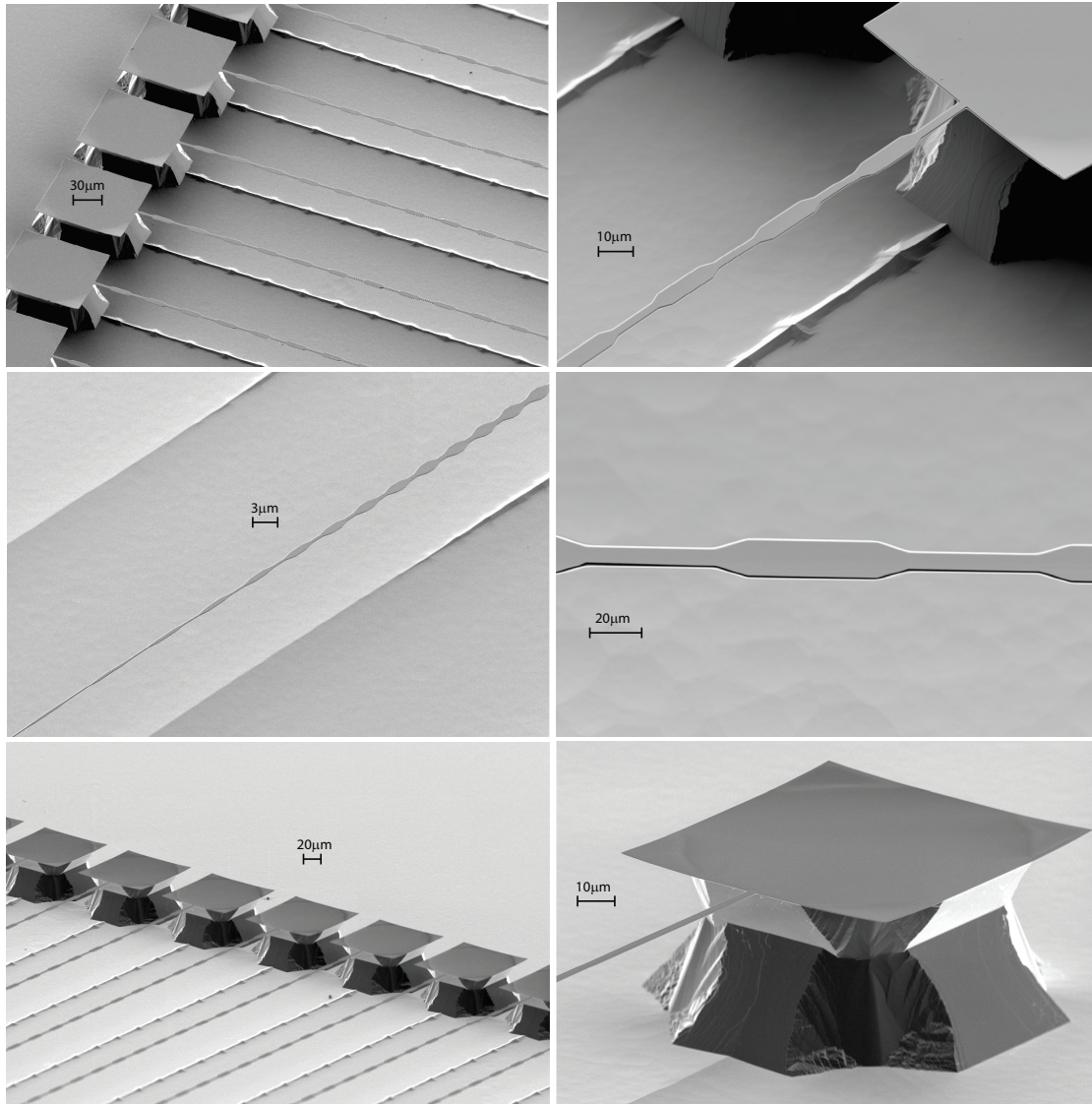
Figure 2.24 – **Few selected SEM image of released devices.** The pictures on the bottom are taken from a 70 degree angle and shows the shape of the silicon pillar under the clamping pads. If the etching time is too long, the pillars will be undercut. We optimize the etching time to be 25 minutes for the maximum beam width of $\sim 6.5\mu$m. The middle left picture illustrates the tapering of the width of the beam that leads to co-localization of the mode shape and the region of enhanced stress.

width of the structure. Too short KOH etching time, will case that we will have silicon pieces still attached to the baems. To long etching time, will leads to undercutting the silicon pillars at each opposite end (under the pads) and overhanging near the clamping points. The bath should have a low level of turbulence in order to avoid dragging of the high aspect ratio beams, but the liquid still have to be mixed up in order to allow fresh KOH to reach to the chips. Therefore, we used a Teflon magnetic Spin bar to mix the solution at 150-200rpm. After 25min

KOH, the samples are then rinsed in the water bath. We monitor the pH of the running water bath until the pH reaches bellow 8.

Figure 2.24 shows the SEM image of few exampled structures after KOH undercut (also after CPD drying). If the cleaning procedure is followed properly and a clean KOH bath is used, the final samples look very clean and will have ultra high quality resonances.

Neutralization of the potassium in HCL bath

One major difficulty of KOH etching is the potassium deposition on the surface of the structures. If the samples are dried immediately after KOH undercut, a white salt will appear on top of the chips that has contaminated all the beams. This white powder is the potassium salt left by evaporation of KOH. To neutralize and dissolve the potassium salt, chips are transferred into a costume made HCL bath with 37% concentration. Samples are left in the acid for 2 hours while the solution is slowly mixed using a Teflon magnetic Spin bar rotating at 150-200 rmp . After 2 hours, the samples are again rinsed by water until the pH of the water bath is reaches above 6. It is important that we keep the flow of the water to the minimum to avoid any turbulence in the water bath. Finally, the samples are transferred to the CPD machine while submerged in a beaker full of water.

CPD drying

Figure 2.25 – **The CPD machine at EPFL fabrication facility.** For this project we use Automegasamdri®-915B critical point drier machine.

The last and most crucial step of the process is the drying process. Statistically we lost most

of our samples during this step because either the CPD machine did not reach the critical point or strong turbulence in the liquid specially during the first few seconds of filling cycle or just because of contamination exists in the CPD machine. By experience, we learn that CPD machine accumulates a certain type of dust if it is not used regularly. The source of which it is still unknown for us. If the CPD machine is contaminated, the said dust particles will be deposited on the structures and make them unusable. Therefore, before the start of the CPD process, we first proceed with the cleaning of the CPD machine. The CPD chamber (see figure 2.25) is first cleaned by acetone, IPA and ethanol using a cleanroom tissue followed by drying with nitrogen gun. Then depending on the frequency of the usage of the machine in the past, we run 1 or 2 empty cycles with the machine by loading a dummy silicon wafer instead of our chips (the silicon wafer helps to see the dust after the CPD process is finished). We continue the empty runs until now dust particles is observed at the end of the CPD process.

As we explained before, it is important that we have no water droplets in the CPD chamber (too much of water in the CPD chamber prevents the machine to reach the critical point). Therefore, before loading the chip holder into the CPD chamber, we first switch the bath from the water (samples were kept submerged in the water during the transfer from the HCL bath to CPD machine) ethanol and leave the sample in ethanol bath for few minutes. Then the samples are transferred in to the CPD chamber and the chamber lid is carefully tightened to allow no leakage once pressure increase. The proper tightening of the lit is crustal to maintain the pressure and reach the super critical stage. Then the machined is first cooled down before starting to fill the chamber with liquid CO_2. It is important that we let the system to cool to temperature of at least 10^oC before starting the process. Otherwise we risk the chance of not achieving the critical point. The other important point while working with CPD machine is that if the valves are fully opened, a strong turbulence is generated in the first few second where the machine is filling the chamber with liquid CO_2 (this is because of the high pressure tank of CO_2 that rushes the CO_2 into the chamber). This could lead to breaking of our fragile high aspect ratio samples. Therefore our best practice is to close the filling valve at the beginning of the process and slowly open it to avoid strong turbulence in the liquid. The rest of the CPD process is fully automatic. We normally purge the chamber for 12-15 minutes with CO_2 in-order to make sure no ethanol is left in the chamber. Then machine increases the temperature and pressure until it reaches the super critical phase at ~1250 psi at 36 ^{o} C. Once the critical point is achieved, the system automatically switch to venting mode were is slowly vent the chamber from the super critical phase in to the gas phase.

One the CPD process is finished, the samples are collected and load into gel packs and transferred to the lab for the measurement. We normally inspect the sample at this stage via the optical microscope and SEM in order to make sure no contamination is visually observe of the samples and to make sure which beams are broken or collapsed and which ones are properly released. I would like to finish this chapter by showing the SEM image of a full corrugated (3 mm in total length and 58 unitcells):
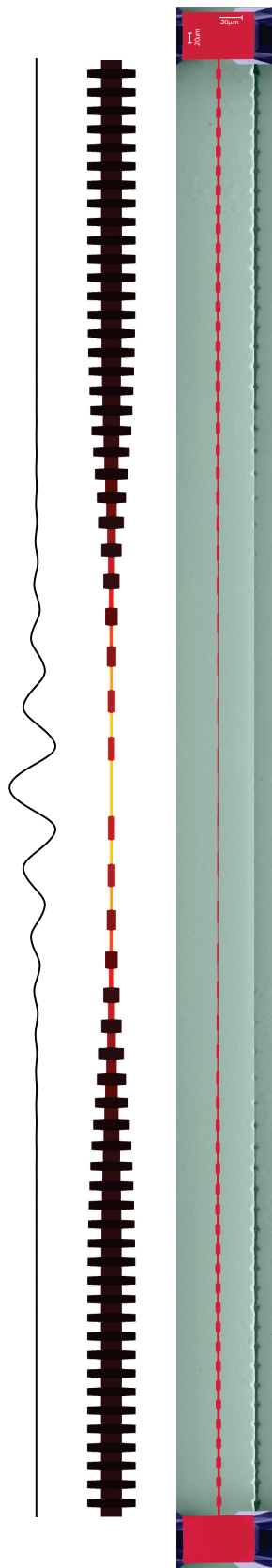
Figure 2.26 – **False color SEM image of a Si$_3$N$_4$ tapered soft-clamped beam with the total length of 3 mm and 29 unitcells on each side of the central defect.** Due to extreme aspect ratio of our devices, showing the entire geometry in one image is difficult. To construct the current SEM image, 25 individual SEM images from different parts of the beam where super imposed and colored in photoshop where red represents Si$_3$N$_4$ beams, green represents the silicon substrate and blue is the silicon pillars. The SEM image is vertically scaled for perspective. On the top, we can find the color coding for stress profile in the beam and the localized mode shape.

3 Outlook

3.1 Quantum optomechanics at room temperature and its challenges

Since the birth of the field of cavity opto-mechanics, the idea of "putting mechanics into quantum mechanics"[8] and observing the quantum effects of massive classical oscillators became one of the most important goals for this field. Using quantum limited sources (laser light) and high finesse micro-cavities[213][214] strongly in interacts with a high Q micro/nano mechanical objects [7][215][216][217], seems a right approach to achieve this goal. However, it should be emphasized that observing quantum effects of macroscopic objects is incredibly challenging. Besides numerous technical challenges (which are mostly system specific) of dealing with various noise sources (such thermo-refractive noise [121], laser classical noise [120]) and other technical issues such heading[10], absorption [167] and etc., there are two fundamental challenges in regards to observing the quantum effects of the macroscopic objects:

- Their low frequency

- Their large mass

For the first challenge, if we are interested to observe the quantum behavior of macroscopic mechanical oscillators, we have to observe them at the relevant energy scale: the ground state (GS) of mechanical oscillator, $E_{\text{GS}} = \hbar\Omega_m$. However, the enemy other quantum optomechanic experiments is the random classical Brownian motion of the oscillator and because of the low frequency of mirco/mechanical oscillators, their thermal energy — $E_{\text{th}} = k_B T$ is significantly larger than their ground energy, $\bar{n}_{\text{th}} = \frac{k_B T}{\hbar\Omega_m} \gg 1$. In other words, the the quantum effects that we are trying to observe are completely masked by the much larger thermal motion of the oscillator. For a ~ 1 MHz oscillator, even at the lowest cryogenic temperature at state of the art dilution refrigerators, $T_{\text{min}} \approx 10\text{mK}$, still the thermal occupation is $\bar{n}_{\text{th}}(T = 10 \text{ mK}) \approx 200$. This is contrast with atoms and molecules and other "traditional" quantum object that because of their high frequency, their ground state energy is significantly larger than their thermal motion

even at room temperature, $\hbar\omega_{\text{optical photon}} \gg k_B T$. In other words, systems with resonance frequency bellow $\omega_{\text{GS stability}} = \frac{k_B T}{\hbar} = 6.2$ THz at room temperature ($T = 300$ K), statistically don't have a stable ground state when they in contact with their thermal environments. Even if we could prepare them at their ground state (by methods such as sideband cooling [167],[170], [218], [219],[172] or feedback cooling [11], [10]), every thermal phonon in the environment is energetic enough on average to excite mechanical oscillator to a random thermal state and destroy the our quantum coherent state. This represent the first fundamental challenge in regards with observing the quantum behavior of the mechanical oscillators.

The solution to this challenge is "isolation". Although in a non-zero thermal bath, every phonon (on average) is energetic enough to randomly interact with our resonator and destroy its quantum coherent state, if we manage to isolate our mechanical oscillator from this "phonon bath", the average time that it take for the first phonon to enter on system will increase. We may hope to observe the quantum behaviors of the mechanical oscillator in this short time scale. In other words, although the life time of the ground state in mechanical oscillators is not infinite, if we manage to increase its lifetime beyond a threshold, we can practically observe the quantum behaviors in this short lifetime. Based on the fluctuation-dissipation theorem[220][221][222], a mechanical oscillator absorbs fluctuations from the thermal environment with the same rate that it dissipate its energy in it. Therefore, isolating a mechanical oscillator from its thermal environment (lower fluctuation) means to reduce its energy dissipation and increase it quality factor.

Quantitatively speaking, it can be shown that the average rate that mechanical oscillator exchange phonons with its thermal environment is given by[9]:

$$\Gamma_{\text{decoherence}} = \bar{n}_{\text{th}}\Gamma_m \tag{3.1}$$

where Γ_m is the energy decay rate of the mechanical oscillator. $\Gamma_{\text{decoherence}}$ is commonly known as thermal decoehernce rate and represent the lifetime of the ground state of a quantum of a oscillator with $\hbar\Omega_m \ll k_B T$. The threshold at which the quantum effects of the mechanical oscillator (in principle) can be observe is that the mechanical oscillator can at least perform one coherent oscillation before its decoherence to the thermal bath. This means:

$$\Omega_m > \Gamma_{\text{decoherence}} \implies \Omega_m > \Gamma_m \frac{k_B T}{hf} \implies \boxed{Q \cdot f > \frac{k_B T}{h}} \tag{3.2}$$

where $f = \Omega_m/2\pi$ is the mechanical resonance frequency in Hertz unit and $Q = \Omega_m/\Gamma_m$. Isolating the mechanical oscillator means reducing the $\Gamma_{\text{decoherence}}$. A traditional approach that nearly all quantum opto-mechanical experiments have token, was to reducing the decoherence rate by operating the system at lower temperature (lower $\bar{n}_{\text{th}}$) using expensive cryogenic coolers [223][224][225]. However, we are interested to design a system, capable of observing the quantum effects of the mechanical oscillators at room temperature. Our

motivation behind this goal is that, if the ground state can be achieved at room temperature, it would be a technological breakthrough in the field of quantum opto-mechanics and quantum information. In this scenario, the quantum experiments can be done at any lab in the world without the need of expensive cryogenic systems. Also it could reform the field of quantum computing as the size of the system significantly can be reduced by removing the cryogenic systems. Therefore in this thesis, our approach to reduce the decoherence is via reducing the mechanical damping rate by designing ultra high Q mechanical oscillator. Equation (3.2) at room temperature, reduces to:

$$Q \times f > 6.2 \times 10^{12} \text{ Hz} \tag{3.3}$$

an oscillator which satisfies equation (3.3) is known as "quantum-enabled" at room temperature[12]. In this, we presented mechanical oscillators with record breaking $Q \times f > 10^{15}$ Hz. Such a resonator is extremely isolated from its environment, that it can go through 100s of coherent oscillation before the first thermal phonon can interact with it. In chapter 1, we observed that by taking advantage of dissipation dilution and incorporating a non-uniform phononic crystal, to co-localize the mode shape and regions of high stress, we can engineer mechanical oscillators with unprecedented Q and $Q \times f$. Therefore, with these new ultra high Q mechanical oscillators, the first fundamental challenge in regards with observing the quantum behavior of micro-mechanical resonators at room temperature is solved. The second fundamental challenge however, still is the on the way to achieve this long standing dream. In the following, we will discuss about how we can quantify it and will observe how our ultra high Q mechanical oscillator with their favorably Q/m scaling can help to create opto-mechanical system that are capable of reaching the ground state at room temperature. Then in the next section, we briefly present our ideas on how to integrate these ultra high Q beams in a new class of near field opto-mechanical system that could reach unprecedented performance.

The second obstacle in observing the quantum effect of macroscopic mechanical oscillators is their large mass. Having such a large mass, mean the zero point motion (zpm) — the RMS[1] displacement of the oscillator at the ground state— is indescribably small:,

$$x_{\text{zpm}} = \sqrt{\frac{\hbar}{2 m_{\text{eff}} \Omega_m}} \tag{3.4}$$

where m_{eff} is the effective mass of the oscillator. Zero point motion, determines the length scale at which we are expecting to observe the quantum effects of the mechanical oscillators. For our nano-mechanical oscillator with $m_{\text{eff}} \sim 1\text{pg}$ and $\Omega_m \sim 1$ MHz, the zero point motion is $x_{\text{zpm}} \sim 200$ fm. This means that in order to observe quantum effect of macroscopic objects, we have to perform measurements of dimensions more than 1000 times smaller than the radius of atoms. Achieving such an imprecision is incredibly difficult technical challenge. There are different ways to quantify this issue , but here we decide to quantify it using the the language of rates as enables us to connect it with our first argument regarding $Q \times f$. The problem of observing the quantum behavior of macroscopic objects can be regarded as the completion

---

[1]Route Mean Square

of two rates: measurement rate and thermal decoherence rate. As we mentioned before, thermal decoherence determines the lifetime of a quantum coherent state of a mechanical oscillator. If we are interested to detect these quantum effects, we have to measure and interact with the oscillator during this lifetime. In other words, the measurement rate has to faster than the decoherence rate of the mechanical oscillator $\Gamma_{\text{measurement}} > \Gamma_{\text{decoherence}}$ [10]. The measurement rate in a cavity opto-mechanical system in non-resolved side-band regime[2] is given by[9]:

$$\Gamma_{\text{measurement}} = n_{\text{cav}} \frac{4g_0^2}{\kappa} \tag{3.5}$$

where n_{cav} is the circulating photons in the cavity and g_0 is the vacuum optomechanical coupling rate [226] is the amount of cavity frequency shift for every quanta of mechanical energy in the resonator and is equal to:

$$g_0 = x_{\text{zpm}}G \quad , \quad G = -\frac{\partial \omega}{\partial x} \tag{3.6}$$

where G is the frequency pulling factor and is equal to the amount frequency mechanical induced frequency shift in the optical cavity (ω) per unit of mechanical displacement (x). G depends on the design of the opto-mechanical system and we will revisit it in the next section. Now if we apply our condition to have measurement rates faster than the thermal decoherence rate, we will have:

$$\Gamma_{\text{measurement}} > \Gamma_{\text{decoherence}} \implies n_{\text{cav}} \frac{4g_0^2}{\kappa} > \bar{n}_{\text{th}}\Gamma_m \implies \boxed{\frac{n_{\text{cav}}C_0}{\bar{n}_{\text{th}}} > 1} \tag{3.7}$$

where $C_0 = \frac{4g_0^2}{\kappa\Gamma_m}$ is known as the single photon cooperativity[227][114]. Achieving the condition represented in equation 3.7 is equivalent to the condition for ground state cooling [167],[215], [218],[172] or observing the mechanical oscillator with standard quantum limit (SQL) of imprecision[228][229][122][11], [10]. In fact, in can be shown that $\frac{1}{n_f} = \frac{n_{\text{cav}}C_0}{\bar{n}_{\text{th}}}$, where n_f is the final thermal occupation in the mechanical oscillator in a laser cooling experiment if n_{cav} photons are pumped into the optical cavity or it is the final imprecision if the mechanical oscillator is measured by n_{cav} circulating photons in the cavity.

Starting from cryogenic temperatures and reduced $\bar{n}_{\text{th}}$, many groups were able to achieve the condition in equation (3.7). However, no group has ever been able to achieve the condition of (3.7) at room temperature[3]. One solution to achieve this condition, is to increase n_{cav} by pumping more photons into the cavity. However, many different technical obstacles would limit how many photons that can be poured into an opto-mechanical system. A full review of these technical challenges is outside the scope of this thesis but issues such as two photon

[2]$\Omega_m < \kappa/2$ where κ is the optical cavity's linewidth[170][171]
[3]maybe with the exception of[230] which the results still hasn't been peer reviewed at the time of writing this thesis.

absorption [231], Ohmic heating due to absorption [10], thermo refractive noise [121] and optical non-linearities are among the few examples of such a technical limitation on the maximum circulating power of that can be pumped into the cavity.

Our alternative approach to ground state cooling at room temperature is to design a system with much larger single photon cooperativity. First we observe that how the ultra-high Q mechanical oscillators described in this thesis, would directly benefit the single photon cooperativity, and in the next section, we will present our ideas on how to engineer an new class of optomechanical system based on the near field interactions [123], [125], [126][122], [232] to increase optomechanical coupling strength (G) and achieve single photon cooperativity in the range of $C_0 \sim 10^4 - 10^5$ at room temperature. With these results, quantum optomechanics at room temperature is within the reach.

We start our analysis by observing the scaling of the quantum cooperativity — $C = C_0/\bar{n}_{\text{th}}$ — to the parameters of the mechanical and optical resonator:

$$
\left.
\begin{aligned}
C_0 &= \frac{4g_0^2}{\kappa \Gamma_m} \\
g_0 &= x_{\text{zpm}} G \\
x_{\text{zpm}} &= \sqrt{\frac{\hbar}{2m_{\text{eff}}\Omega_m}} \\
\bar{n}_{\text{th}} &= \frac{k_B T}{\hbar\Omega_m}
\end{aligned}
\right\}
\implies
\boxed{C = \frac{C_0}{\bar{n}_{\text{th}}} \propto \frac{Q}{m_{\text{eff}}\Omega_m}}
\tag{3.8}
$$

Equation (3.8) is an extremely insightful important in regards to designing the high cooperativity systems for quantum optomechanics at room temperature with regards to the mechanical oscillator. It shows that the key to achieve higher cooperativity system is to **(a)** operate at lower frequency (although we argued that working at frequencies lower than $\sim$ 1 MHz creates other technical issue such as dealing with low frequency classical noises and thermo-refractive noise); **(b)** increase the $\frac{Q}{m_{\text{eff}}}$ ratio of the oscillator[4]. In chapter 1, we showed that one the striking and unusual features of our strained enhanced soft-clamped beams is that not only they have increased the Q and $Q \times f$, but also the Q/m of the oscillator (equations (1.131) and (1.120)) is significantly enhanced with our methods. In fact, to the best of our knowledge, our mechanical oscillators have the highest Q, $Q \times f$ and Q/m compare to any other mechanical oscillator of any type and any size at room temperature. Due to enhanced $Q \times f$ and Q/m our resonators compare to previous mechanical resonators, their integration with the previous optomechanical architectures (such as integeration with optical miro-disk resonators [123] or photonic crystal defect cavities[233]) would already significantly enhance their cooperativity. However, in the next section we briefly present our ideas about a new architecture for integration of these UHQ beams which offers much larger optomechanical coupling rate (g_0).

---

[4]This is why we introduced Q/m as one of the two main figures of merit for our mechanical resonators in chapter 1.

In summary, the two fundamental challenges for observing the quantum effects of mechanical oscillators reduces to satisfying these two conditions:

$$\text{Conditions for ground state cooling} \begin{cases} Q \times f > \frac{k_B T}{h} \\[2ex] \frac{n_{\text{cav}} C_0}{\bar{n}_{\text{th}}} > 1 \end{cases} \tag{3.9}$$

It is important to emphasize that the two conditions in equation (3.9) are independent and both have to be satisfied simultaneously in order to achieve the regime where quantum effects of the mechanical oscillators are observable. We showed the first condition is purely a mechanical design. But in addition, having an ultra high Q mechanical resonator also helps with the second condition if we can improve the Q/m. Therefore the two figures of merit for our mechanical oscillators are $Q \times f$ and Q/m.

3.2 Proposed architecture for ultra high C_0 optomechanical system

Near field vs far field

In this section, we briefly review our idea on a new architecture based on the near field interaction between a cavity and an optomechanical system. But before we present our architecture, lets briefly compare the near field and far fields approaches for detection of mechanical motions via optical light. We start by a simple scenario of a non-resonant detection where there are no resonant structure (cavity). Figure 3.1 shows the example of a canonical far field detection scheme where a laser light is reflected of the mechanical object. In fact example closely resemble our actually fiber intereferometery that we used in chapter 1 to characterize our ultra high Q beams.
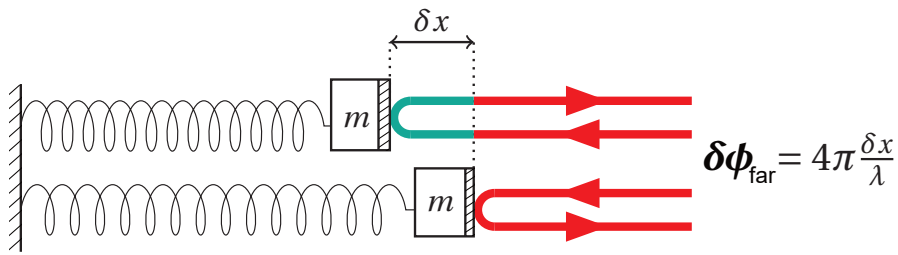
Figure 3.1 – **Canonical example of a far field optical detection of motion.** An optical beam is reflected reflected from the mechanical resonator. When mechanical oscillator moves, the laser light has to travel $2\delta x$ longer and during this process, it accumulates a phase of $\delta\phi = 4\frac{\delta x}{\lambda}$

In this canonical far field technique to measure the motion of the mechanical resonator, the physical optical path length is modulated by the motion of the mechanical oscillator (because the light has to travel more (or less) distant depending on the position of the mechanical resonator). Therefore, the phase shift that gets accumulated by the laser light as a function of

the position of the mechanical resonator is given by:

$$\delta\phi_{\text{far}} = 4\pi\frac{\delta x}{\lambda} \tag{3.10}$$

In an optical detection schematic the phase of the light is measured via for example a balanced homodyne detector (or other phase detection schemes) to give us a measure of the mechanical displacement. Now lets compare the sensitivity of the far field approach to a near field approach. Figure 3.2 shows an example of a near field detection system where an optical waveguide is placed at the proximity of a thin nano-beam. Unlike the far field approach, the physical length of the doesn't change because of the motion of the mechanical resonator. Instead, the motion of the mechanical resonator in the evanescent field of the waveguide, modulates the "effective index" of the waveguide. In order word, the effective index of the mode is a function of the position of the beam, n(x).
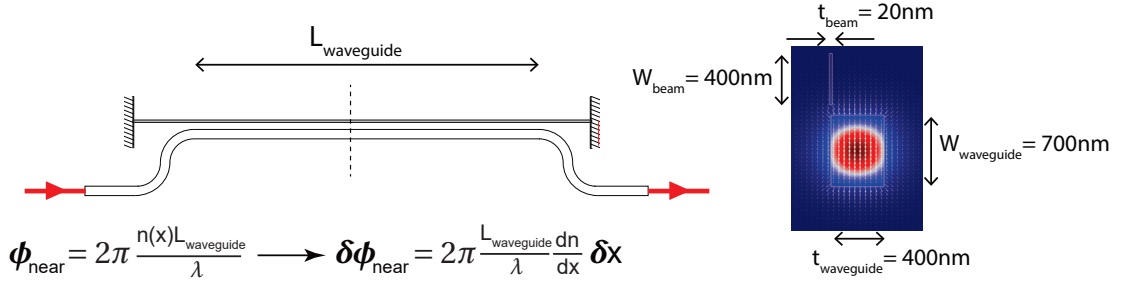
Figure 3.2 – **An example of a near field optical detection of scheme with an optical waveguide and a nano-beam mechanical resonator.** In the near field detection scheme, a nano-beam is (gray) is place in the evanescent field of the optical waveguide. A simulation of the cross section (dashed line) of the waveguide-beam system is plotted on the right. The simulation is performed at wavelength of $\lambda = 1550$ nm and the dimensions for the waveguide and the beam are given in the figure.

The optical photons upon transmission through the waveguide-beams system, accumulate the phase of $\phi = 2\pi\frac{n(x)L_{\text{waveguide}}}{\lambda}$. Therefore the mechanical induced optical phase modulation is given by:

$$\phi_{\text{near}} = 2\pi\frac{n(x)L_{\text{waveguide}}}{\lambda} \implies \delta\phi_{\text{near}} = 2\pi\frac{L_{\text{waveguide}}}{\lambda}\frac{dn}{dx} \tag{3.11}$$

Equation (3.11) already shows the strength of the near field approach to the far field approach. We can indefinitely increase the sensitivity of the near field approach by increasing the length of the waveguide. In addition, the optical refractive index is extremely sensitive to vibration of the mechanical oscillator at the evanescent field of the waveguide (large $\frac{dn}{dx}$). Figure 3.3 shows an FEM simulation perform using COMSOL [187], to determine $\frac{dn}{dx}$ for the given geometry in the inset and wavelength of $\lambda = 1550$ nm. This simulated our the our of the plane mechanical mode and the in-plane polarization of the waveguide. As we can see, for this particular geometry, $\frac{dn}{dx}$ is zero when beam is placed at the center of the waveguide. This is expected because of the symmetry of the optical mode. However, an interesting observation (which is

not obvious) is that $\frac{dn}{dx}$ maximized when the beam is placed exactly at the top or the bottom of the waveguide. We will revisit this fact in the next section as it has a significant impact in the fabrication of our proposed architecture.
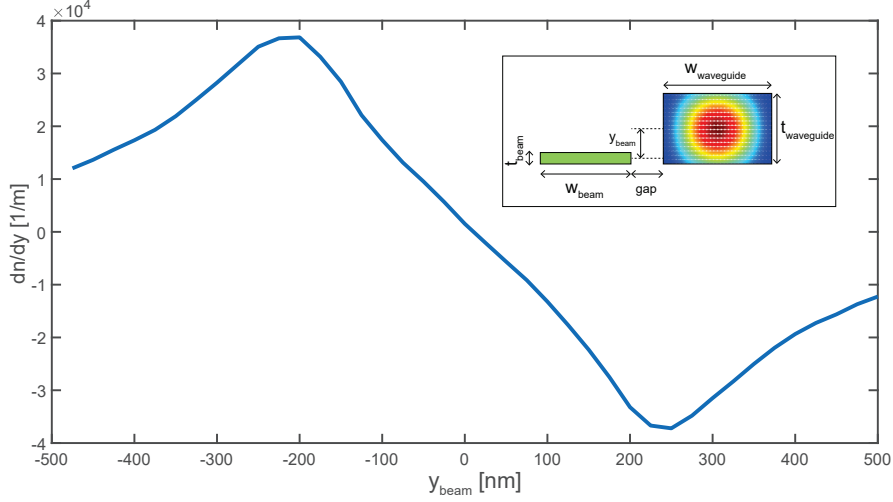
Figure 3.3 – **FEM simulation of $\frac{dn}{dx}$ for a waveguide-beam near field system illustrate in figure 3.2.** $\frac{dn}{dx}$ as a function of vertical position of the beam with respect to the center of the waveguide simulated for the wavelength of $\lambda = 1550$ nm. Inset: the cross section of the waveguide-beam (red) system. The dimensions for this simulation are $w_{\text{waveguide}} = 700\text{nm}, t_{\text{waveguide}} = 400\text{nm}, w_{\text{beam}} = 400\text{nm}, t_{\text{beam}} = 20\text{nm}, \text{gap} = 50\text{nm}$.

In summary, the ratio between the ideal far field and near field sensitivity can be written as:

$$\frac{\delta\phi_{\text{near}}}{\delta\phi_{\text{far}}} = \frac{L_{\text{waveguide}}}{2} \frac{dn}{dx} \tag{3.12}$$

For the example presented in 3.3, and $L_{\text{waveguide}} = 300 \ \mu\text{m}$ (This is roughly the same length as defect length of our highest $Q = 800 \times 10^6$ oscillator in chapter 1), $\frac{\delta\phi_{\text{near}}}{\delta\phi_{\text{far}}} \approx 5.5$. This means that the near field approach is ~ 5.5 times more efficient that ideal case of the far field resonator. It should be noted that the results simulated for in figure 3.3 is for the thinnest beam thickness (20 nm). We can further enhance the $\delta\phi_{\text{near}}$ if increase the thickness of the mechanical resonator (however we saw in equations (1.131) and (1.120) that increasing thickness of mechanical oscillator would leads to reduction of Q/m and won't be beneficial at the end.) Another important note that we have to emphasize is that to derive equation (3.10), we assumed that 100% of the light is reflected back by the mechanical oscillator. However in reality, for a beam with geometry presented in figure 3.3, we can only recover a small fraction of the transmitted light [5] Therefore in reality, $\delta\phi_{\text{far}} \ll 4\pi \frac{\delta x}{\lambda}$ and the ratio between $\delta\phi_{\text{far}}, \delta\phi_{\text{near}}$ is significantly larger than 5.5. However it should be noted that the down side of this increased sensitivity

---

[5]This is because the width of the resonator is much smaller than the spot size and its extremely thin thickness causes most of the light to pass through.

is that not we have to fabricate a waveguide, in few 10s of nano-meter from the mechanical oscillator. Depending on the geometry and the size of the system, this could be an incredibly difficult engineering task.

Now that we have established the sensitivity of the near-field systems compared to far-field systems in a simple non-resonant case, lets switch back the resonate case were a cavity is responsible for interaction between optical and mechanical fields. However it should be noted that the resonant and non-resonant optical detection schemes are not fundamentally different. Figure 3.4 shows an example of the canonical Fabry–Pérot optomechanical cavity (on the right) where one mirror is connected to a mass and spring which can oscillate. This cavity optomechanics system however is not fundamentally significantly different from the far field technique on the left. Placing the second mirror in front of the optical path, would force the laser light to circulate in the cavity and each photon will interact multiple times with cavity. The number of back is forth reflections that each photon experiences in the cavity is determined by "optical finesse" ($\mathcal{F}$)of the cavity [6]. In other word, instead of sending $\mathcal{F}$ number of photons to interact with the mechanical oscillator in the non-resonant case, we make every photon interact $\mathcal{F}$ times with the mechanical oscillator in the resonant scenario. In summary, a cavity only enhances the sensitivity my its $\mathcal{F}$ factor.

non-resonant detection   resonant detection

$$\boldsymbol{\delta\phi} = 4\pi\frac{\delta x}{\lambda} \qquad\qquad \boldsymbol{\delta\phi} = \mathcal{F}\, 4\pi\frac{\delta x}{\lambda}$$
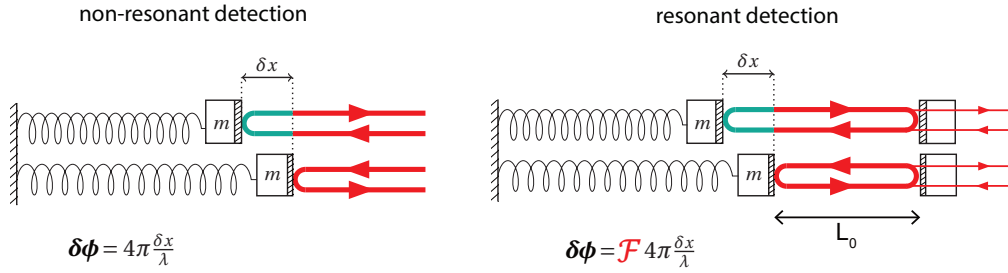
Figure 3.4 – **Canonical example of resonance vs non-resonant read out architecture.** In a resonant readout technique, by placing a second mirror in front of the optical path, we are recirculating photons in the cavity and forcing them to interact with the mechanical oscillator for $\mathcal{F}$ times. Therefore, a cavity enhances the sensitivity by the fineness of the cavity.

However, to adapt to the notation of the last section, its more coherent to the story if we look at the frequency fluctuations of the cavity ($G = -\frac{\partial\omega}{\partial x}$) instead of the phase fluctuations ($\frac{d\phi}{dx}$).

[6]It can be shown that optical finesse is given by:

$$\mathcal{F} = \frac{\omega_c}{\Delta\omega_{\text{FSR}}} = \frac{Q_o}{n_{\text{mode}}} \tag{3.13}$$

where ω_c is the resonance frequency of the cavity, $\Delta\omega_{\text{FSR}}$ is the free spectral range of the cavity, Q_o is the optical Q of the cavity and n_{mode} is the optical mode number of the cavity. It can also be shown that $\mathcal{F}$ is also equal to the ratio of the circulating power in the cavity(P_{cav}) to the input power (P_{in}) when the light is on resonance with the cavity:

$$\mathcal{F} = \frac{\pi P_{\text{cav}}}{2 P_{\text{in}}} \tag{3.14}$$

Therefore, $\mathcal{F}$ is also commonly known as the power enhancement factor. In this case the cavity is regarded as an element that locally store and enhances the power by $\mathcal{F}$.
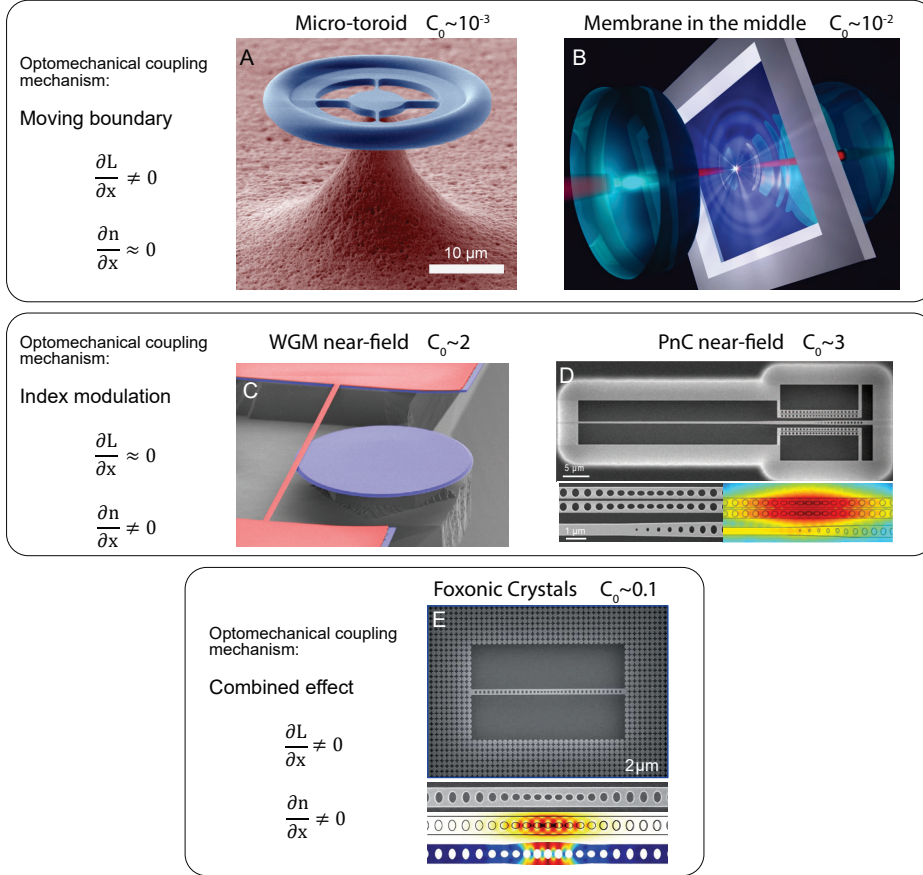
Figure 3.5 – **Literature review for most successful optomechanical systems and their coupling mechanism.** Coupling via moving boundary is the case where the physical length of the cavity (L_0) is modulated due to mechanical motion. Index modulation is the case where the effective index (n) is modulated and the combined effect is when both are modulated. A) Figure and Data taken from[215], B) Figure taken from [234] and data from[235], C) Figure and data taken from [123], D) Figure and data taken from[232] E) Figure taken from [227] and data from [167].

In the general case, the optical path in a cavity is given by $L_{\text{optical-path}} = nL_0$ where L_0 is the physical length of the cavity and n is the refractive index of the material that cavity is made of. In this case, the optical resonance of the cavity is given by:

$$\omega_c = \frac{c n_{\text{mode}}}{n(x) L_0(x)} \tag{3.15}$$

where c is the speed of light in vacuum and n_{mode} is the mode number of the cavity as $n_{\text{mode}}\lambda = n(x) = L_0(x)$. In the most general case, both refractive index and the physical length can be modulated by motion of the mechanical oscillator. Figure 3.5 shows few examples of the different OM systems where the coupling mechanism is either via modulation of physical length of the cavity or refractive index, or both. It is worth noting that the near field (C,D) systems (coupling via refractive index) have systematically much higher C_0 that the moving

boundary systems (A,B). This to some extend proof our previous argument that the near field interaction is significantly stronger than the far-field techniques. However it is important to emphasize that C_0 is not the ultimate parameter. The fundamental parameter for quantum optomechanics is $\frac{n_{\mathrm{cav}} C_0}{\bar{n}_{\mathrm{th}}}$ which was discussed in equation (3.9). Systems like micro-toroid or membrane in the middle systems can compensate their weaker C_0 by pumping more photons in the cavity[7]. We can calculate the frequency puling factor from equation (3.15):

$$G = -\frac{\partial \omega_c}{\partial x} = \underbrace{\frac{\omega_c}{L_0}\frac{\partial L}{\partial x}}_{\substack{\text{coupling due to}\\\text{moving boundaries}}} + \underbrace{\frac{\omega_c}{n}\frac{\partial n}{\partial x}}_{\substack{\text{coupling due to}\\\text{refractive index modulation}}} \tag{3.16}$$

The first term in equation (3.16) represent the coupling mechanism such as (A) , (B) in figure 3.5 where the physical length of the cavity is modulated because of the motion of the mechanical oscillator. We can show [8] that in these systems, $1 < \alpha = \frac{\partial L}{\partial x} < 2\pi$. This type of coupling closely resembles the far field detection scheme in 3.2. On the other hand, the second term in equation 3.16 represents the near-field coupling mechanics such as (C) , (D) in figure 3.5 closely resembles the scheme described in figure 3.2. There are systems such phoxonic crystals [239] such (E) in figure 3.5 which take advantage of both coupling mechanisms. In these system, the motion of high frequency defect mode, changes the physical length of the cavity. But also it changes the refractive index of the silicon through the process of photo-elastic effect[193][240] in the material. However these systems are not the subject of the discussion in the following because it is difficult or impossible to scale the geometry of these crystal because of their specific localized design.

Equation (3.16) already shows why near-field based optomechanical systems are significantly more interactive that the far-field systems. In far-field type systems (such as toroids and membrane in the middle) the optomechanical system reduces with the optical length of the cavity ($G \propto \frac{1}{L_{\mathrm{cavity}}}$) therefore short cavities are favored in these systems. However, shortening the length of the cavity reduces the mode volume (and therefore the maximum number of photons can be pumped) and reduces the optical linewidth. On the other hand, in near field systems, the optomechanical coupling is not a function of the length of the cavity. In fact in these systems it is favored to work with longer cavities to increase to mode volume and increase the linewidth. In fact systems such as (D) in figure 3.5 (near-field photonic crystals) have too short cavities for no reason and that actually limits their performance because we can not pump more than few 1000s of photons in these short cavities. In summary if we have long enough cavities, near field systems will out perform the far-field systems by orders of magnitudes. This simple fact is the core of our proposed ultra high C_0 architecture.

Whispering gallery mode (WGM) based near-field systems have large cavities, but their fun-

---

[7]In membrane in the middle system we can pump up to $N \sim 10^8$ photons in the cavity [235], micro-toroids up to $N \sim 10^6$ [215]. But for photonic crystal systems because of their extremely small mode volume, it is difficult to pump more that few 1000 photon into the cavity before we reach the unset of the two photon absorption [167].

[8]For the breathing mode[236][237][238] of toroids, $L(x) = 2\pi(R+x)$, thus $\alpha = 2\pi$. For membrane in the middles, $L(x) = L_0 + x$, thus $\alpha = 1$

damental issue is that only a small portion of the cavity is interacting with the mechanical oscillator (because of their natural geometry). Therefore by increasing the radius of cavity, actually the percentage of interacting length reduces and results in $G \propto \frac{1}{L_{\text{cavity}}}$ scaling. We can derive this scaling by some back of envelope calculation. We can write the average index of the disk resonator as:

$$n_{\text{avg}} = \frac{n_{\text{ni}} L_{\text{ni}} + n_{\text{i}}(x) L_{\text{i}}}{L_{\text{disk}}} \implies \frac{\partial n_{\text{avg}}}{\partial x} = \frac{\partial n_{\text{i}}}{\partial x} \times \frac{L_{\text{i}}}{L_{\text{disk}}} \tag{3.17}$$

where $n_{\text{ni}}, L_{\text{ni}}$ are the refractive index and the length of the "non-interactive" region of the cavity (yellow region if figure 3.6.A) and $n_{\text{i}}(x), L_{\text{i}}$ are the refractive index and the length of the "interactive" part of the optical micro-disk (the region under the beam.) and $L_{\text{disk}} = L_{\text{i}} + L_{\text{ni}} = 2\pi R$. It can be shown [122] that the interactive part of the beam is almost constant and accounts for less than 5% of the circumference of a micro-disk with typical radius of $\sim 15 - 20 \mu m$. This percentage actually reduces as we move to larger disks. Therefore in these systems, $G \propto \frac{1}{L_{\text{disk}}}$. This issue is illustrated in figure 3.6.
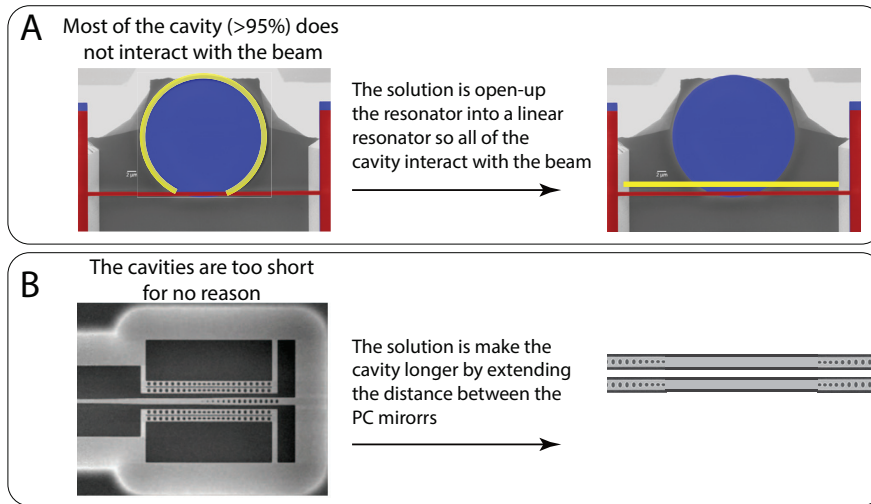
Figure 3.6 – **Fundamental issues with state of the art near-field optomechanical systems.** A) In WGM based near field optomechanical systems, the fundamental issue is that most of the cavity (yellow) does not interact with the mechanical resonator. Therefore these system can not enjoy the favorable scaling by fabricating longer cavities. The solution is to open up the WGM resonator and make is a linear waveguide (yellow line). In this case, the entire length of the cavity interacts with the mechanical beam. We can form a cavity in this scenario by placing photonic crystal (PC) mirrors at each end of the waveguide. B) The fundamental problem of near filed optomechanics system with PC defect mode cavities is that the cavity is too short for no reason. Unlike the far-field systems, having shorted cavities does not increase the optomechanical coupling according to equation (3.16). Because of the their short cavities, the number of the photons we can pump into these systems are very limited which ultimately limits the performance of these systems. On the other hand, silicon is not the best choice of material for the mechanical oscillator as it does not have large intrinsic stress and enjoys the dissipation dilution enhancement.

In equation (3.16) we established that the near field systems are significantly more interactive that the far field systems. If we look at the ratio of the two terms in equation (3.16) we observe:

$$\frac{G_{\text{near-field}}}{G_{\text{far-field}}} = \frac{\partial n}{\partial x} \cdot \frac{\alpha}{n} L_0 \tag{3.18}$$

where $\alpha = \frac{\partial L}{\partial x}$ is a small constant number. Equation (3.18) shows that if we use long cavities, near-field systems can out perform the far-field systems. In addition, in figure 3.3 we show that the sensitivity of refractive index to the mechanical motion is extremely high and could lead to very large interaction strength.

Next we reviewed the two most well known near field optomechanical system in the literature: WGM based near field systems and photonic crystal (PC) based. We observed that unfortunately both of these system have fundamental design flaws that let them to take full advantage of scaling in equation (3.18). This is summarized in figure 3.6. In WGM near-field optomechanical systems, because of the inherent symmetry difference between the beam and the disk, the overlap of the two system is only a fraction of each system's length. That prevents the system to enjoy favorable scaling of G by going to larger cavities. In PC based systems, because of the design of the defect cavities, the optical cavity is too short. In contrast to far-field systems, near-field systems do not benefit from shorter cavities. Shortening the cavity in this case, only reduces the mode volume and therefore the number of the photons that could be pumped into the cavity. It also could lead to lower quality factors if the limiting factor for optical Q is the scattering at the PC mirrors. Another disadvantage of systems presented in figure 3.5.D is that silicon is used for both optical and mechanical resonator. Although crystalline silicon is an excellent optical material, but because it does not have large intrinsic tensile stress, we can not apply the dissipation dilution techniques to increase its quality factor. Therefore, for room temperature quantum optomechanical system, it is best if we use a hybrid structure in which we can take advantages of the both worlds.

In the next section we present our architecture for future quantum optomechanical experiments at room temperature. In this system we try to take advantage of our ultra high Q mechanical oscillators but also by redesigning the optical near-field system, we achieve unprecedented performance compare to any optomechanical system in the past. We will observe that our proposed system is not only quantum enabled at room temperature $Q \times f \gg \frac{k_B T}{h}$ tanks to our UHQ resonators, but offer single photon cooprativity of $C_0 \times 10^4 - 10^5$. In addition, the cavities we used in this system are relativly large and could possible host 100,000 of photon without running into nonlinearities or optical heating effects.

3.3   Quantum enabled ultra high C_0 optomechanical system

The architecture we are proposing is shockingly simple and very similar to the most canonical case of near-field system illustrated in figure 3.2. It consist of the interaction between to straight waveguides. Figure 3.7 shows the 3D rendering of our proposed geometry.

The mechanical element in this optomechanical system consist of a strained enhanced soft-clamped beam (green) designed to operate at its second mode of the defect. Also we have anchored the center of the beam in order to make it mechanically stable and allow for integration of an optical cavity at its few 100 nano-meter proximity without the risk of collapsing. The cavity is made of 20 nm high stress Si_3N_4 layer, and could have the length between 3-7 mm (depending on fabrication difficulties. The longer the beam is, the higher its $Q \times f$ and Q/m will be. But it also become more challenging to fabricate). In chapter1 have already show the preliminary results on the mechanical Q of these anchored beams. Without further optimization, we have already tested beams with similar dimensions and $Q \sim 150$ million at $\Omega_m/2\pi \sim 1$ MHz.

The interesting part about this system is its, optical cavity and its optical design (red). As we discussed in previous section, our design for the optical cavity is incredibly simple. The optical cavity consist of only a straight waveguide placed few hundred nano-meter from the defect of the mechanical resonator. It has almost the same length of the defect mode (half of the physical length of the defect as we work with second order defect mode.). To form a cavity, two optical cavity, we placed two photonic crystal brag mirror reflectors on each end of the optical waveguide, creating essentially a "Fabry–Pérot on waveguide" micro cavity. The cavity is also fabricated from a 400nm high stress Si_3N_4 with the width of the 700nm and designed to operates at wavelength of $\lambda = 1550$ nm. Si_3N_4 is also used for optical cavity as it offers extremely low optical losses [203], and relatively high refractive index in order to generate wide photonic bandgap[242][243]. The motion of the mechanical beam in the evanescent field of the optical cavity, modulates the effective refractive index of the optical mode and thus couples the two system. Near 100% overlap of optical field and mechanical field, leads to a strong optomechanical coupling rate, g_0. between the two degrees on freedom. This combined with the extreme quality factor and small mass of the mechanical oscillator, leads to an unprecedented single photon cooperativity in the range of $C_0 \sim 10^4 - 10^5$.

The optical light is evanescently coupled to the cavity via an optical waveguide with similar dimensions [244]. A tapered fiber also could be used to couple couple light in/out of the cavity[245]. However, based on our previous experience regarding the vibrations of the optical fiber in the experiment, we designed this system with stable and stiff optical waveguide solution. The disadvantage is that we loose the control over the coupling strength and that parameter will be fixed during fabrication but we gained stability in the system . The coupling waveguide is place about $\sim 1\mu$m from the cavity to reach critical coupling condition. The light is coupled in and out of the cavity using a negative tapered design [241]. The negative tapered design matches the impedance of the waveguide to the free space mode of the lensed fiber.
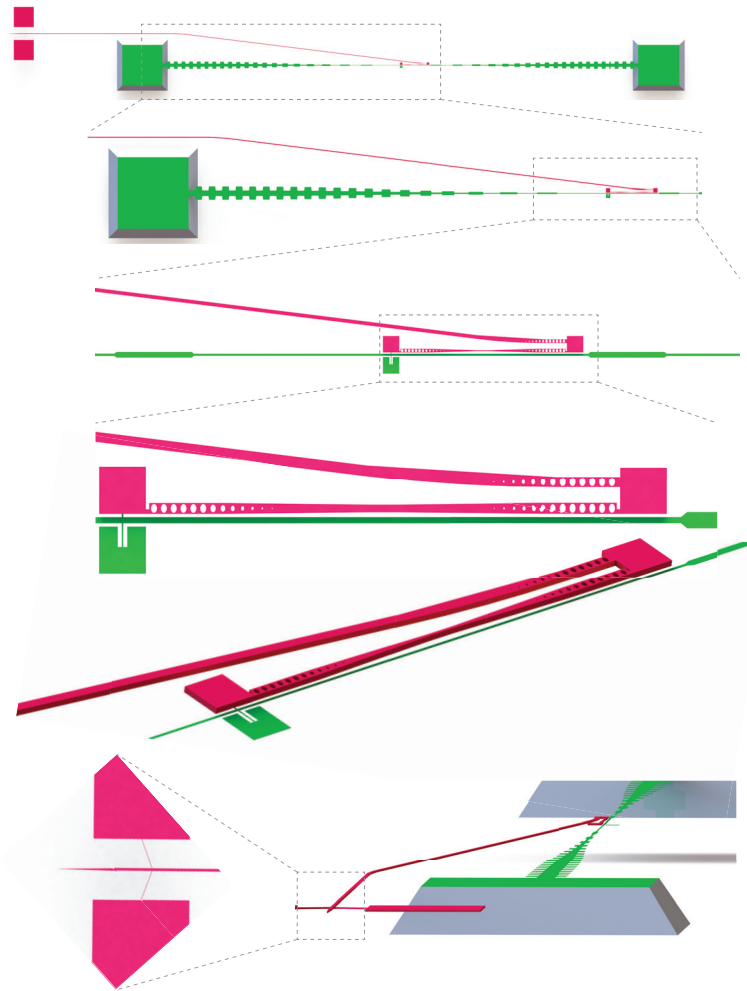
Figure 3.7 – **3D rendering of ultra high C_0 optomechanical system.** Mechanical element (green) is consist of a strained enhanced soft-clamped beam with the length of 4-8 mm and thickness of 20 nm fabricated from high stress Si_3N_4. In chapter 1 we demonstrate $Q \sim 10^9$, $Q \times g \sim 10^{15}$ Hz for the beams with similar dimensions. Here we used 2nd order defect mode with thin anchored at the center of the beam to allow for near field integration without the risk of collapsing the beams and waveguide. The optical element (red) consist of a waveguide with the sample length of the central defect, placed ~ 100nm from the beam. The optical cavity is form by placing two photonic crystal mirrors at the two ends, forming a Fabry–Pérot cavity on the waveguide. The mechanical beam in the evanescent tail of the optical mode of the waveguide, provide a strong optomechanical coupling between the optical and mechanical mode. The near 100% overlap of the two fields, ensures a high coupling rate, g_0. The cavity is pumped evanescently using an optical waveguide of the similar dimensions. The optical light is efficiently coupled from a lensed fiber into the optical waveguide via an inverse-tapered design at the end of the waveguide[241]. The optical cavity and its coupling waveguide are made of 400 nm thick Si_3N_4 layer and have the width of 700 nm. The central part of the waveguide is slightly tapered to allow larger evanescent field on the beam. The designed is optimized for 1550 nm. (the figures are not to scale and are horizontally scratched for perspective.)

In the following we will briefly review few important aspects and preliminary results on the key points of the project and will conclude with a road map for future generation of the students who are interested in implementing this system:

Dimensions of the optical cavity:

The first step of the design, is to select the cross-sectional dimensions of the waveguide. For this designed we only work with horizontal (in-plane) polarization of the light in the waveguide. This is because our simulations showed significantly larger g_0 for this polarization when it is coupled to the out of plane mode of the mechanical resonator. The two main criteria for this selection of cross-sectional dimension of the waveguide is **I)** Waveguide has to stay single mode (at least for the in-plane polarization). This is because photonic crystal mirrors are single mode mirrors and only reflect one mode of the waveguide. **II)** The waveguide has to allow for high refractive index contrast between the holes and the filled regions of the crystal. For the first step of the design, we simulate the mode profile of different cross sections. An example these simulation is illustrated in figure 3.8. These simulations where performed using COMSOL mode analysis package. In figure 3.8 we sweep the width of the waveguide while fixing its thickness. The material refractive index of Si_3N_4 was set at $n_{Si_3N_4} = 2$ and simulation were performed at the optical wavelength of 1550nm.
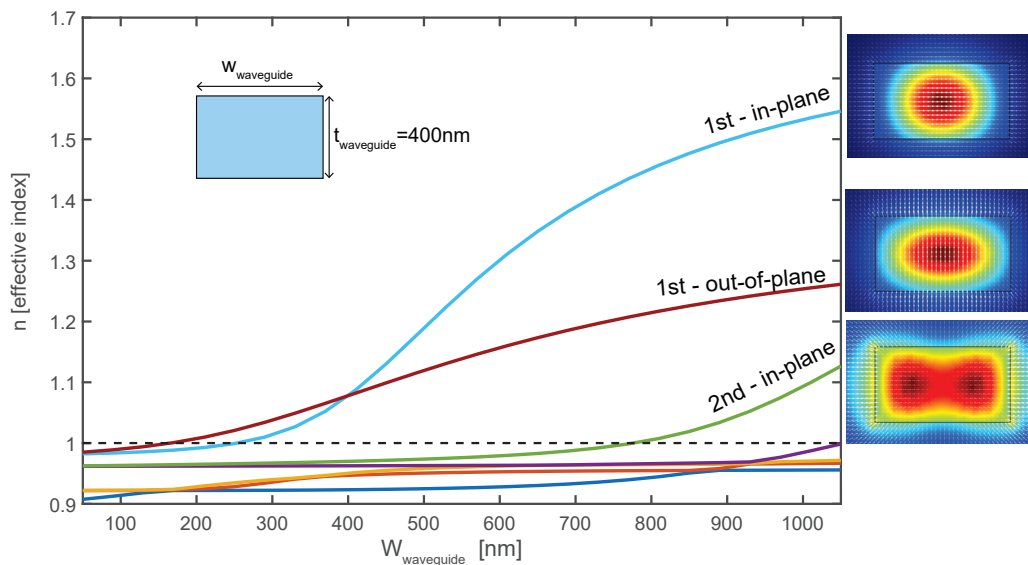
Figure 3.8 – **Waveguide mode simulation at 1550 nm.** Modes below $n = 1$ (dashed line) are not propagative. Inset show the dimensions of the waveguide. The intensity mode shaped are plotted for the three propagative modes. A 400 nm Si_3N_4 is single mode for its in-plane polarization until the width ~ 800 nm.

Many similar simulations were performed where we varied the thickness of the waveguide and look a the width that the waveguide is still single mode. Then we have look at the highest

index that can be achieved while the waveguide is still single mode. For example in 3.8, the highest single mode effective index is $n_{\text{max}} \sim 1.5$. When we drill holes, we alternate between this index and $n \sim 1$. Therefore, the larger the index contrast would be, the larger our bandgap can become. We choose dimensions of 400 nm and 700 nm for the thickness and width of the waveguide at the end of this optimization run.

Simulation of g_0

One we choose the dimensions for the cross section of the waveguide, we can simulate the expected g_0 and C_0 for the system presented in figure 3.7. To calculate g_0, first we need to calculate frequency pulling parameter, G. For this we can use the second term in equation equation (3.16) as $\frac{\partial L}{\partial x} = 0$ in out system.

$$G = \frac{\omega_c}{n} \frac{\partial n}{\partial x} \tag{3.19}$$

To calculate G, we need to simulate $\frac{\partial n}{\partial x}$. For this stimulation we again used COMSOL mode analysis package where we sweep the vertical position of the beam and calculate the effective index of the mode. $\frac{\partial n}{\partial x}$ is then calculated by numerical derivative of $n(x)$. An example of simulations for $\frac{\partial n}{\partial x}$ is presented in figure 3.3. To calculate g_0 we need to know the zero point motion of the oscillator. In chapter 1 we calculate the effective mass of the localized modes at $\Omega_m/2\pi \sim 1$ MHz with the width of 500 nm to be:

$$m_{\text{eff}}(w_{\text{beam}} = 500\text{nm}) \approx 15.1 \text{ pg} \xrightarrow{\Omega_m/2\pi=1 \text{ MHz}} x_{\text{zpm}} = \sqrt{\frac{\hbar}{2m_{\text{eff}}\Omega_m}} \approx 140 \text{ fm} \tag{3.20}$$

An interesting fact about the zero motion of 1D objects is that it is a frequency independent parameter. Because in 1D systems, $\Omega \propto 1/L$, $m_{\text{eff}} \propto L$, thus their product is frequency independent. The zero point motion of the beam, is only a function of the width and the thickness of the beam. Because of the mechanical properties of the beam, we have set the thickness to the thinnest that we can fabricate. However, width is a degree of freedom that we can optimize by choosing the width that maximizes g_0 (the mechanical performance is independent of the width of the beam). But before we optimize the width, lets look at the simulation for g_0.

g_0 as a function of the vertical position of the beam, will follow the same curve as $\frac{\partial n}{\partial x}$ illustrated in figure 3.3. A fortunate non-obvious coincident about the in-plane polarization is that the maximum of g_0 happens when the beam is fabricated either at the bottom or on the top of the beam. This makes the fabrication of the system significantly easier: First a layer of 20 nm for beams can be patterned and etched, then a second layer of 400 nm Si_3N_4 can be deposited on top where we pattern the optical layer (cavity and its waveguide). We will revisit the proposed fabrication process at the end of this section.

Figure 3.9 shows the calculated g_0 as the function of the gap between the mechanical resonator
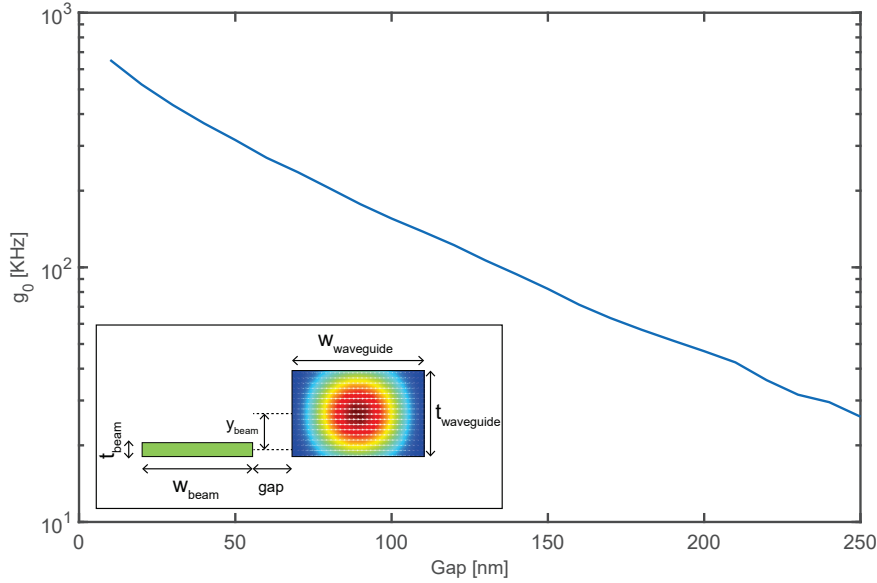
Figure 3.9 – **Simulation of g_0 versus the gap between the waveguide and the mechanical resonator.** g_0 follows an exponential trend when we increase the gap. This suggests that the evanescent field of the waveguide drops exponentially in the air. Parameters for this simulation: $w_{\text{waveguide}} = 700\text{nm}$, $t_{\text{waveguide}} = 400\text{nm}$, $w_{\text{beam}} = 500\text{nm}$, $t_{\text{beam}} = 20\text{nm}$, $t_{\text{beam}} = 200\text{nm}$ (means that the beam is placed at the bottom of the cavity.)

and the cavity. The gap is an important engineering parameter in our near-field system and really the main draw back of the near field systems. As we can see in figure 3.9, the coupling rate (g_0) is an exponential function of the gap. If we could fabricate smaller gaps, we exponentially improve the performance of the system and if we have to back off from the small gaps (because of issues such as collapsing), we exponentially worsen the performance of the system. For this simulation, we first sweep the vertical position to calculate $\frac{\partial n}{\partial x}$ and then we repeat this process for different gaps.

Another important observation from 3.9 is the indescribably high absolute values for g_0 which is on par with the best optomechanical systems in the world [167]. But before we calculate C_0 from these values, lets not forget that our dimensions are not yet optimum and there might be a room for improvement. So far, we have chosen the width and thickness of the waveguide, the vertical position is also set at the bottom of the wave guide, the thickness of the beam is set to 20nm (the thinnest we can fabricate) to determine the mechanical properties of the beam (namely its quality factor). Also figure 3.9 shows that the gap should be as small as we can fabricate. The only remaining degree of freedom is the width of the resonator. In chapter 1 we should that the quality factor of the beam is independent of its width. But we can change the effective mass by tuning the width of the resonator. In one hand, the larger width, increase G as larger mass falls in the evanescent field of the cavity. However, this process saturates as the evanescent fields drops exponentially outside of the waveguide. On the other hand, larger

width results in larger mass and smaller zero point motion. Therefore, we predict that there is an optimum position which g_0 maximizes as the function of width of the resonator.
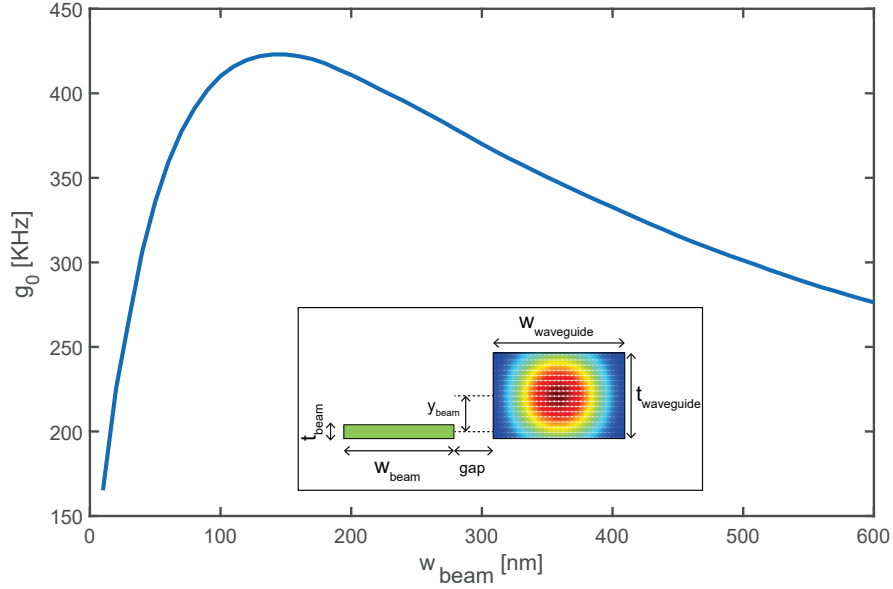
Figure 3.10 – **Optimization of the width of the mechanical oscillator.**In this simulation, we varied the width of the beam ($w_{\text{beam}} = 100$ nm) at a fixed gap=50 nm. The g_0 maximizes at the width of $w_{\text{beam}} \approx 150$ nm with the maximum $g_0/2\pi \approx 450$ KHz. The rest of dimensions are similar to figure 3.9.

In figure 3.10 we try to simulate this effect. What we observe conform our hypothesis. g_0 maximizes at the width of $w_{\text{beam}} \approx 150$ nm with the maximum $g_0/2\pi \approx 450$ KHz. By finding the width of the beam, we select all the cross sectional values of the system. The only remaining design parameter are the photonic crystals to determine the optical quality factor. But before we present the design for the photonic crystal mirrors, lets calculate the single photon cooperativity of this system. The only unknown parameter for us is the optical linewidth. For this we can use the experimental values for the similar geometry that was studied by other groups [246] and achieved $\kappa/2\pi \sim 1.2$ GHz. For our estimation, we will even use lower value of $\kappa/2\pi \sim 4$ GHz.

$$\left.\begin{array}{l} g_0/2\pi = 450 \text{ kHz} \\[2mm] \Gamma_m/2\pi = \dfrac{\Omega_m/2\pi}{Q} = \dfrac{10^6 \text{ Hz}}{100 \times 10^6} = 10 \text{ mHz} \\[2mm] \kappa/2\pi = 4 \text{ GHz} \end{array}\right\} \implies \boxed{C_0 = \dfrac{4g_0^2}{\kappa\Gamma_m} \approx 2 \times 10^4} \qquad (3.21)$$

This value is 4 orders of magnitude larger than the previous generation of optomechanical systems presented in figure 3.5. For completion of this section, let calculate how many intra-cavity photons we need to reach the ground state at room temperature. For a $\Omega_m/2\pi = 1$ MHz oscillator, the thermal occupation is :

$$\bar{n}_{\text{th}} = \frac{k_B T}{\hbar \Omega_m} = 6.2 \times 10^6 \implies C_{\text{cav}}^{GS} \approx 300 \tag{3.22}$$

It means we only need 300 intra-cavity photons to cool this system from room temperature all the way down to is motional ground state. In other words, a factor 6.2 million times cooling by only 300 circulating photons!

With this results, the long standing dream of quantum optomechanics at room temperature is within a reach. However integrating these near field devices are still a technical challenge.

Design of the photonic crystal bandgaps:

The last part of designing this optomechanical system is the design of its optical path, mainly the photonic crystal mirrors and the coupling waveguide. For a photonic crystal we normally have 3 degree of freedom. The length of the pitch and dimensions of the elliptical holes (see inset of figure 3.11). Discussing the details of optimization of the bandgap and geometry of unitcell is beyond the scope of this outlook chapter. But in figure 3.11 we can find an example of such 20 THz wide bandgap. It is important that we try to optimize for larger band-gaps at lower k_x vectors.
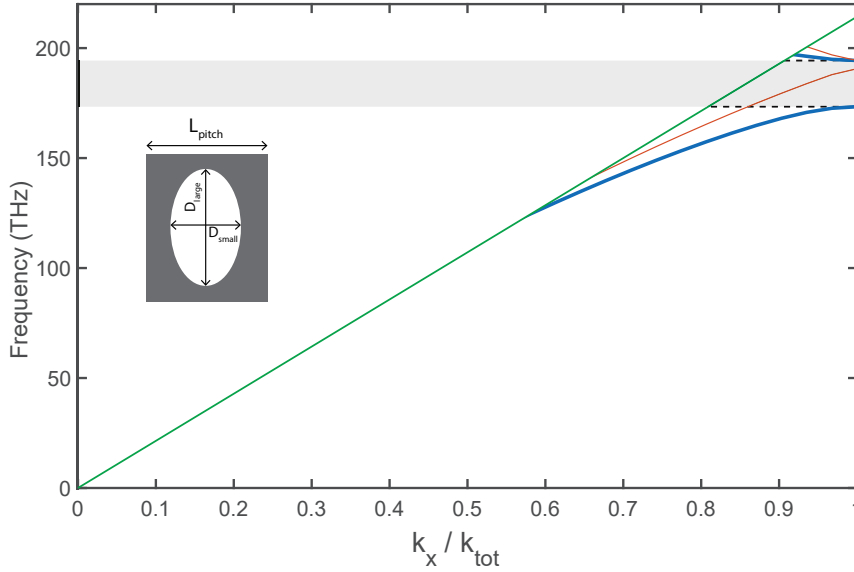
Figure 3.11 – **Example of Si$_3$N$_4$ photonic bandgap.** An example of elliptical unit cell photonic crystal bandgap. Dimension for this simulation are L$_{\text{pitch}}$ = 700nm, D$_{\text{large}}$ = 220nm, D$_{\text{small}}$ = 400nm , w$_{\text{waveguide}}$ = 700nm, t$_{\text{waveguide}}$ = 400nm . Gray area show $\Delta\omega/2\pi \approx 20$ ThHz bandgap centered at 1639 nm for in-plane polarization (blue).

Once the design of the band-gap is completed, we can check the reflectivity of the photonic crystal mirror by performing S parameter simulation. Figure 3.12 shows the example of the geometry to measure the reflectivity of the mirrors. We performed this simulation in using

HFSS -Ansys FEM[247] simulator. For this simulation we lunch electromagnetic waves from one port and look at its reflection and transmission and we repeat the process for the other port. In this way we can calculate the reflection from each side (S_{11}, S_{22}).
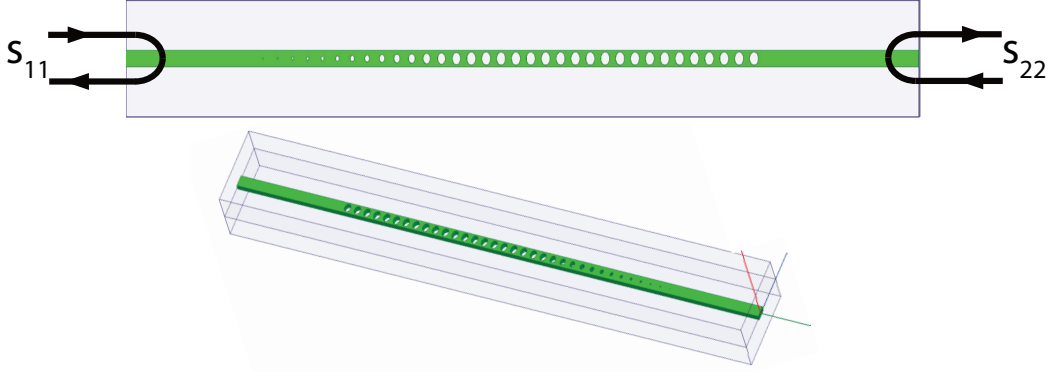
Figure 3.12 – **Simulation setup to measure the reflectivity of PC mirrors**. We perform reflection measurement using FEM simulations by la unching wave at 1550 nm wavelength and observing the reflections from each port, (S-parameters).

In the design of the mirrors, we created a tapered region where the size of the unitcells slowly increases as we penetrate into the PC. This creates an impedance matching condition between the waveguide and the PC region. Figure 3.13 shows the difference between the two situations. Red curve (S_{22}), represents the case where we transit suddenly from the waveguide into the PC mirror region. Since the impedance of the optical waves are different in these two media, such a sharp impedance mismatch creates scattering the border of the two regions. Therefore the reflection of the red curve doesn't approach to 1. But the blue curve S_{11} represents the case where there is taper PC design to creates a smooth transition from the waveguide medium to the PC medium. Such a tapered structure acts as a phase matching connector between the two media where the impedance of the wave planes slowly change so they always remained matched. The longer this transition becomes, the less scattering losses we observe in this transition. We simulate this effect in the inset of figure 3.13 where we increase the number of tapered unitcell from 7 to 15 and then to 30. We plotted the optical finesse of the cavity that is formed by two PC mirrors. Finesse is given by:

$$\mathcal{F} = \frac{1}{1 - r_1 r_2} \tag{3.23}$$

where r_1 and r_2 are the reflectivities of the two mirrors. Here $r_1 = r_2 = S_{11}$. Therefore the parameter plotted in the inset of figure 3.13 is $\mathcal{F} = \frac{1}{1-S_{11}^2}$. In figure 3.13 we can achieve finesses as high as $\mathcal{F} = 2500$. For a cavity with the length of $L_{\text{cav}} \sim 300\mu$m and $n_{\text{eff}} \sim 1.5$, the corresponding Fabry–Pérot optical Q assuming that the material losses are negligible is given by:
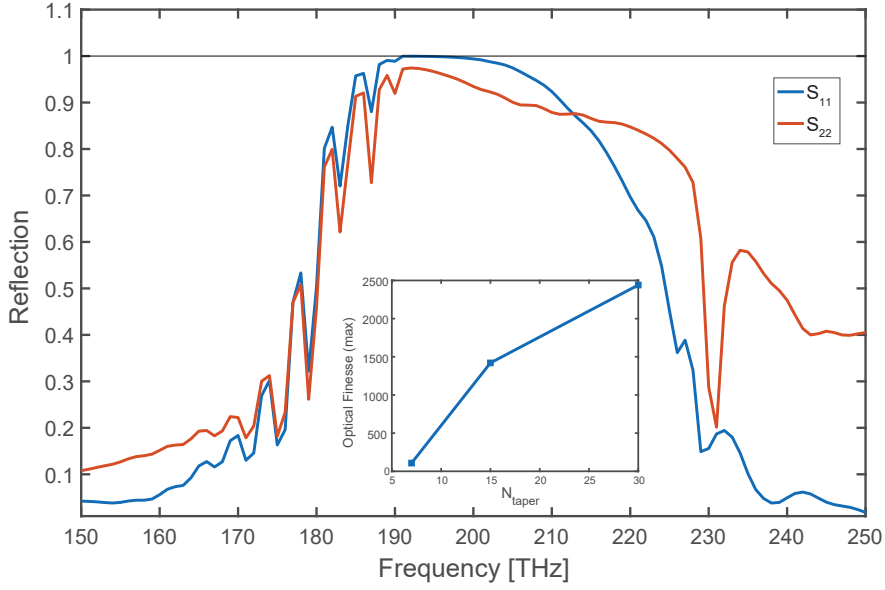
Figure 3.13 – **Reflection simulations for the geometry in figure 3.12**. Red shows the reflection from the side without the phase matching tapering. Without this smooth transition, a lot of scattering is created at the transition from the waveguide to PC region and reflectivity does not approach to 1. Blue shows the case with the tapering structure where a smooth transition from wavegudie to PC region is created and waveplanes remains impedance match. With this tapering strategy, the reflectivity approaches to 1 at the center of the bandgap. Inset shows the optical finesse as the function of number of tapered unitcells. We can achieve finesses as high few thousands with this mirror design. The simulated parameters are $L_{pitch} = 700nm, D_{large} = 540nm, D_{small} = 420nm, w_{waveguide} = 700nm, t_{waveguide} = 400nm$

$$Q_o^{\text{Fabry–Pérot}} = \mathcal{F}\frac{L_{cav}}{n_{eff}\lambda} \approx 3.3 \times 10^5 \implies \kappa/2\pi \approx 600\text{MHz} \tag{3.24}$$

This is a factor of 6, smaller than the κ we used to estimate the lower bound for equation (3.21).

The last topic that we are going to discuss in this section is the simulation of the input/output coupling between the coupling waveguide and the cavity. Figure 3.14 shows an example of input/output coupling simulation between the waveguide and the cavity. In this simulation we used HFSS -Ansys FEM simulation software to simulate the S_{12}. In simulations presented in figure 3.14, we lunch waves at the wavelength of 1550 nm at the bent waveguide and monitors its transmission through the second port at the end of the straight waveguide (cavity). By changing the gap between the two waveguide we can change the external coupling rate. By knowing the intrinsic losses in the cavity κ_0 we can convert the S_{12} coefficient to the external coupling rates κ_{ex} [128].

However, since the losses and κ_0 are still unknown to us, we recommend to the first implementations of this system, the gap between the two waveguide swept experimentally.
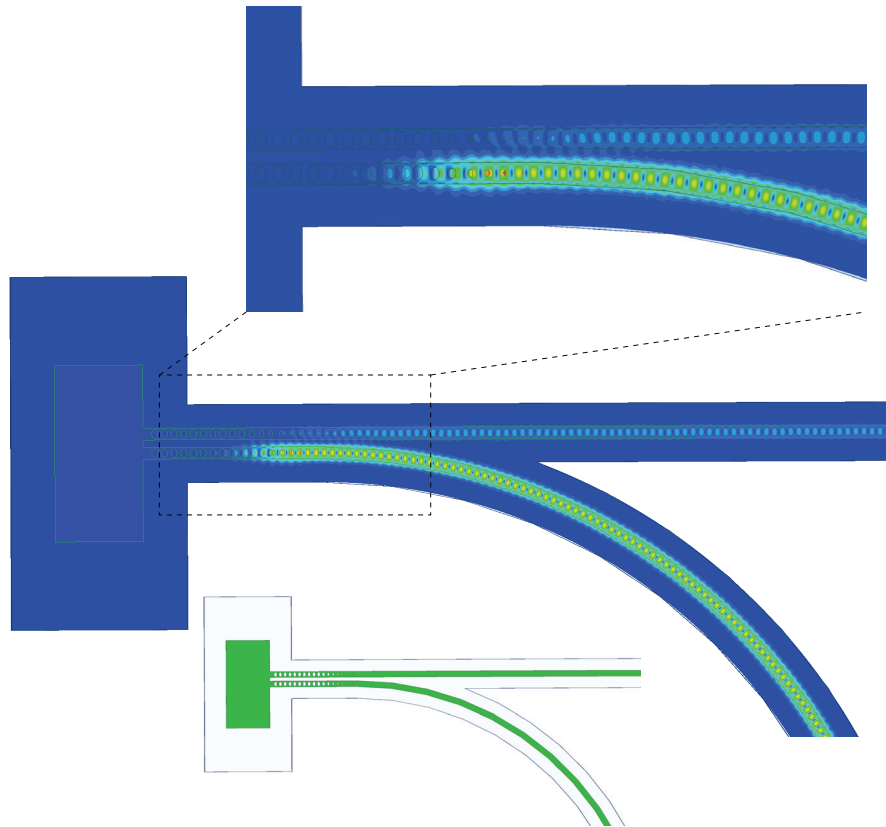
Figure 3.14 – **Example of the FEM input/output simulation.** To simulate the coupling rate between the waveguide and the cavity, a wave is lunched from the curved waveguide and its transmission through the second waveguide is monitors S_{12}. The mechanism of coupling is that the evanescent tails of the mode in the waveguide overlaps with the evanescent tails of the modes in the cavity and an energy transfer bridge is created between the two waveguide. We can change the coupling rate by changing the distance between the coupling waveguide and the cavity.

Proposed fabrication process flow for integration

Figure 3.15 shows the simplified process flow for the integration of the waveguide cavity and UHQ beams. Process starts with LPCVD deposition of the 20 nm high stress Si_3N_4 to form the beam layer (1). Then step (2) we pattern the mechanical beams using ebeam lithography by using HSQ as the resist. Beams are etched in step (3). We have to control the etching parameters in this step to exactly land on the silicon substrate followed by stripping the HSQ in BHF. In this step a 10 nm Al_2O_3 later (light blue) is deposited using atomic layer deposition on top of the beam to form an etch stop layer between the two nitride layers (step 4) . Then the second Si_3N_4 layer is deposited on top using LPCVD deposition (green) with the thickness of 400 nm .This will be our optical layer where optical cavity and its coupling waveguide is pattern using ebeam lithography (step 6). Alignment between the two mechanical and optical masks are the key in this to achieve small gaps. Then the optics layer is etched via
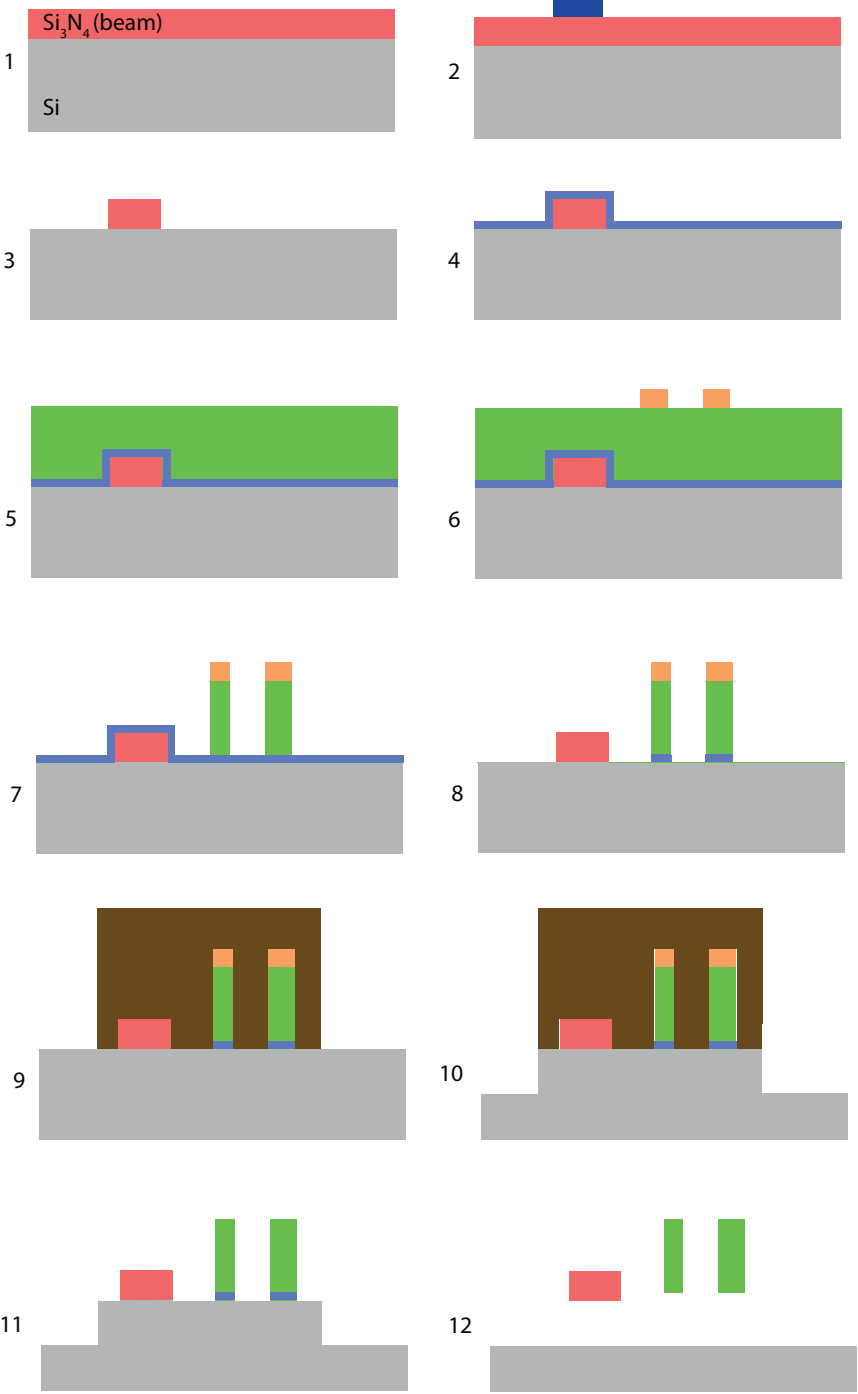
Figure 3.15 – **Proposed process flow for integration of beam and waveguide cavity .**

the Florine chemistry until we land on the Al_2O_3 layer (step 8). The rest of the process from step 9 to step 12 are similar to fabrication of ultra high Q beams. First an upscaled version of

the masked is patterned into a think resist layer and the pattern is then etched deep into the silicon substrate using Bosch process to expose the fast silicon etching faces for KOH undercut step. The upscaled masked is striped in BHF before the KOH (step 11). Finally the samples are released in KOH bath and dried using critical point drier.

We recommend that in the first phase of the implementation, the performance of the cavities and the coupling mechanism is first tested independently. Only when all the aspect of the optical subsystem is fully understood, then we propose to move forward with the full integration of both subsystems. In this regard, I would like to finish this chapter by showing few samples of the waveguide Fabry–Pérot cavities recently fabricate at EPFL as the starting point for the integration:
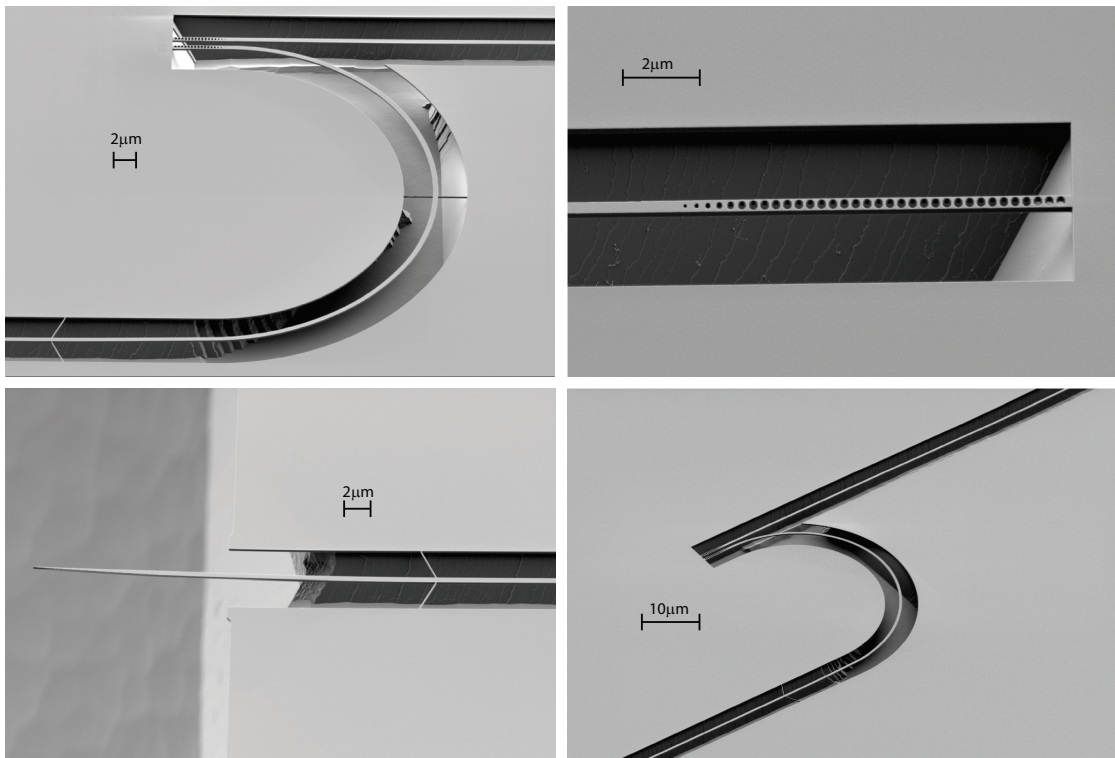
Figure 3.16 – **SEM image of few recently fabricated waveguide Fabry–Pérot cavities.**

A.I Appendix I : Theoretical derivations

A.I.1   Classical simple harmonic oscillator

In this section, we analytically analyze a classical simple harmonic oscillator[1] and drive the solutions for its equations of motion in the time domain (ring-down equation) as well as the frequency domain (mechanical susceptibility), in the most general condition. Next, we discuss the high quality factor regime where $\Omega_m \gg \Gamma_m$, in which the mechanical susceptibility approaches to a Lorentzian line shape near the resonance frequency. At the end of this section, we review the effects of frequency dependent damping rate, $\Gamma_m(\Omega)$, and review different mechanisms of damping such as structural damping versus viscous damping and study their effect on the far off-resonance tails of the mechanical susceptibility.

Eq. (A.I.1) shows the equation of the motion for a classical simple harmonic oscillator.

$$\ddot{x} + \Gamma_m \dot{x} + \Omega_m^2 x^2 = \frac{F_{\text{ext}}}{m_{\text{eff}}} \tag{A.I.1}$$

where Γ_m is the **energy damping rate** and Ω_m is the natural resonance frequency of mechanical oscillator, both expressed in angular units [rad/s], and F_{ext} is the external force applied on the mechanical oscillator. *Effective mass* (m_{eff}) however, has a more complex and ambiguous definition. It is defined together with the amplitude of the $x(t)$ based on the potential energy of the oscillator, $U(t) = \frac{1}{2} m_{\text{eff}} \Omega_m^2 x(t)^2$. For example, in the canonical mass and mass-less spring illustrated in figure A.I.1, the effective mass is equal to the physical mass of the object, $m_{\text{eff}} = m$.

Equation (A.I.1) models any linear resonator, whether if it is a distributed object like a beam

---

[1] In this thesis, a *classical oscillator* is considered an oscillator where its equation of motion is described by Newton's second law of mechanics, Eq. (A.I.1); In contrast, a *quantum oscillator* is an oscillator where its dynamics is governed by Schrodinger's equation:

$$i\hbar \frac{\partial}{\partial t} |\Psi(x,t)\rangle = \hat{H} |\Phi(x,t)\rangle$$

$$\Omega_m = \sqrt{\frac{k}{m}} \qquad\qquad \boldsymbol{\delta\phi} = 4\pi\frac{\delta x}{\lambda}$$
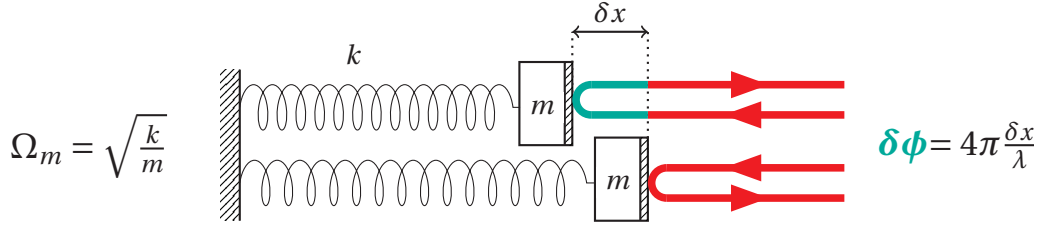
Figure A.I.1 – A canonical example of a mass (mirror) and spring with resonance frequency of Ω_m where the motion of the mechanical oscillator causes a phase shift in the optical laser light with wavelength of λ, shined on the mechanical oscillator. Detecting of the phase fluctuations of reflected light, gives us a measure of mechanical displacement.

or a membrane, or a point shape object like the example in Fig. A.I.1. It can be shown that the effective mass of a doubly clamped beam is roughly equal to the half of beam's physical mass, if the amplitude of the middle part of the beam is chosen for $x(t)$. Therefore, for all intense and purposes, by understanding equation (A.I.1) can understand many aspects of physics governing the high Q resonators:

Mechanical susceptibility :

One of the easiest methods to solve the equation (A.I.1) is to solve it in the frequency domain by taking a Fourier transform from both side of the equation and transform the differential equations to algebraic equations:

$$-\Omega^2 x(\Omega) + i\Gamma_m\Omega x(\Omega) + \Omega_m^2 x(\Omega) = \frac{F_{\text{ext}}}{m_{\text{eff}}} \tag{A.I.2}$$

$$\Rightarrow \chi(\Omega) = \frac{x(\Omega)}{F_{\text{ext}}(\Omega)} = \frac{1/m_{\text{eff}}}{(\Omega_m^2 - \Omega^2) + i\Omega\Gamma_m} \tag{A.I.3}$$

where $\chi(\Omega)$ is the **susceptibility** of the mechanical oscillator and $x(\Omega)$, $F_{\text{ext}}(\Omega)$ are the Fourier transforms of the displacement and external force respectively, according to our definition in section A.I.1:

$$x(\Omega) = \mathcal{F}\Big(x(t)\Big) = \int_{-\infty}^{\infty} x(t)e^{-i\Omega t}dt \tag{A.I.4}$$

$$F_{\text{ext}}(\Omega) = \mathcal{F}\Big(F_{\text{ext}}(t)\Big) = \int_{-\infty}^{\infty} F_{\text{ext}}(t)e^{-i\Omega t}dt \tag{A.I.5}$$

Figure A.I.2 show the spectral density of mechanical susceptibility, $S_{\chi\chi}(\Omega) = \left|\chi(\Omega)\right|^2$ (according to our definition of spectral density in section A.I.1) for different mechanical quality factors where the quality factor is defined as:

$$Q_m \equiv \frac{\Omega_m}{\Gamma_m} \tag{A.I.6}$$
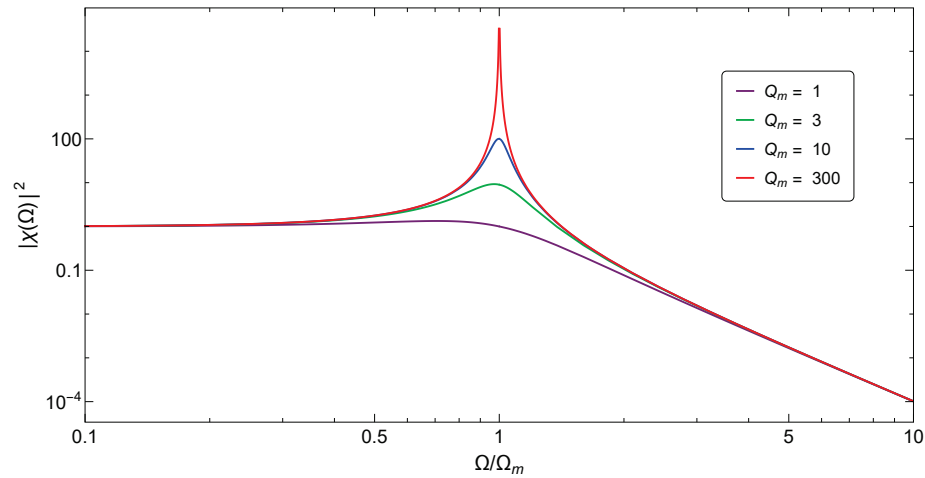
Figure A.I.2 – Spectral density, $S_{\chi\chi}(\Omega) = \left|\chi(\Omega)\right|^2$ of the mechanical susceptibility in the viscous damping regime where $\Gamma_m = $ Const. displayed for different quality factors.

It should be noted that until now, we assumed Γ_m is a constant value with no frequency dependency. This type of damping is known as "viscous damping" where the damping force is proportional to the velocity of the object, $F_{\text{damping}} = -m_{\text{eff}}\Gamma_m\dot{x}$. The constant damping rate can be used to model loss mechanisms such as gas damping [248],[15] but it is shown [108] that it fails to accurately models other damping mechanisms such internal losses (usually caused by friction). Internal losses of a mechanical oscillators is found to obey a more complicated equation where a frequency dependent damping term $\Gamma_m \to \Gamma(\Omega)$ is required to accurately fit the observed mechanical spectrum in the experiments[39]. We will discuss this point at the end of this section and will describe alternative models such "structural damping" [249] that can properly model the internal losses. We will illustrate the effect of frequency dependent damping rate, $\Gamma(\Omega)$, on the off-resonance tails of the mechanical susceptibility.

Impulse response :

In the next step, we look at the time domain response of the equation (A.I.1) . In order to properly calculate the time domain response, we have to know the spectrum of the applied external force, $F_{\text{ext}}(\Omega)$. However without loosing the generality, we can can calculate the

"impulse response" of the simple harmonic oscillator[2]. where:

$$F_{\text{impulse}}(t) = \Delta P \delta(t) \tag{A.I.10}$$

we will observe in the following that a delta Dirac excitation with amplitude of ΔP will transfer momentum of ΔP to the oscillator at $t = 0$. Another advantage of studying the impulse response is that the Fourier transform of the of the delta function is a constant, $\mathcal{F}\left(\delta(t)\right) = 1$.[3] This simplifies the the frequency response of $x(\Omega)$:

$$x_{\text{imp}}(\Omega) = \Delta P \chi(\Omega) = \frac{\Delta P / m_{\text{eff}}}{(\Omega_m^2 - \Omega^2) + i\Omega\Gamma_m} \tag{A.I.12}$$

to calculate the time domain impulse response we need to calculate the inverse Fourier transform of $x_{\text{imp}}(\Omega)$:

$$x_{\text{imp}}(t) = \mathcal{F}^{-1}\left(x_{\text{imp}}(\Omega)\right) = \frac{1}{2\pi}\int_{-\infty}^{\infty}\frac{\Delta P / m_{\text{eff}}}{(\Omega_m^2 - \Omega^2) + i\Omega\Gamma_m}e^{i\Omega t}d\Omega \tag{A.I.13}$$

calculating the integral in the equation (A.I.13) is a difficult task. Instead we try to simplify the eq. (A.I.12) and use the Fourier transform of some standard functions with knows reverse Fourier transform:

$$x_{\text{imp}}(\Omega) = \frac{\Delta P / m_{\text{eff}}}{(\Omega_m^2 - \Omega^2) + i\Omega\Gamma_m} = \frac{\Delta P / m_{\text{eff}}}{\underbrace{\Omega_m^2 - \left(\frac{\Gamma_m}{2}\right)^2}_{\tilde{\Omega}_m^2} + \underbrace{\left(\frac{\Gamma_m}{2}\right)^2 + i\Omega\Gamma_m - \Omega^2}_{\left(\frac{\Gamma_m}{2} + i\Omega\right)^2}} \tag{A.I.14}$$

$$= \frac{\Delta P / m_{\text{eff}}}{\left(\frac{\Gamma_m}{2} + i\Omega\right)^2 + \tilde{\Omega}_m^2} = \frac{\Delta P}{2\tilde{\Omega}_m m_{\text{eff}}}\left[\frac{i}{\Gamma_m + i(\Omega + \tilde{\Omega}_m)} - \frac{i}{\Gamma_m + i(\Omega - \tilde{\Omega}_m)}\right] \tag{A.I.15}$$

---

[2] By knowing the impulse response, $X_{\text{imp}}(t) = \hat{\mathcal{O}}[\delta(t)]$, of a linear differential equation, $\hat{\mathcal{O}}[F(t)]$, we can calculate the response of the system to any external fores by as shown in the following:

$$F_{\text{ext}}(t) = \int_{-\infty}^{\infty}F_{\text{ext}}(\tau)\delta(t - \tau)d\tau \tag{A.I.7}$$

The response of the $\hat{\mathcal{O}}[F_{\text{ext}}(t)]$ is the "convolution" of the external force and impulse response of the system:

$$x(t) = \hat{\mathcal{O}}[F_{\text{ext}}(t)] = \int_{-\infty}^{\infty}F_{\text{ext}}(\tau)\mathcal{O}[\delta(t - \tau)]d\tau = \int_{-\infty}^{\infty}F_{\text{ext}}(\tau)X_{\text{imp}}(t - \tau)d\tau = F_{\text{ext}} \circledast X_{\text{imp}} \tag{A.I.8}$$

where $\circledast$ is operator for convolution and is defined as:

$$f \circledast g = \int_{-\infty}^{\infty}f(\tau)g(t - \tau)d\tau \tag{A.I.9}$$

[3] This can prove by writing down the Fourier transform equation:

$$\mathcal{F}\left(\delta(t)\right) = \int_{-\infty}^{\infty}\delta(t)e^{-i\Omega t}dt = e^{-i\Omega \times 0} = 1 \tag{A.I.11}$$

it is now much simpler to take the reverse Fourier transform of the last two terms of the equation (A.I.15) as we know the Fourier transform of a function in this form[4]. Based on the equation (A.I.18), the reverse Fourier transform the last two terms of eq. (A.I.15) can be written as:

$$\mathcal{F}^{-1}\left(\frac{i}{\Gamma_m + i(\Omega + \tilde{\Omega}_m)}\right) = ie^{\frac{-\Gamma_m}{2}t}e^{-i\tilde{\Omega}_m t}u(t) \tag{A.I.19}$$

$$\mathcal{F}^{-1}\left(\frac{i}{\Gamma_m + i(\Omega - \tilde{\Omega}_m)}\right) = ie^{\frac{-\Gamma_m}{2}t}e^{i\tilde{\Omega}_m t}u(t) \tag{A.I.20}$$

Using eq.(A.I.19) and (A.I.20), and converting the polar form of the complex numbers to their rectangular form[5] we can calculate the time domain impulse response:

$$x_{\text{imp}}(t) = \mathcal{F}^{-1}\left(x_{\text{imp}}(\Omega)\right) = \frac{\Delta P}{2\tilde{\Omega}_m m_{\text{eff}}}\left[ie^{\frac{-\Gamma_m}{2}t}e^{-i\tilde{\Omega}_m t}u(t) - ie^{\frac{-\Gamma_m}{2}t}e^{i\tilde{\Omega}_m t}u(t)\right] \tag{A.I.22}$$

$$= \frac{\Delta P}{2\tilde{\Omega}_m m_{\text{eff}}}e^{\frac{-\Gamma_m}{2}t}\left[\underbrace{ie^{-i\tilde{\Omega}_m t} - ie^{i\tilde{\Omega}_m t}}_{2\sin(\tilde{\Omega}t)}\right]u(t) \tag{A.I.23}$$

therefore $x_{\text{imp}}(t)$ simplifies to:

$$\boxed{x_{\text{imp}}(t) = \frac{\Delta P}{\tilde{\Omega}_m m_{\text{eff}}}e^{\frac{-\Gamma_m}{2}t}\sin\left(\tilde{\Omega}_m t\right)u(t) \quad , \quad \tilde{\Omega}_m = \sqrt{\Omega_m^2 - \left(\frac{\Gamma_m}{2}\right)^2}} \tag{A.I.24}$$

Figure A.I.3 illustrates the time domain impulse reposes a simple harmonic oscillator. We can see that the delta force gives the oscillator a kick at $t = 0$ and but the oscillation amplitude damps with the damping rate of $\Gamma_m/2$ as the time passes (illustrated with the dashed lines as the envelope in Figure A.I.3).

---

[4] To calculate the reverse Fourier transform of eq. (A.I.15) we need the two following Fourier transforms:

1. First the Fourier transform of a decaying exponential:

$$g(t) = e^{-at}u(t) \quad \longrightarrow \quad \hat{g}(\Omega) = \mathcal{F}\left(g(t)\right) = \frac{1}{a + i\Omega} \tag{A.I.16}$$

where $u(t)$ is the step function with the following definition:

$$u(t) = \begin{cases} 1 & \text{if } n \geq 1 \\ 0 & \text{if } n < 0 \end{cases} \tag{A.I.17}$$

2. Frequency shift in Fourier domain:

$$g(t) = e^{i\Omega' t}f(t) \quad \longrightarrow \quad \hat{g}(\Omega) = \mathcal{F}\left(g(t)\right) = \hat{f}(\Omega - \Omega') \tag{A.I.18}$$

[5] Any complex number, C can be written as the following:

$$C = Ae^{i\theta} = A\cos(\theta) + iA\sin(\theta) \tag{A.I.21}$$
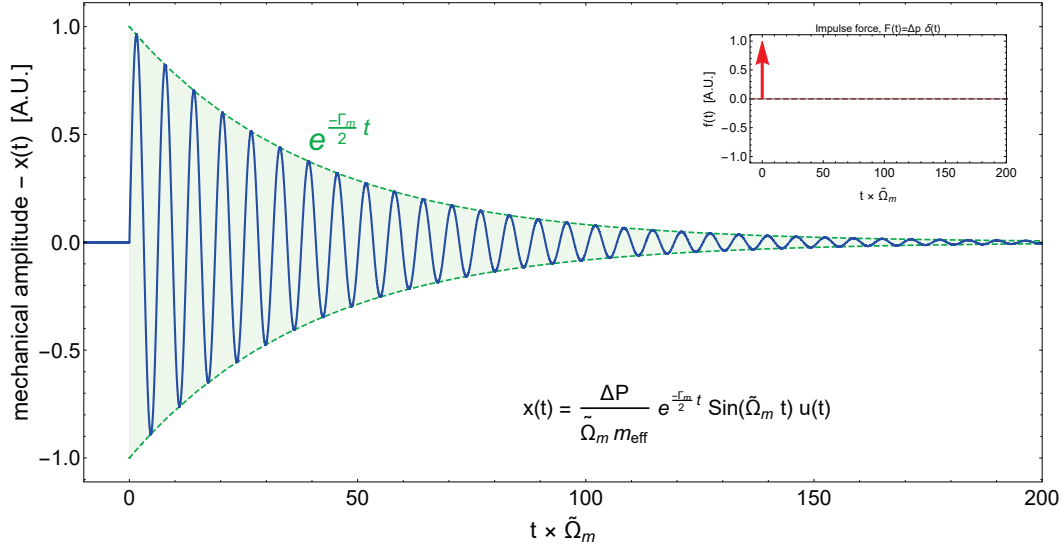
Figure A.I.3 – Impulse response of a simple harmonic oscillator with $Q = 20$. Dashed green lines show the exponential decaying envelope of the damped oscillation. Inset shows the delta Dirac impulse force applied at $t = 0$ to the oscillator.

High Q regime and Lorentzian lineshape :

Before going any deeper into the physics of the damped simple harmonic oscillators, it is insightful to study at the high Q regime where $Q_m \gg 1 \Rightarrow \Omega_m \gg \Gamma_m$. This regime is the most relevant for the mechanical oscillators discussed in this thesis where we can greatly simplify the time domain solutions as well as the mechanical susceptibility (figure A.I.2) especially its resonance frequency. First we simplify the power spectral density of the mechanical susceptibility near its resonance frequency using our derivation in equation (A.I.14):

$$\chi(\Omega) = \frac{1/m_{\text{eff}}}{(\Omega_m^2 - \Omega^2) + i\Omega\Gamma_m} = \frac{1}{m_{\text{eff}}} \times \frac{1}{\Gamma_m + i(\Omega + \tilde{\Omega}_m)} \times \frac{1}{\Gamma_m + i(\Omega - \tilde{\Omega}_m)} \tag{A.I.25}$$

$$S_{\chi\chi}(\Omega) = \left|\chi(\Omega)\right|^2 = \frac{1}{m_{\text{eff}}^2} \times \frac{1}{|\Gamma_m + i(\Omega + \tilde{\Omega}_m)|^2} \times \frac{1}{|\Gamma_m + i(\Omega - \tilde{\Omega}_m)|^2} \tag{A.I.26}$$

where $\tilde{\Omega}_m = \sqrt{\Omega_m^2 - \left(\frac{\Gamma_m}{2}\right)^2}$. Near the resonance frequency, $\Omega \sim \Omega_m$ we can use the following simplifications:

$$\boxed{\Omega \sim \Omega_m \quad , \quad \Omega_m \gg \Gamma_m \Longrightarrow \begin{cases} \tilde{\Omega}_m \longrightarrow \Omega_m \\ |\Gamma_m + i(\Omega + \tilde{\Omega}_m)|^2 \longrightarrow 4\Omega_m^2 \end{cases}} \tag{A.I.27}$$

with this assumptions, we can simplify the power spectral density to:

$$S_{\chi\chi}(\Omega) = \left|\chi(\Omega)\right|^2 = \frac{1}{4m_{\text{eff}}^2\Omega_m^2} \times \frac{1}{(\Omega - \Omega_m)^2 + \Gamma_m^2} = \frac{\pi}{2m_{\text{eff}}^2\Omega_m^2}\mathcal{L}(\Omega - \Omega_m, \Gamma_m) \tag{A.I.28}$$

where $\mathcal{L}(\Omega, \Gamma)$ is known as "Lorentzian lineshape" and defined as the following:

$$\mathcal{L}(\Omega, \Gamma) = \frac{\Gamma/2\pi}{(\Omega)^2 + (\Gamma/2)^2} \tag{A.I.29}$$

in which:

$$\int_{-\infty}^{\infty} \mathcal{L}(\Omega, \Gamma) d\Omega = 1 \tag{A.I.30}$$

Lorentzian lineshape is very useful is describing the physics of linear cavities. As demonstrated in eq. (A.I.28), the spectral shape (or the power transfer function) of any linear high Q resonator, whether it is mechanical, optical or electrical, can be approximated by a Lorentzian lineshape near its resonance frequency. Figure A.I.4 shows the Lorentzian lineshape for $Q = 10$.
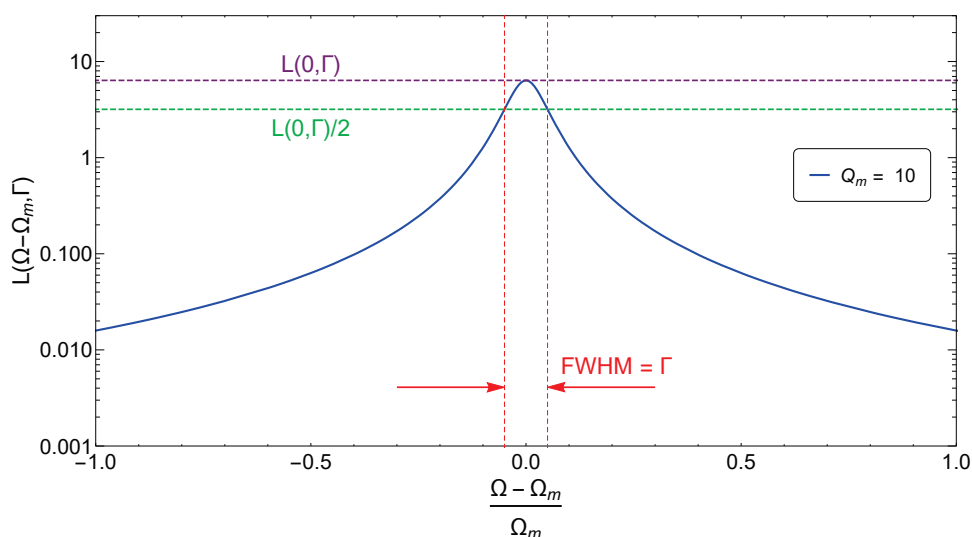
Figure A.I.4 – Lorentzian linewidth for the oscillator with $Q = 10$ plotted in the normalized frequency. "*Full Width Half Maximum*" (FWHM) is equal to the oscillator **energy** damping rate, Γ.

It should be noted that Γ is usually known as the "*Full Width Half Maximum*" (FWHM) especially in the field of optics and microwaves. This is because:

$$\mathcal{L}(\pm\Gamma/2, \Gamma) = \frac{1}{2}\mathcal{L}(0, \Gamma) \tag{A.I.31}$$

as illustrated in figure A.I.4 , the full width where the Lorentzian is equal to the half of its peak value, is equal to FWHM = Γ.

The consequences of the high Q, illustrated in eq. (A.I.27) also helps to simplify the time domain impulse response:

$$\Omega_m \gg \Gamma_m \Longrightarrow x_{\mathrm{imp}}(t) = \frac{\Delta P}{\Omega_m m_{\mathrm{eff}}} e^{\frac{-\Gamma_m}{2}t} \sin(\Omega_m t) u(t) \tag{A.I.32}$$

Energy decay rate versus amplitude decay rates:

In the next step, ts it useful to look at the evolution of energy of the oscillator over time and calculate its decay rate and compare it to the amplitude decay rate we calculate in (A.I.32) to be $\Gamma_m/2$. For this first we need to calculate the velocity of the oscillator by taking a derivative of the equation (A.I.32) :

$$\dot{x}_{\text{imp}}(t) = \frac{\Delta P}{m_{\text{eff}}} e^{\frac{-\Gamma_m}{2}t} \cos(\Omega_m t) u(t) - \underbrace{\frac{1}{2Q_m} \times \frac{\Delta P}{m_{\text{eff}}} e^{\frac{-\Gamma_m}{2}t} \sin(\Omega_m t) u(t)}_{\approx 0 \,,\, \text{negotiable compare to first term}} \tag{A.I.33}$$

$$\dot{x}_{\text{imp}}(t) \approx \frac{\Delta P}{m_{\text{eff}}} e^{\frac{-\Gamma_m}{2}t} \cos(\Omega_m t) u(t) \tag{A.I.34}$$

the first observation from equation (A.I.34) is that the momentum at $t = 0$, is equals to

$$P(t = 0) = m_{\text{eff}} \cdot \dot{x}_{\text{imp}}(t = 0) = \Delta P \tag{A.I.35}$$

this proves our previous statement that a delta Dirac impulse force with amplitude of Δp acts as in instant kick to the oscillator and transfers the momentum δP to it at $t = 0$.

We can calculate the total energy of the oscillator from eq. (A.I.34) and (A.I.32) to be:

$$U_p(t) = \frac{1}{2} m_{\text{eff}} x(t)^2 \Omega_m^2 = \frac{\Delta P^2}{2 m_{\text{eff}}} e^{-\Gamma_m t} \sin^2(\Omega_m t) u(t) \tag{A.I.36}$$

$$U_k(t) = \frac{1}{2} m_{\text{eff}} \dot{x}(t)^2 = \frac{\Delta P^2}{2 m_{\text{eff}}} e^{-\Gamma_m t} \cos^2(\Omega_m t) u(t) \tag{A.I.37}$$

$$\boxed{U_{\text{tot}}(t) = U_k(t) + U_p(t) = \frac{\Delta P^2}{2 m_{\text{eff}}} e^{-\Gamma_m t} u(t)} \tag{A.I.38}$$

Equations (A.I.36), (A.I.37), (A.I.38) shows that energy decay as $U(t) \propto e^{-\Gamma_m t}$ and amplitude as $x(t) \propto e^{-\frac{\Gamma_m}{2}t}$. In summary:

$$\text{Energy decay rate} \longrightarrow \Gamma_m$$

$$\text{Amplitude decay rate} \longrightarrow \frac{\Gamma_m}{2}$$

This is a simple but important outcome for experimentalists working with high Q resonators. As we will see in chapter 1, a common experimental method to measure the mechanical quality factors of a high Q mechanical oscillator is to drive them using an external drive such as piezo drive, and by turning off the drive observe the free oscillations of the resonator as it looses the

energy. A method know as "*ringdown*" method. By fitting the envelope to an exponential, we can measure the damping rate of the oscillation. However we should be careful if we are fitting to the amplitude ($\propto x(t)$) or the energy of the oscillation ($\propto x(t)^2$) as these two lead to two different damping rates.

Another definition in this regard is the time constant or lifetime of the oscillator defined as the following:

$$\tau \equiv 1\Gamma_m \tag{A.I.39}$$

During the time span of τ, a free oscillating resonator looses $1 - e^{-1} = 63\%$ of its initial energy. Normally a lifetime of a classical oscillator is consider to be 5τ where in which the oscillator looses $1 - e^{-5} = 99\%$ of its initial energy. We will observe in chapter 3 that τ is also the time constant that a classical oscillator exchange fluctuation with it thermal environment.

Driven step response and mechanical ringdown:

Fo completion of this section, lets consider a more physical scenario. It should be noted that in the real experiments, we do not have access to a delta Dirac excitation force ($F_{\text{ext}} = \Delta P \delta(t)$). An ideal ringdown measurement performs as the following: First we drive the mechanical mode of the interest with an oscillatory force in resonance with the natural resonance frequency of the mode, Ω_m, then turn off the force at $t = 0$ and observe the decay of the free oscillations of the mechanical oscillator. Therefore the applied force in a real ringdown experiment illustrate in figure A.I.5 and has following derivation:

$$F_{\text{ringdown}}(t) = \Gamma_m \sqrt{2m_{\text{eff}}U_0} \sin(\Omega_m t) u(-t) \tag{A.I.40}$$

where U_0 is the energy of the oscillator during the driving period. We can calculate the step response of the mechanical oscillator by convolution eq. (A.I.40) and (A.I.32) according to our derivation at eq. (A.I.9) :

$$x_{\text{ringdown}}(t) = -\frac{\sqrt{2U_0/m_{\text{eff}}}}{\Omega_m} \cos(\Omega_m t) \left(1 + (e^{-\frac{\Gamma_m}{2}t} - 1) u(t)\right) \tag{A.I.41}$$

$$U(t) = U_0 \left(1 + (e^{-\Gamma_m t} - 1) u(t)\right) \tag{A.I.42}$$

figure A.I.5 shows the ringdown of the oscillator in response to a driving force highlighted in equation (A.I.40). We can see that for the times $t < 0$ oscillator follows the driving force with 90 degree phase lag and for $t > 0$ where the drive is off, resonators starts is free ringdown until it is completely damped.

For completion of this section, it should be noted that due to technical challenges, the ring-
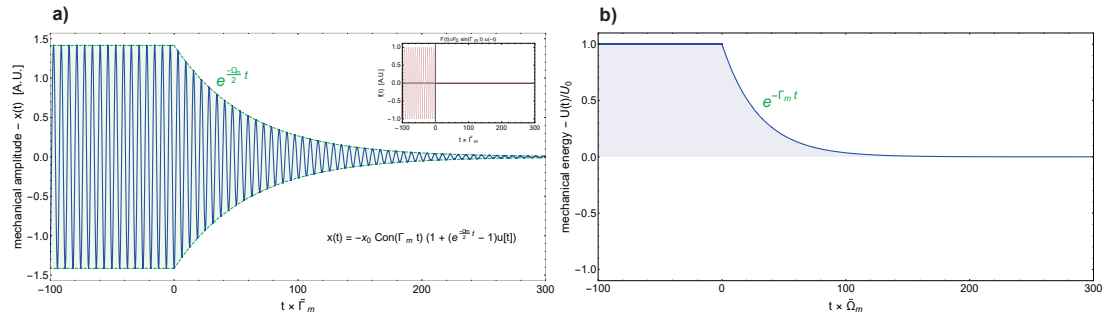
Figure A.I.5 – a) Ringdown of the mechanical oscillator with Q=30 to a sinusoidal force that turns off at $t = 0$ (inset). b) The total energy of the oscillator as a function of time. The energy decay rate Γ_m is two times the decay rate of the amplitude, $\Gamma_m/2$

down method describe above is not actually the procedure we used in the experiment in section 1 to measure ultra high mechanical resonators. In the real experiments, when dealing with mechanical resonators with extreme Q factors (e.g. $Q > 10^8$), it is difficult to lock to the resonance frequency of the resonator and constantly drive it before turning off the drive. This is because the strong resonance frequency fluctuations of the oscillator which is are much larger than its linewidth, $\Delta\Omega_{RMS} \gg \Gamma_m$, for UHQ resonators. The actual measurement apparatus is described is chapter 1 but in summary, in the actual experiment we sweep the frequency of the drive around the resonance frequency of the mechanical resonator. For a brief amount of time, our drive will be on-resonance with the oscillator which is enough to excite the oscillation to a level where we can detect the amplitude with acceptable signal to noise. Once the mechanical amplitude reaches a certain threshold, the drive turns off and we observe the free oscillation of the resonator and determine the Q by fitting and exponential to its ringdown. In that sense, our experimental approach in closer to a δ excitation and the impulse response since the resonator and drive are interacting for a very brief time when they are in-resonance.

PnC band diagram of a periodic mass and spring:

In this section we will analytically calculate the dispensation diagram of the canonical example of a phononic crystal where an infinite chain unitcells with two different masses and a identical strings are connected to each other (see figure A.I.6)
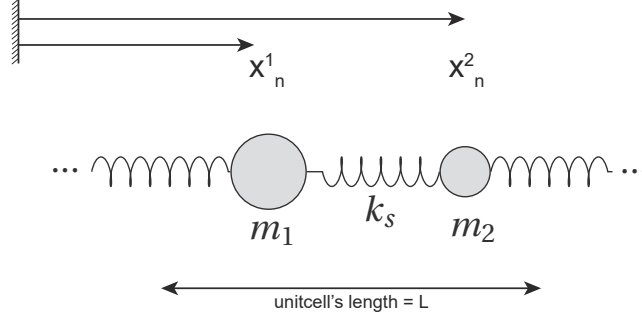
Figure A.I.6 – A canonical example of a phonoic crystal unitcell with two different masses, m_1, m_2 as connected in an infinite chain via the identical spring with the spring constant of k_S

The Newtonian equations of motion governing the dynamics of the two masses of the unitcell is given by:

$$\begin{cases} m_n^1 \ddot{x}_n^1 = k_s(x_n^2 - x_n^1) - k_s(x_n^1 - x_{n-1}^2) \\ m_n^2 \ddot{x}_n^2 = k_s(x_{n+1}^1 - x_n^2) - k_s(x_n^2 - x_n^1) \end{cases} \tag{A.I.43}$$

We can solve these equations of motion in the Fourier domain (assuming both resonators are oscillating at the same frequency):

$$\begin{cases} -\left(\frac{\Omega}{\Omega_1}\right)^2 x_n^1 = x_n^2 - 2x_n^1 + x_{n-1}^2 \\ \\ -\left(\frac{\Omega}{\Omega_2}\right)^2 x_n^2 = x_{n+1}^1 - 2x_n^2 + x_n^1 \end{cases} \tag{A.I.44}$$

Where $\Omega_1^2 = \frac{k_s}{m_1}$, $\Omega_2^2 = \frac{k_s}{m_2}$ are the natural resonance frequency of the individual pieces of the unitcell. Now since we a a periodic condition with transnational symmetry, the Floquet boundary condition dictates that the displacements are also periodic in x direction as:

$$\begin{cases} x_n^1 = A_1 e^{i\lambda(n-\frac{1}{2})} \\ x_n^2 = A_2 e^{i\lambda(n+\frac{1}{2})} \end{cases} \tag{A.I.45}$$

where A_1, A_2 are the amplitudes of motion for the two oscillator and λ is the special frequency

173

motion. Equation (A.I.44) reduces to:

$$\begin{cases} -\left(\frac{\Omega}{\Omega_1}\right)^2 A_1 e^{-\frac{i\lambda}{2}} = A_2 e^{\frac{i\lambda}{2}} + A_2 e^{-\frac{i\lambda}{2}} - 2A_1 e^{-\frac{i\lambda}{2}} \\ \\ -\left(\frac{\Omega}{\Omega_1}\right)^2 A_2 e^{\frac{i\lambda}{2}} = A_1 e^{-\frac{i\lambda}{2}} + A_1 e^{\frac{i\lambda}{2}} - 2A_2 e^{\frac{i\lambda}{2}} \end{cases} \implies \begin{cases} -\left(\frac{\Omega}{\Omega_1}\right)^2 = 2\alpha\cos(\lambda/2) - 2 \\ \\ -\left(\frac{\Omega}{\Omega_2}\right)^2 = \frac{2}{\alpha}\cos(\lambda/2) - 2 \end{cases} \qquad \text{(A.I.46)}$$

where $\alpha = \frac{A_2}{A_1 e^{-\frac{i\lambda}{2}}}$. The equation (A.I.46) is a second order equation that can be solved. The solutions to this equation is:

$$\Omega_\pm = \sqrt{(\Omega_1^2 + \Omega_2^2) \pm \sqrt{(\Omega_1^2 + \Omega_2^2)^2 - 4\Omega_1^2\Omega_2^2\sin^2(\lambda)}} \qquad \text{(A.I.47)}$$
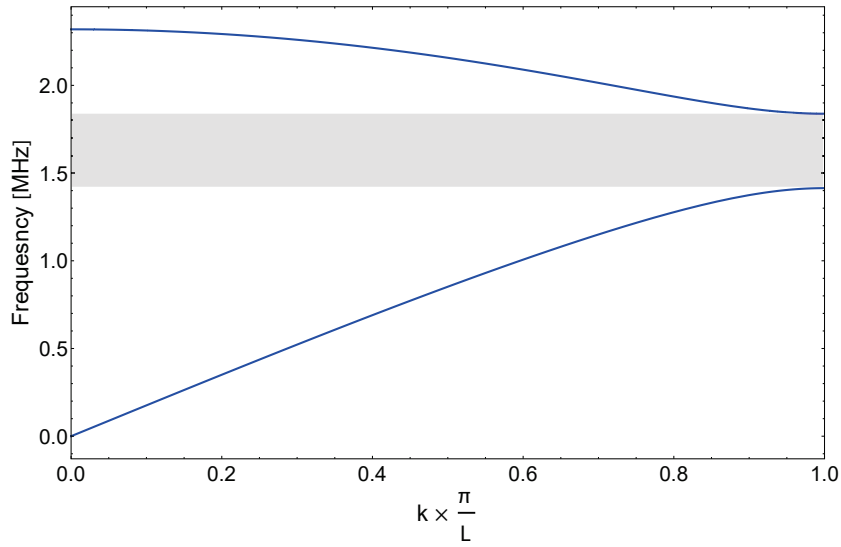
Figure A.I.7 – Dispersion diagram for the cavonical phononic crystals when $\Omega_1/2\pi = 1$ MHz and $\Omega_2/2\pi = 1.3$ MHz

Figure A.I.7 shows the plot of Ω_+ and Ω_- for the resonance frequencies of $\Omega_1/2\pi = 1$ MHz and $\Omega_2/2\pi = 1.3$ MHz.

Now we can calculate the width of the bandgap to be:

$$\Delta\Omega_{\text{BG}} = \Omega_+(1) - \Omega_-(1) = \sqrt{2}|\Omega_2 - \Omega_1| \qquad \text{(A.I.48)}$$

Therefore the width of the band gap depend on the frequency (mass) difference between the two pieces of the unitcell.

A.II Appendix II : Ultra high vacuum chamber

A.II.1   Gas damping in high Q mechanical oscillators

One of the major limitations of working with ultra high Q mechanical oscillator is the gas damping effect [250][251] [252][248][95]. In to supress gas damping, operate our measurement in an ultra high vacuum (UHQ) chamber. But to design this chamber, we need to at which pressure our experiments has to operate before we design the vacuum chamber. An analytical derivation on gas damping can be found at [253]. It can be shown that there are two regimes with different scaling laws for pressure in the gas damping[254]:

- Free molecular flow (FMF) regime at low pressures (P) where $Q_{\text{gas}} \propto \frac{1}{P}$

- Viscose regime at high pressures where $Q_{\text{gas}} \propto \frac{1}{\sqrt{P}}$

Since in this thesis we are interested in studying the intrinsic losses of nano-mechanical resonators in vacuum, the gas FMF is the regime that might concerns us. In this regime, the gas damping of a doubly clamped beam can be analytically calculated to be[248],[255]:

$$Q_{\text{gas-FMF}} = \nu \frac{\Omega h}{P} \tag{A.II.1}$$

where Ω is the mechanical frequency, h is the resonator's thickness, P is the pressure and η is a constant factor given by:

$$\nu = \rho \sqrt{\frac{\pi R T}{32 M}} \approx 3 \times 10^5 \text{ m/s} \tag{A.II.2}$$

where, ρ is the density resonator ($\rho_{\text{Si}_3\text{N}_4} \approx 3200$ Kg $\cdot$m^{-3}), $R = 8.314$ J/mol. K is the universal gas constant, $T = 300K$ is the temperature and M is the molar weight of the gas ($M \approx 28.97$ g/mol is the air mixture). We would like to re-arrange the equation A.II.1 in order to find the best operating pressure for our experiments:

$$P = 6 \times 10^{-8} \text{ mbar} \times \frac{10^9}{Q_{\text{gas}}} \times \frac{\Omega/2\pi}{1 \text{ MHz}} \times \frac{h}{20\text{nm}} \tag{A.II.3}$$

Equation (A.II.3) means that if we operate at the pressure of $P = 10^{-8}$ mbar, the quality factor associated with the gas damping is 1 billion. Due the additive nature of the loss mechanisms:

$$Q^{-1}_{\text{measured}} = Q^{-1}_{\text{material}} + Q^{-1}_{\text{gas}} \tag{A.II.4}$$

this means that the if we are trying to measure a mechanical Q_{material} of 1 billion, we will underestimate the quality factor by a factor of 2. Therefore, we have to operate at UHV pressures below $P_{\text{chamber}} < 10^{-8}$ mbar in order order to reduce the effect of gas damping below 10% on the measured quality factor if we are trying to measure quality factors as high as 1 billion.

This is more than 1 order of magnitude lower than the lowest pressure of the operational vacuum chambers in our lab. Therefore, as one the major projects of this thesis, we have designed and build a UHV vacuum chamber, capable of operating at pressures bellow 10^{-8} mbar with baking and at $9 \times 10^{-9} - 1 \times 10^{-8}$ mbar without baking. In the nend section, we review the design of this UHV chamber.

A.II.2 Design requirements for the UHV chamber

Now that we established the operating pressure of the chamber ($P_{\text{chamber}} < 10^{-8}$ mbar), before presenting the details of the design, lets look at the over all design of the main chamber:
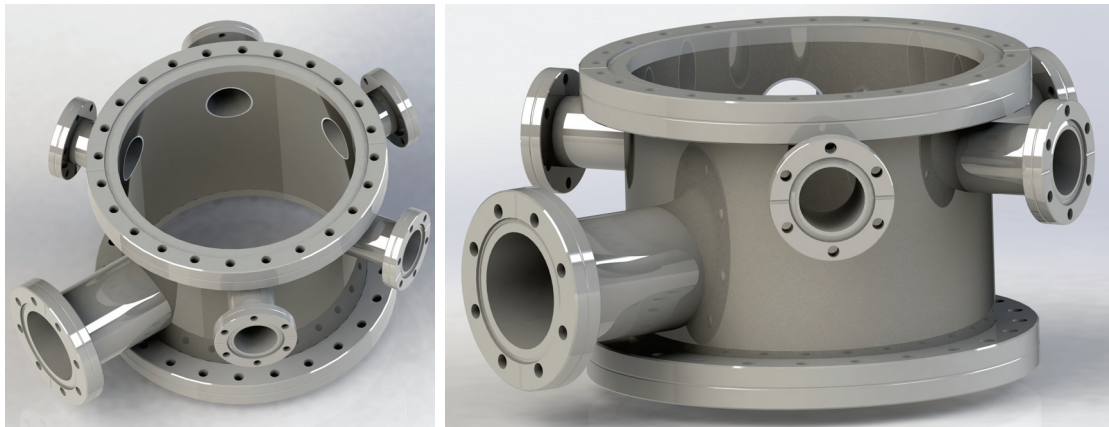
Figure A.II.1 – **3D rendering of the the main chamber.** The main chamber consist of a cylinder with the inner diameter of 200mm and height of 156mm made of 5mm thick stainless steel shits. Five CF-40 flanges symmetrically welded on the sides of the cylinder to province access to inside and a CF-63 flange is designed for connection to the ion pump. Two CF-200 flanges are also designed for the top (view port) and the bottom (blank).

Figure A.II.1 shows the 3D rendering of the main chamber. For this project, we choose 200mm as the diameter of the our chamber. Although this size is much bigger than our experiment (we may be able to fit our experiment in half of this size), but having a bit larger space, makes the assembly of the parts much easier and would provides the room for future upgrades if some other parts needed to be installed. The downside of having larger chamber is that more volume of the chamber means longer pumping time. In addition, it creates larger surface and thus more out gassing.

Before we continue with the design, it is important to emphasize that since we are targeting a UHV design, all the flanges and connection in this chamber is chosen to be ConFlat (CF) Flanges. In CF flanges, seal mechanism is a "knife-edge" (a sharp wedge) that is machined below the flange's flat surface. By tightening the bolts, knife edges make annular grooves on each side of a soft metal gasket (usually a cooper gasket). The extruded metal fills all the machining marks and surface defects in the flange, yielding a leak-tight. Such a sealing is compatible with pressures as low as 10^{-13} mbar and can be baked up to 450 °C[256].

For access to the main chamber, two CF-200 flanges are designed for the top (view port) and the bottom (blank) and five CF-40 flanges symmetrically on the side of the cylinder and one CF-63 for the ion pump access. The reason behind choosing a larger flange for ion pump is that because the air flow conductance scales with the area of the cross section of the flange, $C \propto A$ [257]. Therefore, it scales with square of the diameter of the flange. Having a larger flange, for ion pump, significantly increases the air flow conductance and reduces the pumping time. The CF-40 flanges are designed to be as close as possible to the top view port. This is because the focal distance of the microscope objective is limited to few cm and the samples have to moved up close to view port. So the chamber is designed to have the minimum gap between the center of the flange the the top of the view port. On the other hand, the ion pump flange is place on the lower height. This is because ion pumps could deposit contamination on the faces in front of them and we want to avoid the contamination to be deposited on our chips. Therefore we placed in the lower height compare to the experiment. The chamber is manufactured, welded, seal tested and chemically cleaned by Pfeiffer Vacuum.

The main pumping source of the chamber is coming from an ion pump (figure A.II.2). The ion pump is a great solution for our chamber as it does not have any mechanical parts that could shake the chamber during the experiment. Ion pumps however are designed to work at low pressures and can not start from ambient pressure. Therefore, after completion of the assembly of the chamber, the ion pump and the main chamber were pumped by a turbo pump for one week to evacuate the gas and contamination from the chamber and the ion pump before the ion pump was tuned on for the first time. In the normal mode of operation, we never open the main chamber and the valves that connects the ion pump to the main chamber is open and ion pump is constantly pumping on the main chamber. Also it is important to note that it is a good practice to not expose the ion pump to the air for a long time. Therefore, ion pump was the last item that was installed in the setup and quickly was pumped down to low pressures. In the events that we have to open the chamber (for example to install new
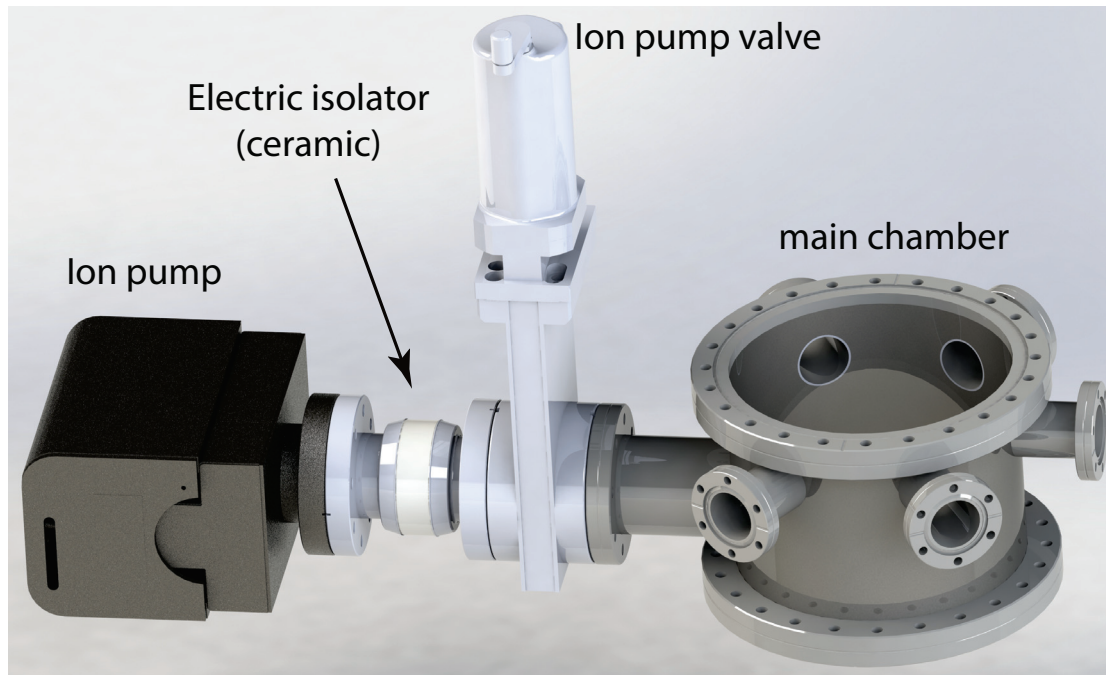
Figure A.II.2 – **Connection of the ion pump to the main chamber.** The ion pump (Model: 45S from Gamma vacuum with 45l/s pumping power) is connected via a UHV compatible gate valve (ModelL SVV 063 HF, UHV gate valve from Pfeiffer Vacuum) to the main chamber. In the normal operating procedure, the gate valve is always kept open and ion pump is constantly pumping on the chamber. When the chamber has to be opened, the gate valve is closed to keep the ion pump under vacuum and then the main chamber is vented. Since ion pumps work with high voltages (7kV here), the ion pump is electrically isolated by via a ceramic electrical break (UVH compatible 7k CF-63 break from MDC vacuum). This also creates a thermal isolation from the main chamber the the ion pump and the main chamber could be baked separately.

equipment for new experiments in future), the ion pump is isolated from the rest of the system by closing the gate valve and kept under vacuum. It its important to note that we electrically isolate the ion pump from the main chamber using a ceramic break. This is because the ion pump operates at high voltages (∼ 7KV). Its leakage to the main chamber could damage the sensitive electronics inside the chamber. The ceramic break also creates a temperature isolation from the main chamber and the main chamber and ion pump can separately be baked without affecting each other.

Now that we have the main parts of the system in-place, lets review the main constrains and future applications of this vacuum chamber before introducing the other part of the systems.

- **Fast sample transfer capability :** The most important innovation in this vacuum chamber is its fast loading and unloading capabilities via a small load lock. In the field of optomechanics we usually change samples with very often (to test different quantities or
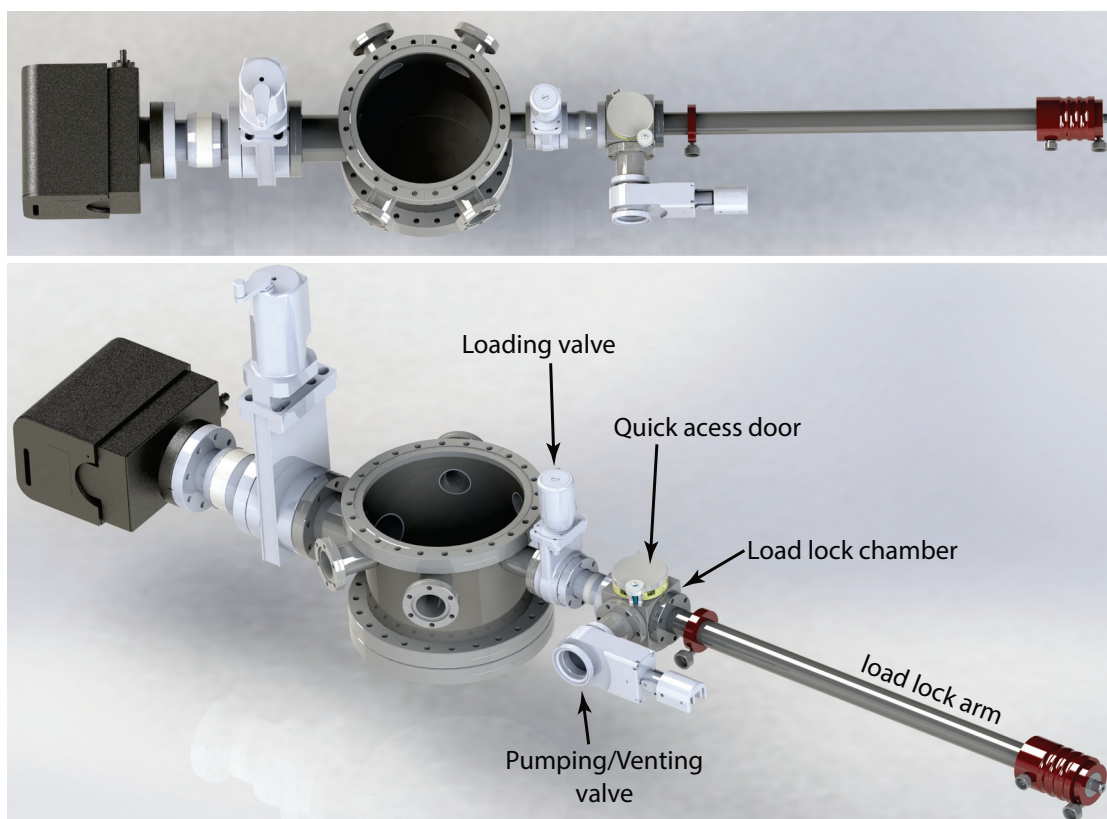
Figure A.II.3 – **Fast loading unloading of the chips via a custom made load-lock system.**
Instead of venting and opening the entire system for every sample switch, the chips are
transfered in vacuum though a custom made load lock. During the loading phase the small
load lock chamber (CF-40 Cube from Pfeiffer Vacuum) is vented though the venting valve (SVV
040 HA, HV gate valve from Pfeiffer Vacuum). We can access the load lock chamber though a
quick access door (665210 -QuickDoor, 2.75"ClearanceHoles from MDC vacuum). The chips
are mounted on a especially designed chip holder and screwed to the end of the load lock
arm (Magnetically coupled Rotary/Linear Feedthrough MDM from Pfeiffer Vacuum). Then
the load lock chamber is pumped by a turbo pump through the the pumping valve. Since
the load lock chamber is small and is always kept under vacuum, it quickly pumps down to
below 10^{-5}mbar. Below this pressure, it is safe to open the loading valve the push the chip
holder via the load lock arm into the main chamber and load it into its position. Once the
sample is loaded, the load lock arm is unscrewed from the chip holder and retracted to the
initial position. The loading vale is then closed. Also the pumping valve is closed to keep the
load lock chamber at vacuum to avoid dust and contamination accumulation.

look for the sample with the best performance). In our previous generations of vacuum
chamber, the only way to load a new chip was to vent the entire system, open the view
port and load the sample in the sample holder. This made the measurement process
extremely lengthy and inefficient as often we had to wait for several days to reach the
pressures below 10^{-7}. This practice also had a negative effect on the lifetime of the ion
pumps.
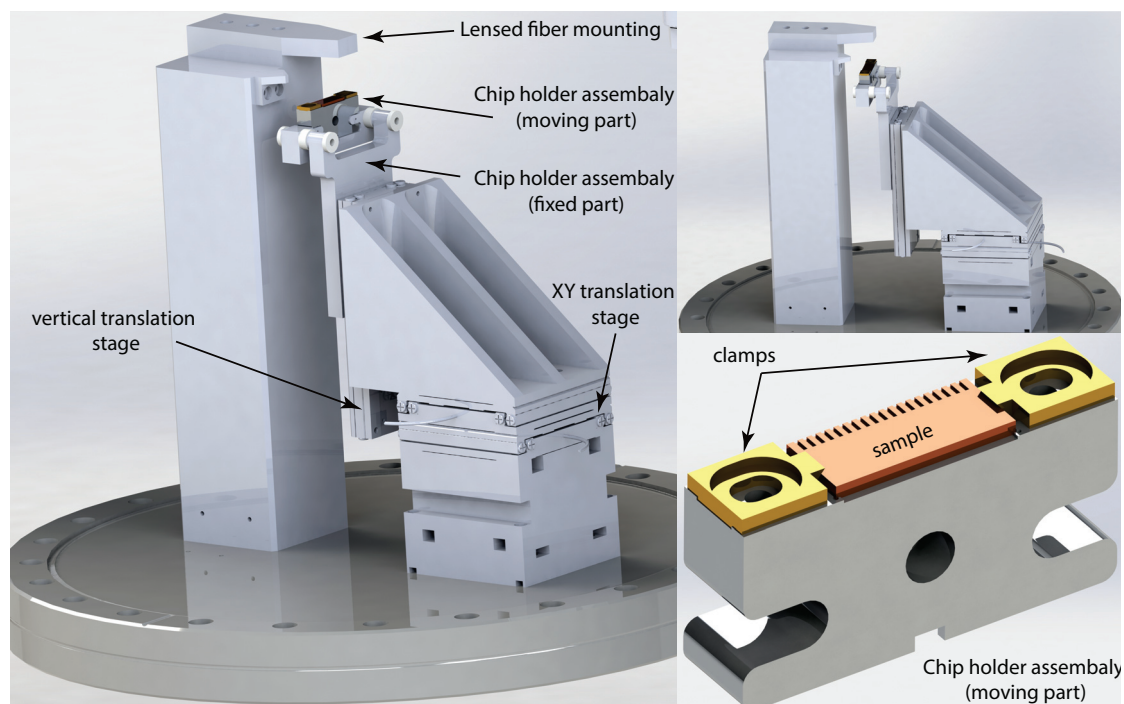
Figure A.II.4 – **UHV compatible XYZ translation stages and chip holder assembly.** The XY stages (two ECSx5050 stages from attocube) are used to navigate the sample under the optical lenses fiber. The vertical stage is used to bring down the sample from the measurement position and align it to the load lock arm. Since the distance between the lensed fiber and load lock are is about 60mm, ECSx3080 linear translation stage was used with the help of a L-bracket. During the loading, an automated program position the stage in front of the load lock arm and the moving part of the samples holder is slide on/off the fixed part. The chip is firmly clamped to the chip holder via the two yellow clamps.

Our solution to this problem was to use the same technique that is used in SEM microscopes to change samples Via a load lock (see figure A.II.3). In this way, samples can be transferred from ambient pressure to UHV pressure (10^{-8} mbar), in the mater of less than 10 minutes. In this system, samples are mounted on an especially design chip holder, and loaded at the end of a magnetically coupled load-lock arm and transferred into the main chamber in vacuum.

- **3D translation stage for alignment :** In order to navigate the samples during the measurement and bring the chip holder up and down for loading position, we used a3 linear translation stages and a L-bracket to construct a 3D stage that has the range cover the distance between the view port and the load lock arm. Also in the design, we placed room via the bottom holder for additional goniometers and rotation stage for future upgrades.

- **Top view port for alignment with microscope :** The next item is the the top view port. We often have to align the beams with the fiber interferometer. Therefore, we placed a
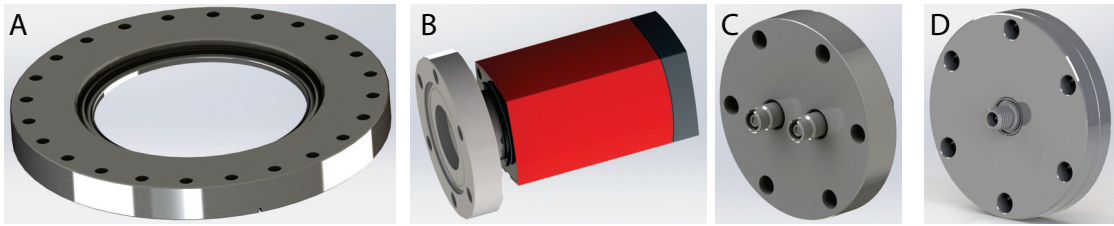
Figure A.II.5 – **Different UHV compatible components in the vacuum chamber.** A) CF 200 10" OD glass view port, B) Pirani/Cold Cathode gauge PKR, C)780nm Single mode FC/APC fiber feedthroughs, D) Grounded SMA feedthroughs

CF 200 view port on top of the main chamber in order to be able to look into the chip via an optical microscope. For this we used 10"OD, Glass zero profile viewport from MDC vacuum.

- **Pressure readout - vacuum gauges :** Two vacuum gauges are used in this project. The first one used to monitor the pressure of the main chamber and the second one is connected to the load lock chamber.

- **Optical access - fiber feedthrough :** The previous method in our group to couple light in and out of the cavity was to use a costume made Teflon piece which was sealed via a swagelok and vacuum glue. Although that method was efficient for HV chambers, it is not compatible with UHV chamber. For our fiber feedthrough, we used UHV compatible CF40 single mode FC/APC fiber feedthroughs from Vacuum Co. These fiber feed through have less that 1% insertion loss. Although for fiber interferometery we only need one feed line, we used a 2 port feed through for possible future applications on transmission measurements (for example using a tapered optical fiber).

- **Electrical access - electrical feedthrough :** We have glued a thin piezo drive underneath the fix part of the chip holder to be able to drive the resonance of our UHQ beam resonators. The piezo is connected via an SMA feed through. For this we used the 3 port grounded CF 40 SMA feed throughs from Kurt J. Lesker Company. Although for this experiment we only need one SMA port, we installed a 3 port for future possible upgrades.

- **Control access - control feedthrough :** Two 9pin gold plated feed through were installed using a T-junction. One is used to control the attocube stages and one is reserved for future usage (for example to control a heater inside the vacuum chamber to bake the samples in vacuum).

- **Thermal and electrical isolation :** In order to thermally (for baking purposes) and electrically isolate the system from the optical table, 16 alumina isolation disks where used under different part of the setup . The have a diameter of 45mm and thickness 10mm costume made by LSP Industrial Ceramics, Inc.
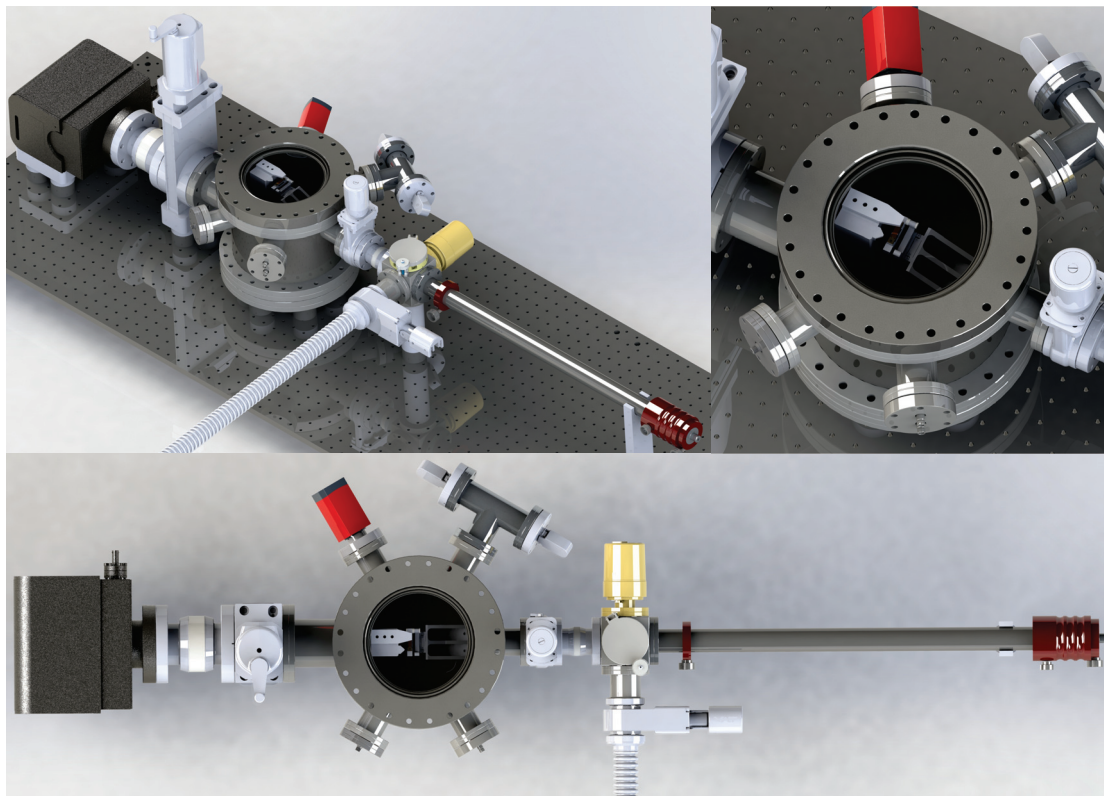
Figure A.II.6 – **3D rendering of the UHV chamber** The system was design using SolidWork in which the design files are publicly available (see the Open Science appendix)

- **Vibration isolation and mechanical stability :** In order to damp the vibrations coming from the environment, we place Sorbonne pills underneath the alumina disk. This also helps to level the entire setup if a minor misalignment exist in the final assembly. For this we used AV6 Sorbothane Feet from Thorlabs.

Below we can see the full 3D rendering of the vacuum chamber. It is important to note to avoid the weight anchoring effects, several aluminum pieces where fabricated to be place under some components (such as ion pump and load lock to adjust for the height difference).

A.II.3   Assembly and cleaning procedure

The UHV chamber was assembled over the course several months. The most important consideration during the assembly is the cleaning of the components. In UHV chambers, if the sealing are done properly, the final pressure is the determined where the "out gassing" and pumping rates reach an equilibrium. Any organic contamination such as finger prints and oil leftovers from the machining will create a significant out gassing for the chamber. So we took extra measure to be extremely careful with our handling of the equipment during the assembly phase. For example all the components that where inside the chamber had to
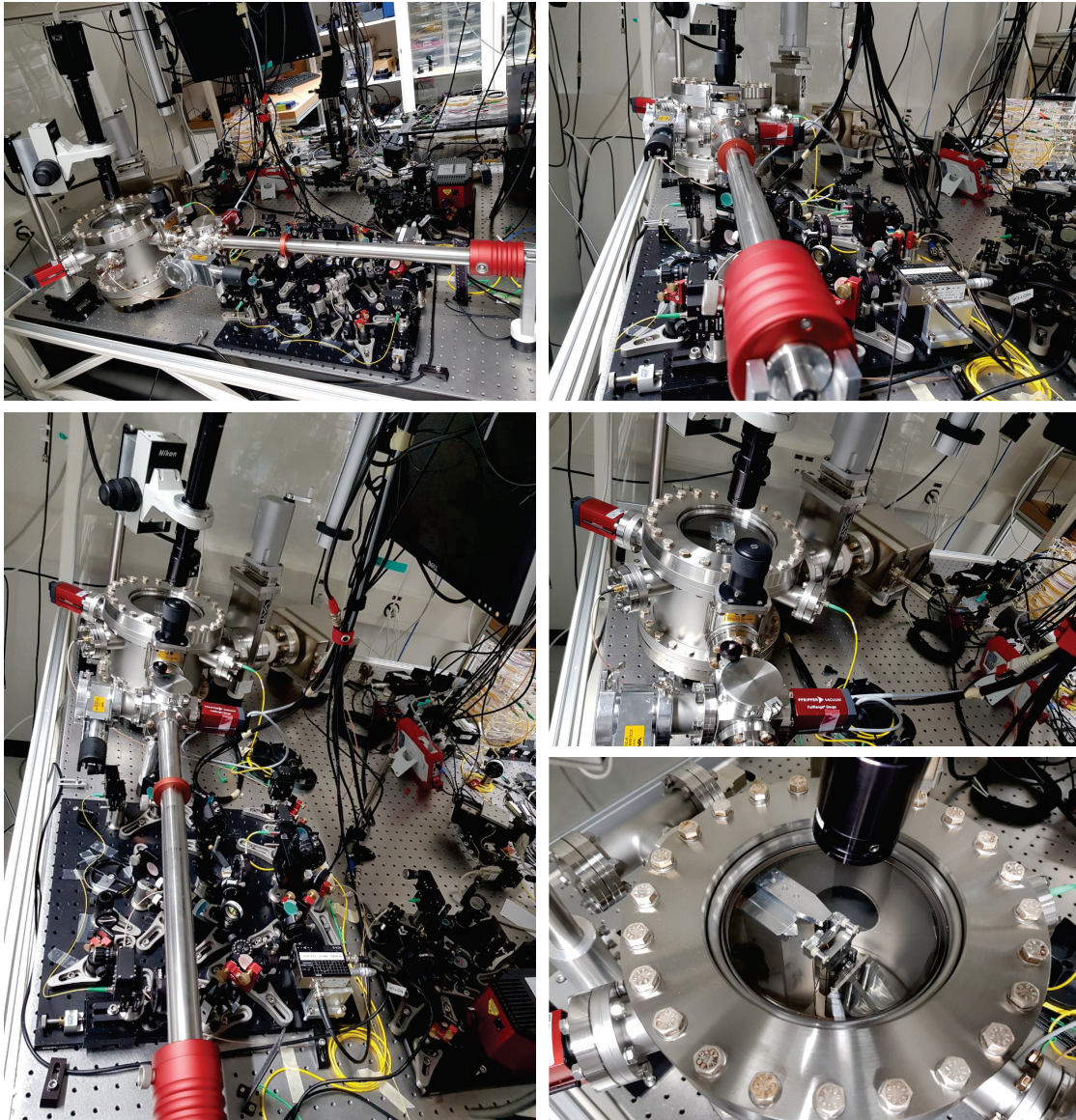
Figure A.II.7 – **Images of the assembled setup.** The optical setup underneath the load lock arm is the balanced homodyne interferometer that used to detect the phase of the reflected light from the lensed fiber.

be only touched with clean gloves. Also we performed the following cleaning steps for every component that was installed in the chamber (except from the translation stage as they were not compatible with the solvent where certified as UHV clean):

- 15min sonication in water and soap mixture at 60 ^{o}

- 15min sonication in acetone at 50 ^{o}

- 15min sonication in methanol at 50 ^{o}

- 15min sonication in IPA at 50 ^{o}

- Drying with clean nitrogen gun

In figure A.II.7, we can find few images of the setup at the end of the assembly phase. After the end of assembly, we have pumped the ion pump, the load lock and the main chamber via a turbo pump for 7days though the vent/pumping valve at the load lock. After reaching the pressure of $\sim 10^{-6}$mbar, we perform a Helium leak check to only find the the system has no major leak. At this point the ion pump was turned on and the system were left the to pump on its own for few weeks. After few weeks, the pressure of the system was stabilized between $9 \times 10^{-9} - 10^{-8}$ mbar. This pressure was low enough that we could measure mechanical quality factors in excess of 800 million. To reach even lower pressure, the chamber has to be baked at 180 ^{o}C (that is the maximum recommended temperature for the translation stages) for several days in order to speed up the out gassing of the trapped molecules on the surfaces.

A.III Appendix III : Open science

Data availability statement

Based on our commitment to the new movement in the scientific community in regards to "open science", all the original data and the data analysis codes are publicly available in the following address:

doi: 10.5281/zenodo.1323821

This includes:

- The Mathematica code that numerically solve Euler Bernoulli equations and we used for design of the the beams and fitting to the measured data

- COMSOL simulation files for stress relaxation in 3D

- The C++ codes that generate the fabrication masks

- The original GDS and l-edit files associated to the masks that were used to fabricated corrugated beams

- Original SEM and optical images presented in the thesis

- The figure data for all the simulated or measured figures in this thesis

- The raw data for all the measurements performed in this thesis

- All the original solid-work drawings for the vacuum chamber and the KOH chip holder

- The codes for GUI Matlab data acquisition software that was written to control and readout the vacuum chamber and other instruments for the measurement (Network Analyzer, spectrum analyzer, oscilloscope and etc.)

Bibliography

[1] LIGO Scientific Collaboration and Virgo Collaboration, "Observation of Gravitational Waves from a Binary Black Hole Merger," *Physical Review Letters*, vol. 116, p. 061102, Feb. 2016.

[2] Y. T. Yang, C. Callegari, X. L. Feng, K. L. Ekinci, and M. L. Roukes, "Zeptogram-Scale Nanomechanical Mass Sensing," *Nano Letters*, vol. 6, pp. 583–586, Apr. 2006.

[3] M. S. Hanay, S. Kelber, A. K. Naik, D. Chi, S. Hentz, E. C. Bullard, E. Colinet, L. Duraffourg, and M. L. Roukes, "Single-protein nanomechanical mass spectrometry in real time," *Nature Nanotechnology*, vol. 7, pp. 602–608, Sept. 2012.

[4] A. N. Cleland and M. L. Roukes, "A nanometre-scale mechanical electrometer," *Nature*, vol. 392, pp. 160–162, Mar. 1998.

[5] A. G. Krause, M. Winger, T. D. Blasius, Q. Lin, and O. Painter, "A high-resolution microchip optomechanical accelerometer," *Nature Photonics*, vol. 6, pp. 768–772, Nov. 2012.

[6] D. Rugar, R. Budakian, H. J. Mamin, and B. W. Chui, "Single spin detection by magnetic resonance force microscopy," *Nature*, vol. 430, pp. 329–332, July 2004.

[7] T. J. Kippenberg and K. J. Vahala, "Cavity Optomechanics: Back-Action at the Mesoscale," *Science*, vol. 321, pp. 1172–1176, Aug. 2008.

[8] K. C. Schwab and M. L. Roukes, "Putting Mechanics into Quantum Mechanics," *Physics Today*, vol. 58, pp. 36–42, July 2005.

[9] M. Aspelmeyer, T. J. Kippenberg, and F. Marquardt, "Cavity optomechanics," *Reviews of Modern Physics*, vol. 86, pp. 1391–1452, Dec. 2014.

[10] D. J. Wilson, V. Sudhir, N. Piro, R. Schilling, A. Ghadimi, and T. J. Kippenberg, "Measurement-based control of a mechanical oscillator at its thermal decoherence rate," *Nature*, vol. 524, pp. 325–329, Aug. 2015.

[11] M. Rossi, D. Mason, J. Chen, Y. Tsaturyan, and A. Schliesser, "Measurement-based quantum control of mechanical motion," *arXiv:1805.05087 [quant-ph]*, May 2018.

[12] C. A. Regal and K. W. Lehnert, "From cavity electromechanics to cavity optomechanics," *Journal of Physics: Conference Series*, vol. 264, no. 1, p. 012025, 2011.

[13] G. I. González and P. R. Saulson, "Brownian motion of a mass suspended by an anelastic wire," *The Journal of the Acoustical Society of America*, vol. 96, pp. 207–212, July 1994.

[14] S. A. Fedorov, N. J. Engelsen, A. H. Ghadimi, M. J. Bereyhi, R. Schilling, D. J. Wilson, and T. J. Kippenberg, "Generalized dissipation dilution in strained mechanical resonators," *arXiv:1807.07086 [cond-mat, physics:physics]*, July 2018.

[15] V. B. Braginsky, V. P. Mitrofanov, and V. I. Panov, *Systems with Small Dissipation.* University of Chicago Press, 1985.

[16] H. Cavendish, "XXI. Experiments to determine the density of the earth," *Philosophical Transactions of the Royal Society of London*, vol. 88, pp. 469–526, Jan. 1798.

[17] P. J. Mohr, D. B. Newell, and B. N. Taylor, "CODATA recommended values of the fundamental physical constants: 2014," *Reviews of Modern Physics*, vol. 88, p. 035009, Sept. 2016.

[18] "Cavendish experiment," *Wikipedia*, May 2018. Page Version ID: 843226054.

[19] C. V. Boys, "The Newtonian Constant of Gravitation," *Nature*, vol. 50, p. 571, Oct. 1894.

[20] C. V. Boys, "On the Newtonian Constant of Gravitation," *Philosophical Transactions of the Royal Society of London. A*, vol. 186, pp. 1–72, 1895.

[21] H. C. Nathanson and R. A. Wickstrom, "A resonant-gate silicon surface transistor with high-q band-pass properties," *Applied Physics Letters*, vol. 7, pp. 84–86, Aug. 1965.

[22] A. M. Nicolson, "Generating and transmitting electric currents," Aug. 1940.

[23] A. E. Habti and F. O. Bastien, "Low temperature limitation on the quality factor of quartz resonators," *IEEE Transactions on Ultrasonics, Ferroelectrics, and Frequency Control*, vol. 41, pp. 250–255, Mar. 1994.

[24] F. R. Lack, G. W. Willard, and I. E. Fair, "Some Improvements in Quartz Crystal Circuit Elements," *Bell System Technical Journal*, vol. 13, no. 3, pp. 453–463.

[25] E. P. EerNisse, "Quartz Resonator Frequency Shifts Arising from Electrode Stress," in *29th Annual Symposium on Frequency Control*, pp. 1–4, May 1975.

[26] S. Galliou, M. Goryachev, R. Bourquin, P. Abbé, J. P. Aubry, and M. E. Tobar, "Extremely Low Loss Phonon-Trapping Cryogenic Acoustic Cavities for Future Physical Experiments," *Scientific Reports*, vol. 3, p. 2132, July 2013.

[27] A. Einstein, "Näherungsweise Integration der Feldgleichungen der Gravitation," *Sitzungsberichte*, pp. 688–696, 1916.

[28] J. Weber, "Detection and Generation of Gravitational Waves," *Physical Review*, vol. 117, pp. 306–313, Jan. 1960.

[29] M. E. Gertsenshtein and V. I. Pustovoĭt, "On the Detection of Low-Frequency Gravitational Waves," *Soviet Journal of Experimental and Theoretical Physics*, vol. 16, p. 433, 1963.

[30] R. Weiss, "Electromagnetically Coupled Broadband Gravitational Antenna," p. 23, Apr. 1972.

[31] D. S. Lemons and A. Gythiel, "Paul Langevin's 1908 paper "On the Theory of Brownian Motion" ["Sur la théorie du mouvement brownien," C. R. Acad. Sci. (Paris) 146, 530–533 (1908)]," *American Journal of Physics*, vol. 65, pp. 1079–1081, Nov. 1997.

[32] H. J. McSkimin, "Measurement of Elastic Constants at Low Temperatures by Means of Ultrasonic Waves–Data for Silicon and Germanium Single Crystals, and for Fused Silica," *Journal of Applied Physics*, vol. 24, pp. 988–997, Aug. 1953.

[33] O. L. Anderson and H. E. Bömmel, "Ultrasonic Absorption in Fused Silica at Low Temperatures and High Frequencies," *Journal of the American Ceramic Society*, vol. 38, no. 4, pp. 125–131.

[34] H. E. Bömmel, "Ultrasonic Attenuation in Superconducting Lead," *Physical Review*, vol. 96, pp. 220–221, Oct. 1954.

[35] A. G. Smagin, "A study of high-Q quartz crystal plates," *Measurement Techniques*, vol. 3, pp. 792–795, Sept. 1960.

[36] A. G. Smagin and E. P. Vysokosov, "Excitation of quartz lenses with clearances in a parallel field," *Measurement Techniques*, vol. 6, pp. 260–262, Mar. 1963.

[37] A. G. Smagin, "A quartz resonator for a frequency of 1 MHz with a Q-value of 4.2×109 at a temperature of 2 K," *Cryogenics*, vol. 15, pp. 483–485, Aug. 1975.

[38] D. F. McGuigan, C. C. Lam, R. Q. Gram, A. W. Hoffman, D. H. Douglass, and H. W. Gutche, "Measurements of the mechanical Q of single-crystal silicon at low temperatures," *Journal of Low Temperature Physics*, vol. 30, pp. 621–629, Mar. 1978.

[39] D. J. Wilson, *Cavity Optomechanics with High-Stress Silicon Nitride Films*. Phd, California Institute of Technology, June 2012.

[40] W. Duffy, "Acoustic quality factor of molybdenum and tungsten at low temperatures," *Journal of Applied Physics*, vol. 72, pp. 5628–5634, Dec. 1992.

[41] R. Nawrodt, A. Zimmer, T. Koettig, C. Schwarz, D. Heinert, M. Hudl, R. Neubert, M. Thürk, S. Nietzsche, W. Vodel, P Seidel, and A. Tünnermann, "High mechanical Q-factor measurements on silicon bulk samples," *Journal of Physics: Conference Series*, vol. 122, no. 1, p. 012008, 2008.

[42] R. Nawrodt, A. Zimmer, S. Nietzsche, M. Thürk, W. Vodel, and P. Seidel, "A new apparatus for mechanical Q-factor measurements between 5 and 300K," *Cryogenics*, vol. 46, pp. 718–723, Oct. 2006.

[43] C. R. Locke, M. E. Tobar, and E. N. Ivanov, "Monolithic sapphire parametric transducer operation at cryogenic temperatures," *Review of Scientific Instruments*, vol. 71, p. 2737, June 2000.

[44] C. R. Locke, M. E. Tobar, and E. N. Ivanov, "Properties of a monolithic sapphire parametric transducer: Prospects of measuring the standard quantum limit," *Classical and Quantum Gravity*, vol. 19, no. 7, p. 1877, 2002.

[45] S. Gras, L. Ju, and D. G. Blair, "Influence of grooves and defects on the sapphire test mass Q -factor," *Classical and Quantum Gravity*, vol. 21, no. 5, p. S1121, 2004.

[46] A. Schroeter, R. Nawrodt, R. Schnabel, S. Reid, I. Martin, S. Rowan, C. Schwarz, T. Koettig, R. Neubert, M. Thürk, W. Vodel, A. Tünnermann, K. Danzmann, and P. Seidel, "On the mechanical quality factors of cryogenic test masses from fused silica and crystalline quartz," *arXiv:0709.4359 [gr-qc]*, Sept. 2007.

[47] J. R. Smith, G. Cagnoli, D. R. M. Crooks, M. M. Fejer, S. Goßler, H. Lück, S. Rowan, J. Hough, and K. Danzmann, "Mechanical quality factor measurements of monolithically suspended fused silica test masses of the GEO 600 gravitational wave detector," *Classical and Quantum Gravity*, vol. 21, no. 5, p. S1091, 2004.

[48] A. M. Gretarsson, G. M. Harry, S. D. Penn, P. R. Saulson, W. J. Startin, S. Rowan, G. Cagnoli, and J. Hough, "Pendulum mode thermal noise in advanced interferometers: A comparison of fused silica fibers and ribbons in the presence of surface loss," *Physics Letters A*, vol. 270, pp. 108–114, May 2000.

[49] S. Rowan, S. M. Twyford, R. Hutchins, J. Kovalik, J. E. Logan, A. C. McLaren, N. A. Robertson, and J. Hough, "Q factor measurements on prototype fused quartz pendulum suspensions for use in gravitational wave detectors," *Physics Letters A*, vol. 233, pp. 303–308, Sept. 1997.

[50] R. Nawrodt, A. Zimmer, T. Koettig, S. Nietzsche, M. Thürk, W. Vodel, and P. Seidel, "High mechanical Q-factor measurements on calcium fluoride at cryogenic temperatures," *The European Physical Journal Applied Physics*, vol. 38, pp. 53–59, Apr. 2007.

[51] Z. Yan, L. Ju, S. Gras, C. Zhao, and D. G. Blair, "High mechanical quality factor of calcium fluoride (CaF2) at room temperature," *The European Physical Journal Applied Physics*, vol. 30, pp. 189–192, June 2005.

[52] S. Rowan, G. Cagnoli, P. Sneddon, J. Hough, R. Route, E. K. Gustafson, M. M. Fejer, and V. Mitrofanov, "Investigation of mechanical loss factors of some candidate materials for the test masses of gravitational wave detectors," *Physics Letters A*, vol. 265, pp. 5–11, Jan. 2000.

[53] S. Kimura, T. Suzuki, and H. Hirakawa, "Low frequency antenna for gravitational radiation," *Physics Letters A*, vol. 81, pp. 302–304, Jan. 1981.

[54] E. Coccia and T. O. Niinikoski, "Acoustic quality factor of an aluminium alloy for gravitational wave antennae below 1 K," *Lettere al Nuovo Cimento (1971-1985)*, vol. 41, pp. 242–246, Oct. 1984.

[55] A. V. Cumming, A. S. Bell, L. Barsotti, M. A. Barton, G. Cagnoli, D. Cook, L. Cunningham, M. Evans, G. D. Hammond, G. M. Harry, A. Heptonstall, J. Hough, R. Jones, R. Kumar, R. Mittleman, N. A. Robertson, S. Rowan, B. Shapiro, K. A. Strain, K Tokmakov, C. Torrie, and A. A. van Veggel, "Design and development of the advanced LIGO monolithic fused silica suspension," *Classical and Quantum Gravity*, vol. 29, no. 3, p. 035003, 2012.

[56] A. L. Kimball and D. E. Lovell, "Internal Friction in Solids," *Physical Review*, vol. 30, pp. 948–959, Dec. 1927.

[57] L. G. Villanueva and S. Schmid, "Evidence of Surface Loss as Ubiquitous Limiting Damping Mechanism in SiN Micro- and Nanomechanical Resonators," *Physical Review Letters*, vol. 113, p. 227201, Nov. 2014.

[58] Y. Tao, *Nanomechanical Systems with Small Dissipation.* Thesis, Massachusetts Institute of Technology, 2015.

[59] G. Cagnoli, J. Hough, D. DeBra, M. M. Fejer, E. Gustafson, S. Rowan, and V. Mitrofanov, "Damping dilution factor for a pendulum in an interferometric gravitational waves detector," *Physics Letters A*, vol. 272, pp. 39–45, July 2000.

[60] B. H. Houston, D. M. Photiadis, M. H. Marcus, J. A. Bucaro, X. Liu, and J. F. Vignola, "Thermoelastic loss in microscale oscillators," *Applied Physics Letters*, vol. 80, pp. 1300–1302, Feb. 2002.

[61] R. Lifshitz and M. L. Roukes, "Thermoelastic damping in micro- and nanomechanical systems," *Physical Review B*, vol. 61, pp. 5600–5609, Feb. 2000.

[62] C. Zener, "Internal Friction in Solids II. General Theory of Thermoelastic Internal Friction," *Physical Review*, vol. 53, pp. 90–99, Jan. 1938.

[63] L.D. Landau & E.M. Lifshitz, *Theory of Elasticity*.

[64] K. Kunal and N. R. Aluru, "Akhiezer damping in nanostructures," *Physical Review B*, vol. 84, p. 245450, Dec. 2011.

[65] H. H. Barrett and M. G. Holland, "Critique of Current Theories of Akhieser Damping in Solids," *Physical Review B*, vol. 1, pp. 2538–2544, Mar. 1970.

[66] A. Akhieser, "On the absorption of sound in solids," *J. Phys.(Ussr)*, vol. 1, p. 277.

Bibliography

[67] H. E. Bömmel and K. Dransfeld, "Excitation and Attenuation of Hypersonic Waves in Quartz," *Physical Review*, vol. 117, pp. 1245–1252, Mar. 1960.

[68] S. Hunklinger and W. Arnold, "3 - Ultrasonic Properties of Glasses at Low Temperatures," in *Physical Acoustics* (W. P. Mason and R. N. Thurston, eds.), vol. 12, pp. 155–215, Academic Press, Jan. 1976.

[69] R. N. Kleiman, G. Agnolet, and D. J. Bishop, "Two-level systems observed in the mechanical properties of single-crystal silicon at low temperatures," *Physical Review Letters*, vol. 59, pp. 2079–2082, Nov. 1987.

[70] W. A. Phillips, "Two-level states in glasses," *Reports on Progress in Physics*, vol. 50, no. 12, p. 1657, 1987.

[71] T. Faust, J. Rieger, M. J. Seitner, J. P. Kotthaus, and E. M. Weig, "Signatures of two-level defects in the temperature-dependent damping of nanomechanical silicon nitride resonators," *Physical Review B*, vol. 89, p. 100102, Mar. 2014.

[72] R. Nawrodt, C. Schwarz, S. Kroker, I. W. Martin, R. Bassiri, F. Brückner, L. Cunningham, G. D. Hammond, D. Heinert, J Hough, T. Käsebier, E.-B. Kley, R. Neubert, S. Reid, S. Rowan, P. Seidel, and A. Tünnermann, "Investigation of mechanical losses of thin silicon flexures at low temperatures," *Classical and Quantum Gravity*, vol. 30, no. 11, p. 115008, 2013.

[73] A. M. Gretarsson and G. M. Harry, "Dissipation of mechanical energy in fused silica fibers," *Review of Scientific Instruments*, vol. 70, pp. 4081–4087, Sept. 1999.

[74] J. Rieger, A. Isacsson, M. J. Seitner, J. P. Kotthaus, and E. M. Weig, "Energy losses of nanomechanical resonators induced by atomic force microscopy-controlled mechanical impedance mismatching," *Nature Communications*, vol. 5, Mar. 2014.

[75] D. J. Wilson, C. A. Regal, S. B. Papp, and H. J. Kimble, "Cavity Optomechanics with Stoichiometric SiN Films," *Physical Review Letters*, vol. 103, p. 207204, Nov. 2009.

[76] S. Chakram, Y. S. Patil, L. Chang, and M. Vengalattore, "Dissipation in Ultrahigh Quality Factor SiN Membrane Resonators," *Physical Review Letters*, vol. 112, p. 127201, Mar. 2014.

[77] I. Wilson-Rae, R. A. Barton, S. S. Verbridge, D. R. Southworth, B. Ilic, H. G. Craighead, and J. M. Parpia, "High-Q Nanomechanics via Destructive Interference of Elastic Waves," *Physical Review Letters*, vol. 106, p. 047205, Jan. 2011.

[78] S. S. Verbridge, J. M. Parpia, R. B. Reichenbach, L. M. Bellan, and H. G. Craighead, "High quality factor resonance at room temperature with nanostrings under high tensile stress," *Journal of Applied Physics*, vol. 99, p. 124304, June 2006.

[79] R. S. Jacobsen, K. N. Andersen, P. I. Borel, J. Fage-Pedersen, L. H. Frandsen, O. Hansen, M. Kristensen, A. V. Lavrinenko, G. Moulin, H. Ou, C. Peucheret, B. Zsigri, and A. Bjarklev, "Strained silicon as a new electro-optic material," *Nature*, vol. 441, pp. 199–202, May 2006.

[80] M. J. Süess, R. Geiger, R. A. Minamisawa, G. Schiefler, J. Frigerio, D. Chrastina, G. Isella, R. Spolenak, J. Faist, and H. Sigg, "Analysis of enhanced light emission from highly strained germanium microbridges," *Nature Photonics*, vol. 7, pp. 466–472, June 2013.

[81] G. D. Cole, P.-L. Yu, C. Gärtner, K. Siquans, R. Moghadas Nia, J. Schmöle, J. Hoelscher-Obermaier, T. P. Purdy, W. Wieczorek, C. A. Regal, and M. Aspelmeyer, "Tensile-strained InxGa1-xP membranes for cavity optomechanics," *Applied Physics Letters*, vol. 104, p. 201908, May 2014.

[82] G. González, "Suspensions thermal noise in the LIGO gravitational wave detector," *Classical and Quantum Gravity*, vol. 17, no. 21, p. 4409, 2000.

[83] V. B. Braginsky, V. P. Mitrofanov, and K. V. Tokmakov, "On the thermal noise from the violin modes of the test mass suspension in gravitational wave antennae," *Physics Letters A*, vol. 186, pp. 18–20, Mar. 1994.

[84] V. B. Braginsky, V. P. Mitrofanov, and S. P. Vyatchanin, "Isolation of test masses in the advanced laser interferometric gravitational-wave antennae," *Review of Scientific Instruments*, vol. 65, pp. 3771–3774, Dec. 1994.

[85] N. A. Robertson, G. Cagnoli, D. R. M. Crooks, E. Elliffe, J. E. Faller, P. Fritschel, S. Goßler, A. Grant, A Heptonstall, J. Hough, H. Lück, R. Mittleman, M. Perreur-Lloyd, M. V. Plissi, S. Rowan, D. H. Shoemaker, P. H. Sneddon, K. A. Strain, C. I. Torrie, H. Ward, and P. Willems, "Quadruple suspension design for Advanced LIGO," *Classical and Quantum Gravity*, vol. 19, no. 15, p. 4043, 2002.

[86] G. Cagnoli, L. Gammaitoni, J. Hough, J. Kovalik, S. McIntosh, M. Punturo, and S. Rowan, "Very High Q Measurements on a Fused Silica Monolithic Pendulum for Use in Enhanced Gravity Wave Detectors," *Physical Review Letters*, vol. 85, pp. 2442–2445, Sept. 2000.

[87] A. V. Dmitriev, S. D. Mescheriakov, K. V. Tokmakov, and V. P. Mitrofanov, "Controllable damping of high- Q violin modes in fused silica suspension fibers," *Classical and Quantum Gravity*, vol. 27, no. 2, p. 025009, 2010.

[88] D. M. Tanner, J. A. Walraven, K. Helgesen, L. W. Irwin, F. Brown, N. F. Smith, and N. Masters, "MEMS reliability in shock environments," in *2000 IEEE International Reliability Physics Symposium Proceedings. 38th Annual (Cat. No.00CH37059)*, pp. 129–138, 2000.

[89] M. Imboden and P. Mohanty, "Dissipation in nanoelectromechanical systems," *Physics Reports*, vol. 534, pp. 89–146, Jan. 2014.

[90] A. H. Ghadimi, S. A. Fedorov, N. J. Engelsen, M. J. Bereyhi, R. Schilling, D. J. Wilson, and T. J. Kippenberg, "Elastic strain engineering for ultralow mechanical dissipation," *Science*, vol. 360, pp. 764–768, May 2018.

[91] Y. Tsaturyan, A. Barg, E. S. Polzik, and A. Schliesser, "Ultracoherent nanomechanical resonators via soft clamping and dissipation dilution," *Nature Nanotechnology*, vol. 12, pp. 776–783, June 2017.

[92] C. Reinhardt, T. Müller, A. Bourassa, and J. C. Sankey, "Ultralow-Noise SiN Trampoline Resonators for Sensing and Optomechanics," *Physical Review X*, vol. 6, p. 021001, Apr. 2016.

[93] R. A. Norte, J. P. Moura, and S. Gröblacher, "Mechanical Resonators for Quantum Optomechanics Experiments at Room Temperature," *Physical Review Letters*, vol. 116, p. 147202, Apr. 2016.

[94] D. W. Carr, S. Evoy, L. Sekaric, H. G. Craighead, and J. M. Parpia, "Measurement of mechanical resonance and losses in nanometer scale silicon wires," *Applied Physics Letters*, vol. 75, pp. 920–922, Aug. 1999.

[95] K. L. Ekinci and M. L. Roukes, "Nanoelectromechanical systems," *Review of Scientific Instruments*, vol. 76, p. 061101, June 2005.

[96] D. R. Southworth, R. A. Barton, S. S. Verbridge, B. Ilic, A. D. Fefferman, H. G. Craighead, and J. M. Parpia, "Stress and Silicon Nitride: A Crack in the Universal Dissipation of Glasses," *Physical Review Letters*, vol. 102, p. 225503, June 2009.

[97] P. Temple-Boyer, C. Rossi, E. Saint-Etienne, and E. Scheid, "Residual stress in low pressure chemical vapor deposition SiNx films deposited from silane and ammonia," *Journal of Vacuum Science & Technology A: Vacuum, Surfaces, and Films*, vol. 16, pp. 2003–2007, July 1998.

[98] Q. P. Unterreithmeier, T. Faust, and J. P. Kotthaus, "Damping of Nanomechanical Resonators," *Physical Review Letters*, vol. 105, p. 027205, July 2010.

[99] S. Schmid, K. D. Jensen, K. H. Nielsen, and A. Boisen, "Damping mechanisms in high-Q micro and nanomechanical string resonators," *Physical Review B*, vol. 84, p. 165307, Oct. 2011.

[100] P.-L. Yu, K. Cicak, N. S. Kampel, Y. Tsaturyan, T. P. Purdy, R. W. Simmonds, and C. A. Regal, "A phononic bandgap shield for high-Q membrane microresonators," *Applied Physics Letters*, vol. 104, p. 023510, Jan. 2014.

[101] A. H. Ghadimi, D. J. Wilson, and T. J. Kippenberg, "Radiation and Internal Loss Engineering of High-Stress Silicon Nitride Nanobeams," *Nano Letters*, vol. 17, pp. 3501–3505, June 2017.

[102] R. A. Minamisawa, M. J. Süess, R. Spolenak, J. Faist, C. David, J. Gobrecht, K. K. Bourdelle, and H. Sigg, "Top-down fabricated silicon nanowires under tensile elastic strain up to 4.5%," *Nature Communications*, vol. 3, p. 1096, Oct. 2012.

[103] T. Zabel, R. Geiger, E. Marin, E. Müller, A. Diaz, C. Bonzon, M. J. Süess, R. Spolenak, J. Faist, and H. Sigg, "Top-down method to introduce ultra-high elastic strain," *Journal of Materials Research*, vol. 32, pp. 726–736, Feb. 2017.

[104] I. Pikovski, M. R. Vanner, M. Aspelmeyer, M. S. Kim, and Č. Brukner, "Probing Planck-scale physics with quantum optics," *Nature Physics*, vol. 8, pp. 393–397, May 2012.

[105] P.-L. Yu, T. P. Purdy, and C. A. Regal, "Control of Material Damping in High-Q Membrane Microresonators," *Physical Review Letters*, vol. 108, p. 083603, Feb. 2012.

[106] T. Corbitt, C. Wipf, T. Bodiya, D. Ottaway, D. Sigg, N. Smith, S. Whitcomb, and N. Mavalvala, "Optical Dilution and Feedback Cooling of a Gram-Scale Oscillator to 6.9 mK," *Physical Review Letters*, vol. 99, p. 160801, Oct. 2007.

[107] K.-K. Ni, R. Norte, D. J. Wilson, J. D. Hood, D. E. Chang, O. Painter, and H. J. Kimble, "Enhancement of Mechanical Q Factors by Optical Trapping," *Physical Review Letters*, vol. 108, p. 214302, May 2012.

[108] P. R. Saulson, "Thermal noise in mechanical experiments," *Physical Review D*, vol. 42, pp. 2437–2445, Oct. 1990.

[109] J. L. Routbort and H. S. Sack, "Background Internal Friction of Some Pure Metals at Low Frequencies," *Journal of Applied Physics*, vol. 37, pp. 4803–4805, Dec. 1966.

[110] J. Hu, Z. Marciniak, and J. Duncan, *Mechanics of Sheet Metal Forming*. Elsevier, Apr. 2002.

[111] A. Moridi, H. Ruan, L. C. Zhang, and M. Liu, "Residual stresses in thin film systems: Effects of lattice mismatch, thermal mismatch and interface dislocations," *International Journal of Solids and Structures*, vol. 50, pp. 3562–3569, Oct. 2013.

[112] T. Capelle, Y. Tsaturyan, A. Barg, and A. Schliesser, "Polarimetric analysis of stress anisotropy in nanomechanical silicon nitride resonators," *Applied Physics Letters*, vol. 110, p. 181106, May 2017.

[113] "Cauchy–Schwarz inequality," *Wikipedia*, June 2018. Page Version ID: 844964910.

[114] J. D. Teufel, D. Li, M. S. Allman, K. Cicak, A. J. Sirois, J. D. Whittaker, and R. W. Simmonds, "Circuit cavity electromechanics in the strong-coupling regime," *Nature*, vol. 471, pp. 204–208, Mar. 2011.

[115] W. W. Jr, S. P. Timoshenko, and D. H. Young, *Vibration Problems in Engineering*. John Wiley & Sons, Feb. 1990.

[116] B. M. Zwickl, W. E. Shanks, A. M. Jayich, C. Yang, A. C. Bleszynski Jayich, J. D. Thompson, and J. G. E. Harris, "High quality mechanical and optical properties of commercial silicon nitride membranes," *Applied Physics Letters*, vol. 92, p. 103125, Mar. 2008.

[117] R. Zhang, C. Ti, M. I. Davanço, Y. Ren, V. Aksyuk, Y. Liu, and K. Srinivasan, "Integrated tuning fork nanocavity optomechanical transducers with high fMQM product and stress-engineered frequency tuning," *Applied Physics Letters*, vol. 107, p. 131110, Sept. 2015.

[118] A. H. Ghadimi, D. J. Wilson, and T. J. Kippenberg, "Dissipation engineering of high-stress silicon nitride nanobeams," *arXiv:1603.01605 [cond-mat, physics:physics, physics:quant-ph]*, Mar. 2016.

[119] "Membrane Devices for Transmission Electron Microscopy." https://www.norcada.com/products/nitride-windows-tem/.

[120] P. W. Milonni and J. H. Eberly, *Laser Physics*. Hoboken, N.J: Wiley, 1 edition ed., Mar. 2010.

[121] N. M. Kondratiev and M. L. Gorodetsky, "Thermorefractive noise in whispering gallery mode microresonators: Analytical results and numerical simulation," *Physics Letters A*, vol. 382, pp. 2265–2268, Aug. 2018.

[122] G. Anetsberger, O. Arcizet, Q. P. Unterreithmeier, R. Rivière, A. Schliesser, E. M. Weig, J. P. Kotthaus, and T. J. Kippenberg, "Near-field cavity optomechanics with nanomechanical oscillators," *Nature Physics*, vol. 5, pp. 909–914, Dec. 2009.

[123] R. Schilling, H. Schütz, A. H. Ghadimi, V. Sudhir, D. J. Wilson, and T. J. Kippenberg, "Near-Field Integration of a SiN Nanobeam and a SiO2 Microcavity for Heisenberg-Limited Displacement Sensing," *Physical Review Applied*, vol. 5, p. 054019, May 2016.

[124] G. Anetsberger, E. M. Weig, J. P. Kotthaus, and T. J. Kippenberg, "Cavity optomechanics and cooling nanomechanical oscillators using microresonator enhanced evanescent near-field coupling," *Comptes Rendus Physique*, vol. 12, pp. 800–816, Dec. 2011.

[125] E. Gavartin, P. Verlot, and T. J. Kippenberg, "A hybrid on-chip optomechanical transducer for ultrasensitive force measurements," *Nature Nanotechnology*, vol. 7, pp. 509–514, Aug. 2012.

[126] D. V. Thourhout and J. Roels, "Optomechanical device actuation through the optical gradient force," *Nature Photonics*, vol. 4, no. 4, pp. 211–217, 2010.

[127] M. Cai, O. Painter, and K. J. Vahala, "Observation of Critical Coupling in a Fiber Taper to a Silica-Microsphere Whispering-Gallery Mode System," *Physical Review Letters*, vol. 85, pp. 74–77, July 2000.

[128] S. M. Spillane, T. J. Kippenberg, O. J. Painter, and K. J. Vahala, "Ideality in a Fiber-Taper-Coupled Microresonator System for Application to Cavity Quantum Electrodynamics," *Physical Review Letters*, vol. 91, p. 043902, July 2003.

[129] M. L. Gorodetsky and V. S. Ilchenko, "Optical microsphere resonators: Optimal coupling to high-Q whispering-gallery modes," *JOSA B*, vol. 16, pp. 147–154, Jan. 1999.

[130] R. Pourabolghasem, A. Khelif, S. Mohammadi, A. A. Eftekhar, and A. Adibi, "Physics of band-gap formation and its evolution in the pillar-based phononic crystal structures," *Journal of Applied Physics*, vol. 116, p. 013514, July 2014.

[131] D. Feng, W. Jiang, D. Xu, B. Xiong, and Y. Wang, "Acoustic wave characterization of silicon phononic crystal plate," *Applied Physics Letters*, vol. 107, p. 091907, Aug. 2015.

[132] D. B. Sirdeshmukh, L. Sirdeshmukh, and K. G. Subhadra, "Lattice Vibrations," in *Atomistic Properties of Solids*, Springer Series in Materials Science, pp. 329–372, Springer, Berlin, Heidelberg, 2011.

[133] A. F. J. Levi, "Lattice Vibrations," IOP Publishing, 2016.

[134] F.-C. Hsu, J.-C. Hsu, T.-C. Huang, C.-H. Wang, and P. Chang, "Design of lossless anchors for microacoustic-wave resonators utilizing phononic crystal strips," *Applied Physics Letters*, vol. 98, p. 143505, Apr. 2011.

[135] F.-C. Hsu, J.-C. Hsu, T.-C. Huang, C.-H. Wang, and P. Chang, "Reducing support loss in micromechanical ring resonators using phononic band-gap structures," *Journal of Physics D: Applied Physics*, vol. 44, no. 37, p. 375101, 2011.

[136] C. M. Lin, J. C. Hsu, D. G. Senesky, and A. P. Pisano, "Anchor loss reduction in ALN Lamb wave resonators using phononic crystal strip tethers," in *2014 IEEE International Frequency Control Symposium (FCS)*, pp. 1–5, May 2014.

[137] H. Zhu and J. E. Y. Lee, "AlN piezoelectric on silicon MEMS resonator with boosted Q using planar patterned phononic crystals on anchors," in *2015 28th IEEE International Conference on Micro Electro Mechanical Systems (MEMS)*, pp. 797–800, Jan. 2015.

[138] L. Sorenson, J. Fu, and F. Ayazi, "Linear acoustic bandgap arrays for spurious mode suppression in piezoelectric MEMS resonators," in *2011 Joint Conference of the IEEE International Frequency Control and the European Frequency and Time Forum (FCS) Proceedings*, pp. 1–5, May 2011.

[139] M. Eichenfield, J. Chan, A. H. Safavi-Naeini, K. J. Vahala, and O. Painter, "Modeling dispersive coupling and losses of localized optical and mechanical modes in optomechanical crystals," *Optics Express*, vol. 17, p. 20078, Oct. 2009.

[140] R. A. Barton, B. Ilic, A. M. van der Zande, W. S. Whitney, P. L. McEuen, J. M. Parpia, and H. G. Craighead, "High, Size-Dependent Quality Factor in an Array of Graphene Mechanical Resonators," *Nano Letters*, vol. 11, pp. 1232–1236, Mar. 2011.

[141] I. H. Jafri, H. Busta, and S. T. Walsh, "Critical point drying and cleaning for MEMS technology," in *MEMS Reliability for Critical and Space Applications*, vol. 3880, pp. 51–59, International Society for Optics and Photonics, Aug. 1999.

[142] K. E. Bean and K. E. Bean, "Anisotropic etching of silicon," *IEEE Transactions on Electron Devices*, vol. 25, pp. 1185–1193, Oct. 1978.

[143] "3D CAD Design Software." https://www.solidworks.com/home-page.

[144] M. J. Süess, *Highly Strained Si and Ge Microand Nanobridges for Micro- and Optoelectronic Applications.* PhD thesis, ETH Zurich, 2014.

[145] J. Li, Z. Shan, and E. Ma, "Elastic strain engineering for unprecedented materials properties," *MRS Bulletin*, vol. 39, pp. 108–114, Feb. 2014.

[146] J. Feng, X. Qian, C.-W. Huang, and J. Li, "Strain-engineered artificial atom as a broad-spectrum solar energy funnel," *Nature Photonics*, vol. 6, pp. 866–872, Dec. 2012.

[147] P. R. Chidambaram, C. Bowen, S. Chakravarthi, C. Machala, and R. Wise, "Fundamentals of silicon material properties for successful exploitation of strain engineering in modern CMOS manufacturing," *IEEE Transactions on Electron Devices*, vol. 53, pp. 944–964, May 2006.

[148] D. Yu, J. Feng, and J. Hone, "Elastically strained nanowires and atomic sheets," *MRS Bulletin*, vol. 39, pp. 157–162, Feb. 2014.

[149] A. Castellanos-Gomez, R. Roldán, E. Cappelluti, M. Buscema, F. Guinea, H. S. J. van der Zant, and G. A. Steele, "Local Strain Engineering in Atomically Thin MoS2," *Nano Letters*, vol. 13, pp. 5361–5366, Nov. 2013.

[150] H. Yamaguchi, "GaAs-based micro/nanomechanical resonators," *Semiconductor Science and Technology*, vol. 32, no. 10, p. 103003, 2017.

[151] S. Manzeli, A. Allain, A. Ghadimi, and A. Kis, "Piezoresistivity and Strain-induced Band Gap Tuning in Atomically Thin MoS2," *Nano Letters*, vol. 15, pp. 5330–5335, Aug. 2015.

[152] M. Poggio, C. L. Degen, H. J. Mamin, and D. Rugar, "Feedback Cooling of a Cantilever's Fundamental Mode below 5 mK," *Physical Review Letters*, vol. 99, p. 017201, July 2007.

[153] M. Poggio and C. L. Degen, "Force-detected nuclear magnetic resonance: Recent advances and future challenges," *Nanotechnology*, vol. 21, no. 34, p. 342001, 2010.

[154] N. Matsumoto, K. Komori, Y. Michimura, G. Hayase, Y. Aso, and K. Tsubono, "5-mg suspended mirror driven by measurement-induced backaction," *Physical Review A*, vol. 92, p. 033825, Sept. 2015.

[155] J. a. P. Moura, R. A. Norte, J. Guo, C. Schäfermeier, and S. Gröblacher, "Centimeter-scale suspended photonic crystal mirrors," *Optics Express*, vol. 26, pp. 1895–1909, Jan. 2018.

[156] C. Lee, X. Wei, J. W. Kysar, and J. Hone, "Measurement of the Elastic Properties and Intrinsic Strength of Monolayer Graphene," *Science*, vol. 321, pp. 385–388, July 2008.

[157] Y. Tao, J. M. Boss, B. A. Moores, and C. L. Degen, "Single-crystal diamond nanomechanical resonators with quality factors exceeding one million," *Nature Communications*, vol. 5, p. 3638, Apr. 2014.

[158] G. D. Cole, W. Zhang, M. J. Martin, J. Ye, and M. Aspelmeyer, "Tenfold reduction of Brownian noise in high-reflectivity optical coatings," *Nature Photonics*, vol. 7, pp. 644–650, Aug. 2013.

[159] R. Fischer, N. S. Kampel, G. G. T. Assumpção, P.-L. Yu, K. Cicak, R. W. Peterson, R. W. Simmonds, and C. A. Regal, "Optical probing of mechanical loss of a Si_{3}N_{4} membrane below 100 mK," *arXiv:1611.00878 [cond-mat, physics:physics]*, Nov. 2016.

[160] M. Yuan, M. A. Cohen, and G. A. Steele, "Silicon nitride membrane resonators at millikelvin temperatures with quality factors exceeding 108," *Applied Physics Letters*, vol. 107, p. 263501, Dec. 2015.

[161] Q. A. Turchette, Kielpinski, B. E. King, D. Leibfried, D. M. Meekhof, C. J. Myatt, M. A. Rowe, C. A. Sackett, C. S. Wood, W. M. Itano, C. Monroe, and D. J. Wineland, "Heating of trapped ions from the quantum ground state," *Physical Review A*, vol. 61, p. 063418, May 2000.

[162] D. Lee, K. W. Lee, J. V. Cady, P. Ovartchaiyapong, and A. C. B. Jayich, "Topical review: Spins and mechanics in diamond," *Journal of Optics*, vol. 19, no. 3, p. 033001, 2017.

[163] C. L. Degen, F. Reinhard, and P. Cappellaro, "Quantum sensing," *Reviews of Modern Physics*, vol. 89, p. 035002, July 2017.

[164] I. Lauer, T. A. Langdo, Z. Y. Cheng, J. G. Fiorenza, G. Braithwaite, M. T. Currie, C. W. Leitz, A. Lochtefeld, H. Badawi, M. T. Bulsara, M. Somerville, and D. A. Antoniadis, "Fully depleted n-MOSFETs on supercritical thickness strained SOI," *IEEE Electron Device Letters*, vol. 25, pp. 83–85, Feb. 2004.

[165] T. J. Kippenberg, J. Kalkman, A. Polman, and K. J. Vahala, "Demonstration of an erbium-doped microdisk laser on a silicon chip," *Physical Review A*, vol. 74, p. 051802, Nov. 2006.

[166] T. J. Kippenberg, S. M. Spillane, D. K. Armani, and K. J. Vahala, "Fabrication and coupling to planar high-Q silica disk microcavities," *Applied Physics Letters*, vol. 83, pp. 797–799, July 2003.

[167] J. Chan, T. P. M. Alegre, A. H. Safavi-Naeini, J. T. Hill, A. Krause, S. Gröblacher, M. Aspelmeyer, and O. Painter, "Laser cooling of a nanomechanical oscillator into its quantum ground state," *Nature*, vol. 478, pp. 89–92, Oct. 2011.

[168] M. Eichenfield, J. Chan, R. M. Camacho, K. J. Vahala, and O. Painter, "Optomechanical crystals," *Nature*, vol. 462, pp. 78–82, Nov. 2009.

[169] X. M. H. Huang, C. A. Zorman, M. Mehregany, and M. L. Roukes, "Nanoelectromechanical systems: Nanodevice motion at microwave frequencies," *Nature*, vol. 421, p. 496, Jan. 2003.

[170] A. Schliesser, R. Rivière, G. Anetsberger, O. Arcizet, and T. J. Kippenberg, "Resolved-sideband cooling of a micromechanical oscillator," *Nature Physics*, vol. 4, pp. 415–419, May 2008.

[171] A. Schliesser, O. Arcizet, R. Rivière, G. Anetsberger, and T. J. Kippenberg, "Resolved-sideband cooling and position measurement of a micromechanical oscillator close to the Heisenberg uncertainty limit," *Nature Physics*, vol. 5, pp. 509–514, July 2009.

[172] J. D. Teufel, T. Donner, D. Li, J. W. Harlow, M. S. Allman, K. Cicak, A. J. Sirois, J. D. Whittaker, K. W. Lehnert, and R. W. Simmonds, "Sideband cooling of micromechanical motion to the quantum ground state," *Nature*, vol. 475, pp. 359–363, July 2011.

[173] K. Jensen, K. Kim, and A. Zettl, "An atomic-resolution nanomechanical mass sensor," *Nature Nanotechnology*, vol. 3, pp. 533–537, Sept. 2008.

[174] H. J. Mamin and D. Rugar, "Sub-attonewton force detection at millikelvin temperatures," *Applied Physics Letters*, vol. 79, pp. 3358–3360, Nov. 2001.

[175] P. Qin, H. Zhu, J. E. Y. Lee, and Q. Xue, "Phase Noise Reduction in a VHF MEMS-CMOS Oscillator Using Phononic Crystals," *IEEE Journal of the Electron Devices Society*, vol. 4, pp. 149–154, May 2016.

[176] X. M. H. Huang, X. L. Feng, C. A. Zorman, M. Mehregany, and M. L. Roukes, "VHF, UHF and microwave frequency nanomechanical resonators," *New Journal of Physics*, vol. 7, p. 247, Nov. 2005.

[177] M. Pandey, "Analysis of Entrainment and Clamping Loss in an Optically Actuated MEMS," Nov. 2007.

[178] D. T. Nguyen, C. Baker, W. Hease, S. Sejil, P. Senellart, A. Lemaître, S. Ducci, G. Leo, and I. Favero, "Ultrahigh Q-frequency product for optomechanical disk resonators with a mechanical shield," *Applied Physics Letters*, vol. 103, p. 241112, Dec. 2013.

[179] I. Wilson-Rae, "Intrinsic dissipation in nanomechanical resonators due to phonon tunneling," *Physical Review B*, vol. 77, p. 245418, June 2008.

[180] G. D. Cole, I. Wilson-Rae, K. Werbach, M. R. Vanner, and M. Aspelmeyer, "Phonon-tunnelling dissipation in mechanical resonators," *Nature Communications*, vol. 2, p. 231, Mar. 2011.

[181] J. Segovia-Fernandez, M. Cremonesi, C. Cassella, A. Frangi, and G. Piazza, "Anchor Losses in AlN Contour Mode Resonators," *Journal of Microelectromechanical Systems*, vol. 24, pp. 265–275, Apr. 2015.

[182] J. Segovia-Fernandez and G. Piazza, "Analytical and Numerical Methods to Model Anchor Losses in 65-MHz AlN Contour Mode Resonators," *Journal of Microelectromechanical Systems*, vol. 25, pp. 459–468, June 2016.

[183] Y.-H. Park and K. C. Park, "High-fidelity modeling of MEMS resonators. Part I. Anchor loss mechanisms through substrate," *Journal of Microelectromechanical Systems*, vol. 13, pp. 238–247, Apr. 2004.

[184] M. Li, H. X. Tang, and M. L. Roukes, "Ultra-sensitive NEMS-based cantilevers for sensing, scanned probe and very high-frequency applications," *Nature Nanotechnology*, vol. 2, pp. 114–120, Feb. 2007.

[185] P. Ivaldi, J. Abergel, M. H. Matheny, L. G. Villanueva, R. B. Karabalin, M. L. Roukes, P. Andreucci, S. Hentz, and E. Defaÿ, "50 nm thick AlN film-based piezoelectric cantilevers for gravimetric detection," *Journal of Micromechanics and Microengineering*, vol. 21, no. 8, p. 085023, 2011.

[186] Q. P. Unterreithmeier, E. M. Weig, and J. P. Kotthaus, "Universal transduction scheme for nanomechanical systems based on dielectric forces," *Nature*, vol. 458, pp. 1001–1004, Apr. 2009.

[187] "COMSOL Multiphysics® Modeling Software." https://www.comsol.com/.

[188] A. Frangi, A. Bugada, M. Martello, and P. T. Savadkoohi, "Numerical modelling of anchor losses in MEMS resonators," in *2012 13th International Thermal, Mechanical and Multi-Physics Simulation and Experiments in Microelectronics and Microsystems*, pp. 1/8–8/8, Apr. 2012.

[189] A. Frangi, A. Bugada, M. Martello, and P. T. Savadkoohi, "Validation of PML-based models for the evaluation of anchor dissipation in MEMS resonators," *European Journal of Mechanics - A/Solids*, vol. 37, pp. 256–265, Jan. 2013.

[190] D. S. Bindel and S. Govindjee, "Elastic PMLs for resonator anchor loss simulation," *International Journal for Numerical Methods in Engineering*, vol. 64, no. 6, pp. 789–818.

[191] R. N. Patel, C. J. Sarabalis, W. Jiang, J. T. Hill, and A. H. Safavi-Naeini, "Engineering Phonon Leakage in Nanomechanical Resonators," *Physical Review Applied*, vol. 8, Oct. 2017.

[192] D. T. Nguyen, W. Hease, C. Baker, E. Gil-Santos, P. Senellart, Aristide Lemaître, S. Ducci, G. Leo, and I. Favero, "Improved optomechanical disk resonator sitting on a pedestal mechanical shield," *New Journal of Physics*, vol. 17, no. 2, p. 023016, 2015.

Bibliography

[193] J. Chan, A. H. Safavi-Naeini, J. T. Hill, S. Meenehan, and O. Painter, "Optimized optomechanical crystal cavity with acoustic radiation shield," *Applied Physics Letters*, vol. 101, p. 081115, Aug. 2012.

[194] F.-C. Hsu, C.-I. Lee, J.-C. Hsu, T.-C. Huang, C.-H. Wang, and P. Chang, "Acoustic band gaps in phononic crystal strip waveguides," *Applied Physics Letters*, vol. 96, p. 051902, Feb. 2010.

[195] V. J. Gokhale and J. J. Gorman, "Approaching the intrinsic quality factor limit for micromechanical bulk acoustic resonators using phononic crystal tethers," *Applied Physics Letters*, vol. 111, p. 013501, July 2017.

[196] A. H. Safavi-Naeini and O. Painter, "Design of optomechanical cavities and waveguides on a simultaneous bandgap phononic-photonic crystal slab," *Optics Express*, vol. 18, pp. 14926–14943, July 2010.

[197] R. P. Feynman, "There's Plenty of Room at the Bottom," *Engineering and Science*, vol. 23, pp. 22–36, Feb. 1960.

[198] T. Zhu and J. Li, "Ultra-strength materials," *Progress in Materials Science*, vol. 55, pp. 710–757, Sept. 2010.

[199] M. Ringbauer, T. J. Weinhold, L. A. Howard, A. G. White, and M. R. Vanner, "Generation of mechanical interference fringes by multi-photon counting," *New Journal of Physics*, vol. 20, no. 5, p. 053042, 2018.

[200] "Golden Gate Bridge." http://goldengatebridge.org/research/factsGGBDesign.php.

[201] J. S. Levy, A. Gondarenko, M. A. Foster, A. C. Turner-Foster, A. L. Gaeta, and M. Lipson, "CMOS-compatible multiple-wavelength oscillator for on-chip optical interconnects," *Nature Photonics*, vol. 4, pp. 37–40, Jan. 2010.

[202] D. J. Moss, R. Morandotti, A. L. Gaeta, and M. Lipson, "New CMOS-compatible platforms based on silicon nitride and Hydex for nonlinear optics," *Nature Photonics*, vol. 7, pp. 597–607, Aug. 2013.

[203] M. H. P. Pfeiffer, J. Liu, A. S. Raja, T. Morais, B. Ghadiani, and T. J. Kippenberg, "Ultra-smooth silicon nitride waveguides based on the Damascene reflow process: Fabrication and loss origins," *Optica*, vol. 5, pp. 884–892, July 2018.

[204] R. D. Schilling, "Development of a monolithic near-field optomechanical system," 2018.

[205] E. Gavartin, "Optonanomechanical Systems for Measurement Applications," 2013.

[206] N. Barnes, "Silicon and SOI Wafer Supplier | Custom films & Processing | SVMI." https://www.svmi.com/.

[207] W. Kern, "The Evolution of Silicon Wafer Cleaning Technology," *Journal of The Electrochemical Society*, vol. 137, pp. 1887–1892, Jan. 1990.

[208] "Tanner L-Edit IC Layout." https://www.mentor.com/tannereda/l-edit.

[209] M. Parikh, "Corrections to proximity effects in electron beam lithography. I. Theory," *Journal of Applied Physics*, vol. 50, pp. 4371–4377, June 1979.

[210] "GenISys - BEAMER." https://www.genisys-gmbh.com/web/products/beamer.html.

[211] *Handbook of Silicon Based MEMS Materials and Technologies.* Elsevier, 2015.

[212] N. Luhmann, A. Jachimowicz, J. Schalko, P. Sadeghi, M. Sauer, A. Foelske-Schmitz, and S. Schmid, "Effect of oxygen plasma on nanomechanical silicon nitride resonators," *Applied Physics Letters*, vol. 111, p. 063103, Aug. 2017.

[213] D. K. Armani, T. J. Kippenberg, S. M. Spillane, and K. J. Vahala, "Ultra-high-Q toroid microcavity on a chip," *Nature*, vol. 421, pp. 925–928, Feb. 2003.

[214] K. J. Vahala, "Optical microcavities." https://www.nature.com/articles/nature01939, Aug. 2003.

[215] E. Verhagen, S. Deléglise, S. Weis, A. Schliesser, and T. J. Kippenberg, "Quantum-coherent coupling of a mechanical oscillator to an optical cavity mode," *Nature*, vol. 482, pp. 63–67, Feb. 2012.

[216] M. Eichenfield, R. Camacho, J. Chan, K. J. Vahala, and O. Painter, "A picogram- and nanometre-scale photonic-crystal optomechanical cavity," *Nature*, vol. 459, pp. 550–555, May 2009.

[217] J. D. Thompson, B. M. Zwickl, A. M. Jayich, F. Marquardt, S. M. Girvin, and J. G. E. Harris, "Strong dispersive coupling of a high-finesse cavity to a micromechanical membrane," *Nature*, vol. 452, pp. 72–75, Mar. 2008.

[218] R. W. Peterson, T. P. Purdy, N. S. Kampel, R. W. Andrews, P.-L. Yu, K. W. Lehnert, and C. A. Regal, "Laser Cooling of a Micromechanical Membrane to the Quantum Backaction Limit," *Physical Review Letters*, vol. 116, p. 063601, Feb. 2016.

[219] T. Rocheleau, T. Ndukum, C. Macklin, J. B. Hertzberg, A. A. Clerk, and K. C. Schwab, "Preparation and detection of a mechanical resonator near the ground state of motion," *Nature*, vol. 463, pp. 72–75, Jan. 2010.

[220] R. Kubo, "The fluctuation-dissipation theorem," *Reports on Progress in Physics*, vol. 29, no. 1, p. 255, 1966.

[221] B. U. Felderhof, "On the derivation of the fluctuation-dissipation theorem," *Journal of Physics A: Mathematical and General*, vol. 11, no. 5, p. 921, 1978.

[222] J. Weber, "Fluctuation Dissipation Theorem," *Physical Review*, vol. 101, pp. 1620–1626, Mar. 1956.

[223] I. Marinkovic, A. Wallucks, R. Riedinger, S. Hong, M. Aspelmeyer, and S. Gröblacher, "An optomechanical Bell test," *arXiv:1806.10615 [cond-mat, physics:physics, physics:quant-ph]*, June 2018.

[224] R. Riedinger, A. Wallucks, I. Marinkovic, C. Löschnauer, M. Aspelmeyer, S. Hong, and S. Gröblacher, "Remote quantum entanglement between two micromechanical oscillators," *arXiv:1710.11147 [cond-mat, physics:physics, physics:quant-ph]*, Oct. 2017.

[225] R. Riedinger, S. Hong, R. A. Norte, J. A. Slater, J. Shang, A. G. Krause, V. Anant, M. Aspelmeyer, and S. Gröblacher, "Non-classical correlations between single photons and phonons from a mechanical oscillator," *Nature*, vol. 530, pp. 313–316, Feb. 2016.

[226] M. L. Gorodetsky, A. Schliesser, G. Anetsberger, S. Deleglise, and T. J. Kippenberg, "Determination of the vacuumoptomechanical coupling rate usingfrequency noise calibration," *Optics Express*, vol. 18, pp. 23236–23246, Oct. 2010.

[227] A. H. Safavi-Naeini, T. P. M. Alegre, J. Chan, M. Eichenfield, M. Winger, Q. Lin, J. T. Hill, D. E. Chang, and O. Painter, "Electromagnetically induced transparency and slow light with optomechanics," *Nature*, vol. 472, pp. 69–73, Apr. 2011.

[228] C. A. Regal, J. D. Teufel, and K. W. Lehnert, "Measuring nanomechanical motion with a microwave cavity interferometer," *Nature Physics*, vol. 4, pp. 555–560, July 2008.

[229] J. D. Teufel, T. Donner, M. A. Castellanos-Beltran, J. W. Harlow, and K. W. Lehnert, "Nanomechanical motion measured with an imprecision below that at the standard quantum limit," *Nature Nanotechnology*, vol. 4, pp. 820–823, Dec. 2009.

[230] J. Cripe, N. Aggarwal, R. Lanza, A. Libson, R. Singh, P. Heu, D. Follman, G. D. Cole, N. Mavalvala, and T. Corbitt, "Observation of a room-temperature oscillator's motion dominated by quantum fluctuations over a broad audio-frequency band," *arXiv:1802.10069 [quant-ph]*, Feb. 2018.

[231] P. E. Barclay, K. Srinivasan, and O. Painter, "Nonlinear response of silicon photonic crystal microresonators excited via an integrated waveguide and fiber taper," *Optics Express*, vol. 13, pp. 801–820, Feb. 2005.

[232] A. H. Safavi-Naeini, S. Gröblacher, J. T. Hill, J. Chan, M. Aspelmeyer, and O. Painter, "Squeezed light from a silicon micromechanical resonator," *Nature*, vol. 500, pp. 185–189, Aug. 2013.

[233] A. G. Krause, T. D. Blasius, and O. Painter, "Optical read out and feedback cooling of a nanostring optomechanical cavity," *arXiv:1506.01249 [physics, physics:quant-ph]*, June 2015.

[234] M. D'Agostino, "Focus: Schrödinger's Drum," *Physics*, vol. 22, Nov. 2008.

[235] T. P. Purdy, P.-L. Yu, R. W. Peterson, N. S. Kampel, and C. A. Regal, "Strong Optomechanical Squeezing of Light," *Physical Review X*, vol. 3, p. 031012, Sept. 2013.

[236] T. J. Kippenberg and K. J. Vahala, "Cavity Opto-Mechanics," *Optics Express*, vol. 15, pp. 17172–17205, Dec. 2007.

[237] A. Schliesser, G. Anetsberger, R. Rivière, O. Arcizet, and T. J. Kippenberg, "High-sensitivity monitoring of micromechanical vibration using optical whispering gallery mode resonators," *New Journal of Physics*, vol. 10, no. 9, p. 095015, 2008.

[238] G. Anetsberger, R. Rivière, A. Schliesser, O. Arcizet, and T. J. Kippenberg, "Ultralow-dissipation optomechanical resonators on a chip," *Nature Photonics*, vol. 2, pp. 627–633, Oct. 2008.

[239] B. Djafari-Rouhani, S. El-Jallal, and Y. Pennec, "Phoxonic crystals and cavity optomechanics," *Comptes Rendus Physique*, vol. 17, pp. 555–564, May 2016.

[240] D. K. Biegelsen, "Photoelastic Tensor of Silicon and the Volume Dependence of the Average Gap," *Physical Review Letters*, vol. 32, pp. 1196–1199, May 1974.

[241] V. R. Almeida, R. R. Panepucci, and M. Lipson, "Nanotaper for compact mode conversion," *Optics Letters*, vol. 28, pp. 1302–1304, Aug. 2003.

[242] M. Davanço, S. Ates, Y. Liu, and K. Srinivasan, "Si 3 N 4 optomechanical crystals in the resolved-sideband regime," *Applied Physics Letters*, vol. 104, p. 041101, Jan. 2014.

[243] K. E. Grutter, M. I. Davanço, and K. Srinivasan, "Slot-mode optomechanical crystals: A versatile platform for multimode optomechanics," *Optica*, vol. 2, p. 994, Nov. 2015.

[244] S. M. Meenehan, J. D. Cohen, S. Gröblacher, J. T. Hill, A. H. Safavi-Naeini, M. Aspelmeyer, and O. Painter, "Silicon optomechanical crystal resonator at millikelvin temperatures," *Physical Review A*, vol. 90, p. 011803, July 2014.

[245] P. E. Barclay, K. Srinivasan, and O. Painter, "Design of photonic crystal waveguides for evanescent coupling to optical fiber tapers and integration with high-Q cavities," *JOSA B*, vol. 20, pp. 2274–2284, Nov. 2003.

[246] R. A. Norte, *Nanofabrication for On-Chip Optical Levitation, Atom-Trapping, and Superconducting Quantum Circuits.* Phd, California Institute of Technology, 2015.

[247] "ANSYS HFSS: High Frequency Electromagnetic Field Simulation Software." //www.ansys.com/products/electronics/ansys-hfss.

[248] S. S. Verbridge, R. Ilic, H. G. Craighead, and J. M. Parpia, "Size and frequency dependent gas damping of nanomechanical resonators," *Applied Physics Letters*, vol. 93, p. 013101, July 2008.

Bibliography

[249] S. A. Fedorov, V. Sudhir, R. Schilling, H. Schütz, D. J. Wilson, and T. J. Kippenberg, "Evidence for structural damping in a high-stress silicon nitride nanobeam and its implications for quantum optomechanics," *Physics Letters A*, vol. 382, pp. 2251–2255, Aug. 2018.

[250] S. Bianco, M. Cocuzza, S. Ferrero, E. Giuri, G. Piacenza, C. F. Pirri, A. Ricci, L. Scaltrito, D. Bich, A. Merialdo, P. Schina, and R. Correale, "Silicon resonant microcantilevers for absolute pressure measurement," *Journal of Vacuum Science & Technology B: Microelectronics and Nanometer Structures Processing, Measurement, and Phenomena*, vol. 24, pp. 1803–1809, June 2006.

[251] D. M. Karabacak, V. Yakhot, and K. L. Ekinci, "High-Frequency Nanofluidics: An Experimental Study Using Nanomechanical Resonators," *Physical Review Letters*, vol. 98, p. 254505, June 2007.

[252] F. R. Blom, S. Bouwstra, M. Elwenspoek, and J. H. J. Fluitman, "Dependence of the quality factor of micromachined silicon beam resonators on pressure and geometry," *Journal of Vacuum Science & Technology B: Microelectronics and Nanometer Structures Processing, Measurement, and Phenomena*, vol. 10, pp. 19–26, Jan. 1992.

[253] K. Brueckner, V. Cimalla, F. Niebelschütz, R. Stephan, K. Tonisch, O. Ambacher, and M. A. Hein, "Strain- and pressure-dependent RF response of microelectromechanical resonators for sensing applications," *Journal of Micromechanics and Microengineering*, vol. 17, no. 10, p. 2016, 2007.

[254] L.D. Landau & E.M. Lifshitz, *Fluid Mechanics*.

[255] M. Bao, H. Yang, H. Yin, and Y. Sun, "Energy transfer model for squeeze-film air damping in low vacuum," *Journal of Micromechanics and Microengineering*, vol. 12, no. 3, p. 341, 2002.

[256] "Kurt J. Lesker Company | CF Flanges Technical Notes | Vacuum Science Is Our Business." https://www.lesker.com/newweb/flanges/flanges_technicalnotes_conflat_1.cfm.

[257] "Conductance." https://www.pfeiffer-vacuum.com/en/know-how/introduction-to-vacuum-technology/fundamentals/conductance/.

Amir H. Ghadimi

Personal Data

Date of Birth:	28 May 1989
Address:	Rue de la Blancherie 34, 1022 Chavannes-près-Renens, Switzerland
Phone:	+41 (0) 78 635 51 23
email:	amirh.ghadimi@gmail.com , amir.ghadimi@epfl.ch
LinkedIn:	https://www.linkedin.com/in/amir-hossein-ghadimi
Skype ID:	amirh.ghadimi

Research Interests

Precision measurement, Quantum optomechanics, High Q mechanical resonators and their applications, Optical frequency COMB, Sensitive accelerometers, Integrated photonics, MEMS

Education

2012 - 2018 **PhD.** in **Electrical Engineering**
Swiss Federal Institute of Technology (EPFL), Switzerland
Dissertation: "Ultra-coherent nano-mechanical resonators for quantum optomechanics at room temperature."
Advisor: Tobias Kippenberg
Committee : Michael Roukes, Guillermo Villanueva, Phillip Feng, Christophe Moser

2009 - 2012 **B.Sc.** in **Physics** | Double Major (GPA 5.25/6)
Sharif University of Technology (SUT), Iran

2007 - 2012 **B.Sc.** in **Electrical Engineering, Electronics** | Double Major (GPA 5.25/6)
Sharif University of Technology (SUT), Iran
Thesis: "Laser-superconductor interaction modeling on non-uniform time variant transmission lines"

Professional Experience

Nov 2018-present Postdoc research scientist in the group of Prof. Dalziel Wilson in college of optical science at university of Arizona (Pending US VISA).
Project: Developing new cryogenic cavity optomechanics experiment.

Fall 2017 Organizer of FEM simulation workshops as part of OMT-ETN H2020 Marie Curie Network

Summer 2014 Organizer of FEM simulation workshops as part of CQOM-INT Marie Curie Network

Jun-Sep 2012 Summer research internship at Deutsche Electron Synchrotron (DESY)

Jun-Sep 2011 Summer research internship at CERN

Sep 2007 - June 2012 Teaching assistant in Sharif University of Technology for General physics, Electromagnetic I &II, Electronics circuits I &II &III, Digital electronics and FGPA

Sep 2005 - June 2012 Physics Olympiad teacher at Farzanegan high school

Awards and Honors

Oct 2018 Fellowship at Swiss Center for Electronics and Microtechnology (CSEM)
June 2018 Swiss Nanotechnology **best PhD award** at Swiss nano convention
April 2018 **Best paper award** at 2018 European time and frequency forum
Nov. 2017 Awarded fellowship to join AIT camp at Brazil organized by venture lab
Mar. 2012 **Ranked 23rd** among about 100,000 participants in the nationwide university entrance exam for master degree in electrical engineering
2007-2012 Awarded scholarship from Iran National Elite Foundation,
Oct. 2007 Awarded Dean's Honor by Prof. S. Sohrabpour, the president of Sharif University of Technology
Sep. 2007 **Ranked 12th** among about 500,000 participants in the nationwide university entrance exam for bachelor degree in electrical engineering

207

PUBLICATIONS

- **A.H. Ghadimi**, S.A. Fedorov, N.J. Engelsen, M.J. Bereyhi, R. Schilling, D.J. Wilson, T.J. Kippenberg. "Elastic strain engineering for ultralow mechanical dissipation",
  Science, eaar6939, 2018

- **A.H. Ghadimi**, D.J. Wilson, T.J. Kippenberg. "Radiation and internal loss engineering of high-stress silicon nitride nanobeams",
  Nano letter, Vol 17, Issue 6, pp 3501–3505, 2017

- M.J. Bereyhi, A Beccari, S.A. Fedorov, **A.H. Ghadimi**, R. Schilling, D.J. Wilson, N.J. Engelsen, T.J. Kippenberg. "Clamp-tapering increases the quality factor of stressed nanobeams",
  Arxiv, arXiv:1810.00414, 2018

- S.A. Fedorov, N.J. Engelsen, **A.H. Ghadimi**, M.J. Bereyhi, R. Schilling, D.J. Wilson, T.J. Kippenberg. "Generalized dissipation dilution in strained mechanical resonators",
  Arxiv, arXiv:1807.07086, 2018

- V. Sudhir, D.J. Wilson, R. Schilling, H. Schütz, S.A. Federov, **A.H. Ghadimi**, A. Nunnenkamp, T.J. Kippenberg. "Appearance and Disappearance of Quantum Correlations in Measurement-Based Feedback Control of a Mechanical Oscillator",
  Physical Review X, Vol. 7, Issue 1, 2017

- R. Schilling, H. Schütz, **A.H. Ghadimi**, V. Sudhir, D.J. Wilson, T.J. Kippenberg. "Near-Field Integration of a SiN Nanobeam and a SiO$_2$ Microcavity for Heisenberg-Limited Displacement Sensing",
  Physical Review Applied, Vol. 5, Issue 5, 2016

- D.J. Wilson, V. Sudhir, N. Piro, R. Schilling, **A.H. Ghadimi**, T.J. Kippenberg. "Measurement-based control of a mechanical oscillator at its thermal decoherence rate",
  Nature, Vol. 524, pp. 325-329, 2015

- S. Manzeli, A. Allain, **A.H. Ghadimi**, A. Kis. "Piezoresistivity and strain-induced band gap tuning in atomically thin MoS2",
  Nano letter, Vol. 15, pp. 5330–5335, 2015

RESEARCH HIGHLIGHTS (CHRONOLOGICAL)

- State-of-the-art low-noise readout of nanomechanical motion [Nature 2015]: imprecision 40 dB below that at the SQL and measurement rate approaching the thermal decoherence rate.

- Measurement-based feedback cooling of a solid state mechanical oscillator to near its motional ground state ($n \sim 5$ phonons) [Nature 2015].

- Demonstration of Piezoresistivity and bandgap tuning by strain in MoS$_2$ 2D atomic sheets [Nano letter 2016].

- Monolithic integration of near-field optomechanical system based on high Q optical disk resonators and Si$_3$N$_4$ beams with $C_0 \sim 1$ [APL 2016].

- Observing the first quantum coherent string shape resonators at room temperature ($Q \times f \sim 10^{13} Hz > \frac{k_B T}{h}$) [Nano letter 2017].

- Demonstrating the radiation shielding for VHF-UHF mechanical resonators via 1D phononic crystals [Nano letter 2017].

- Observation of quantum measurement back-action (radiation pressure shot noise) and strong imprecision-backaction correlations (ponderomotive light squeezing and motional sideband asymmetry) in a feedback-stabilized optomechanical system [PRX 2017].

- Observation of radiation pressure shot noise and imprecision-backaction correlations in a room temperature optomechanical system [PRX 2017].

- UHQ nanomechanics: Use of strain-engineering to realize solid state mechanical oscillators with unprecedented Q factors (8×10^8) and $Q \times f$ product (10^{15} Hz) at room temperature [Science 2018].

- Generalized theory of dissipation dilution in high strained resonators for arbitrary mode shape and geometry [Arxiv 2018].

- Demonstration of Q enhancement due to tapering of clamping point [Arxiv 2018].

Technical Skills

Micro/Nano fabrication	• Expert in photonic integration (Optical high Q micro-cavities, photonic crystals, waveguide coupling, Si and Si_3N_4 passive optics on chip) • Expert in MEMS devices (Ultra high Q mechanical resonators, liquid and gas phase undercut, stress/strain engineering and etc.) • Expert in lithography techniques (e-beam lithography, deep UV photo-lithography and mask design) • Expert in etching techniques (RIE etching techniques, IBE, FIB, Bosch processing, CMP polishing) • Expert in thin film deposition (Metal evaporation, sputtering, LPCVD and etc.) • Expert in standard metrology tools (SEM, EDX, AFM, mechanical and optical profilometry, ellipsometry and etc.)
FEM simulations	• Experts in mechanical, optical, microwave simulations, H-spice, radiation patterns and loss modeling. • Advance experience with COSMOL, ANSYS, Sonet, H.Spice
Optics (free space, fiber and integrated)	• Free space and fiber based optical circuits (AOM, EOM, polarization optics and etc.) • Optical interrogation techniques such as interferometry • Homodyne/Hetrodyne detection • Locking/tracking techniques • Optical feedback control of mechanical oscillators

Languages

Persian:	Native
English:	Fluent
French:	Basic

References

Prof. Tobias Kippenberg:	Head of laboratory of LPQM at EPFL, PhD Thesis Advisor. Phone: +41 (0) 21 693 44 28, Email: tobias.kippenberg@epfl.ch
Prof. Dalziel Wilson:	Professor of Optical Sciences, at university of Arizona, The lab senior Scientist and project manager during my PhD at EPFL. Phone: +1 (520) 621-2584, Email: dalziel@optics.arizona.edu
Prof. Guillermo Villanueva:	Head of Advance MEMS group at EPFL, PhD Thesis mentor and thesis committee. Phone: +41 (0) 21 693 11 87, Email: guillermo.villanueva@epfl.ch
Prof. Khashayar Mehrany:	Professor at Sharif university of technology (SUT), BSc Thesis Advisor. Phone: +98 (0) 21 66 164 326, Email: mehrany@sharif.edu